Cranfield University
College of Aeronautics

Ph.D. Thesis
Academic Year 1993-94

Holger Babinsky

A Study of Roughness in Turbulent Hypersonic Boundary-Layers

Supervisor: Dr. J. A. Edwards

December 1993

This thesis is submitted in partial fulfilment of the requirements for the Degree of Doctor of Philosophy

Abstract

The influence of large scale regular roughness on a Mach 5 turbulent boundary layer and a compression corner was investigated on axisymmetric wind tunnel models. Three types of roughness were examined; a series of square cavities at two different sizes and a 45 degree sawtooth. Typical sizes ranged from 50% to 100% of an undisturbed boundary layer thickness. The roughness was limited to a short region followed by a smooth surface. Compression corners were formed by 15° and 20° flares located downstream of the roughness. The flow in the wind tunnel was investigated in detail to obtain knowledge on operating conditions and flow quality. Liquid crystal thermography was developed for routine use in hypersonic blow-down wind tunnels with superior spatial resolution and experimental uncertainties in the range of traditional techniques.

The effect on flow parameters downstream of the last roughness element were found to differ significantly for the different quantities. Velocity profiles were found to be less full and skin friction was found to be reduced for all streamwise distances. Surface heat transfer was increased in a short region limited to 1.5 boundary layer thicknesses behind the roughness whereas surface pressure was not affected. Sawtooth shaped roughness was found to cause a stronger disturbance than square cavities of twice the size. Little influence of the roughness was noted on the flow over the compression corner. The flow over the 20° compression corner showed an increase in upstream influence for the sawtooth shaped roughness as well as the larger cavities. Surface pressure measurements did not indicate a separation in any case. Heat transfer measurements revealed a peak located approximately 0.25 boundary layer thicknesses behind the corner. No such feature was found in the surface pressure distributions. It is suggested that a small scale separation is located very close to the corner causing the peak in heat transfer at reattachment without any effect on surface pressures. The existence of such a separation has been confirmed by surface flow visualisations for both flares.

Acknowledgements

The list of people who have helped (not always voluntarily) to achieve the results presented in this thesis is so long that I start wondering if I have done any work myself. Nevertheless I want to try to mention most.

Firstly there is my supervisor Dr. John Edwards who managed to give me support when I was demoralised because the windtunnel flow turned out to be nothing like the textbooks say and who brought me back to earth when I felt as if I deserved the Nobel prize for taking a decent schlieren photograph. Most importantly he gave me the freedom to try and do things my way. I want to extend my thanks to the DRA who supported this work under Contract No. 2028/203/RARDE(FH).

I was very lucky to have the opportunity to discuss a number of the issues cropping up in this thesis with Prof. George Inger. He came to Cranfield as a visiting Professor and ended up spending many tea-breaks talking to me. Another thankyou has to go to Prof. John Stollery who always found time in his busy schedule to discuss my work and offer useful advise.

The single person who has contributed most of his time to this thesis (apart from me that is) is David Brant at DRA Fort Halstead. He spent weeks, probably months sitting next to me at the windtunnel and never got bored pushing the right buttons at the right time. I also want to thank everybody else at Fort Halstead, particularly Dr. K.C.Phan and the technical staff for their support.

I believe we have often been able to successfully use techniques which were new to Cranfield. This was only possible due to the superb design and very careful, not to say pedantic, manufacturing. I must give a particularly big thankyou to everyone in our workshop.

Table of Contents

1. Introduction 1

2. Experimental Facilities and Measurement Techniques 9
   2.1 The College of Aeronautics Hypersonic Gun Tunnel 10
   2.2 The DRA Fort Halstead HSST 11
   2.3 Measuring Equipment 13
      2.3.1 Data Acquisition Hardware 13
      2.3.2 Traverse Rig 13
      2.3.3 Reservoir, Pitot and Static Pressure Measurements 16
      2.3.4 Total Temperature Measurement 19
      2.3.5 Boundary Layer Profiles 21
      2.3.6 Accuracy of Measurements 30
   2.4 Calibration of the HSST 34
      2.4.1 Reservoir Pressure 34
      2.4.2 Total Temperature 35
      2.4.3 Pitot Pressure 38
      2.4.4 Summary and Conclusions 45

3. Heat Transfer Measurement 48
   3.1 Traditional Techniques 48
   3.2 Liquid Crystal Thermography 53
      3.2.1 Overview 53
      3.3.2 Automatic Colour Detection 55
      3.3.3 Colour Temperature Calibration 61
      3.3.4 Determination of Surface Heat Transfer 68
      3.3.5 Accuracy of Measurements 74

4. Experimental Investigation of Large Scale Roughness 77
   4.1 Models and Configurations 77
   4.2 Schlieren Pictures 80
   4.3 Surface Pressure Measurements 81
   4.4 Boundary-Layer Profiles 84
   4.5 Surface Heat Transfer 89

5. Conclusions 119

6. References 122

7. Tables 129

Nomenclature

A	Constant in boundary layer profile formula (eq. 2.11)
a^*	Factor in VanDriest compressibility transformation (eq. 2.4)
B	Constant in boundary layer profile formula (eq. 2.11) or intensity of blue signal
b^*	Factor in VanDriest compressibility transformation (eq. 2.4)
c	Specific heat
C_p	Specific heat at constant pressure
c_f	Skin friction coefficient $\frac{2\tau_w}{\rho_e u_e^2}$
C_H	Heat transfer coefficient $\frac{\dot{q}}{\rho_e u_e C_p (T_0 - T_w)}$
C^*	Constant in law of the wall
G	Intensity of red signal
H	Hue
I	Intensity or brightness
k	Constant in law of the wall or thermal conductivity
M	Mach number
p	Pressure
Pr	Prandtl number
$\mathring{q}$	Surface heat transfer per unit area
R	Ideal gas constant or intensity of red signal
r	Recovery factor
Re	Reynolds number
Re_H	Reynolds number based on probe height

$Re\delta_2$	Reynolds number based on boundary layer momentum thickness
St	Stanton number $\frac{\dot{q}}{\rho_e u_e C_p (T_{aw} - T_w)}$
T	Temperature
T_H	Heater temperature
T_s	Surface temperature increase
t	Time
u	Velocity in x-direction
u_τ	Shear velocity $\sqrt{\frac{\tau_w}{\rho_w}}$
u^+	Velocity in law of the wall coordinates
u^*	Transformed velocity (eq. 2.4)
W	Coles' wake function
x	x-coordinate, usually measured from the hingeline
y	y-coordinate, usually measured from the surface
y^+	law of the wall variable $\frac{y u_\tau}{\nu_w}$
α	Thermal diffusivity
γ	Ratio of specific heats
δ	Boundary layer thickness
ν	kinematic viscosity
Π	Wake parameter
τ	Surface shear stress or integration variable in heat transfer equations
ρ	Density

Subscript

$_a$	Adiabatic
$_e$	Condition at boundary layer edge
$_p$ or $_{pit}$	Pitot
$_{res}$	Reservoir conditions
$_s$	Conditions at surface
$_w$	Conditions at wall
$_0$	Total conditions or reference conditions
$_\infty$	Free stream conditions or conditions for $t \mapsto \infty$

Superscript

$\bar{}$	Mean property

Coordinate system:

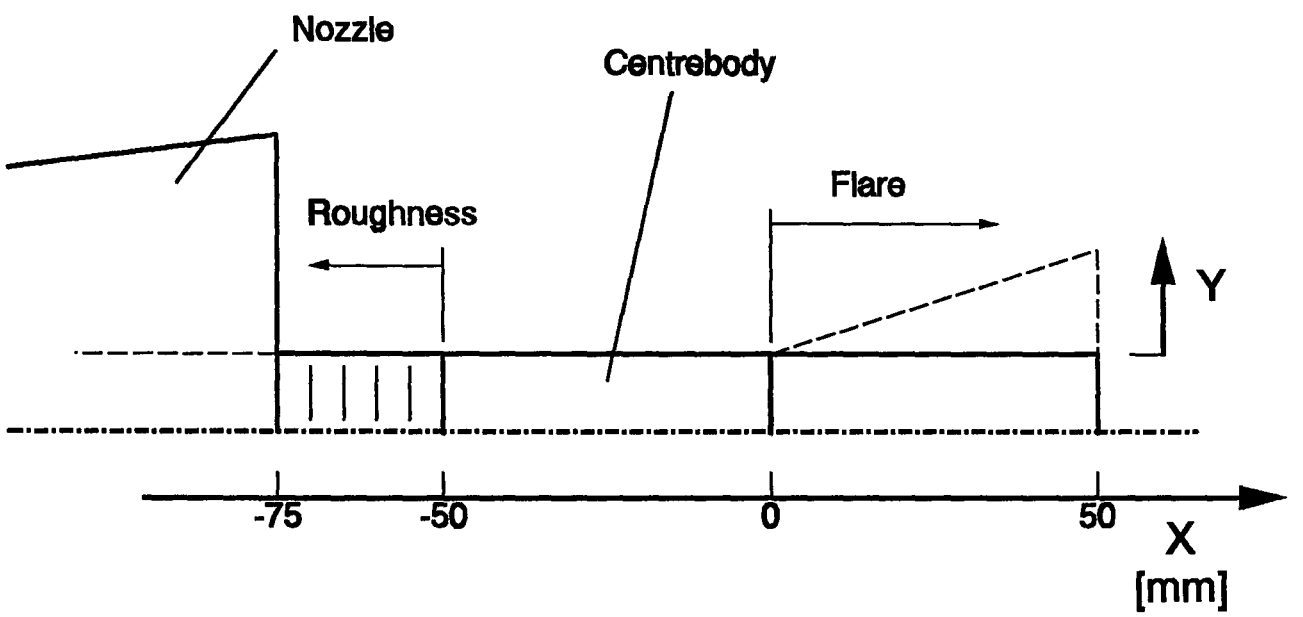

1. Introduction

In recent years the area of hypersonic aerodynamics has gained more importance as the number of practical applications has increased[1]. The first man made object to reach hypersonic velocities was a second stage that had been added to a V-2, while re-entering into the atmosphere. This took place on February 24th, 1949 at White Sands in the USA. From there progress has been remarkable. The first plane to reach speeds above Mach 5 was the American X-15 in 1961. The main application for hypersonic aerodynamics, however, remained the re-entry of spacecraft into the earth's atmosphere. This domain is usually dominated by blunt objects in free fall with relatively little control over their flight path.

With the Space Shuttle, the first re-entry configuration resembling an aircraft has been developed. It is re-usable and has significant control over its flight path. This has lead to a host of new developments and ideas, such as hypersonic passenger transport and the next generation of satellite launchers. A major effort has been started in the USA with the development of the National Aero-Space Plane (NASP) and similar projects exist all over the world such as the Sänger programme in Germany and the Japanese Hope. The problems involved in these developments, however, are huge and have recently caused a significant down-scaling of the intended aims of these projects.

Apart from the area of space flight, it is weapons technology that has been the ground for an increasing interest in hypersonic aerodynamics. Future generations of missiles and projectiles are expected to enter the domain of high Mach numbers and encounter very similar problems to the ones highlighted by research into space craft and hypersonic airplanes.

These new applications have increased the importance of research into hypersonic flow around control surfaces such as fins and flaps. Problems of flow separation due to adverse pressure gradients combined with the high shear stresses and, above all, heat transfer rates associated with re-attachment have become the focus of attention and a large amount of research has been directed to investigate these effects on relatively simple configurations. The advances in computational fluid dynamics (CFD) have helped to study these problems. The most successful approach is often a combination of experimental and computational techniques.

In the real world, however, things are not always as ideal as the models in the wind tunnels and CFD simulations. Between a full scale flying object and the equivalent model lie a host of developments and other considerations than just the aerodynamics have to be met to achieve a working solution. One of these difficulties is the area of surface roughness. From an aerodynamic point of view it is best avoided altogether but this may not always be possible. Machined

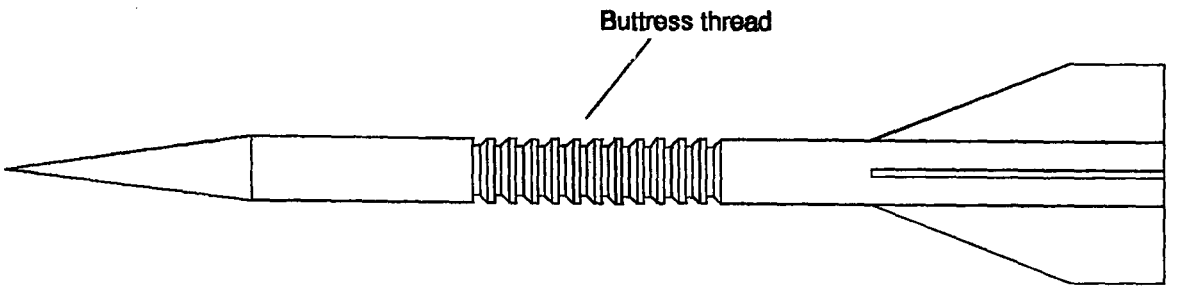

Fig. 1.1 Simplified drawing of a generic projectile, showing the location and relative size of the buttress thread.

surfaces always exhibit a certain degree of non-uniformity that may influence the aerodynamic performance. This type of surface roughness is usually very small compared to aerodynamic parameters such as the boundary layer thickness. The roughnesses to be addressed here belong to the group of large scale roughnesses where a typical dimension is comparable to the boundary layer thickness. One examples of such a roughness is found in the heat shield of the Space Shuttle orbiter. This shield is necessary for thermal protection during re-entry but for engineering reasons it consists of a large number of tiles with small gaps between them, thus giving cavities in the smooth surface. The problem that gave rise to this thesis comes from a different application, a hypersonic projectile. A sketch of such a device is seen in Fig. 1.1. It can be seen that an area of rather large thread-like roughness exists in the centre of the cylindrical part of the projectile. These buttress-threads are necessary to allow the projectile to be housed in an outer shell (sabot) which transmits the acceleration forces during the firing from a gun. Once the projectile leaves the gun barrel, aerodynamic forces split the sabot and it is removed from the projectile. The flight of such projectiles is usually at sea level and very high velocities, entering the hypersonic regime. This requires the investigation of this subject for turbulent boundary layers.

The buttress threads are of the order of a boundary layer thickness in depth and therefore have a significant impact on the flow in this region. There are usually control surfaces or stabilisers downstream of this roughness such as fins or flares. These elements are the origin of regions of adverse pressure gradients and can cause flow separation.

The flow situation that is to be investigated is sketched in Fig. 1.2. An oncoming turbulent boundary layer encounters a step change in surface roughness from smooth to rough. In this rough region the boundary layer parameters will change and the profile emerging at the end of the roughness is significantly different from an undisturbed turbulent boundary layer profile. Downstream of the roughness the boundary layer will relax towards a smooth surface profile. Finally a region of adverse pressure gradient is encountered. The flow behaviour through this

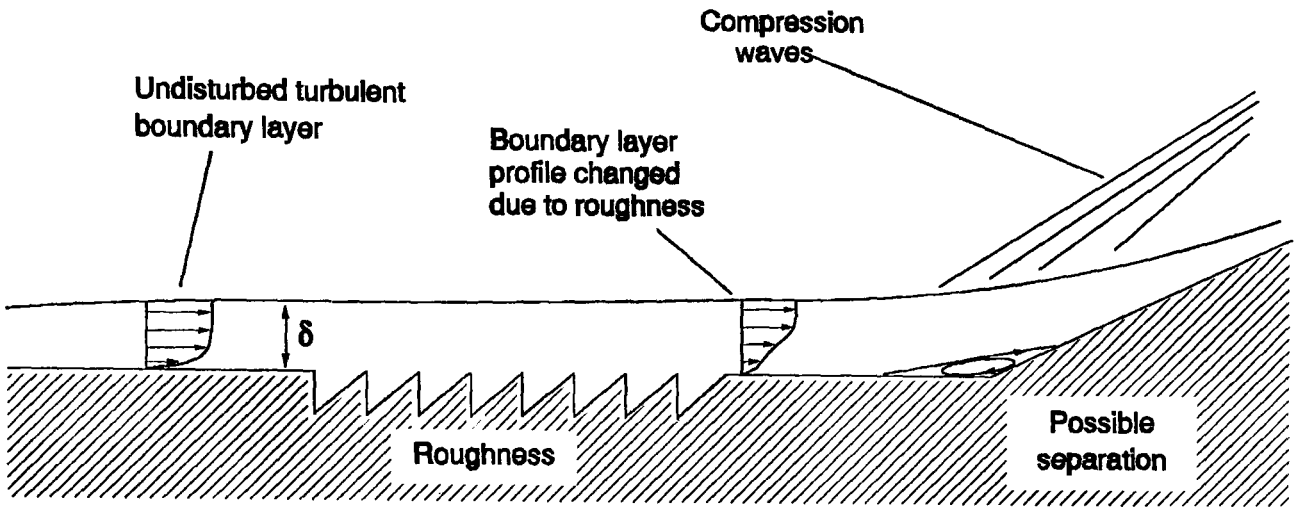

Fig. 1.2 Schematic flow over roughness and downstream adverse pressure gradient

interaction is expected to be dependant on the shape of the oncoming boundary layer which is modified by the roughness. This can cause severe changes in the flowfield and associated parameters. If a flow separation is encountered the effectiveness of control surfaces or stabilising elements will be severely reduced due to the widening of the interaction. Surface heat transfer can reach very large values at re-attachment. The sensitivity of the flow to changes in the oncoming boundary layer profile is studied in this thesis.

The first problem to be addressed is the effect of large scale roughness on a compressible turbulent boundary layer. Due to the small amount of research available on this topic the experience gained in incompressible flow and for small scale roughness can provide some insight into the basic mechanisms. Turbulent boundary layer profiles in incompressible flows have been found to be correctly described in certain parts of the boundary layer by an analytic expression known as the log-law[2]. The influence of surface roughness on the profile shape has been investigated by Nikuradse[3] who introduced a sandgrain roughness parameter. This allows the computation of boundary layer profiles over rough surfaces using the log-law. The range of validity can be extended to roughnesses of any given shape by representing them in terms of an equivalent sandgrain roughness. Some work has been done to include large scale roughnesses in this fashion. Antonia et al[4,5] investigated the response of an incompressible turbulent boundary layer to a step change in roughness from a smooth wall to a surface covered with regularly spaced cavities. They concluded that it takes less than 20 boundary layer thicknesses for the velocity profile to change to the equivalent rough profile. The effective changes in the velocity profile are similar to those encountered by Grass et al[6] over similar surfaces. In log-law coordinates the effective origin of the velocity profile lies below the peaks of the roughness elements and the velocities are displaced to lower values in the region of validity of the law of the wall. These two effects are the 'shift of origin' (Δy) and the

'velocity shift' or velocity defect ($\Delta u/u_\tau$) and can be found similarly for sandgrain roughness. In physical coordinates the velocity profile will appear to be less full due to these changes. To express these effects in terms of the theoretical treatment of the equivalent sandgrain roughness, correlations have been developed by those authors and others in similar cases[7].

By using a transformation function the validity of the log law can be extended to compressible flows as shown by several investigators such as Winter and Gaudet[8,9,10] and Fernholz and Finley[11]. Laganelli and Scaggs[12] extend the equivalent sandgrain methodology to compressible flow. Due to the difficulties associated with measurements in supersonic flows, investigations of roughness effects on log-law coefficients are fewer in number. Most authors only measure velocity profiles without comparing those with the law of the wall as it is common in incompressible flow. Velocity profiles for flows over larger roughnesses (10% of δ) were included in the papers of Disimile and Scaggs[13,14,15,16] and Maurice and Seibert[17]. All authors agree that velocity profiles over the rough surfaces are less full and report an increase in boundary layer thickness due to roughness. These effects are often more severe when the Reynolds number is increased. Research by Czarnecki and Monta[18,19] suggests that the drag caused by surfaces displaying regular roughness is mainly due to wave drag rather than skin friction and that this drag is only mildly influenced by the existence of heat transfer. The reduced velocities near the surface can explain the relatively low drag contribution due to skin friction. A computational study by Christoph and Fiore[20] confirms these observations for Mach 5.75. The work by Holden[21,22,23] also found that the heat transfer on rough surfaces reached up to three times the smooth wall value.

The size of the roughnesses addressed here is of the order of a boundary layer thickness and the type is a regularly spaced two-dimensional perturbation of sawtooth shape. The flow over such a roughness is sketched in Fig. 1.3. The boundary layer separates from the outer edge of one roughness element and subsequently re-attaches at the next. A small region of re-circulating flow is enclosed by the separating streamline.

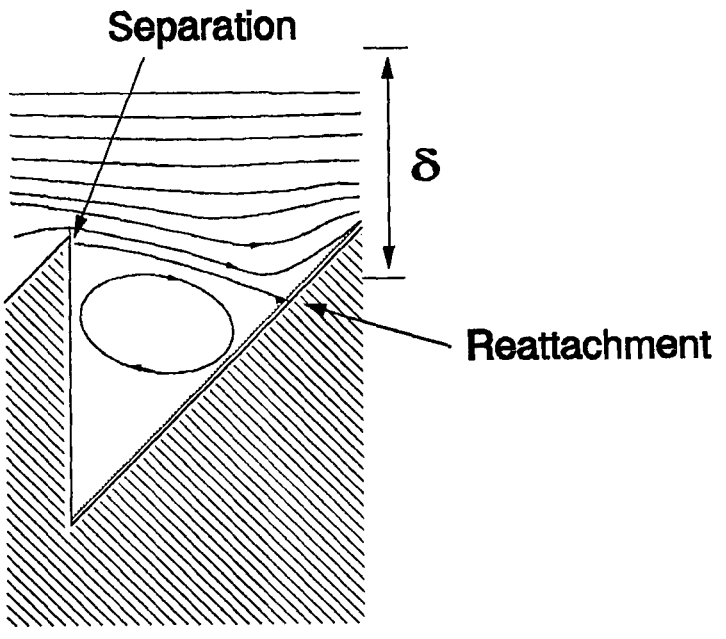

Fig. 1.3 Schematic of the flow over a sawtooth shaped roughness element

A similar type of flow is encountered over a series of cavities which is given

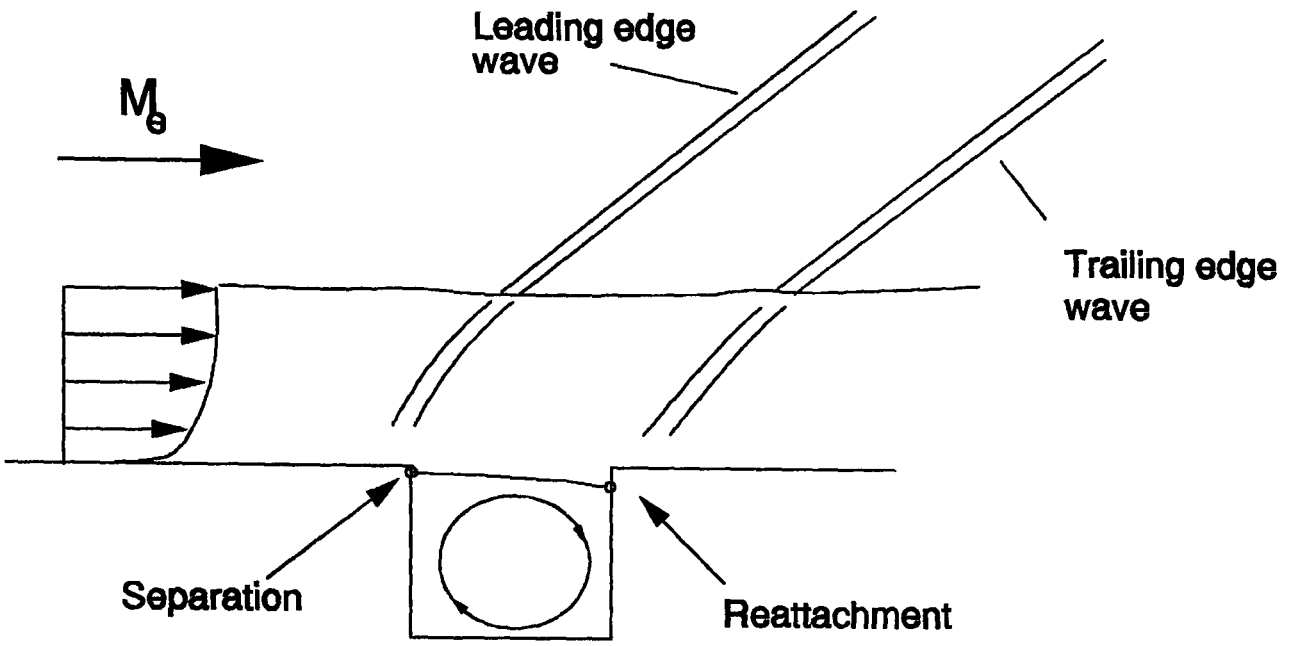

Fig. 1.4 Schematic of time-mean supersonic cavity flow. Taken from an interferogram in Ref.24

schematically in Fig. 1.4 taken from an interferogram obtained by Zhang and Edwards[24]. The velocity profiles given in this paper show similar effects to those observed for other types of roughness.

Of particular interest here is the question of how the modified boundary layer profile behaves as the surface changes back to a smooth wall. Berg[25] investigated this problem in hypersonic flow and found that it took a distance of about 10 δ downstream of a step change from rough to smooth for a turbulent boundary layer to relax to mean properties comparable to a smooth wall flow. The opposite process from smooth to rough took 14 δ. Comparable work for regular large scale roughness in compressible flow has been reported by Edwards and Zhang[26] for Mach numbers of 1.5 and 2.5. The velocity profiles behind two cavities were found to be less full. The boundary layer thickness and surface skin friction was reduced. These changes were observed to persist for some time after the roughness. This may put a downstream adverse pressure gradient in the region of a boundary layer that has been significantly altered due to roughness.

An experiment undertaken by Holden[21] showed for the first time that an unseparated compression corner flow can exhibit a large scale separation if the surface is changed from smooth to rough. Since then several investigations into the influence of roughness on a turbulent shock-boundary layer interaction have been reported by the same researcher[22,23]. Similar investigations were performed by Disimile and Scaggs[13-16] for larger roughnesses. Their measurements included surveys of the boundary layer profiles and comparisons of a rough and smooth

wall compression corner flow. The separation length was found to be 10-12 times larger than in a comparable smooth case. Maurice and Seibert[17] investigated the effect of Reynolds number on a compression corner flow fitted with roughness. No information is given on the extent of the separation and a smooth wall reference case is not yet reported. All of these studies investigated roughness stretching all the way through the interaction.

The problem to be investigated here is rather a short stretch of roughness (10-20 δ) followed by a smooth surface upstream of a region of adverse pressure gradient. The modification of the oncoming boundary layer profile is expected to be similar to the effects caused by blowing. Viosinet[27] investigated the effect of roughness and blowing on a turbulent boundary layer at Mach 2.9 and found that both increased the thickness and made profiles less full. Holmes and Squire[28] investigate the effect of blowing on a boundary layer interaction and found the interaction length to be increased by upstream blowing and peak pressures were found to decrease. A study by Selig and Smits[29] found that blowing upstream of a Mach 2.84 compression corner increased the length of the separation. It can be expected that a large scale roughness located upstream of a shock/boundary layer interaction has similar effects.

The sensitivity of compression corner flow to changes in the oncoming boundary layer profile is be discussed in a paper by Holden[30] which studies the structure of turbulent boundary layers in hypersonic separations. He concludes that the wall layer is the origin of separation and contains the principal information of the boundary layer. This portion of the profile is most likely to be influenced by roughness or blowing.

To date no investigation has been performed which combines the effect of a boundary layer disturbed by a surface roughness of finite length with a downstream adverse pressure gradient on a smooth surface. The distance between the end of the roughness and the location of the interaction plays a crucial role as it determines how far the boundary layer has relaxed before encountering the pressure gradient. Judging from the results available it seems appropriate to aim for a distance of less than 10 boundary layer thicknesses. The simplest type of adverse pressure gradient which also offers the largest database of previous research is the compression corner. The corner interaction contains similar flow features as the fin induced interaction without the complexity of the problem. It therefore seems more suited for a fundamental study. A review paper by Stollery[31] gives an overview over the principal flow features and includes a number of experimental results. A schematic of the flow over such a configuration is shown in Fig. 1.5. Heat transfer, skin friction and surface pressure show a significant increase on the compression corner compared to the values in the oncoming boundary layer. The region during which these parameters change is referred to as the interaction length. In the case of separated flow the shock system in the corner will display two distinct waves originating from the separation and reattachment point. In such a case the skin friction shows

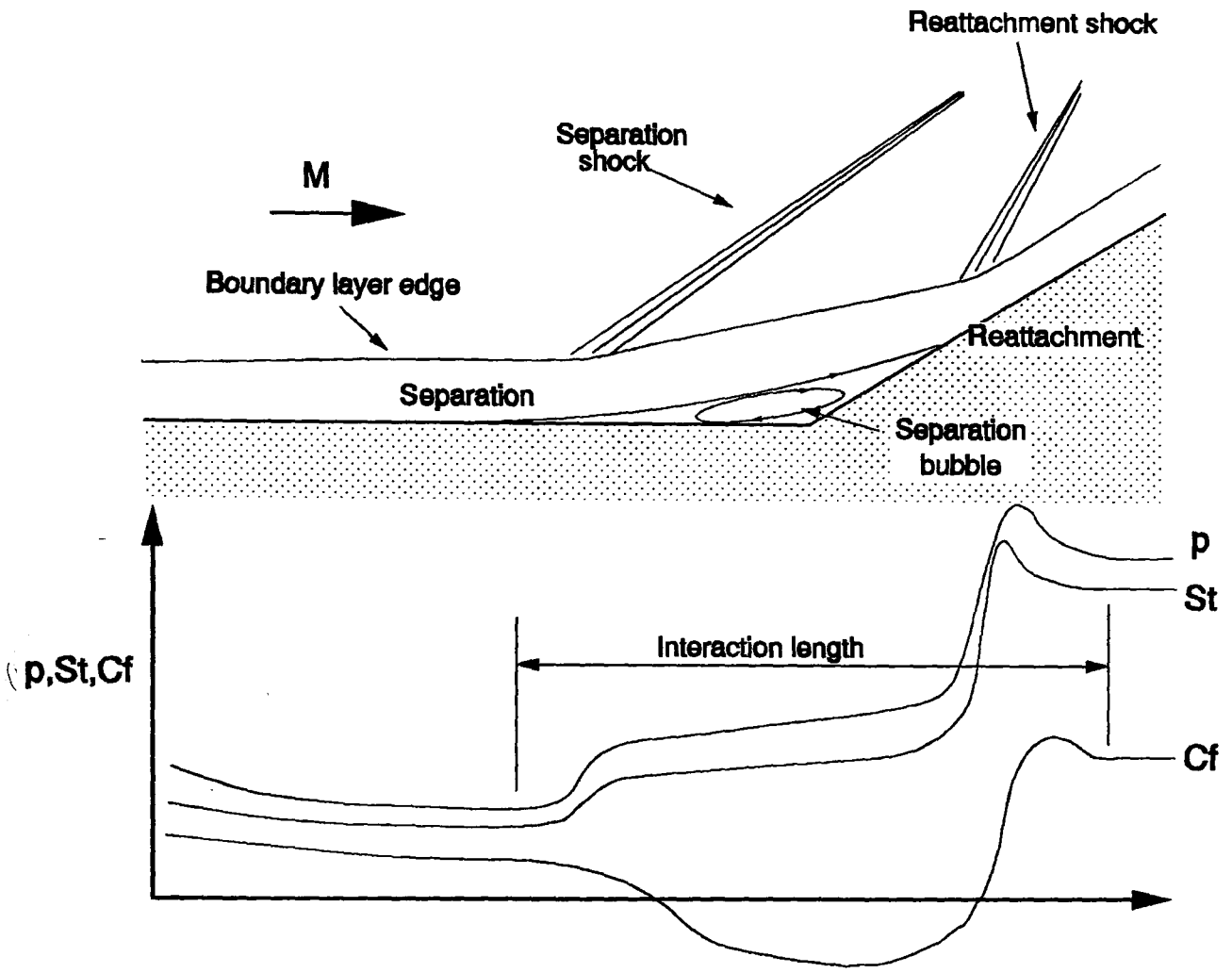

Fig. 1.5 Principal flow features in hypersonic compression corner

negative values associated with the reversed flow in the separation bubble. The heat transfer and pressure display an increase at the separation point followed by a short plateau area before rising onto the values downstream of the corner. All three parameters can exhibit an overshoot downstream of the hingeline before reaching a constant plateau. The close similarity between the pressure and heat transfer distributions has been pointed out by Coleman and Stollery[32] who used this fact to develop a simple correlation.

The investigation in this work will supply a database of measurements that can be used to compare with the predictions of CFD codes. For this purpose it is important to have a well defined flow field. Rudy et al[33] compared the results of a two-dimensional CFD prediction with a flat plate compression corner experiment and found that they did not agree on the length of the separated region. However, a simulation of the same problem with a three-dimensional code simulating the flow over the span of the plate including edge effects compared very well with the experimental results. The difficulty lies in the nature of the 'two-dimensionality' of the flat plate experiments. Even though no spanwise variations

were reported the flow did not behave the same as in real two-dimensional flow which would require a flat plate of infinite span. Three dimensional computations are very expensive and in general only late stages in the development of a CFD code. For these reasons it is preferable to perform experiments on an axisymmetric configuration as this allows quasi-two-dimensional computation and ensures that the same conditions exist for the experiment and the computation. The compression corner flow is therefore modelled by a cylinder flare junction.

The roughness shapes investigated in this work are a sawtooth roughness and multiple square cavities. The size of a roughness element is varied of up to a boundary layer thickness. For the reasons given above the distance between the roughness end and the compression corner is of the order of 5 δ.

The flow parameters measured in the course of this work will include surface pressures and heat transfer as well as boundary layer pitot pressure profiles. The latter can be used to derive velocity profiles and discuss the results in a law-of-the-wall approach. It is also possible to estimate the skin friction from near wall measurements of total pressure if the log law is assumed to hold. This has first been demonstrated by Preston[34] and the associated measurement technique is named after him. An investigation by Sigalla[35] extended the approach to compressible flow. An alternative is to use velocity measurements away from the wall and fit these to a logarithmic profile in log-law co-ordinates until the law of the wall is obtained. More sophisticated formulations can be used to include the effects of pressure gradients and roughness.

It has been pointed out by Dolling[36] that supersonic turbulent separated flows always reveal a certain degree of unsteadiness. Measurements of mean features may not reflect a real flow but rather an average of several different flow states. For this reason surface pressures are measured with as high a temporal resolution as possible.

To provide an accurate description of the flow conditions in the test facility, a detailed flow survey of the wind tunnel is presented as part of Chapter 2. This section also deals with the associated measurement techniques and gives estimates for the experimental errors for each measurement. The requirement for very high resolution heat transfer measurements led to the development of liquid crystal thermography for the wind tunnels used in this thesis. For this reason it was felt appropriate to single out this technique from the other experimental methods and the developments are described, together with an overview of traditional techniques, in Chapter 3.

In general all necessary figures are included in the text to allow for easy reading. When discussing experimental results, however, a large amount of data needs to be presented. To avoid the occurrence of several pages of figures within the text the results are presented together at the end of Chapter 4.

2. Experimental Facilities and Measurement Techniques

The main part of the work reported in this thesis was carried out in the supersonic blow-down wind tunnel (HSST) at DRA Fort Halstead, but some supportive work has also been carried out in the College of Aeronautics Gun Tunnel. Both facilities will be introduced in this chapter.

This section of the thesis contains a detailed description of all the experimental techniques and equipment used in this work. It is strongly believed that especially for the purposes of comparing experimental results to computer code predictions an accurate assessment of experimental errors is necessary and this is therefore included wherever possible. It is also with CFD validation in mind that the flow quality of the HSST has been investigated in detail. Such a survey had not been carried out on all the nozzles available for the tunnel and where nozzle calibration data was available it had been obtained some time ago and the agreement of running conditions could not be guaranteed. Furthermore it was not at all clear at the beginning of this work which wind tunnel configuration was best suited for the investigation and the nozzle calibration gave the data necessary to arrive at a decision.

When introducing the techniques necessary for measurements within the turbulent boundary layer, some theoretical aspects of boundary layer profiles will be discussed. In this particular area the measurement and analysis of results are strongly connected and therefore presented together.

2.1 The College of Aeronautics Hypersonic Gun Tunnel

The College of Aeronautics gun tunnel was installed originally at Imperial College in London and a detailed description can be found in Ref.37. The facility consists of an intermittent, free piston, compression heater feeding a hypersonic nozzle and subsequent working section and dump tank. A general layout is shown in Fig. 2.1.

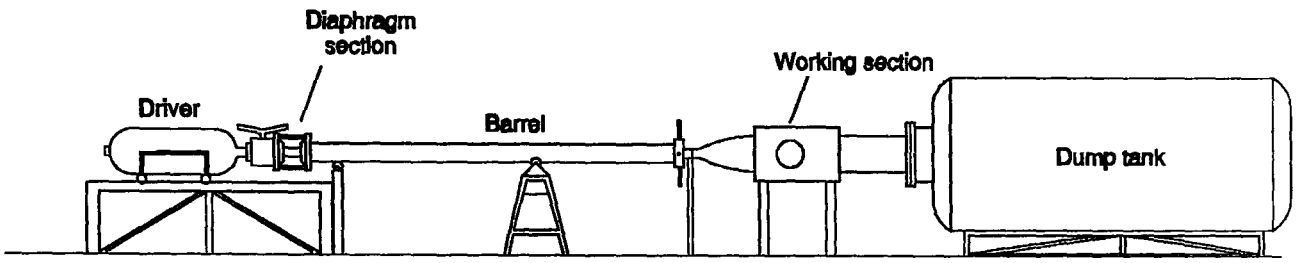

Fig. 2.1 The College of Aeronautics Hypersonic Gun Tunnel

A high pressure driver vessel supplies air of up to 2000 psi (13.7×10^6 N/m^2) to the barrel section. Two aluminium diaphragms are used to separate the driver gas from the piston before a run. The flow is started by bursting the diaphragms. The piston compresses the test gas, usually air at atmospheric pressure, giving total pressures of up to 10^7 N/m^2 and total temperatures of up to 1290 K. The test gas then expands through an axisymmetric contoured nozzle reaching a Mach number of 8.2. The useful running time depends on the test conditions and can lie between 20 and 80 milliseconds.

The useful flow in the test section has a diameter of about 0.12 - 0.15 m, the length of the working section is 0.20 m. Downstream of the test section is the diffuser and vacuum tank which is evacuated before a run.

By varying the pressure in the driver gas vessel a variety of Reynolds numbers can be achieved, ranging from 4.5×10^6 m^{-1} to 9.0×10^6 m^{-1}. This puts most experiments in the transitional regime. Even with very large models it is difficult to investigate a fully developed turbulent boundary layer in this facility unless some means of tripping is employed.

2.2 The DRA Fort Halstead HSST

The DRA Fort Halstead HSST is a supersonic intermittent pressure vacuum tunnel. The available Mach number ranges from M=4 to M=6, depending on the nozzle used. A schematic diagram of the tunnel, taken from Hurdle[38], is shown in Fig. 2.2.

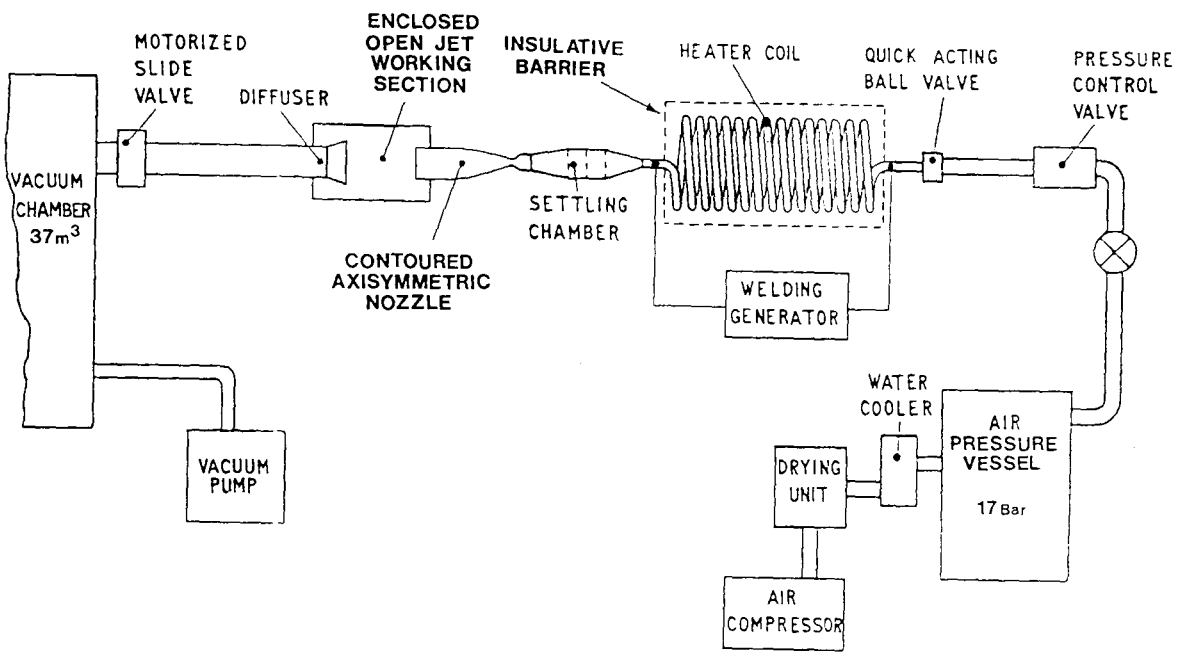

Fig. 2.2 Diagram of the Fort Halstead HSST wind tunnel (from Ref.38)

High pressure air is stored in a storage vessel after passing through a drying unit. The operating pressure is controlled through a commercial dome valve and can be set to any value up to 200 psi (1.4×10^6 N/m^2). The air is heated in a heater coil of 30 m length and 37.5 mm inside diameter to avoid liquefaction. The coil temperature can be set to up to 700 K. To reduce the heat loss the coil is embedded in a box filled with granules of high temperature insulator (Mica-fil). The operating temperature can be reached after approximately 40 minutes of heating, depending on the desired temperature. After passing through the heater the working gas then reaches a settling chamber which has been designed to give a uniform temperature distribution in the working section as reported in Ref.38. Two Mach 5 contoured axisymmetric nozzles (with and without centrebody) and two contoured nozzles without centrebody for M=4 and M=6 are available. The working section accommodates two vertical schlieren windows to allow flow visualisation. The diffuser is positioned 0.4 m downstream of the nozzle exit, and can be moved by approximately 0.3 m in streamwise direction. Between the working section and the vacuum tank is a motorised slide valve,

which allows opening of the working section without pressurising the vacuum tank. The flow is started by opening a fast acting ball-valve. Useful steady running times are up to 10 seconds.

The flow conditions can be varied by changing supply pressure and heater temperatures. The flow conditions achieved for different operating conditions and the extent of useful flow inside the working section are described in the HSST nozzle calibration (Section 2.5).

2.3 Measuring Equipment

This section describes the hardware used for data acquisition as well as the methodologies employed in the measurements. Where extensive post-processing is needed to extract physical parameters from the measured data the necessary theory is also discussed.

2.3.1 Data Acquisition Hardware

All signals were amplified using a FYLDE modular multi-channel amplifier, consisting of a power supply monitor (FE-M14-DS), several transducer conditioning modules (FE-492-BBS) and differential amplifiers (FE-254-GA). The conditioning modules were used as power supply for the pressure transducers. The signals were recorded simultaneously at a sampling rate of up to 200kHz with a Microlink 4000 data acquisition and control rig. Once an experiment was completed, the data was downloaded to an IBM compatible PC via a parallel IEEE488 (GPIB) interface. Post-processing of the measurements was performed on the PC and on a SUN workstation.

2.3.2 Traverse Rig

In order to measure flow properties at various locations throughout the working section of the HSST an appropriate rig was designed and built to allow a probe to be moved through the flow during a wind tunnel experiment. One aim of the design was to cause as little disturbance of the flow as possible. This was achieved by using only a single shaft to hold the probes and placing the driving mechanism outside of the working section. The shaft was designed to be as rigid as possible while still being light enough to be moved at sufficient speed. A linear stepper motor is used to drive the probe holder. Two linear ball bearings guide the shaft and reduce the friction. These bearings are adjustable, thus allowing the play to be minimised. A diagram of the general assembly can be seen in Fig. 2.3. The design leaves sufficient space to incorporate a linear displacement sensor if a more accurate knowledge of the probe position is required. In the current investigation this was found to be unnecessary.

The traverse rig can be mounted at two streamwise location in the working section wall either on the top or bottom face. The probe holder is designed to allow a horizontal displacement of the probe, thus measurements can be taken at every location in a vertical plane inside the working section.

Part of the rig is mounted outside the working section, therefore the design has to be capable of sealing the atmospheric air from the evacuated working section.

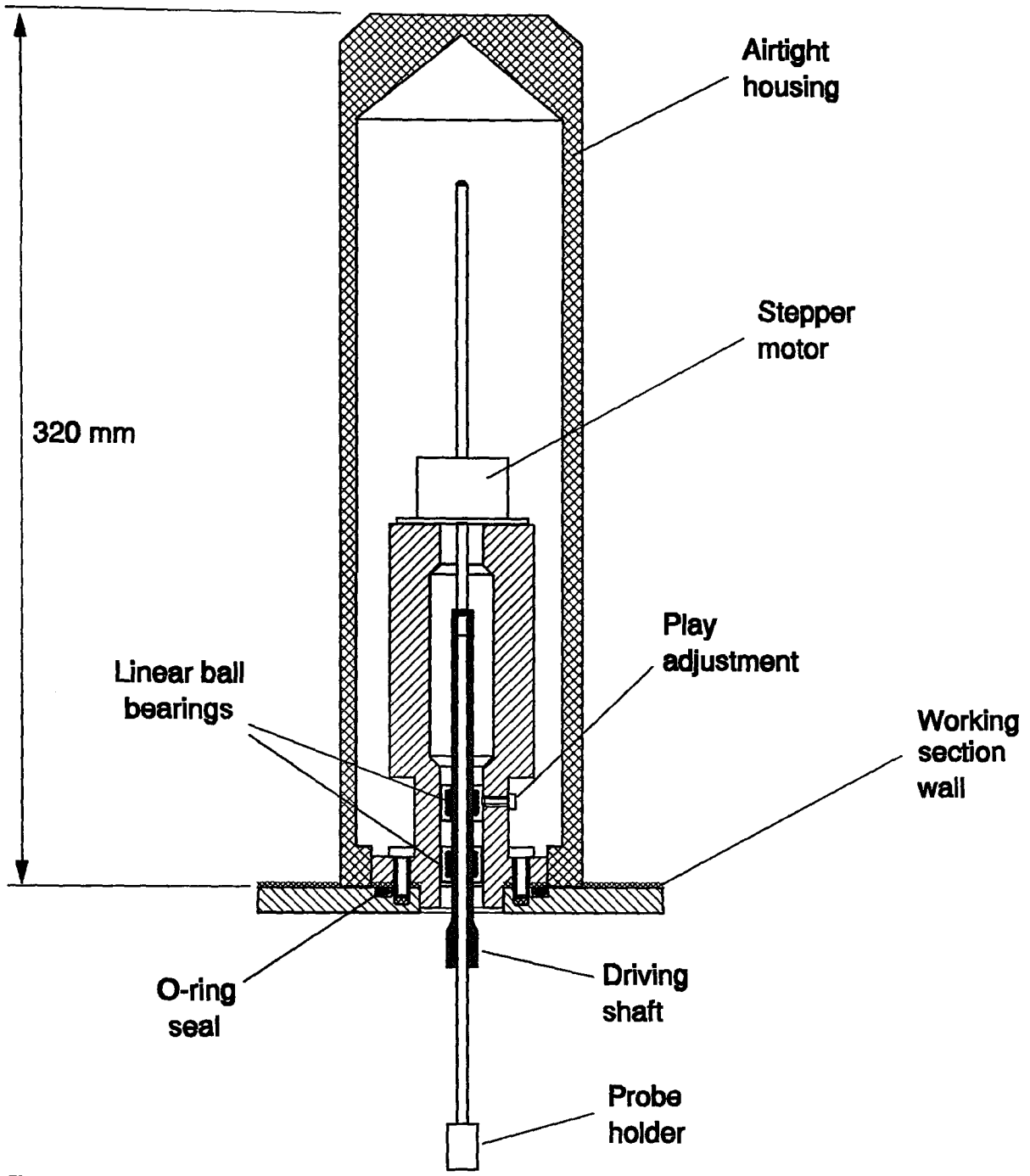

Fig. 2.3 Traverse rig

This was achieved by using an airtight housing which is fitted over the traverse rig onto the outer wall of the working section.

The stepper motor allows a linear movement at a maximum speed of 17 mm/s. The maximum travel is 60 mm. Several lengths of probe shaft are available to undertake traverses in different areas of the flow. In addition the rig can be mounted underneath the working section to extend upwards into the flow.

The motor is controlled through a stepper motor controller card included in the Microlink 4000 data acquisition and control rig. The card can be programmed from the PC by incorporating special commands into a standard BASIC computer program. Possible command sequences give control over stepping rate, stepping distance and start/stop sequences. A useful feature of the control-card is the

possibility to include a single bit output into the command sequence. This was used as a trigger signal for the data acquisition, thus allowing the recording of measurements to start simultaneously with the motor movement.

Fig. 2.4 shows the traverse rig mounted on top of the working section with the contoured Mach 5 nozzle installed. A variety of probes have been used with this rig and these will be discussed in the following sections.

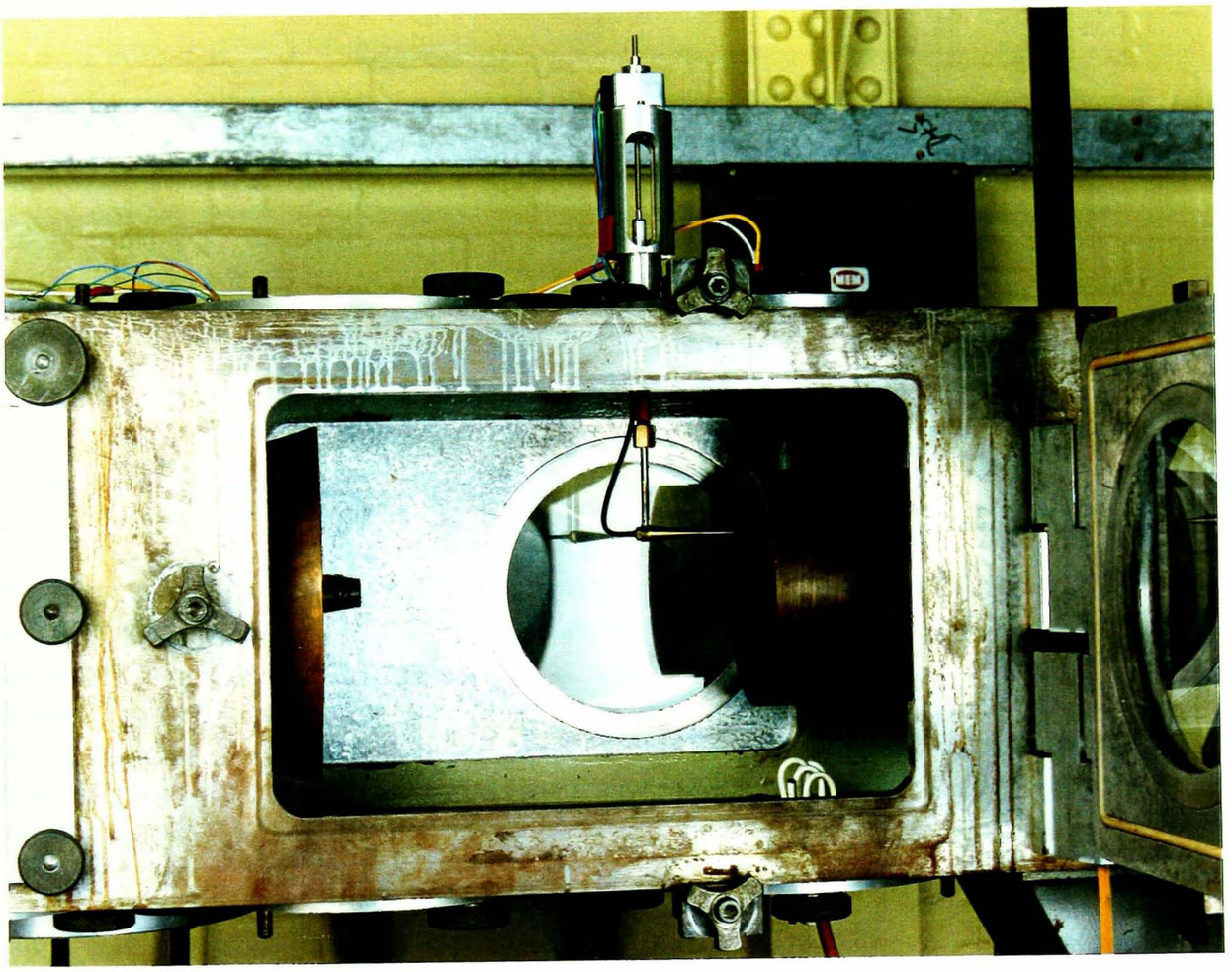

Fig. 2.4 Traverse rig and pitot pressure probe mounted in the HSST. The housing has been removed to expose the rig and stepper motor.

2.3.3 Reservoir, Pitot and Static Pressure Measurements

The total pressure in the settling chamber was recorded for each run with a simple pitot probe located downstream of the flow straighteners. As the flow in the settling chamber is subsonic, a relatively simple pitot probe design could be used, in this case a metal tube bent to an angle of 90°, facing the flow. The transducer (ENTRAN EPNM-M10W-15AZ2) was mounted outside of the nozzle. Its measuring range is 0-15 bar absolute. Throughout this thesis the total pressure measured at this location is referred to as reservoir pressure and will be used as the total pressure in Mach number calculations.

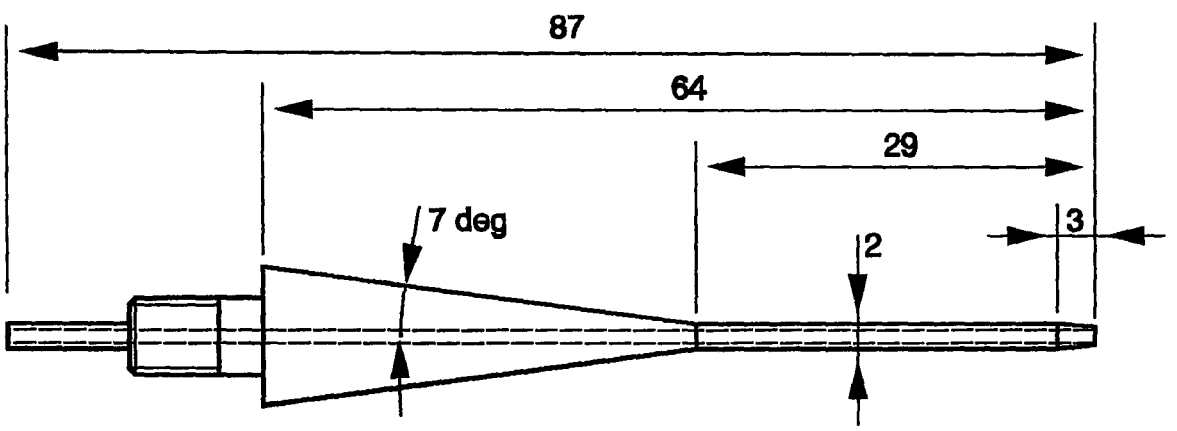

Fig. 2.5 Free stream pitot pressure probe. All dimensions in mm

The pitot pressure in the working section was measured with a simple pitot probe as seen in Fig. 2.5. The probe was held in position by the traverse rig. In early tests a pressure transducer was attached directly to the rear of the probe. It was found that during the course of a test, the probe temperature increased substantially due to aerodynamic heating, causing a noticeable drift in the transducer calibration. This was particularly severe in experiments performed at high heater temperatures (above 600 K). As this calibration drift could not be compensated for, the measurements were found to be unsatisfactory. Therefore it was decided to mount the transducer in the roof of the working section. Connected to this large amount of metal the transducer temperature stayed sufficiently constant to eliminate any changes in the calibration. The time response of the probe has obviously been reduced due to the larger length of connecting tube between the probe and the transducer, but this was found to cause no problems for measurements in the free stream.

The free stream static pressure has also been measured using a probe design as suggested by Pope and Goin[39]. A drawing of the probe can be seen Fig. 2.6. In a similar manner to the measurement of pitot pressure the transducer was mounted in the working section wall.

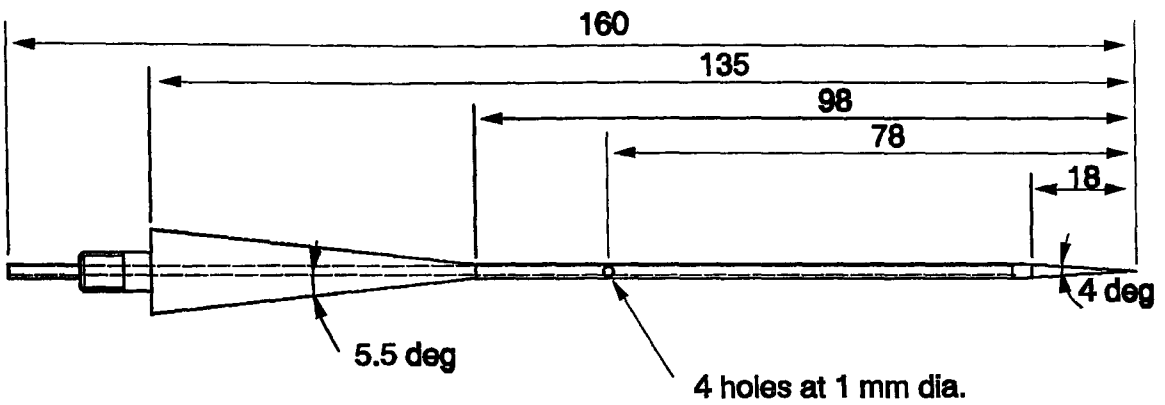

Fig. 2.6 Static pressure probe. All dimensions in mm

Pitot and static pressures in the free stream were measured with standard Kulite XCS-190-15D transducers with a range of 0-15psi differential. Wall static pressures were measured with Kulite XCS-062-15A pressure transducers which were manufactured to our specification of shortest possible length. This allows the transducers to be fitted inside the models to achieve the best possible

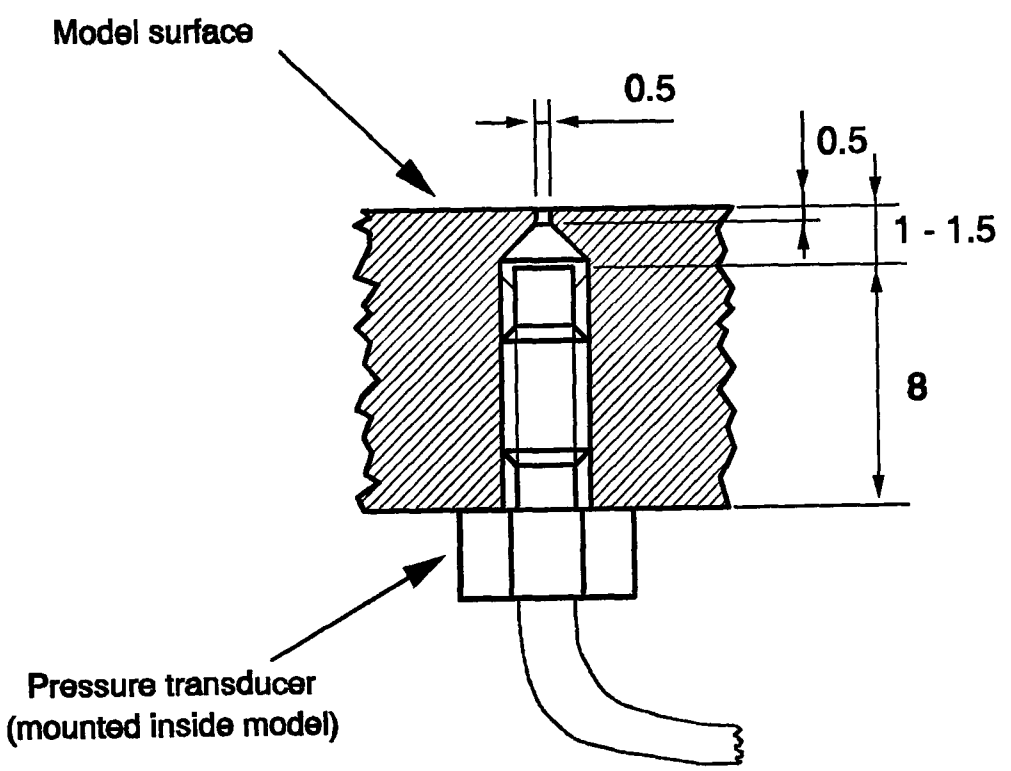

Fig. 2.7 Static pressure port on a wind tunnel model. All dimensions in mm

accuracy and time response. An example of the design of a static pressure probe and the transducer location can be seen in Fig. 2.7.

All pressure transducers used were checked for linearity using a dead weight tester and then calibrated before each wind tunnel run. This calibration was performed by recording the output of the transducers at a known atmospheric and vacuum pressure in the working section. The output of the transducers can then be converted by assuming a linear behaviour between these two points. Most experimentally measured pressures fall into this range.

2.3.4 Total Temperature Measurement

The total temperature probe used was similar to a design suggested by Pope and Goin[39] based on early work by Winkler[40]. Using their data, the recovery factor of the probe was estimated to be 0.98 for high settings of heater temperature (700K) and 0.997 for low settings (400K). Initially a thermocouple junction fabricated in-house was used but the response time of the probe was insufficient. This was due to the comparably large size of the thermocouple wires employed at that stage (0.2 mm). Therefore a new thermocouple design has been used, manufactured by the Paul Beckman Company, consisting of a micro-disk[41] with a diameter of $2x10^{-3}$ inch (0.05 mm) and a thickness of 10^{-4} inch ($2.5x10^{-3}$ mm). The wires leading to the micro-disk junction have a diameter of 10^{-3} inch (.025 mm). A drawing of the probe and the micro-disk is given in Fig. 2.8.

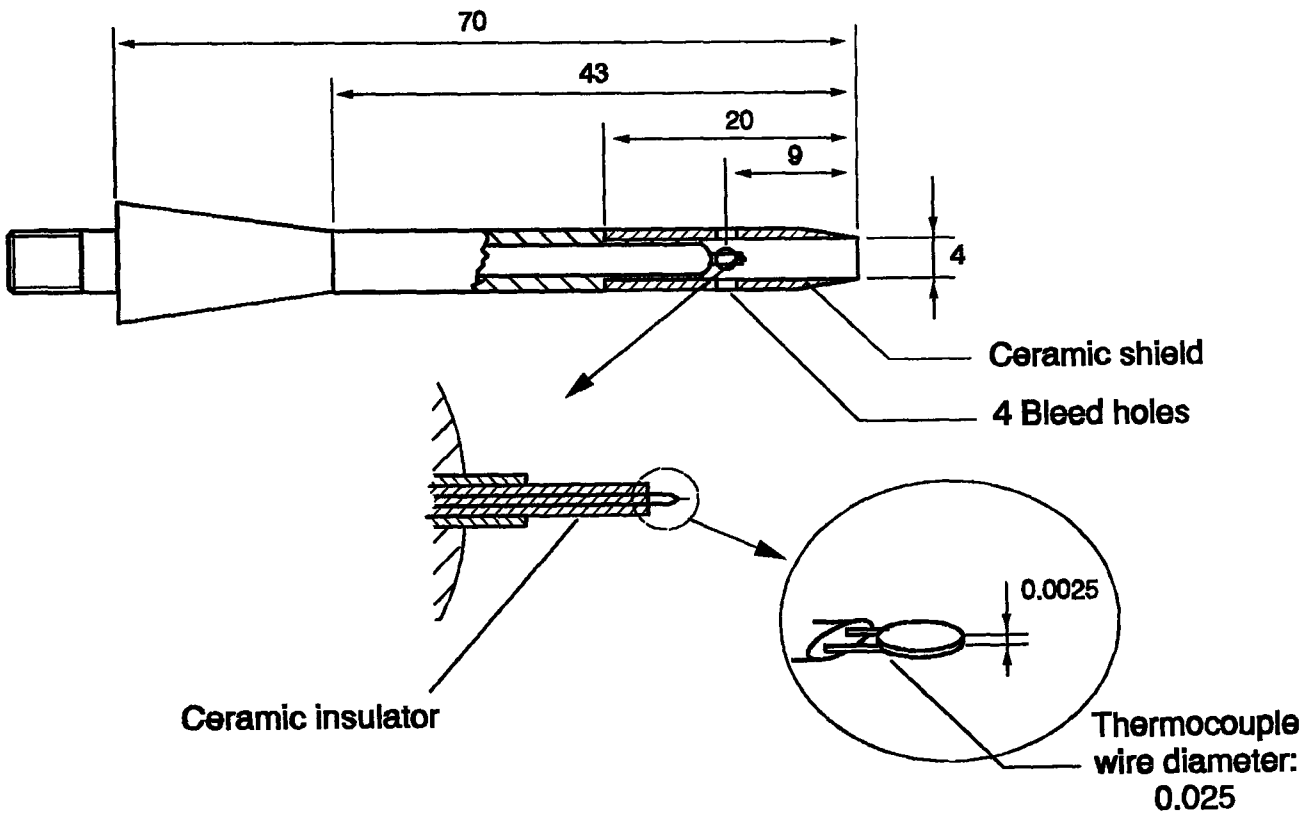

Fig. 2.8 Total temperature probe and thermocouple junction design

It was also found that the size of the bleed holes in the shield of the total temperature probe had a significant influence on the response time. An example is shown in Fig. 2.9. The venting hole diameter was experimentally selected to give sufficient response time with the smallest possible diameter.

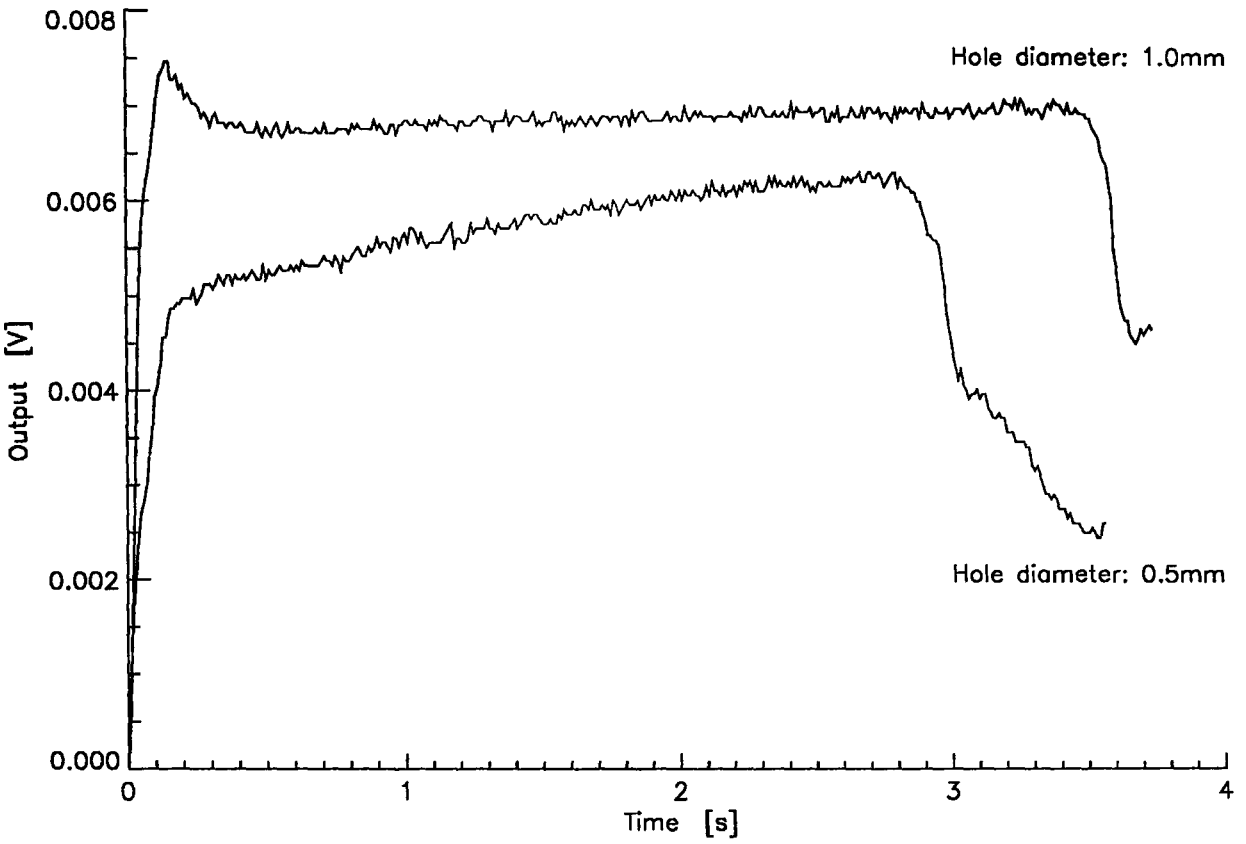

Fig. 2.9 Total temperature signals for two sizes of bleed holes

2.3.5 Boundary Layer Profiles

Several flattened head pitot probes have been manufactured for the measurement of pitot pressures within the boundary layer. Apart from a horizontal probe two inclined probes were used to survey the boundary layers on the flares. Each probe was measured individually to obtain the dimensions of the probe mouth. Typically a probe measured 0.2 mm in height and 1.5 mm in width. The opening was 0.1 mm high with a wall thickness of 0.05mm either size. A boundary layer was surveyed by mounting the probe onto the traverse rig and moving the probe through the boundary layer at a known step rate. This gave typically 15 measurements per step and about 200 steps inside the boundary layer in one experiment, lasting approximately 4 seconds.

The pressure transducer was mounted as close as possible to the probe opening, while still avoiding the problems of interaction with the boundary layer flow due to the bulk of the transducer. Care had to be taken not to expose the transducer to too much aerodynamic heating as this was likely to change the calibration. The final design can be seen in Fig. 2.10. The probe allows for streamwise movement to set the traverse location accurately. In order to improve the positional accuracy

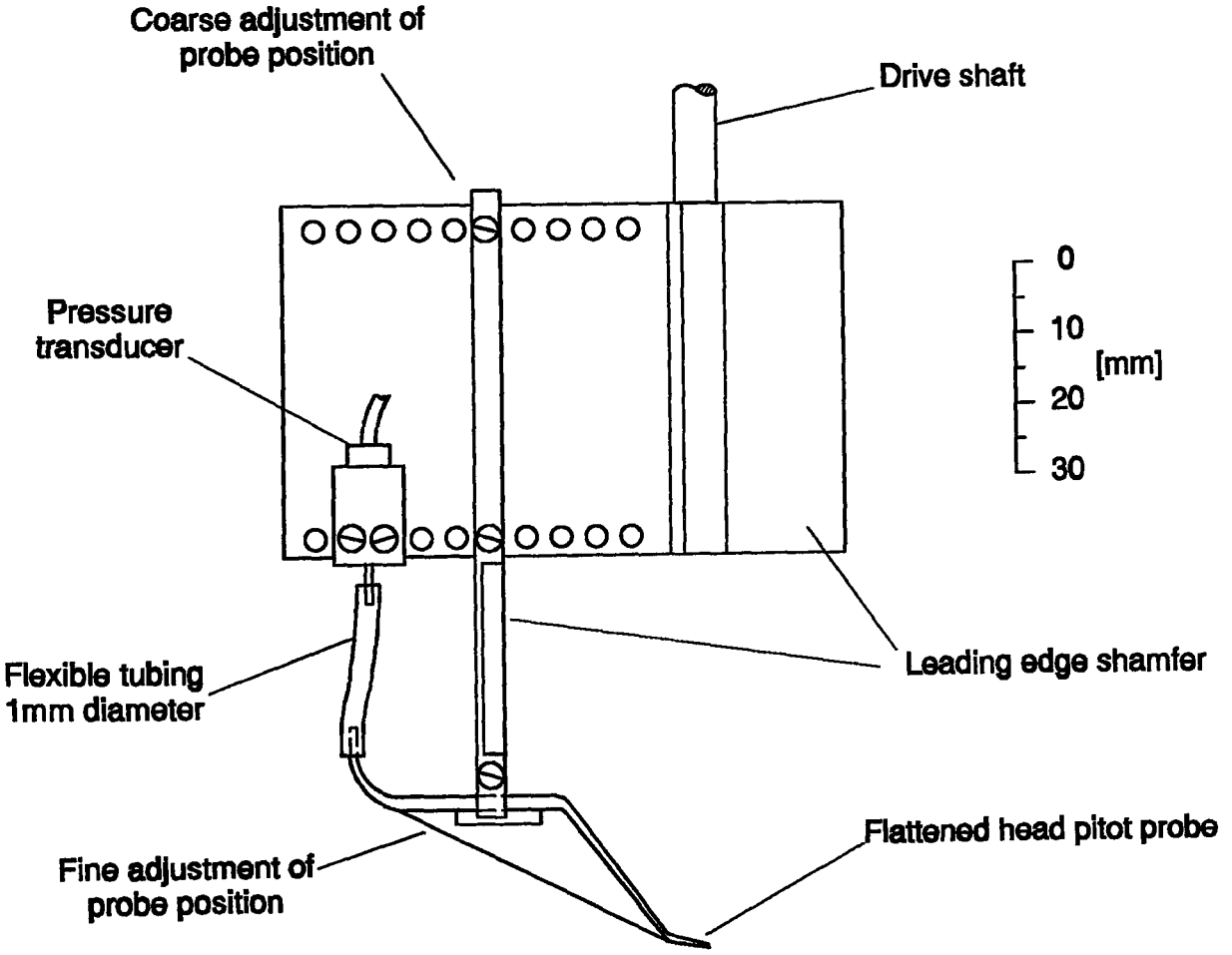

Fig. 2.10 Boundary layer pitot probe, attached to traverse rig

of the traverse rig the design incorporated an electrical contact to obtain a signal when the probe touched the model surface. All the models tested were manufactured from non-conductive material. Therefore a small strip of copper, typically 1mm wide, was embedded into the surface to provide the electrical contact. In most cases the traverse was performed moving towards the surface, so that together with a known stepping rate the probe position could be calculated accurately to one step size.

It had to be ensured that the response time was sufficient to obtain an accurate reading at each position as the probe moves through the flow. Comparisons of measurements in the free stream indicated no difference between the large pitot probe used for the nozzle calibration and the boundary layer probe. When moving towards the model surface the probe Reynolds number, Re_H, changes significantly and a reduction of response time has to be expected. In order to investigate this effect the same boundary layer was surveyed twice with opposite directions of probe movement. In one experiment the probe would start at the surface and move towards the edge of the boundary layer and in the second experiment the direction was reversed. Any effects of response time then show up in the resulting signals, as the probe moves from higher pressures to lower

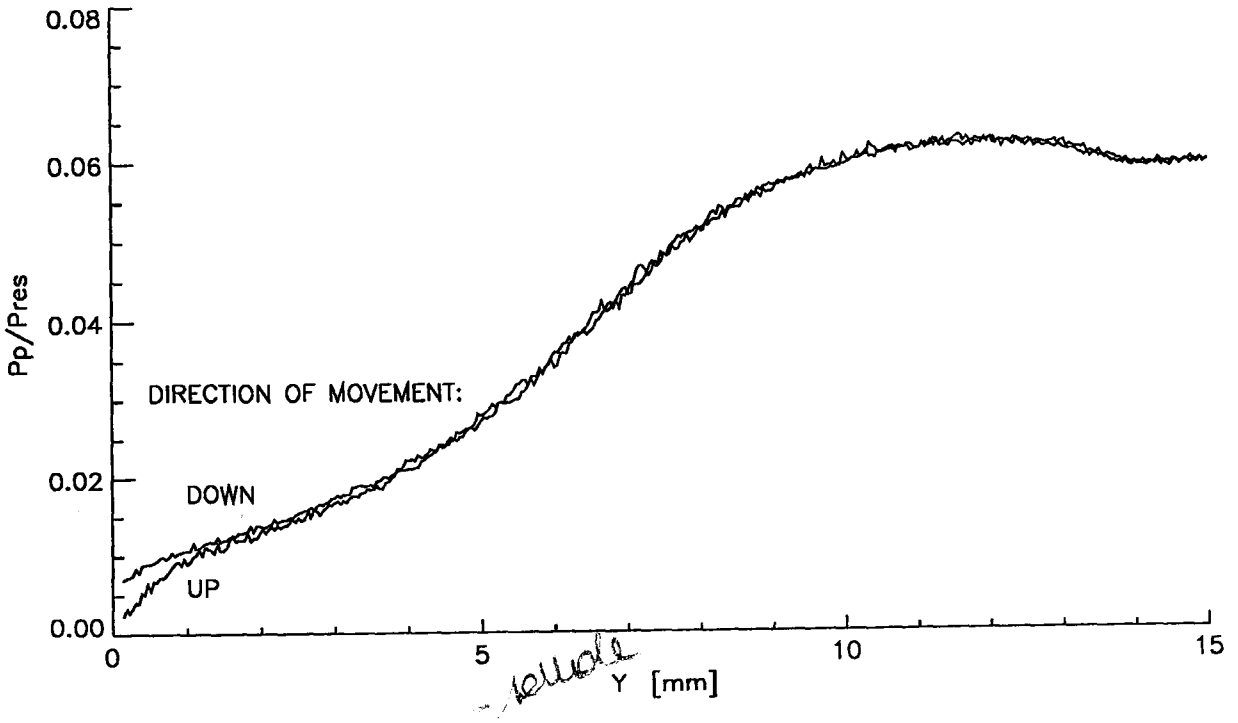

Fig. 2.11 Pitot pressures measured in the centrebody boundary layer for two different directions of probe movement.

ones in one case and the opposite in the other. Fig. 2.11 shows the outcome of this experiment. The measured pressures agree very well apart from the region closest to the surface. Attempts to optimise the performance of the probe by reducing the distance between probe mouth and transducer were made, but the result given in Fig. 2.11 could not be improved without a major re-design of the

probe. To obtain more accurate values very close to the wall, measuring times of up to one second are necessary at each position. Due to the large amount of profiles surveyed this was not feasible. Therefore the following approach was chosen to obtain the boundary layer velocity profiles. The measurements were taken just as described moving the probe from the free stream towards the surface. After touching the surface the probe was left in position and pressures were recorded for a further 2 seconds. This was sufficient to obtain a steady state value for the location closest to the wall. In the analysis of the results the probe Reynolds number was computed for each probe position. An example is given in Fig. 2.12, showing the probe Reynolds number dependant as a function of the wall distance for a traverse on the centrebody. Response time problems are likely to occur for Reynolds numbers based on probe height of below 200. All pressures obtained below this value were disregarded in the theoretical analysis apart from the value nearest to the wall. All the results shown in this thesis include the values obtained at small Reynolds numbers only for completeness. It must also be noted that the value nearest to the wall will be affected by probe displacement effects which will be discussed in subsection 2.3.6

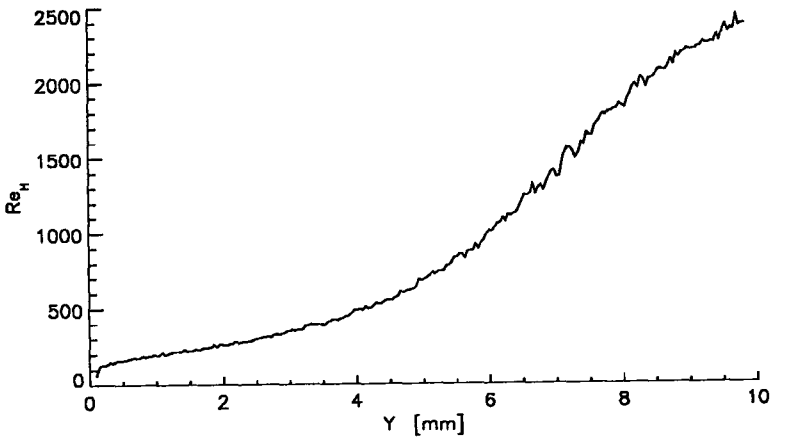

Fig. 2.12 Reynolds number dependent on probe size for the boundary layer profile on the smooth centrebody

Before obtaining velocity profiles from the measured data, Mach number profiles have to be calculated. These can be obtained from the ratio of pitot and static pressure. Since static pressure profiles have not been measured the thin shear layer approximation of constant static pressure within the boundary layer is adopted. Surface pressures have been measured within 3 mm of the traverse position, simultaneously with the pitot profiles. From the ratio of wall and pitot pressures the local mean Mach number can be calculated using the Rayleigh pitot formula as given in Ref.42:

$$\frac{p_t}{p_w} = \left(\frac{(\gamma+1)M^2}{2}\right)^{\gamma/(\gamma-1)} \left(\frac{(\gamma+1)}{2\gamma M^2-(\gamma-1)}\right)^{1/(\gamma-1)} \qquad \textit{for } M > 1 \tag{2.1}$$

$$\frac{p_t}{p_w} = \left(1+\frac{(\gamma-1)}{2}M^2\right)^{\gamma/(\gamma-1)} \qquad \textit{for } M < 1$$

To reduce Mach number profiles to velocity, the static temperature distribution throughout the boundary-layer is required. Static temperatures inside the

boundary-layer can not be measured with traditional techniques. The size of the total temperature probe prevents useful measurements of T_0 within the boundary-layer. For this reason the static temperature has been assumed to depend upon the mean velocity and free stream total temperature according to Crocco's velocity-temperature relation modified by VanDriest for Prandtl numbers different from unity as given in Ref.11:

$$\frac{T}{T_e} = \frac{T_w}{T_e} + \frac{T_{aw}-T_w}{T_e}\frac{u}{u_e} - r\frac{\gamma-1}{2}M_e^2\left(\frac{u}{u_e}\right)^2 \qquad (2.2)$$

Using

$$u = M\sqrt{\gamma R T} \qquad (2.3)$$

this can be re-arranged to give a quadratic relationship for the unknown temperature T. Once the static temperature distribution is calculated, the velocity profile can be computed with Eq.(2.3). Several authors, such as Holden[30] and Meier et al[43,44], have made the observation that the temperature distributions derived from their total temperature measurements did not match Crocco's relationship particularly close to the wall. Each author suggests alternative formulations but to date no universally valid function is available. Therefore it was decided to stay with Crocco's formulation as it offers the most widely accepted approximation. Fernholz and Finley[11] discussed a large number of compressible turbulent boundary layer data and found good agreement with Crocco's relationship in most cases. They also concluded that the law of the wall holds for supersonic flows even with heat transfer and a pressure gradient, if a suitable compressibility transformation has been used. The suggested transformation is similar to the form suggested by Van Driest[45] but valid for Prandtl numbers different from unity:

$$u^* = \frac{u_e}{b^*}\arcsin\left(\frac{2b^{*2}\frac{u}{u_e} - a^*}{\sqrt{a^{*2}+4b^{*2}}}\right)$$

with:

$$a^* = \frac{T_e}{T_w}\left(1 + r\frac{\gamma-1}{2}M_e^2\right) - 1 \qquad (2.4)$$

$$b^* = \sqrt{r\frac{\gamma-1}{2}M_e^2\frac{T_e}{T_w}}$$

This transformation has also been used by Holden[30] at Mach numbers above 10 who remarks that the validity was restricted for high Mach numbers and highly cooled walls. The current work is performed at significantly lower Mach numbers

with wall temperatures close to adiabatic and therefore the above transformation is assumed to be suitable. The log-law then reads as:

$$\frac{\overline{u^*}}{u_\tau} = \frac{1}{k} \ln \frac{y u_\tau}{\nu_w} + C^* \qquad (2.5)$$

with:

$$\begin{aligned} k &= 0.40 \\ C^* &= 5.10 \end{aligned} \qquad (2.6)$$

where $\overline{u^*}$ is the transformed mean velocity.

The coefficients k and C* have been chosen according to their incompressible values as suggested by Fernholz and Finley[11] who give the following reasoning:

"A comparison of measurements with the logarithmic law of the wall and the determination of the wake strength are obviously affected by the choice of the 'log-law constants' (k and C*). (...) Since the constants are experimentally determined we feel that it is not possible to state that one set of values is correct and have stayed with the values used here. Firstly, because we relied on Coles' thorough investigation and secondly, because a visual comparison of this log-law with a large quantity of the data presented in raw form, in AGARDograph 223, suggests that it provides a good description which would not be materially improved by changing to any of the other pairs of values given in table (...), which presents a selection taken from four of the most thorough investigations."

When examining the influence of roughness on a boundary layer profile, an influence on the log-law coefficients has to be expected. Nevertheless the examined data will be compared to the law of the wall with the above coefficients to highlight any deviations caused by roughness.

To plot the experimental velocity profiles in law of the wall coordinates it is necessary to have a knowledge of the wall shear stress τ_w at the profile location. This quantity is difficult to measure and in the course of this work this has not been attempted. A possible alternative is to fit the experimental data to a theoretical velocity profile, incorporating the wall shear stress as an unknown. A suitable profile has been derived by Mathews, Childs and Paynter[46] which extends Coles' wall/wake law to compressible flow. Thomas et al[47] have compared the results of Preston tube measurements of skin friction with the value obtained from fitting their profiles to Mathews et al 's theoretical profile in a M=1.4 shock/boundary layer interaction and found good agreement, even through the interaction. Similar results are reported by Dolling[48] for a Mach number of 5 and by Mathews et al[46] for Mach numbers between 1.4 and 4 . The profile was originally derived for adiabatic flow, but following the procedures in Ref.46 a

solution for non-adiabatic boundary layers can be obtained. Starting by introducing a wake function into the law of the wall (Eq.(2.5)):

$$\frac{\overline{u^*}}{u_\tau} = \frac{1}{k}\ln\frac{y u_\tau}{\nu_w} + \frac{\Pi}{k} W\left(\frac{y}{\delta}\right) + C^* \qquad (2.7)$$

where W is Coles' universal wake function[49]. For mathematical convenience this can be replaced by:

$$W\left(\frac{y}{\delta}\right) = 1 - \cos\left(\pi \frac{y}{\delta}\right) \qquad (2.8)$$

The wake parameter Π can be determined by inserting the boundary condition

$$y = \delta$$
$$u^* = u_e^*$$
$$W = 2$$

into ((2.7)), giving:

$$\frac{\Pi}{k} = \frac{1}{2}\left(\frac{u_e^*}{u_\tau} - \frac{1}{k}\ln\frac{\delta u_\tau}{\nu_w} - C^*\right) \qquad (2.9)$$

Inverting the compressibility transformation (2.4) and transforming u_e gives:

$$\frac{u}{u_e} = \frac{\sqrt{a^{*2}+4b^{*2}}}{2b^{*2}} \sin\left(\arcsin\left(\frac{2b^{*2}-a^*}{\sqrt{a^{*2}+4b^{*2}}}\right)\frac{u_\tau u^*}{u_e^* u_\tau}\right) + \frac{a^*}{2b^{*2}} \qquad (2.10)$$

Substituting (2.7) into (2.10) and using (2.8) and (2.9) gives, after a few simplifications the velocity profile for a non-adiabatic boundary layer:

$$\frac{\overline{u}}{u_e} = A \sin\left(\arcsin(B)\frac{u_\tau}{u_e^*}\left(\frac{1}{k}\ln\frac{y}{\delta} + \frac{u_e^*}{u_\tau} - \frac{\Pi}{k}\left(1+\cos\pi\frac{y}{\delta}\right)\right)\right) + \frac{a^*}{2b^{*2}}$$

with: (2.11)

$$A = \frac{\sqrt{a^{*2}+4b^{*2}}}{2b^{*2}}$$

$$B = \frac{2b^{*2}-a^*}{\sqrt{a^{*2}+4b^{*2}}}$$

In the case of an adiabatic wall a* reduces to 0 and the equation simplifies to:

$$\frac{\overline{u}}{u_e} = \frac{1}{b^*}\sin\left(\arcsin(b^*)\frac{u_\tau}{u_e^*}\left(\frac{1}{k}\ln\frac{y}{\delta}+\frac{u_e^*}{u_\tau}-\frac{\Pi}{k}\left(1+\cos\pi\frac{y}{\delta}\right)\right)\right) \qquad (2.12)$$

and:

$$b^* = \left(\frac{\frac{\gamma-1}{2}M_e^2}{\frac{T_{aw}}{T_e}}\right)^{\frac{1}{2}} = \frac{\frac{\gamma-1}{2}M_e^2}{1+\frac{\gamma-1}{2}M_e^2} \qquad (2.13)$$

which is equivalent to the formula derived in Ref.46.

After calculating the necessary derivatives it is now possible to use a standard least-squares curve fitting routine to fit the measured velocity profile to the theoretical profile. This will supply the unknown parameters δ, c_f and u_e. The velocity at the boundary layer edge u_e is not an unknown quantity as such, it can be determined from the velocity profiles. In cases where a significant variation of static pressure throughout the boundary layer was present the calculated velocities will become increasingly inaccurate with growing distance from the wall. For this reason the edge velocity was treated as an unknown and the discrepancy between the iterated value and the measured profile can be seen as a measure of the accuracy of the profile. Such a large discrepancy was observed in all cases near the hinge line where a strong static pressure gradient in y-direction is to be expected, due to the interaction shock system extending into the boundary layer. Both velocity profiles and the results of the curve fitting procedure in these locations are only presented here as a matter of completeness but have to be regarded as inaccurate.

Fig. 2.13 shows the result of the curve fitting procedure with two boundary layer profiles compared with the equivalent experimental data. The profiles have been measured on the centrebody with and without the influence of surface roughness. It can be seen that the agreement is very good apart from the near-wall region where the measurements are known to be inaccurate, due to the increase in response time of the probe. As described earlier, these values have been ignored by the curve fitting procedure. The value nearest the wall has been obtained with the probe touching the wall. At this distance the probe may actually be positioned partly in the sublayer where the derived velocity profile is no longer valid. It is interesting to note that the formula describes the profile distorted by roughness very well. This is probably due to the fact that the surface at this point is smooth.

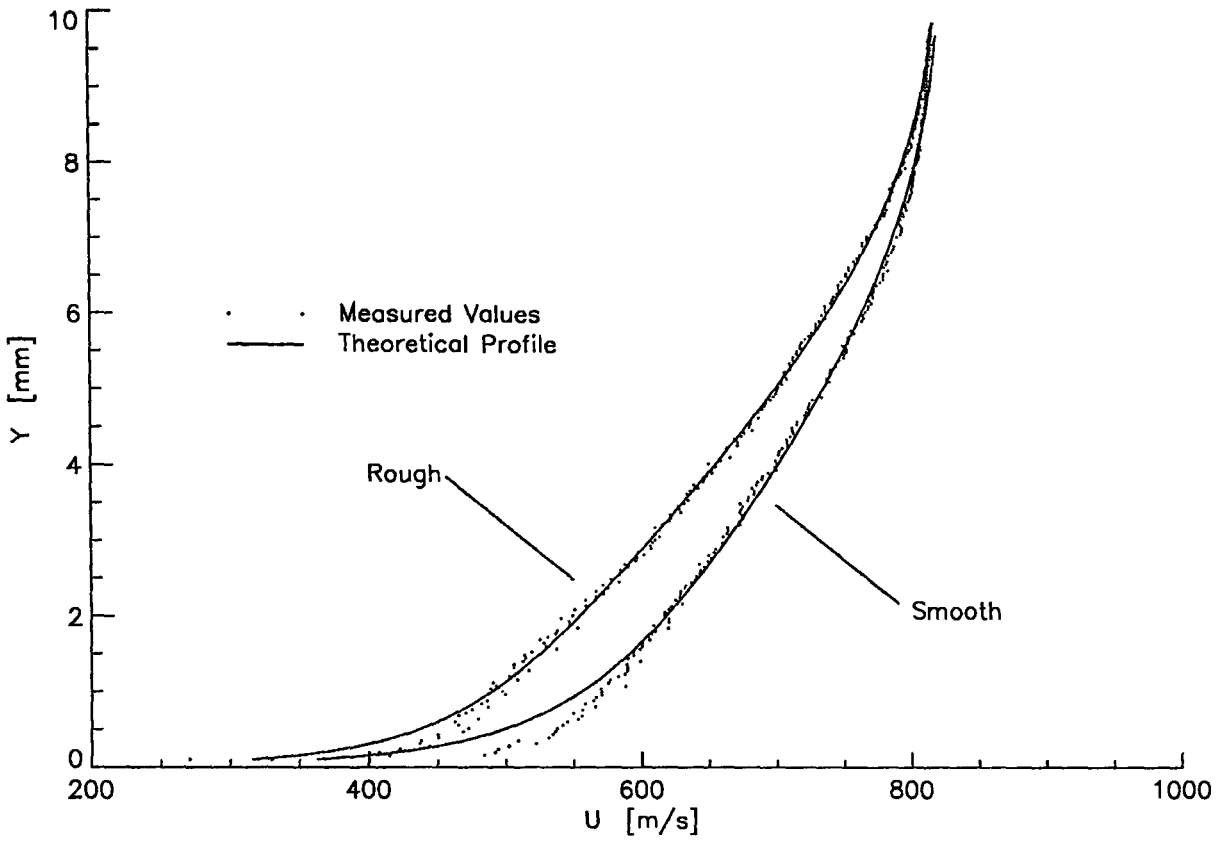

Fig. 2.13 Measured and theoretical velocity profiles on the smooth and rough centrebody (roughness type: sawtooth)

Once the curve-fitting is completed an estimate of skin friction is obtained. This allows the data to be plotted in log-law coordinates:

$$u^+ = \frac{u}{u_\tau}$$
$$y^+ = \frac{y u_\tau}{\nu_w} \qquad (2.14)$$

with:

$$u_\tau = \sqrt{\frac{\tau_w}{\rho_w}} = M_e \sqrt{c_f} \sqrt{\frac{\gamma R T_w}{2}}$$

Fig. 2.14 shows a measured velocity profile together with the theoretical profile obtained from the curve-fitting procedure in comparison with the log law. The data points that have been regarded as inaccurate and were therefore ignored in the curve-fitting are marked. It can be seen that the theoretical profile approaches the log-law asymptotically and matches the data well, apart from the near wall values which give velocities above the expected values. Similar overestimations of velocity at low Reynolds numbers have been reported by Winter, Smith and Gaudet[8].

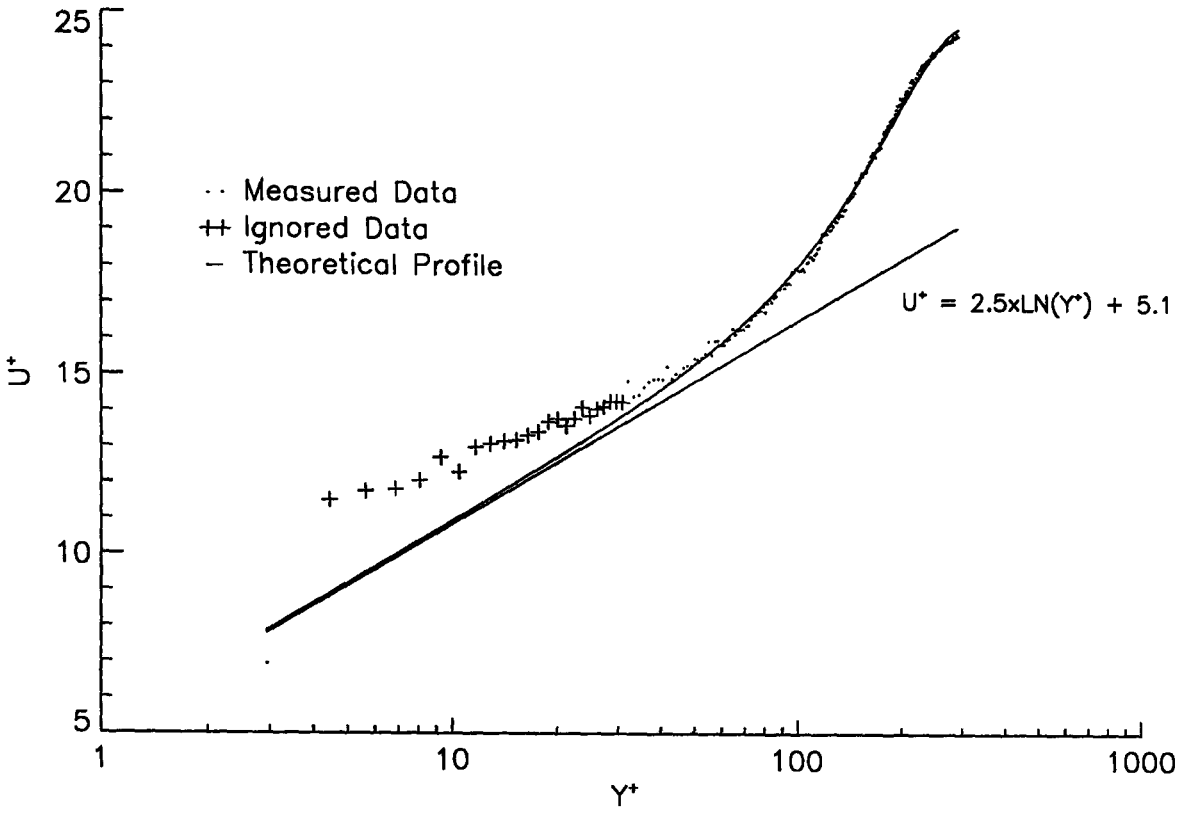

Fig. 2.14 Comparison of measures velocities, theoretical best-fit profile and log-law for a boundary layer profile on the smooth centrebody

The boundary layer exhibits a strong wake component. According to Ref.11 this can be caused by a variety of reasons such as pressure gradients, upstream temperature history effects and wall heat transfer, all of which are likely to be found in the flow under investigation here and will be discussed at a later stage.

As a result of the large wake parameter and the uncertainty of near-wall measurements the part of the boundary-layer profile that lies in the log-law region is very small, even for a relatively undisturbed boundary-layer without roughness. This is unfortunate as it prevents an investigation into the variation of the log-law coefficients due to roughness. All results presented here are fitted to equation (2.11) to obtain a skin friction coefficient. The profiles are then plotted in log-law parameters against the law of the wall with standard coefficients (k=0.4 C^*=5.1). In this fashion the profiles can than be compared qualitatively.

2.3.6 Accuracy of Measurements

Before the calibration of the HSST nozzles is presented all measurements described so far have to be investigated as to their degree of accuracy. This will set the standard that can be expected from the nozzle calibration data and the results of the experimental investigation presented in this thesis. For the purposes of CFD code validation it is important to have an honest assessment of the experimental uncertainties. It also needs to be remembered that not only the results are subject to these uncertainties but also the inflow conditions as they will be presented in the nozzle calibration.

All pressure transducers used in this study have been checked for calibration factors and linearity prior to their use. In all cases deviations from a linear output in the range of interest were lower than 0.5% of the full scale output. For pressures well below the full range this can introduce an uncertainty of up to 1%. Before every experiment the transducer calibration was checked by measuring the output at atmospheric and vacuum pressure, both of which could be determined with highly accurate barometers. For each of the transducers used these calibrations agreed to within 0.2%. All transducers were supplied with a temperature compensation within the expected range. Nevertheless care was taken to install transducers either outside of the flow or attached to a sufficiently large amount of metal acting as a heat sink to avoid deviations from the calibration due to aerodynamic heating of the transducer body. In summary, the pressure transducers have a degree of accuracy of better than 0.7% deviation for the full range and better than 1.5% for measurements utilising only a fraction of the range.

All measured quantities will be subject to errors due to the measurement principle, probe design or assumptions made on the flow state around the measuring device. A good summary of possible errors and the current state-of-the-art in measuring aerodynamic properties in supersonic turbulent flow is given by Meier[50]. The analysis of the experimental errors for the different measurements used in this thesis will closely follow the guidelines laid out in their report.

The pitot pressure measurements in the free stream and the settling chamber were performed with relatively large cylindrical pitot tubes with chamfered leading edges. Due to the size of the probes (2 mm) Reynolds number effects can be neglected. Possible errors could be introduced due to incorrect alignment with the flow direction but as reported by Gracey[51] even for very large angles of attack up to 20° no significant errors in pitot pressures are present. In the current investigation the alignment with the flow is certainly very much better, so that errors due to flow angularity with respect to the pitot probe can be neglected.

For the boundary layer pitot pressure surveys a much smaller flattened head pitot probe was used. The lowest Reynolds number based on probe height was found

to be of the order of 100. As stated in Ref.50 this is still large enough to neglect influences of viscous effects on the measured pressures but as reported earlier a substantial increase of response time due was noted in these low Reynolds numbers. Attempts have been made to eradicate this effect by ignoring all data measured at probe Reynolds numbers below 200 and it is believed that this approach was successful.

Near the surface of the model two effects have to be considered. Firstly the probe is in a region of large total pressure gradient and the actual opening of the probe will be subject to this pressure distribution. The pressure measured by the probe will not necessarily coincide with the total pressure at the centre of the probe. A study undertaken by Mabey[52] reports that probe displacement corrections of up to 30% of the probe height may be necessary. Due to the fact that the near-wall data is ignored in this work this correction is not necessary here. A second source of error is caused by the displacement of the flow when the probe is touching the wall. The value nearest to the wall given in the results may correspond to an effective probe position further away from the wall, at the most by about one third of the probe height.

The static pressures measured are in general at the lower end of the range of the transducers. This does cause problems as the signal to noise ratio deteriorates. In general though it has been found that the aerodynamic noise was well above any electrical noise caused by the transducers. For the lowest pressures measured, such as the centrebody static pressures, this was up to 5% of the signal, hence a certain filtering of the data was necessary. A further source of error is the determination of the vacuum pressure before the run. The barometer used was accurate to 0.2 mm of mercury (26.6 N/m^2). This uncertainty is negligible for measured pressures of the order of the pitot pressure, but for pressures of the order of the free stream static pressure, this causes an error of 2%. The transducers used in surface pressure measurements were mounted inside the model as close to the surface as possible. A certain temperature change of the transducers during an experiment can therefore not be excluded and an influence of the corresponding shift in calibration on the measured result of up to 1% has to be taken into account. Finally the influence of a finite hole size of the surface pressure tapping has to be taken into account. Following the analysis described in Ref.50 this can be estimated to be less than 0.7%.

The free stream static pressure probe is very sensitive to alignment errors as described in Ref.39. This will be the largest source of error in the present investigation as the probe alignment was difficult and could only be achieved within approximately 2°. Hence the probe error due to flow displacement could be up to 5%. Additionally the signal to noise ratio at the low pressures measured in the free stream was not ideal, similar to the remarks made on the wall pressure measurements.

All pressures measured will be subject to variations due to changes in the supply pressure of the wind tunnel. These deviations will be discussed in detail in the section dealing with the wind tunnel nozzle calibration. This is not an actual measurement error, as these variations are entirely physical, but does cause difficulties when comparing the results of different runs or measurements taken at different times during the same run. For this reason all measured pressures are non-dimensionalised by the reservoir pressure measured simultaneously. To obtain an absolute value of any measured pressure this value has to be multiplied by the average reservoir pressure, as given in the nozzle calibration results. Obviously this approach increases the signal to noise ratio for the measurements, but as the reservoir pressure can be measured very accurately with a relatively low noise level this does not present major problems and the advantages far outweigh the disadvantages.

To summarise, it can be said that the pressures given will be subject to an error of less than 1% for results of the order of the free stream pitot pressure and 8% for the surface pressure measurements. The static pressure measured in the free stream has the largest amount of uncertainty, nearing 10%. It is recommended that the measurement of total pressure is used and the static pressure is computed using the Mach number determined from the pitot pressure measurements as this gives a smaller uncertainty.

The total temperature probe is subject to a variety of possible measurement errors. These are mainly due to heat conduction through the thermocouple wires, radiation losses, deviations in the thermocouple output from the theory and effects due to the incomplete stagnation of the flow inside the probe. In order to achieve sufficient response time, bleed holes have been incorporated in the design. These will cause a flow inside the probe. Some of these effects have been taken into account in the probe recovery factor but uncertainties remain. In total, errors in total temperature are expected to be of the order of 5%.

All results that involve traversing a probe through the flowfield will be subject to errors in probe position. The traverse rig can be controlled to a step size of 0.002" (0.05 mm). For large traverse distances (several 10 mm) it is possible that the stepper motor 'misses' a few steps at the start of its movement, before reaching the steady velocity. This can be checked by moving the probe backwards and forward, with the flow on to increase the drag on the device. The maximum deviation from the expected probe position was found to be 3 steps (0.15 mm). For the results given in the nozzle calibration this is negligible as the error in determining the initial position of the probe with a ruler is much larger (1 mm). For measurements inside the boundary layer a further uncertainty in probe position is caused by the design of the probe. As the boundary layer pitot probe is more fragile, a change in position at flow start due to bending of the structure has to be considered. All these factors have been reduced in significance by introducing an electrical contact between the probe and the model surface. The 'touching down' of the probe moving towards the wall could be

determined accurately by monitoring this signal and the uncertainty in probe position is back to the size of a step (0.05 mm).

The determination of boundary layer velocity profiles is subject to a number of assumptions. First a constant static pressure has been assumed inside the boundary layer. By calculating the Mach number at the edge of the boundary layer using wall and pitot pressure and comparing this with a calculation based on pitot and reservoir pressure a discrepancy can be noticed. This is mainly due to a variation in static pressure inside the boundary layer. Obviously this discrepancy was largest in regions of shock-boundary layer interaction where a pressure gradient is expected in the boundary layer. The error in Mach number in these regions was up to 30%. In an undisturbed boundary layer the discrepancy in Mach number was of the order of 5% giving a guideline for the error in velocity due to variations in boundary layer static pressure. A further significant assumption is the usage of Crocco's velocity-temperature relationship (Eq.(2.2)). No sufficiently accurate figures for the actual static temperature are available but judging from published data the error caused by the assumption of Crocco's law is estimated to be of the order of 10%. Finally the experimental errors in determining the wall and pitot pressures inside the boundary layer have to be considered. Summarising all factors the boundary layer velocity profiles are subject to an uncertainty of at least 30% for the undisturbed boundary layer. These results are therefore not recommended for CFD code validation. For this reason all measured pitot pressures are given in an appendix to this thesis as these will be subject to much smaller uncertainties.

The experimental uncertainties for for all types of measurement are summarised below:

Pitot pressures in free stream:	< 1%
Pitot pressures in boundary layer:	< 1% to 5% (near surface)
Surface/wall pressures:	< 8%
Total temperatures:	5%
Velocity profiles: (outside pressure gradient regions)	< 30%
Positional accuracy:	
Free stream traverses:	1.2 mm
Boundary layer traverses:	0.05mm
Skin friction:	Unknown

2.4 Calibration of the HSST

The DRA Fort Halstead HSST has been through a period of very little use in the recent past. Previous results of wind tunnel calibrations are available (Ref.38) but not all possible wind tunnel configurations had been tested. The flow conditions for a number of operating conditions and wind tunnel configurations were unknown at the beginning of this project. Therefore two nozzles were chosen for a closer examination, the contoured Mach 5 nozzles with and without centrebody. The reasons for this decision were that the experimental work was to be undertaken at as high a Mach number as possible whilst still providing turbulent flow over the roughnesses to be investigated. The Mach 6 contoured nozzle was therefore dismissed as it was expected to provide an insufficiently high Reynolds number while the Mach 4 nozzle was lacking in flow speed.

The following investigation therefore has two aims, first to provide the flow data necessary to define the inflow for a successful CFD code validation, the second to arrive at a decision which nozzle to use for the current investigation. It is possible to either use the non-centrebody nozzle with a sufficiently long model to ensure turbulent flow in the area of interest or to use the other nozzle and incorporate the models to be tested into the centrebody, using its large length to grow a turbulent boundary layer.

The reservoir conditions determined are applicable to both nozzles.

2.4.1 Reservoir Pressure

Fig. 2.15 gives the recorded pressures in the settling chamber for two wind tunnel runs of approximately 9s and 13s running time with a heater temperature of 373 K. It can be seen that the pressure rises to the operating condition in 0.7 seconds and then shows a small drop during the useful running time. Additionally it was found that the level of pressure can only be controlled within certain limits. The actual level of supply pressure varies between runs by about 5% with a tendency to increase in subsequent runs.

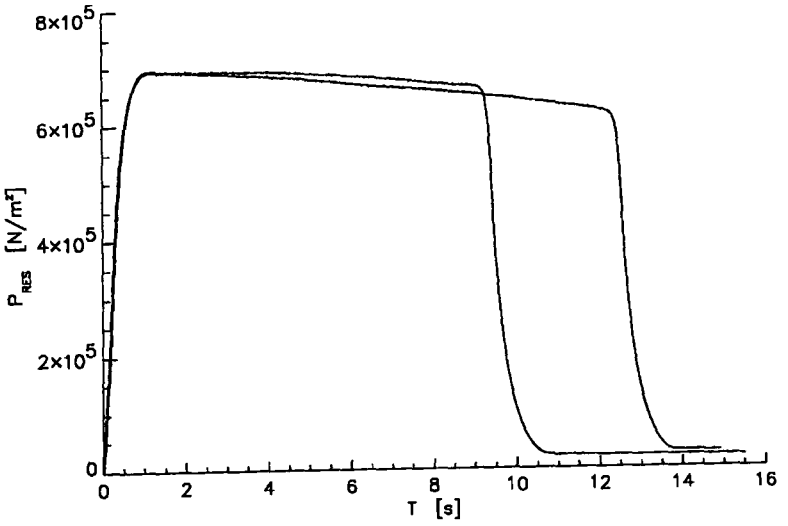

Fig. 2.15 Pressure in settling chamber during two runs

The influence of heater coil temperature on the pressure behaviour in the settling chamber was also investigated. Fig. 2.16 shows the measured reservoir pressures for a variety of heater temperatures during the first seven seconds of a run. It can be seen that the pressures increase during the running time for higher temperatures and decrease for lower heater temperatures. The total variation of reservoir pressure during a typical testing time of 7s was found to be within 4%.

In summary a variation of the supply pressure level of 5% followed by an actual variation during a run of up to 4% has been observed for the same setting of dome valve pressure.

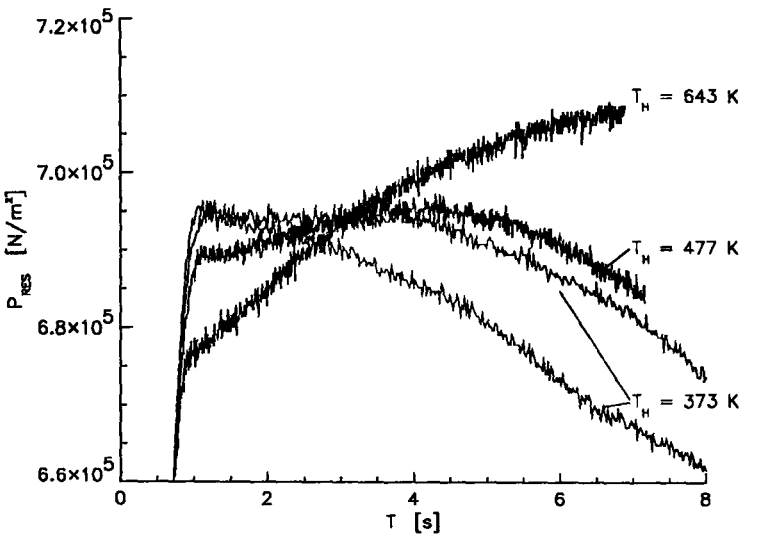

Fig. 2.16 Pressures recorded in settling chamber during several runs for a variety of heater temperatures. Note the enlarged scale.

2.4.2 Total Temperature

The total temperatures measured in the working section for the centrebody and non-centrebody nozzle agreed to within the measurement accuracy. This was to be expected as the total temperature is dependent on the reservoir conditions only which are the same for both configurations. To avoid repetition of data all figures given here represent data recorded with the centrebody nozzle.

Fig. 2.17 shows the total temperature recorded in the working section for the duration of a run. The probe was located at the nozzle exit outside of the nozzle or centre-body boundary-layer. It can be seen that, once steady flow is achieved, the total temperature varies mildly, displaying a small rise of 2% during the whole running time. It was found that, similar to the supply pressure, the actual level of total temperature achieved varied between runs for the same heater temperature setting. This variation was found to be within 3%.

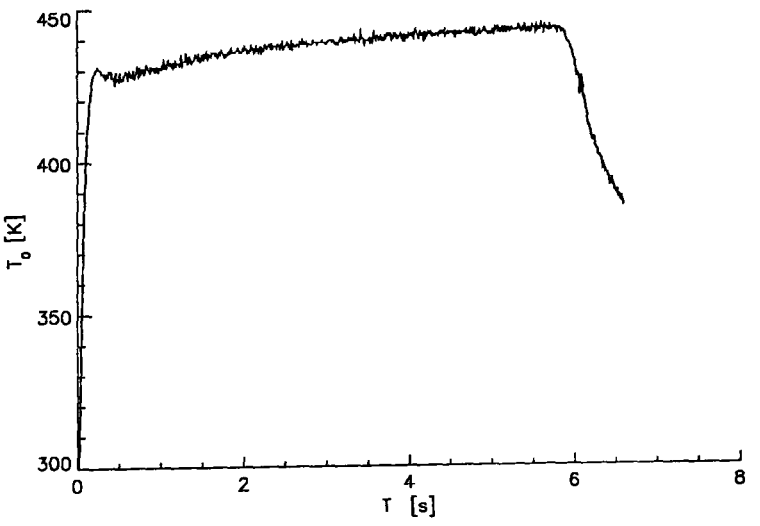

Fig. 2.17 Total temperature measured within working section during run. T_H=388K

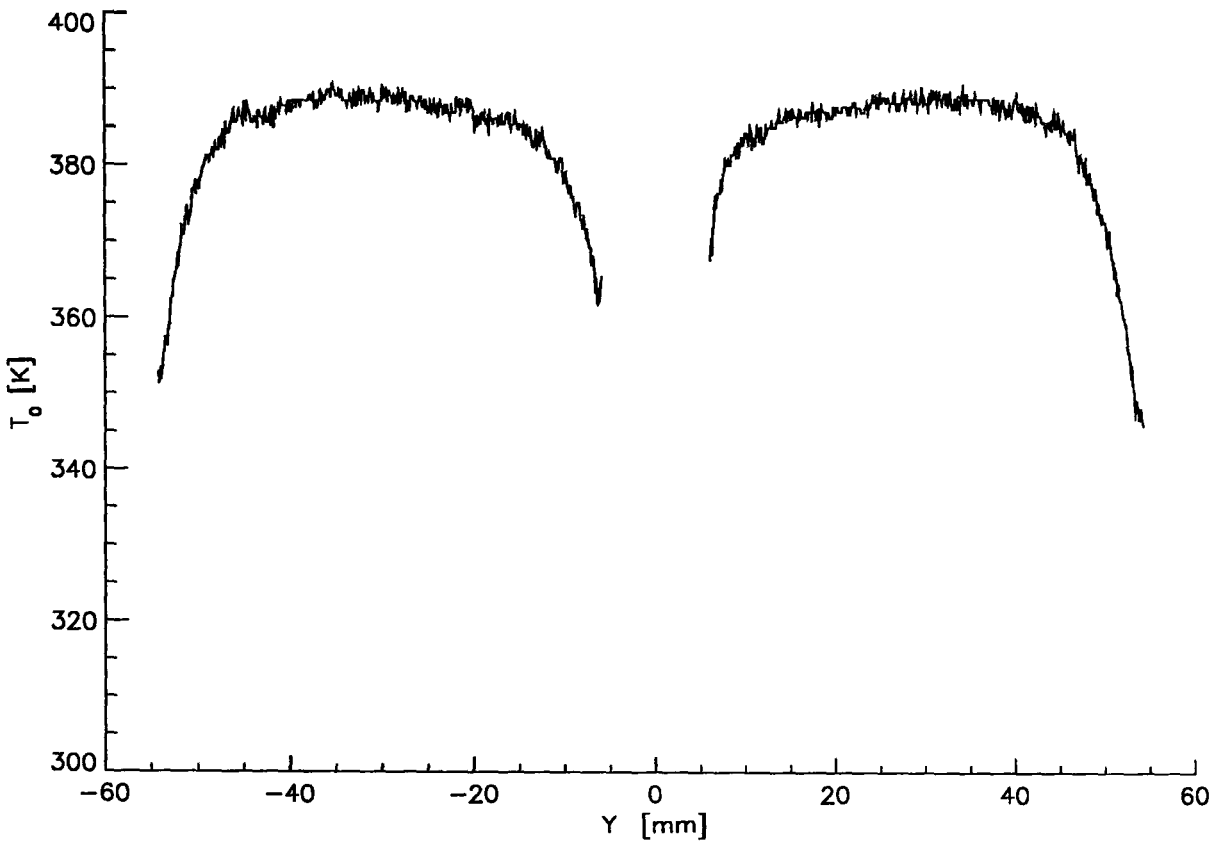

Fig. 2.18 Total temperatures above and below centrebody at nozzle exit. T_H=373K

As it was not possible to measure the total temperature routinely at one position in the flow no suitable normalisation could be used to eliminate the influence from variations on the measured temperature traverses. Hence the traverse data not only shows the variations within the flow but also contains some variations due to the change in temperature during the running time and from run to run. When comparing results the influence of those variations has to be taken into account. Fig. 2.18 shows two total temperature traverses obtained at the nozzle exit. It can be seen that, apart from within the boundary-layer, the temperature distribution throughout the flow is relatively even and symmetrical.

The next item investigated was the relationship between the total temperatures and the set heater temperatures. Fig. 2.19 shows the measured temperatures along traverses above the centrebody for three different heater temperatures, spanning the possible range of the tunnel. It can be seen that the traces are roughly proportional to the heater temperatures.

Fig. 2.20 gives the achieved total temperatures as a function of the heater settings. In all cases the total temperatures are seen to be above the heater temperatures.

The variations for the same setting of heater temperature between different runs are of the order of ±3%, the change during the run is of the order of ±2%.

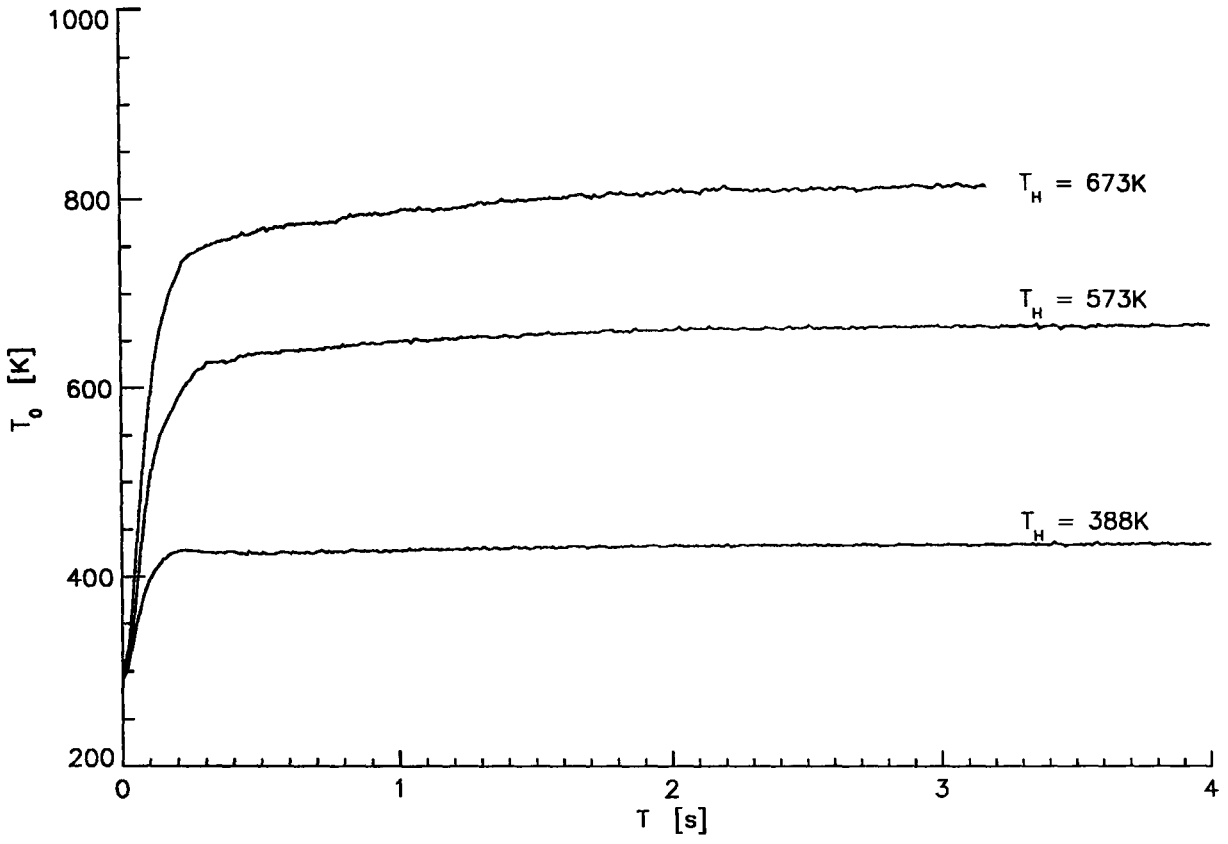

Fig. 2.19 Total temperatures in free stream for a variety of heater temperature settings

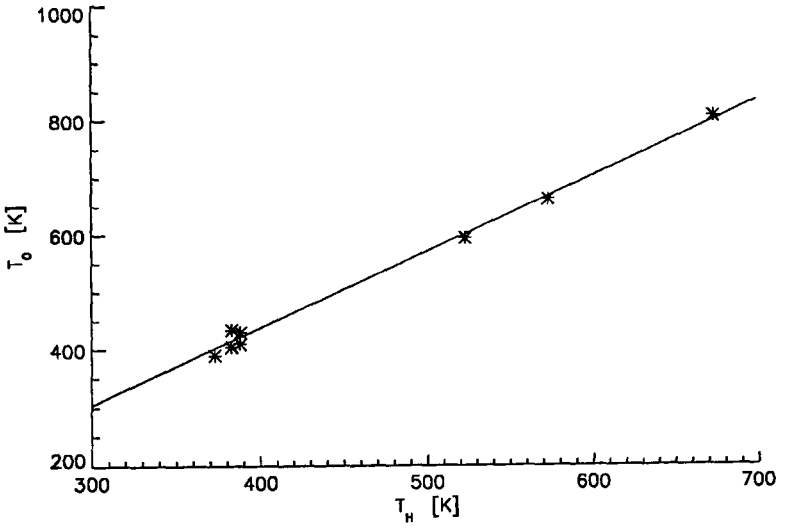

Fig. 2.20 Measured total temperatures for different heater temperature settings

2.4.3 Pitot Pressure

Fig. 2.21 shows the pitot pressure recorded at one location in the working section for the Mach 5 nozzle with centrebody. The flow takes about 0.7 s to develop and then reaches a plateau region. At the end of the run a sharp pressure peak is observed, associated with the strong shock during the breakdown of the flow. A small variation in pitot pressure can be observed during the run. This is caused by changes in the supply pressure. It is possible to completely eliminate the variation of pressure measurements caused by the variation in supply pressure, if all measured pressures are normalised with a simultaneously recorded reservoir pressure. This gives a constant ratio of pitot pressure with reservoir pressure and it can be concluded that the Mach number does not vary throughout the useful running time of the tunnel.

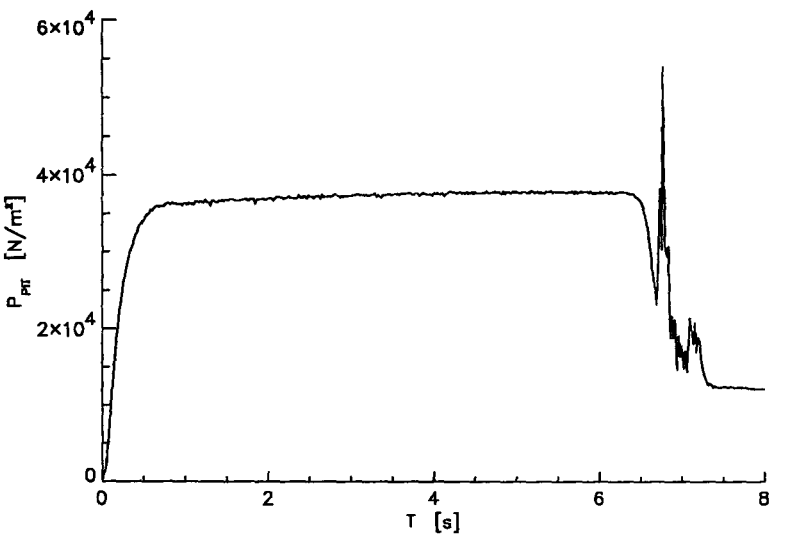

Fig. 2.21 Pitot pressure during run inside the working section for the centrebody nozzle.

Traverses in the non-centrebody nozzle

When measuring the pitot pressures within the working section by traversing the pitot probe through the flow, the variations due to the supply pressure are excluded, as described above. Hence the pressures are given as non-dimensional p_{pitot}/p_{res}.

The first nozzle to be investigated is the Mach 5 nozzle without centrebody. The nozzle exit diameter is 152 mm. The flow is assumed to be symmetrical around the centreline, so only single

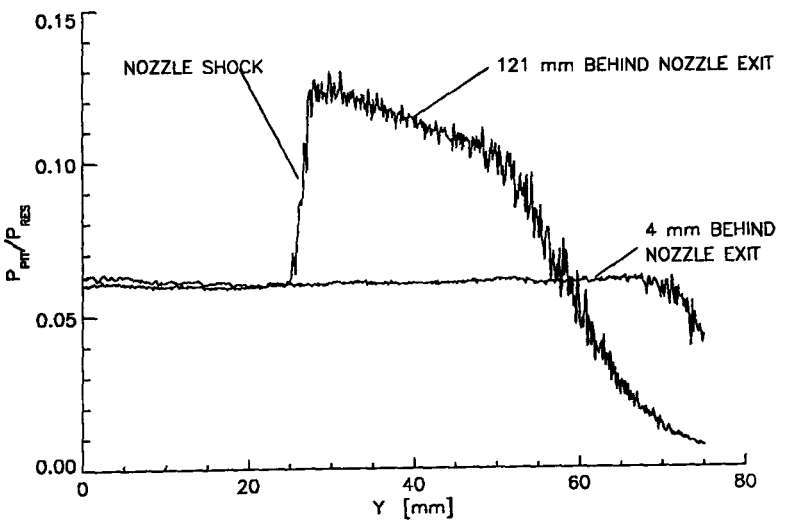

Fig. 2.22 Pitot pressures measured in the non-centrebody nozzle at two radial traverse positions.

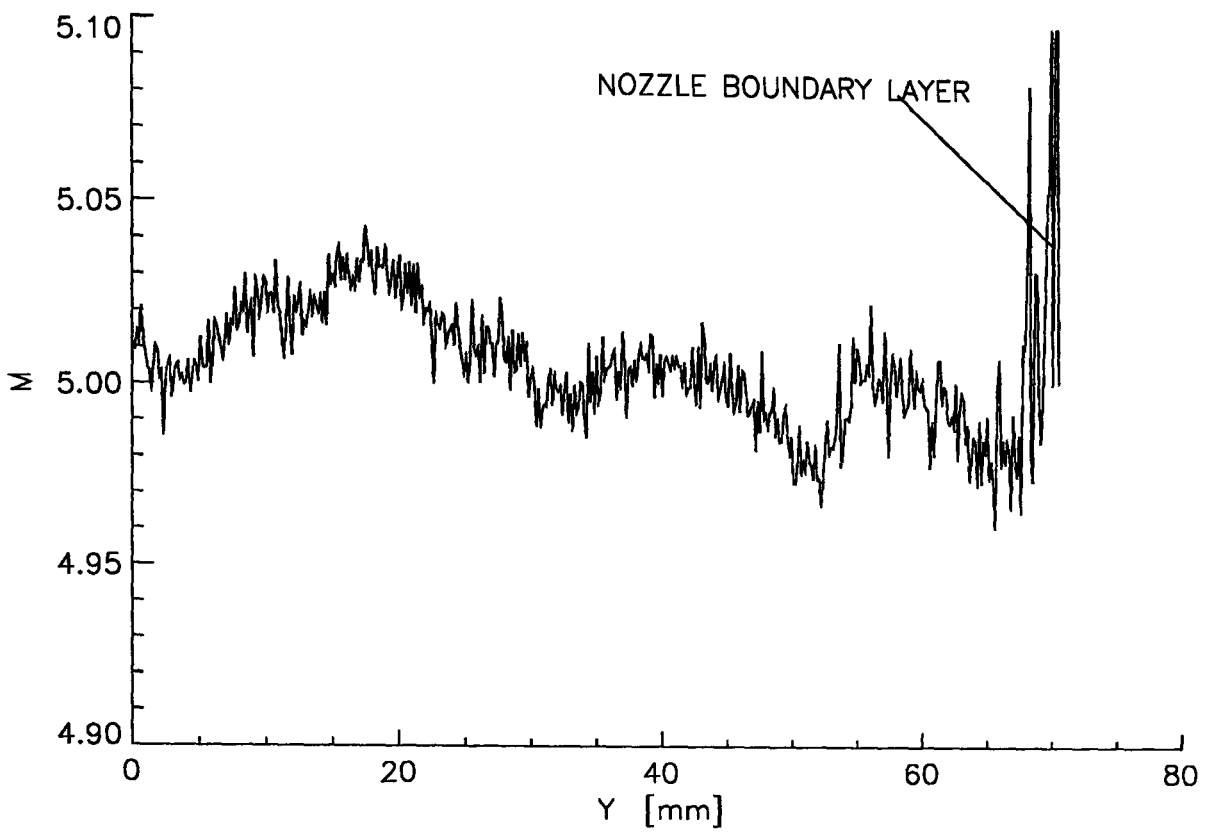

Fig. 2.23 Mach number distribution at the nozzle exit of the Mach 5 non-centrebody nozzle

sided traverses will be presented here. Fig. 2.22 shows the pitot pressures measured at two traverse locations, 4mm and 121mm behind the nozzle exit. The traverse at the downstream position exhibits a strong jump in pressure indicating an oblique shock originating from the nozzle edge. This nozzle shock is caused by a pressure difference between the outer pressure in the working section and the free stream pressure of the flow inside the nozzle. The strength of this nozzle shock can be reduced by improving the performance of the diffuser or by reducing the blockage in the working section. During the measurements performed on the centrebody nozzle it was detected that the model mount caused a large amount of blockage. It is suggested that a re-design of the model mount can improve the size of the useful flow significantly by reducing the blockage and thus dropping the pressure in the working section. The areas of useful flow, inside the nozzle shock can be seen clearly in Fig. 2.22. Within the useful flow the pitot pressure was found to stay within a band of ± 2% from the mean value. This causes a variation of less then 0.02% in free stream Mach number. The distribution of Mach number at the nozzle exit is shown in Fig. 2.23. The Mach number has been calculated by assuming a normal shock in front of the pitot probe and using the reservoir and pitot pressures to give the ratio of total pressure through the shock. This is not valid in the nozzle boundary layer and the apparent increase of Mach number at the edge of the flow is not physical. The wave-like variations in Mach number are often observed in nozzles designed using the method of characteristics and a boundary layer displacement effect correction as reported by Korte[53] and Jacobs and Stalker[54].

Traverses in the centrebody nozzle

For the centrebody nozzle the assumption of axisymmetric flow is not necessarily justified. If the centrebody is not perfectly aligned in the centre of the nozzle the flow may contain significant non-uniformities. For these reasons the flow in the centrebody nozzle has been examined in more detail. Pitot pressure traverses have been performed at four streamwise positions, between 62 mm upstream and 110 mm downstream of the nozzle exit. All traverses have been recorded above and below the centrebody.

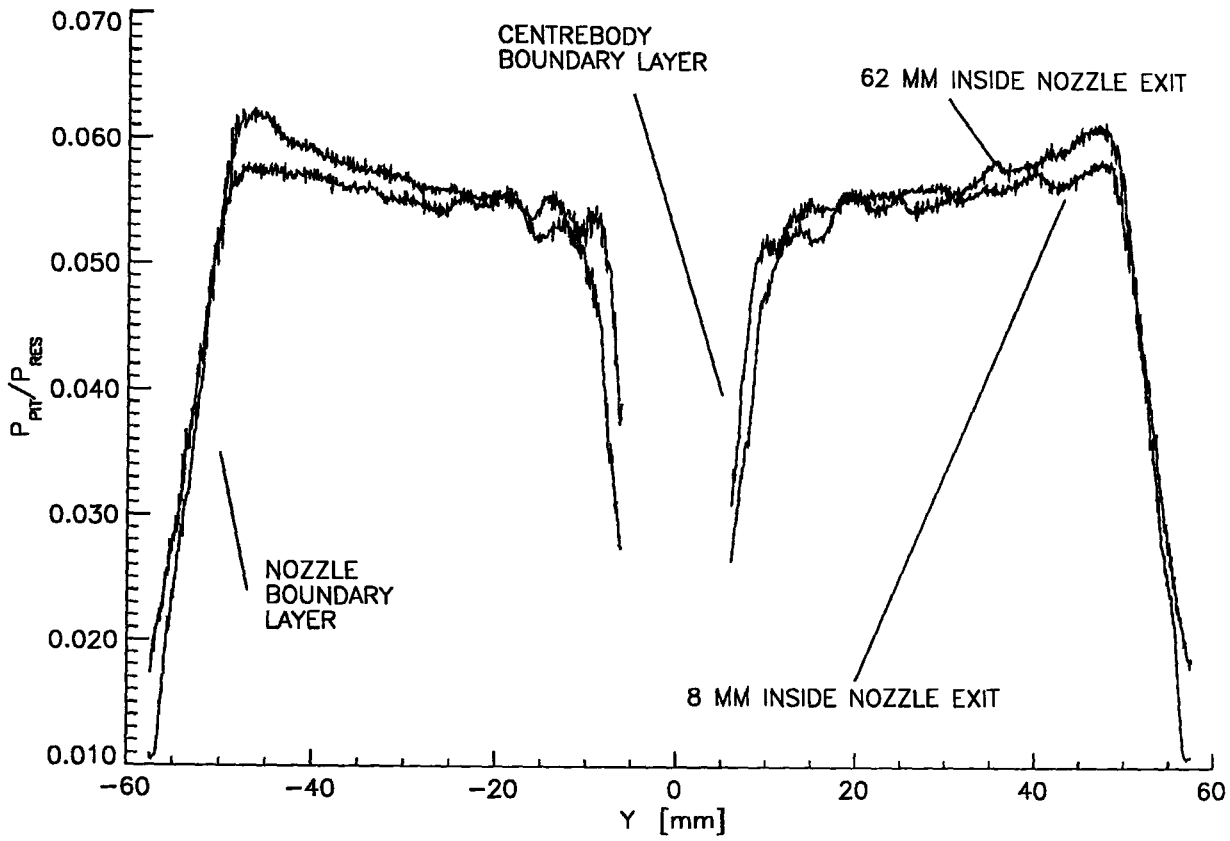

Fig. 2.24 Pitot traverses inside the centrebody nozzle

Fig. 2.24 shows the results of four traverses recorded 62mm inside the nozzle and near the nozzle exit (8 mm inside) above and below the centrebody. While at the upstream position the flow is not expected to be fully developed and some variation is anticipated, the flow near the nozzle exit should give an account of the quality of the useful flow. It can be seen that the pressure variations near the nozzle exit are smaller than further upstream, although some wave patterns in the pressure profiles are apparent. All four traverses display a certain degree of symmetry around the centre-line. The sharp drop in pressure to either side of the traces represents the nozzle and centre-body boundary-layers, both appear to be 10-15 mm in thickness.

Fig. 2.25 shows the results obtained further downstream of the nozzle exit. Even at the most downstream location no sign of a sudden pressure change due to the nozzle shock is visible. The pressures at the outer edges of the flow show a

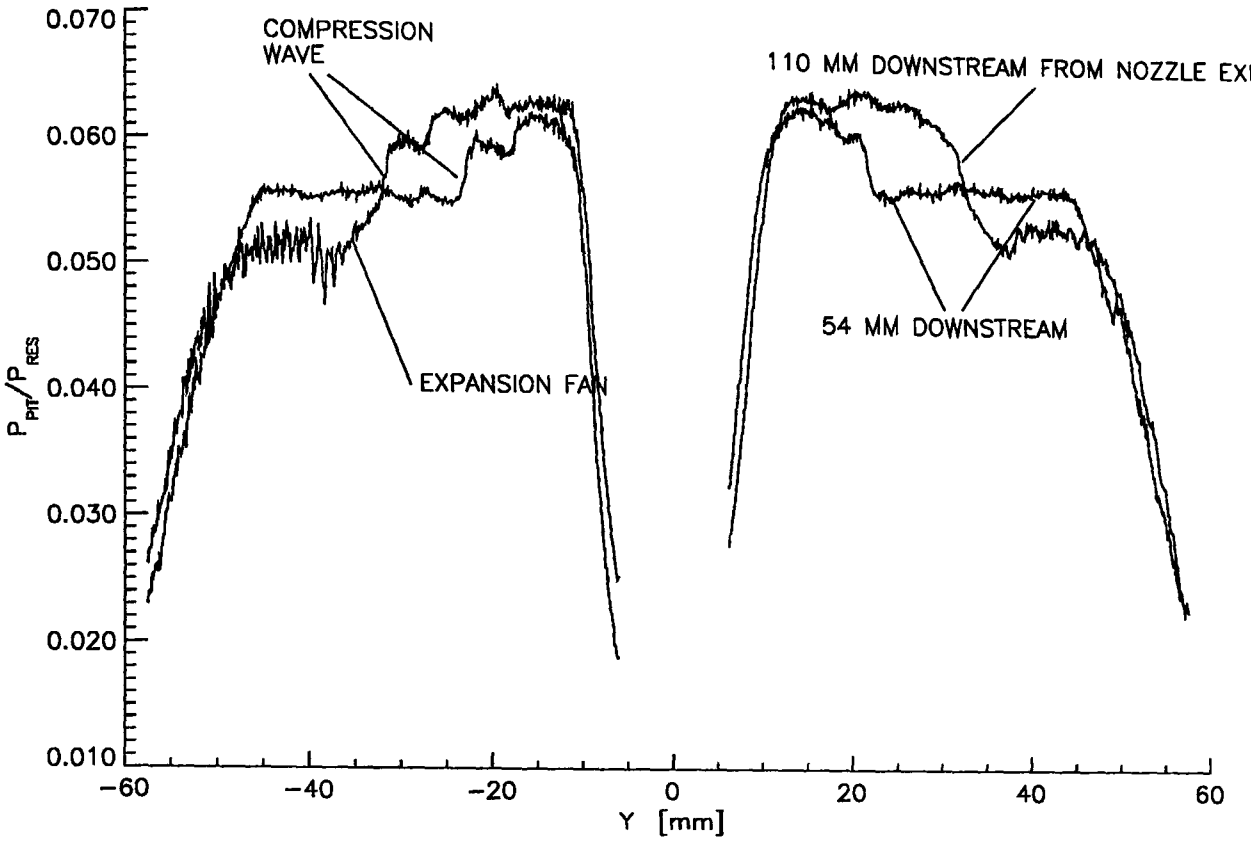

Fig. 2.25 Pitot pressures in the working section of the centrebody nozzle

certain drop compared to the measurements recorded further upstream. This is an indication that the nozzle shocks have been eradicated completely and been replaced by an expansion fan. The useful flow is subject to several variations. The dominant feature is a step like pressure variation with the step in pressure moving away from the centre-body and apparently strengthening further downstream. This phenomenon is symmetrical about the centre-line. A possible cause is a pressure wave within the useful flow. The centre-body has been checked for surface irregularities and was found to be perfectly smooth compared to the boundary-layer thickness. An investigation of the nozzle and centrebody geometry did not reveal any unusual features. Irregularities of surface slopes, concentricity and roundness were all found to be within reasonable limits. Hence the disturbance has to originate elsewhere. The symmetry of the phenomenon suggests a possible mismatch of the nozzle contour with the expanding flow.

Further information can be obtained from Fig. 2.26, giving the Mach number distribution for the traverses inside the working section. As the pitot profiles were relatively symmetrical around the centreline only the upper part of the working section is given. It can be seen that the Mach number varies between 5.15 and 4.95 in the useful flow. The compression wave noted earlier reduces the Mach number by about 0.1 and its location is also indicated. A number of other, smaller, distortions are also apparent in the flow. The average Mach number is around 5.08 with an overall variation of 4%. Compared with the performance of the non-centrebody nozzle discussed earlier (Fig. 2.23) this nozzle delivers flow of considerably poorer quality.

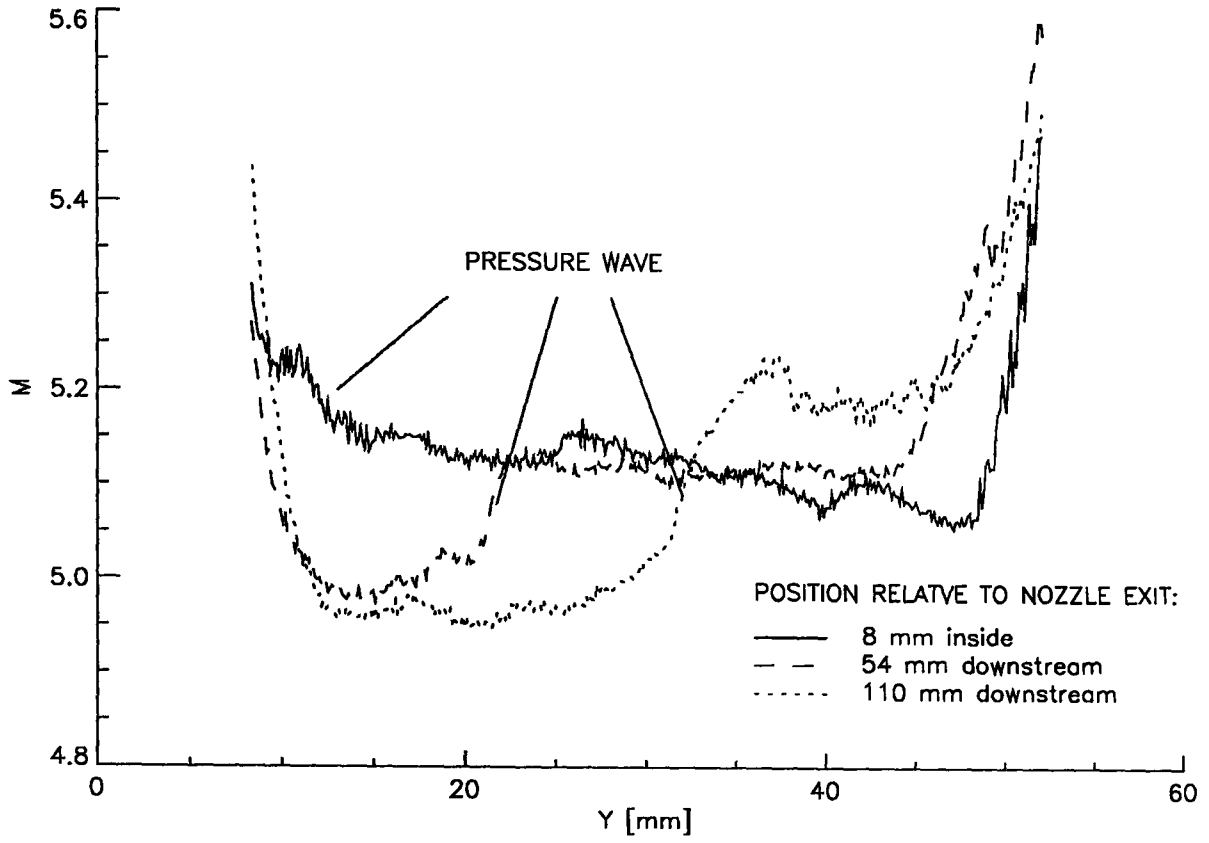

Fig. 2.26 Mach number distribution along three traverse positions above the centrebody in the Mach 5 nozzle.

Generally supersonic nozzles are designed with a method of characteristics solution for the inviscid flow between the throat and the exit and an additional correction to account for the displacement effect of the boundary-layer. The design goal is to achieve a uniform flow at the nozzle exit with all expansion waves cancelled out by the shape of the nozzle. If this is not fully achieved expansion or compression waves can be formed at the nozzle wall and spread into the useful flow. In the case of compression waves the wave pattern will gradually converge and form a shock. The pressure pattern of such a feature will therefore steepen and become more defined further downstream while it may be more difficult to detect upstream when the waves are still spread out. By comparing the location of the pressure jump in the traces of Fig. 2.26 it was found that the wave has probably reflected from the centre-body somewhere near the location of the second traverse (8mm inside nozzle) in Fig. 2.24. This explains why no sign of this pressure jump can be found at this location and why the pressures within the centrebody boundary-layer appear to be higher than upstream. At the most upstream traverse station within the nozzle no obvious sign of such a pressure rise can be found. The compression waves may be too spread at this location to make detection within the overall variation of the pressures possible.

It is known that the nozzle was originally designed for a free stream Mach number of 5. The existence of areas with a Mach number as high as 5.15 at the nozzle exit suggests that the original design of the Mach number distribution in

the streamwise direction was not followed by the actual nozzle. In fact substantial parts of the flow appear to overshoot the design Mach number of 5. The nozzle contour is not matched to this, higher, Mach number and compression waves form as a result. A similar deviation from the design point of a supersonic nozzle was reported by Beckwith et al[55] for their supersonic nozzle. The cause for this discrepancy was given as a sudden change in slope of the centreline design Mach number as illustrated by Fig. 2.27. In such a case, the flow does not follow the design conditions but rather exhibits an overshoot followed by a compression wave. It seems likely that the wave structure in the centrebody nozzle is caused by a similar problem. A survey of the pitot pressure along the inside of the nozzle would be able to clarify this situation, as the Mach number distribution could then be obtained. This can not be performed with the currently available equipment and has to be left for future work.

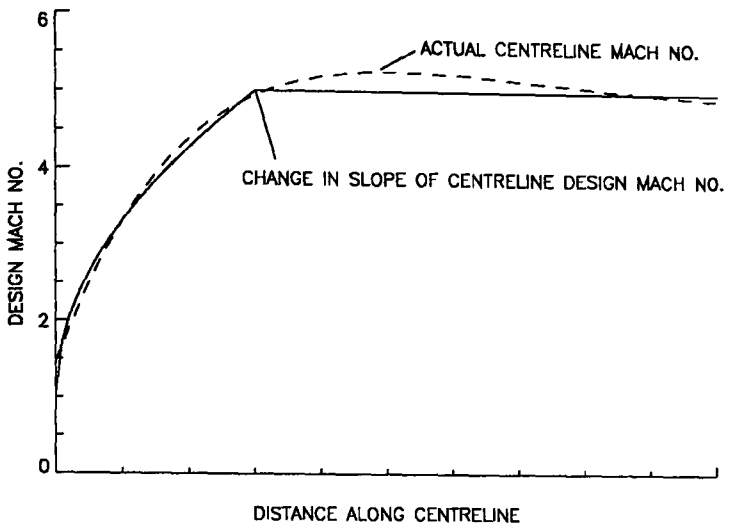

Fig. 2.27 Sudden change of slope in the design Mach number for a supersonic nozzle as possible cause for nozzle overexpansion.

As it is desirable to operate the wind tunnel at a variety of heater temperatures to change the Reynolds number and total enthalpy of the flow, the influence of heater temperature on the flow quality has been investigated. Fig. 2.28 gives the pitot pressures at the exit of the centrebody nozzle for two extremes in the heater temperature, namely 373 K and 633 K. It can be seen that the pressure pattern is virtually unchanged, hence the influence of heater temperature on flow quality is negligible. Due to the change of Reynolds number however a change in boundary-layer parameters has to be anticipated.

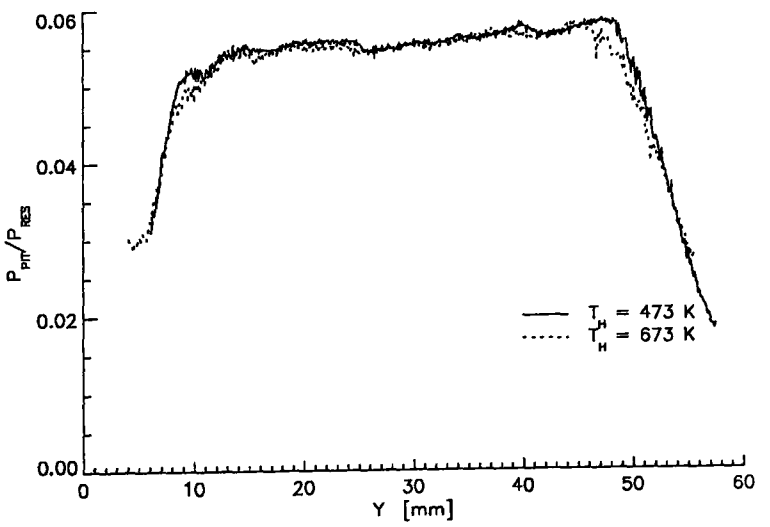

Fig. 2.28 Influence of heater temperature on pitot pressure distribution in the centrebody nozzle

During the investigation two additional causes of severe changes in the flow quality of the centrebody nozzle have been found. The first was a set of waves formed due to a leakage at a centrebody connection, the second was the appearance of strong nozzle shocks due to an increase in working section pressure caused by a sting mount located at the diffuser entry. The data presented in this report has been obtained with the sting mount removed and no measurable leakage into the flow from the centrebody. As a result of these observations it is recommended that the design of the sting mount be changed as it causes a large amount of blockage, thus reducing the useful flow area.

The location of the expansion fan originating from the nozzle exit and the compression wave inside the useful flow are important features to be considered when designing experiments to be performed with this nozzle. For this reason the locations of the major features of the flow in the working section are given in Fig. 2.29.

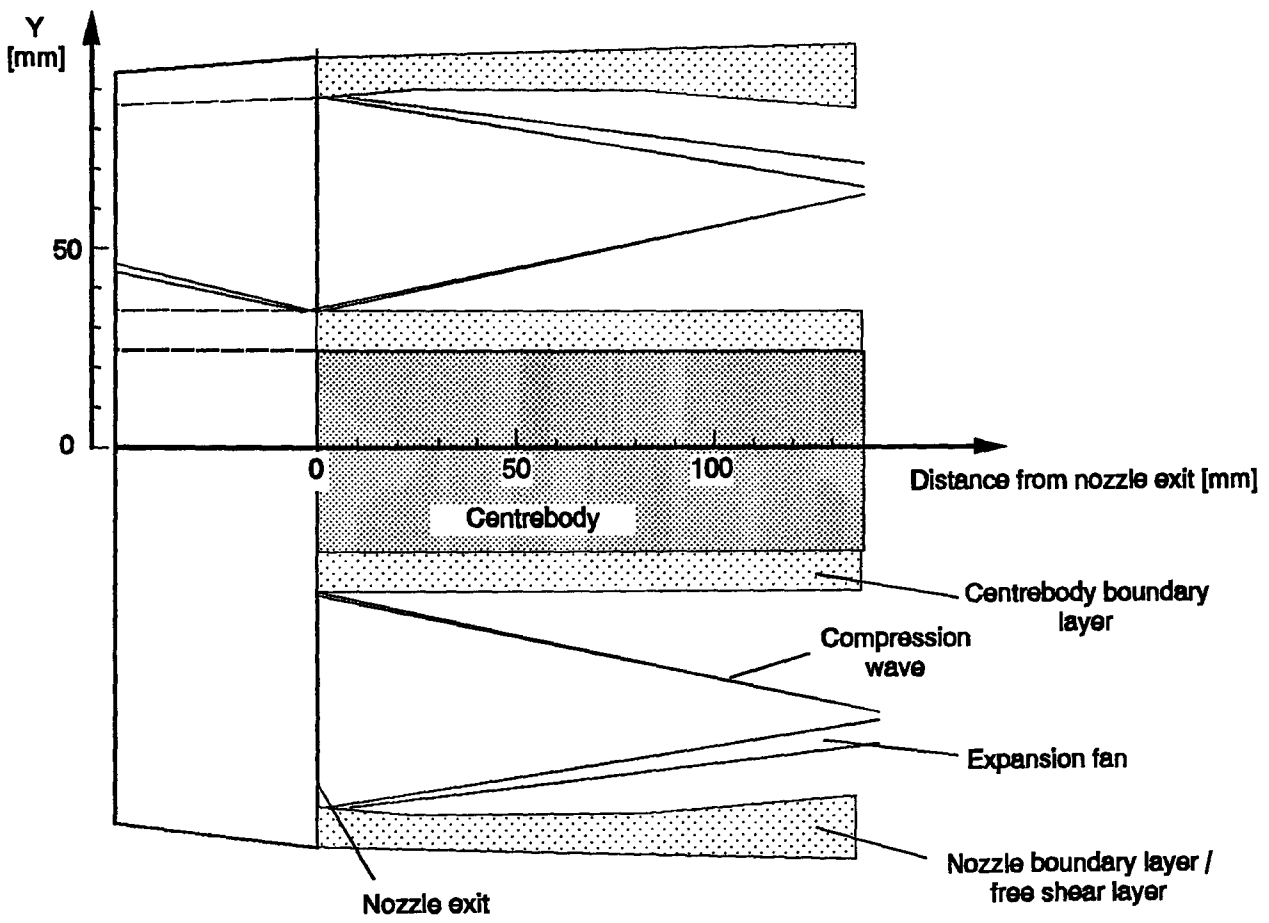

Fig. 2.29 Major flow features and dimensions for the Mach 5 centrebody nozzle.

2.4.4 Summary and Conclusions

The results of the wind tunnel nozzle calibrations are summarised to give an overview of the main characteristics of the facility. The reservoir conditions are assumed to be equivalent for both nozzles and are only given once.

Reservoir / total pressure:	
Valve setting 174psi ($1.20 \times 10^6 N/m^2$):	644.7×10^3 N/m^2 ± 3.7%
Valve setting 200psi ($1.38 \times 10^6 N/m^2$):	716.3×10^3 N/m^2 ± 3.5%
Max. variation during run:	5%

Total temperature (outside of boundary-layers):	
Heater temperature setting 373K:	393K ± 3%
Heater temperature setting 523K:	600K ± 3%
Heater temperature setting 673K:	809K ± 3%
Max. variation during run:	4%

Average free stream unit Reynolds number (Flow nominally at Mach 5):

Valve setting 200psi; Heater setting 373K:	13.237×10^6 m^{-1}
Valve setting 200psi; Heater setting 523K:	6.812×10^6 m^{-1}
Valve setting 200psi; Heater setting 673K:	4.370×10^6 m^{-1}
Valve setting 174psi; Heater setting 373K:	11.919×10^6 m^{-1}
Valve setting 174psi; Heater setting 523K:	6.133×10^6 m^{-1}
Valve setting 174psi; Heater setting 673K:	3.934×10^6 m^{-1}

The Reynolds number varies for the same setting of dome pressure and heater temperature by ± 5% due to the variation in reservoir conditions.

Mach 5 non-centrebody nozzle:

Diameter of useful flow at nozzle exit:	130 mm
Mach number in useful flow:	5.0 ± 0.4 %
Pitot pressure in useful flow:	$0.062 \times P_t$ ± 2 %
Static pressure in useful flow:	$0.0019 \times P_t$ ± 5.6 %

Mach 5 centrebody nozzle:

Centrebody diameter:	50.8 mm
Diameter of useful flow at nozzle exit:	146 mm
Mach number in useful flow:	5.07 ± 2 %
Pitot pressure in useful flow:	$0.057 \times P_t$ ± 6.7 %
Static pressure in useful flow:	$0.0017 \times P_t$ ± 10 %

An overview of the dependence of Reynolds number on heater temperature is given in Fig. 2.30.

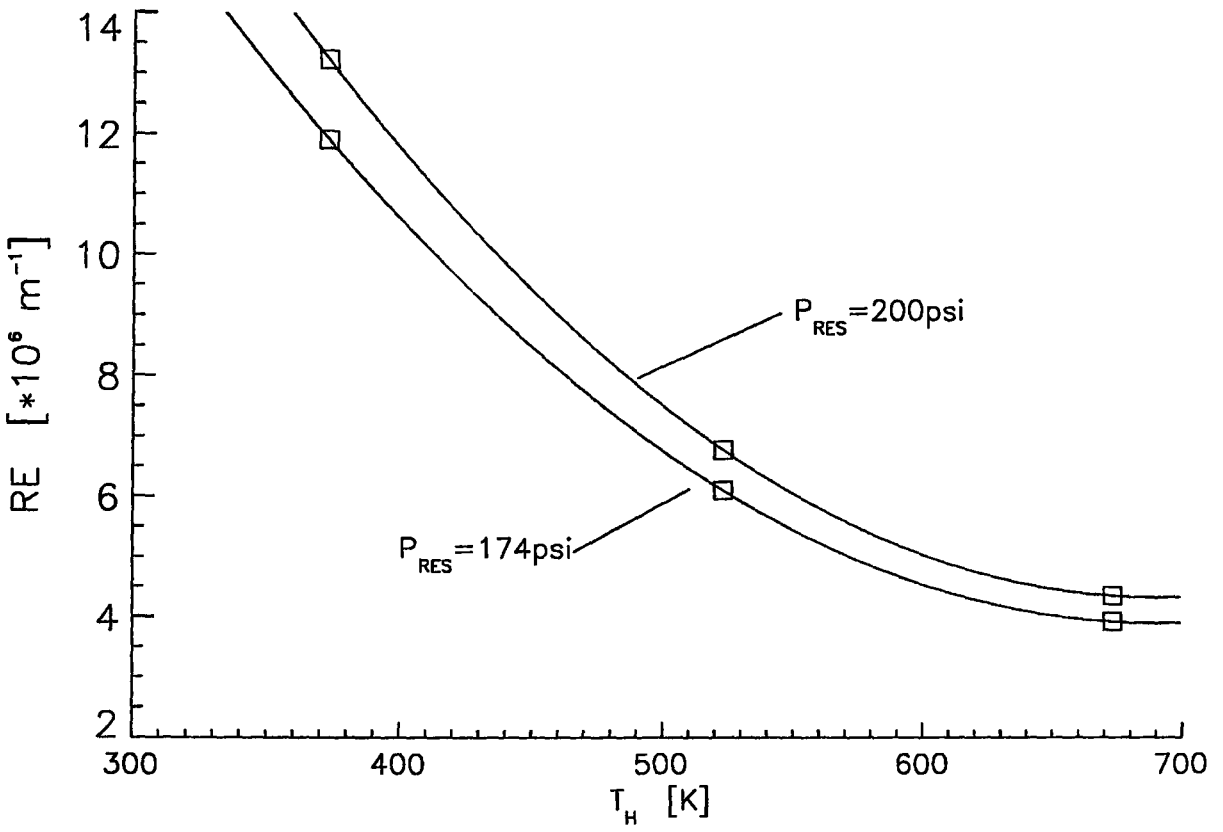

Fig. 2.30 Free stream Reynolds numbers in the HSST for various settings of supply pressure and heater temperature.

The data collected in this investigation allows a quantitative judgement of the flow quality in the HSST Mach 5 nozzles. The results obtained can serve as a guideline for the design of future experiments in this facility.

It was found that, after a startup time of approximately 0.7 seconds, steady flow conditions prevail for up to 10 seconds. When the vacuum pressure before the run is at the lowest level possible with the current equipment (0.2 Torr) and the blockage is kept to a minimum, a running time of 13 seconds is possible. During the steady flow period the reservoir conditions vary mildly, this being 5% in

pressure and 2% in temperature with subsequent effects on other flow parameters.

Between several runs at the same settings of heater temperature and dome valve pressure the actual levels of supply pressure and total temperature show variations of 7% in pressure and 6% in temperature.

To eliminate deviations in measured quantities due to these uncertainties in reservoir conditions, all pressure measurements will be accompanied by a simultaneous measurement of reservoir pressure and all heat transfer measurements by a measurement of total temperature in the working section.

The flow quality in the working section was found to be very different for the two nozzles. While the non-centrebody nozzle exhibited a very uniform flowfield with only 0.4% variation in Mach number, the centrebody nozzle was subject to relatively large disturbances. A compression wave was found to run right through the useful flow causing a 10% change in pitot pressure and a 3% change in Mach number. Any future experiments using this nozzle have to take the location and strength of this wave into account as it could have a serious effect on the results of an investigation.

By varying supply pressure and heater temperature a wide range of Reynolds numbers can be investigated. The boundary layer on the centrebody is expected to be turbulent in every case due to its length. By using the Mach 5 nozzle without centrebody which produces the same free stream Reynolds numbers, both laminar and turbulent flows can be investigated.

The current study is concerned with the effect of large scale roughness on a turbulent boundary layer and its behaviour downstream of such a roughness entering regions of adverse pressure gradient. As the turbulent length required for such experiments is relatively large compared to the size of a possible model, it was feared that the Reynolds numbers that can be achieved in the non-centrebody nozzle may be too low to produce a turbulent boundary layer of sufficient length. The usage of a trip was not desired as the turbulence in this case may not be representative of the general case. Unfortunately the flow for the centrebody nozzle is subject to relatively large disturbances. Nevertheless it was decided to perform the investigation on the turbulent boundary layer of the centrebody and design models to fit onto it. One advantage of this route is the fact that the boundary layer to be investigated is much larger and therefore easier to survey. Nevertheless the author is aware that this choice is a compromise and does not present an ideal situation.

3. Heat Transfer Measurement

The aim of the present investigation is to produce a set of flow data for a number of model configurations. The scale and position of the flow features to be investigated could not always be determined beforehand, thus making a detailed flow survey necessary. To perform this with standard heat transfer measurement techniques would be extremely time consuming and costly. Liquid crystal thermography (LCT) offers an opportunity to gain the required data within the scope of this project in both cost as well as time and giving a spatial resolution that can not be achieved with traditional techniques.

Before embarking onto the liquid crystal techniques a few traditional methods of heat transfer determination will be discussed as some of these techniques were also used in this project. Furthermore some of the theoretical aspects of other approaches have proved valuable for the development of LCT and have been partly incorporated in its analysis.

3.1 Traditional Techniques

The measurement of heat transfer in hypersonic flow is one of the most important aspects of experimental work in this field. Hence a large amount of literature is dedicated to this subject that can not all be included here. The selection is therefore biased to its direct application to this work.

Most hypersonic wind tunnel facilities belong to the group of short duration facilities. In the widest sense of the meaning this includes all facilities where the running times are too short to reach adiabatic flow over the model. A very good summary of traditional heat transfer measurement techniques in this class of facilities was presented by Schultz and Jones[56]. All techniques employed in these cases are transient techniques, hence they derive the surface heat transfer from transient temperature measurements in combination with a heat conduction model. The two models mainly used are infinite slab, where the wind tunnel model is assumed to consist of one material of infinite thickness; or thin skin, where the model is covered with a thin layer of conductive material and has an insulating surface underneath it so that the surface layer can be treated as an ideal calorimeter. The former technique is more widely used for very short running times as the assumption of infinite thickness is justified when the thermal penetration is small compared to the model dimensions. The latter is applicable to longer running times as constant temperature within the thin skin is one of the assumptions for this technique.

The aim in the current work is to use a method of heat transfer measurement applicable to the hypersonic gun tunnel in Cranfield and the HSST at DRA Fort

Halstead. Therefore only methods employing the infinite slab assumption are discussed here.

By assuming the model to consist of a slab of uniform material of a semi-infinite thickness the heat conduction equation can be greatly simplified and integrated. An additional assumption that proves very useful is to exclude any heat conduction in a direction parallel to the surface (cross-conduction). This assumption is not always justified in regions were the differences in heat transfer between neighbouring points on the surface is very large, hence causing large temperature gradients along the surface. Errors due to this approximation will be discussed later. For now we will assume a one dimensional material as in Fig. 3.1, following the analysis presented in Ref.56. Fourier's equation for heat conduction then simplifies to:

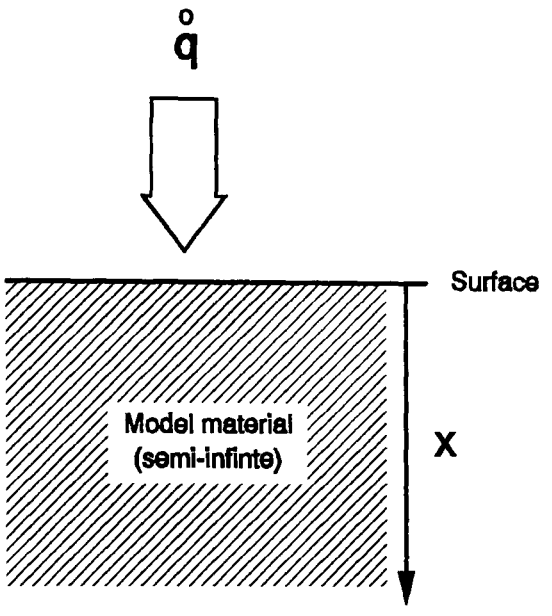

Fig. 3.1 One dimensional semi infinite slab model of heat transfer

$$\frac{\partial^2 T}{\partial x^2} = \frac{1}{\alpha}\frac{\partial T}{\partial t} \tag{3.1}$$

By using the initial condition of constant temperature inside the model material ($T=T_\infty$) and the boundary conditions:

$$-k\left.\frac{\partial T(x,t)}{\partial x}\right|_{x=0} = \dot{q}_s(t)$$
$$T(x\mapsto\infty,t) = T_\infty \tag{3.2}$$

the heat conduction equation can be integrated to yield an analytic solution. Note that $\mathring{q}_s$ is the heat transfer into the model surface. The final solution is given in Ref.56 as:

$$\dot{q}_s(t) = \sqrt{\frac{\rho c k}{\pi}}\,\frac{1}{2}\int_0^t \frac{\frac{dT_s(\tau)}{d\tau}}{(t-\tau)^{1/2}}\,d\tau \tag{3.3}$$

where T_s is the surface temperature rise.

In order to obtain a heat transfer measurement it is now necessary to measure the surface temperature with time. Equation (3.3) can then be integrated to give the desired surface heat transfer. An algorithm for a numerical integration of (3.3) has been developed by Cook and Felderman[57] and some further variations and their effect have been discussed by Simenoides[58]. One disadvantage of the numerical algorithm is that it has a tendency to greatly increase the noise of the solution if the surface temperature distribution contains high frequency fluctuations. As most measured temperature traces will be subject to some experimental noise this leads to a need for smoothing of the integrated heat transfer result.

There are several methods available for the measurement of temperatures on the surface of a model. An important factor in the selection of a technique is the time response of such a method. In very short duration facilities such as the College of Aeronautics gun tunnel running times are of the order of 20 ms. If transition or turbulent fluctuations are to be investigated the response times necessary are even shorter.

One sensor available for these measurements is the platinum thin film surface thermometer (see Refs.56,58). The measuring principle is the change in the resistance of a very thin (0.1 to 1 micron) film of platinum on the surface. The sensitivity of the device has to be carefully calibrated before its use. The response time of such a gauge is better than 1ms. Thin film gauges tend to be sensitive to ablation and erosion which can cause a problem in some facilities, particularly when there are particles in the flowfield.

A more robust device for short duration temperature measurements is the coaxial thermocouple[59] which is used successfully in shock tunnels of even shorter running time than the gun tunnels.[58, 60]. The measuring junction between the two thermocouple materials has to be created by filing or sanding the surface of the gauge, thus blending the two metals. These gauges are less sensitive than thin film gauges but more resistant to damage. The output does not need to be calibrated as reliable calibrations are available in the literature. The thermal coefficients of the device, however, have to be known to extract heat transfer values.

Both of the above methods are subject to noise problems as the measured output is very small. The further increase of noise due to the numerical integration of the temperature traces can be avoided by using analogue integration circuits, but this does not give an output of temperature which may be required. The smoothing qualities of an analogue circuit have to be modelled with digital filters for the numerical integration. A further difficulty of the above methods is that both require a lot of skill and time in the manufacturing of models and sensors and experience in calibration and operation.

In the current investigation a more simple device was needed to compare heat

transfer measurements with liquid crystal thermography. As the majority of the work was conducted in the HSST and only mean data was required, time response considerations were not the most important factor. The sensor was not required to have a high spatial resolution as results in areas of interest were expected to be obtained with liquid crystals. It was therefore decided to use stick-on surface thermocouples supplied by RS[61]. These were relatively inexpensive and easy to apply to previously made models. A further advantage is that the use of plastic as model material posed no problems for the application of these sensors. The surface temperature could be recorded with a time response sufficient for the HSST and the numerical integration as described in Ref.58 was employed. The output of the K-type thermocouples was converted into degrees Celsius using a thermocouple amplifier manufactured at Cranfield. A typical temperature history is shown in Fig. 3.2. During the experimental investigation it was noticed that the microchip used in this amplifier did not perform to scientific levels of accuracy. This was particularly noticeable in a zero-shift of up to ±1°C. Fortunately the determination of heat transfer only depends on the relative change in temperature so that this had little influence on the final values of $\dot{q}$. The integrated heat transfer history for the thermocouple trace of Fig. 3.2 is given in Fig. 3.3.

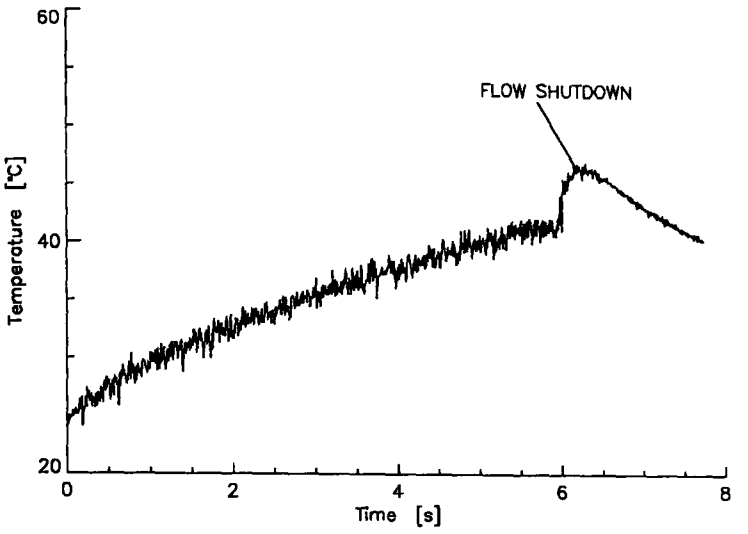

Fig. 3.2 Surface temperature measured with a thin film thermocouple in the HSST

A careful examination of all the factors involved concluded that the measurement errors of thin film gauges and coaxial thermocouples are currently of the order of 20% for short duration facilities (Simenoides[58]) which agrees with the value given by Denman et al[62] for measurements performed in a gun tunnel. In the case of the surface thermocouples used in the HSST the temperature can only be recorded to ±1°C, causing an error in heat

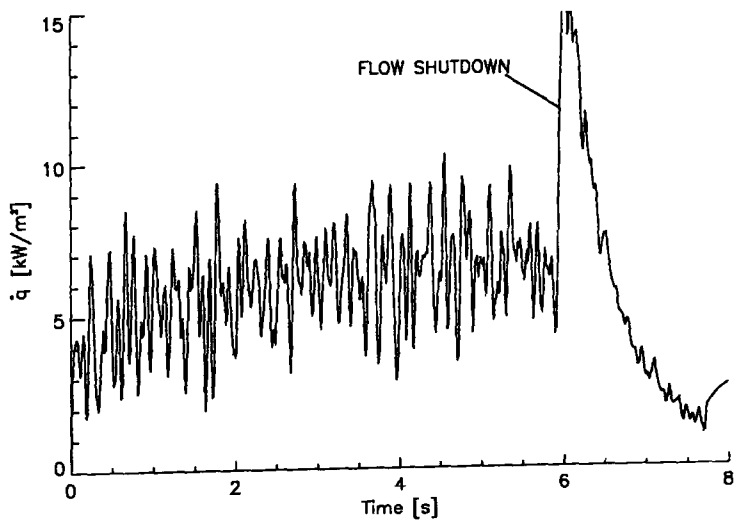

Fig. 3.3 Heat transfer measured with a thin film thermocouple in the HSST

transfer of approximately 10% and a noise to signal ratio of the final heat transfer history of 30%. These values could be improved substantially by using a higher quality thermocouple amplifier and an overall uncertainty of less than 5% in mean heat transfer in the HSST could be achieved.

All of the techniques described can only measure the surface heat transfer at one location. If more detailed flowfield information is required a large number of sensors need to be placed on the model. In most cases this is limited due to constraints on space. The heat flux measurement of an individual gauge will be an average over its surface area. This can lead to erroneous results in regions of very localised peaks or valleys of heat transfer. If variations of heat transfer exist in a presumably two-dimensional flowfield, such as the variations observed in transitional flows or due to leading edge disturbances, the placement of the sensor will be crucial to the measurement. The conclusions drawn from such a result can be misleading.

It is therefore highly desirable to have access to a heat transfer measurement technique that can provide data over the whole model surface while still being easy to apply to allow the testing of a large number of configurations. Even if the accuracy of such a technique was reduced compared to traditional methods, the results can give information on the flow structure and where to place more reliable, and more expensive, gauges.

One technique capable of measuring heat transfer over the whole surface of a model is infrared thermography. The surface radiation of a model is recorded by a camera sensitive to infrared radiation and then converted into a temperature using a pre-determined calibration curve. This technique has been used successfully in supersonic flows by a variety of researchers such as Carlomagno[63], Westby[64] and Boerrigter[65]. Unfortunately it requires expensive equipment and wind tunnel windows transparent to infrared radiation. All authors also report problems with the spatial resolution of this method. This prohibits its use for the present work.

For this reason it was decided to use liquid crystals to perform the desired heat transfer measurements.

3.2 Liquid Crystal Thermography

Liquid crystals are available as a surface coating that selectively reflects light depending on the surface temperature and shear stress. If the underlying material absorbs light (black surface), this selective reflection will be visible as a colour change for different shear stresses and temperatures. The types of liquid crystals possessing these qualities are referred to as thermochromic liquid crystals. The temperature range and bandwidth of liquid crystals can be controlled by mixing several types of ingredients. Possible bandwidths range from fractions of a degree C to about 40 °C, useful ranges are from -30°C up to 115°C.

If such a material is encapsulated in binder material the colour response due to shear stress can be suppressed and only the dependency on the temperature remains. The encapsulation also serves to hold the liquid crystal capsules together and allows the use as a surface coating with a solid appearance. It is this colour change of encapsulated thermochromic liquid crystals that can be used to measure the surface temperature of wind tunnel models and therefore determine the heat transfer.

3.2.1 Overview

The first use of liquid crystals in aerodynamic testing was reported in 1968 by Klein[66]. Encapsulated liquid crystals are now widely used in aerodynamic applications for surface flow visualisation and heat transfer measurements. An overview is given in Hallcrest[67].

Currently there are two major techniques for obtaining quantitative information from a liquid crystal response. The key difficulty is to convert the liquid crystal information which is available as an image into an estimate of the surface temperature.

The first approach that is used by a number of researchers[68] is to use a liquid crystal mixture with a very narrow bandwidth, say half a degree C. A similar technique is to use a wide band liquid crystal mixture and only observe one particular colour transition[69]. As the surface temperatures experienced during a typical experiment vary over a much larger range, only a very small portion of the surface will actually display a colour, or the particular colour transition. The appearance will most likely be that of a narrow 'strip' of liquid crystal response that 'moves' along the surface during the course of an experiment. An image processing routine can then be used to pick out the maximum intensity of this 'strip' which gives the locations on the model surface which are at the temperature of the liquid crystal response. The bandwidth of the liquid crystal mixture will determine the accuracy of the temperature detection, although measures can be introduced to improve on this if necessary. By recording a large

number of frames during the course of a run it is possible to follow the 'movement' of the liquid crystal response over the whole surface. After the tracing of this line it is possible to know the time during the run at which almost every point on the surface reached the liquid crystal response temperature. Applying certain assumptions to the heat transfer history this information is sufficient to obtain the heat transfer for the whole surface. The advantage of this technique is that it requires only relatively simple image processing to detect the liquid crystal response and colour recording equipment is not needed. If necessary, the information can be obtained manually by investigating all available images, for example on a videotape. The line of liquid crystal response at each moment in time (or frame on the video-recording) is equivalent to a contour of heat transfer. A disadvantage of this technique is that a large number of frames need to be analysed to give a high resolution result. In short duration facilities the maximum frame rate of the camera may put a limit to this number. If the image quality is poor it may not be possible always to detect the liquid crystal response everywhere, thus leading to incomplete data.

An alternative technique is to use a wideband liquid crystal. If the bandwidth is large enough to span all temperatures experienced on the model surface, then the different colours displayed will correspond to different heat transfer rates. A single frame contains heat transfer information over a large part of the model surface. If several frames are available for analysis the accuracy can be significantly improved as multiple measurements are obtained for each surface location. By comparing the colour response with a pre-determined liquid crystal calibration, the surface temperatures can be determined. An obvious improvement of such a technique is to use an automatic process to perform this comparison as the human eye is subjective. One such option is to view the liquid crystal response through a number of bandpath filters that allow only one wavelength of light to pass. This has been successfully applied by Akino et al[70,71] for steady state heat transfer measurements. In the limited time available in short duration facilities however, it is impossible to scan the same image with a large number of filters. It is therefore necessary to develop a numerical algorithm to distinguish between the different colours displayed by the surface coating. Such an approach has been taken by several researchers (Refs.72, 73, 74) for low speed flows and convection problems. In all these cases a calibration experiment has been performed before the actual measurement to determine the colour temperature relation of the liquid crystals. The setup was than kept the same as far as possible and a flow was applied. This procedure is virtually impossible in an hypersonic wind-tunnel as severe restrictions exist on the access to the working section. In most cases camera and lighting conditions have to be changed between different experiments. Camci et al[72] also remarked on the reduced sensitivity of liquid crystals in the blue region resulting in a reduction of accuracy.

For these reasons the narrow bandwidth technique is more widely used in high speed wind tunnel applications. The advances suggested here aim to overcome

some of the problems and develop a suitable technique for use in a wide variety of short duration wind tunnels. The first problem to be addressed is the automatic detection of colour, to allow a digital determination of surface temperatures. Then the application of wide band liquid crystal thermography to both experimental facilities will be discussed.

3.3.2 Automatic Colour Detection

The reflected colour of a liquid crystal coating is dependent on its temperature. It is this effect that can be used to measure temperatures with a liquid crystal coating. Unfortunately this is not the only influence on the colour reflected by the liquid crystal coating. Before describing the colour detection technique, these influences are discussed in more detail.

The first factor to be considered is the wavelength spectrum of the light source used for illumination. As the colour displayed by the liquid crystal is produced by selectively reflecting a particular wavelength, its intensity will depend on the intensity of the same wavelength in the oncoming spectrum. In the extreme case of a single wavelength lightsource a colour can only be displayed if the reflected wavelength matches the lightsource, hence only one colour will be visible in a very narrow band of temperatures. This effect can be used to reduce the colour bandwidth of a narrow bandwidth liquid crystal. For a wide band mixture it is therefore desirable to use a lightsource of a uniform spectrum containing all visible wavelengths. This may not always be possible and care has to be taken to use the same illumination when comparing the liquid crystal response between a calibration experiment and the actual measurement.

A further influence on the detected colour is the inclination of the surface towards the observer. If this angle gets very large the observed colour can be very different for the same liquid crystal temperature. The effect is particularly large for so called neat or pure liquid crystal coatings, where colours can vary considerably for only small changes in viewing angle. This is due to the fact that in such a case most of the liquid crystal molecules are aligned perpendicular to the surface. Encapsulated liquid crystals however contain liquid crystals packed into small spheres surrounded by binder material. Therefore the angles that the encapsulated liquid crystals make with the surface are randomly distributed. The colour seen from an observer is therefore a mixture of wavelengths for all these different viewing angles. This results in a much reduced sensitivity of the observed colour from the viewing angle. Current research suggests that up to 20° deviation from the normal is acceptable.

The next important factor is the angle of illumination towards the liquid crystal coating. When observing a surface from the same position a considerable difference in colour can be noticed if the position of the illumination source is

varied. This is another important factor when comparing calibration and experiment.

Finally the influence of the recording equipment needs to be mentioned. In most cases a video camera will be used to record the liquid crystal response during an experiment. The colour of the images stored on the videotape will depend on the camera that has been used and the adjustment of it. Most modern video cameras perform a white balance to modify their sensitivity to give a suitable colour range for the illumination. If the same colour is recorded with the same illumination, but different settings of white balance, the resulting recording will be different.

To reduce the importance of these factors, a colour-temperature calibration of the liquid crystal mixture has to be performed under exactly the same conditions as the experiment. Calibrations supplied by the manufacturer may not be sufficient to achieve measurements of suitable accuracy.

Wind tunnel models to be used for a liquid crystal experiment have to be manufactured out of a black material or covered with a layer of black paint. A paint layer will introduce uncertainties due to its thickness and thermal properties. For this reason all models used have been manufactured out of a black, easily machinable, plastic material with low thermal conductivity (ERTALYTE).

The first problem to be addressed is the quantification of colour. In broadcasting technology, the colour of an image is usually understood as the relation between the intensities in the three primary colours, red, green and blue. Most modern image digitisers follow this pattern by quantifying each colour as three 8 bit numbers corresponding to these primary colours. Therefore the colour information available will be coded as the image intensities in those three bands (RGB). The liquid crystal response, recorded at one particular temperature will be given as the relative intensities in red, green and blue. To compare these with the temperature they need to be reduced to a single value. It was found that a useful quantity for such a comparison is the hue as defined in the standard HLS colour system. An investigation by Camci et al[72] found that the hue value calculated for one colour remains constant for large changes in image intensity or illumination.

In order to investigate the suitability of colour detection to evaluate the temperature of a liquid crystal coating a wind tunnel model has been fitted with a thermocouple and a layer of liquid crystals has been applied. The change in surface temperature was measured and the corresponding colour change in the vicinity of the thermocouple has been recorded with a standard CCD video camera (Panasonic NV-S7B). Several frames of the video recording have then been digitised with a standard framegrabber card with 8 bit resolution in each colour. The RGB values recorded in the near vicinity of the thermocouple location are shown in Fig. 3.4 as a function of the thermocouple temperature. The values obtained at each temperature have been averaged over a sample area of 8 by 10 pixels, equivalent to an area on the model of 4 by 5 mm. The liquid crystals

used here are of the type Licritherm TCS 811, manufactured by Merck-BDH. The colour range starts at 27.6°C and ends at 41.5°C. It can be seen that the liquid crystal response starts in the red colourband for low temperatures and ends in the blue region for high temperatures. In this particular example the maximum temperature was still below the end of the liquid crystal range, therefore the colour at the highest temperature is still in a blue-green region. If the temperature reached a higher level, the green response would reduce and only a blue intensity would remain. Outside the liquid crystal bandwidth the intensities are not zero. This is due to light being reflected from the model surface and noise caused by the recording equipment. In a real experiment a black model surface will never appear to be completely black. The illumination will cause reflections and the model surface may have deficiencies that are the source of additional reflections. The actual colour response due to the liquid crystals will also be subject to a scaling depending on the intensity of the illumination.

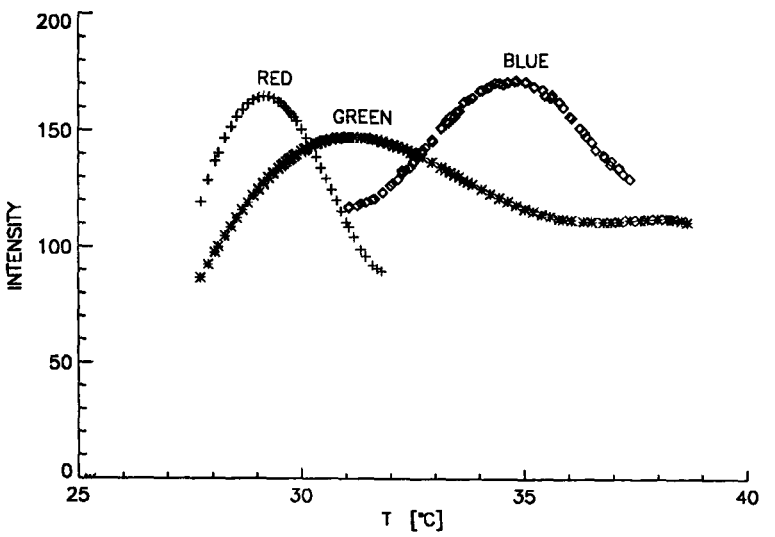

Fig. 3.4 Average response of a liquid crystal coating as a function of temperature in the RGB system.

To reduce the impact of these problems an image of the model surface is recorded before the surface reached the liquid crystal response temperature. In a wind tunnel this can easily be achieved by recording an image with the flow off. This image can now be digitally subtracted from every frame recorded during the run. This helps to normalise the response, although the noise on each colour band is obviously increased. A further advantage is that areas that display a response in both cases such as a reflection on the surface, will be removed. The colour values now determined at the thermo-couple location are given in Fig. 3.5. It can be seen that the intensities are lower and the maxima are similar for the three colours. Now it is possible to ignore all

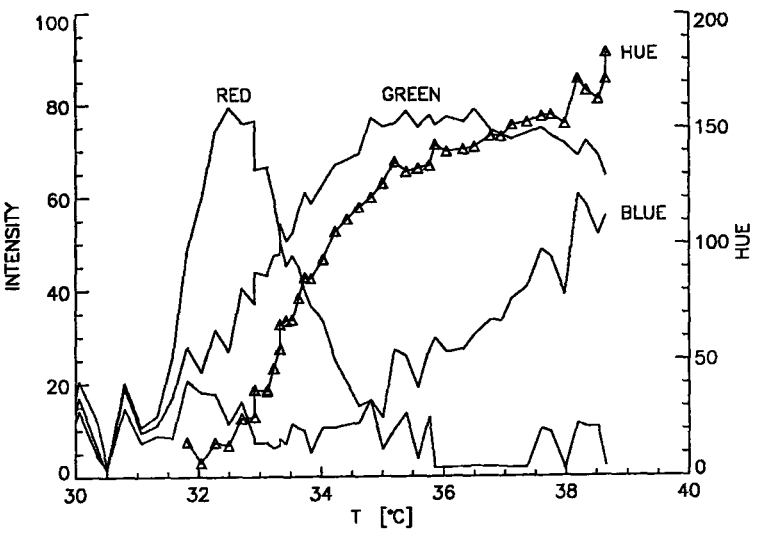

Fig. 3.5 Response of a liquid crystal coating in the RGB system after differencing with the flow-off image.

intensities below a certain threshold, thus leaving only the real liquid crystal response. A useful threshold level in this example would be around an intensity of 15. Using this technique obviously changes the apparent response of a liquid crystal mixture but the influence of illumination and background material are greatly reduced. With digital image processing each pixel of the image is now treated as described, first subtracting the RGB levels of the flow-off image and then thresholding the intensities, before calculating a hue value. The formula used to obtain the intensity I and the hue H are, as given in Ref.73:

$$I = \frac{R + G + B}{3}$$

$$H = \frac{90 - \arctan\left(\frac{F}{\sqrt{3}}\right) + \begin{cases} 0 & \text{for } G > B \\ 180 & \text{for } G < B \end{cases}}{360} \qquad (3.4)$$

where:

$$F = \frac{2R - G - B}{G - B}$$

The easiest way to perform this calculation is to use a standard RGB to HSI (Hue, Saturation, Intensity) transformation available with most image processing software. The thresholding can be performed after this transformation using the computed values for intensity. The hue values that have been achieved in the vicinity of the thermocouple in the example are also shown in Fig. 3.5. It can be seen that the hue value determined this way appears to be a good measure of colour to be used for a calibration.

Fig. 3.6 shows a cylinder-flare model in the HSST working section covered with liquid crystals. The first picture shows a flow-off image, the second gives the liquid crystal response during the run and at the bottom the result of the differencing and thresholding can be seen. The resulting colour values have been multiplied by a constant as the resulting picture would otherwise be too dark. It can be seen that all parts of the image that do not display a liquid crystal response have been removed successfully. This includes the white paint markings and the reflections caused by the thermocouples. The colour response throughout the cylinder is relatively uniform, even on the sides where the illumination was much poorer. It is also interesting to note that there is very little colour change in a spanwise direction even though the viewing angles are well in excess of 20°.

The video signal supplied to the framegrabber is in S-VHS format and has a resolution of 400 lines. The resolution of the framegrabber is 766x574 pixels. After differencing two images, the noise has obviously increased. As the resolution of the digitised image is above the resolution of the original image, a

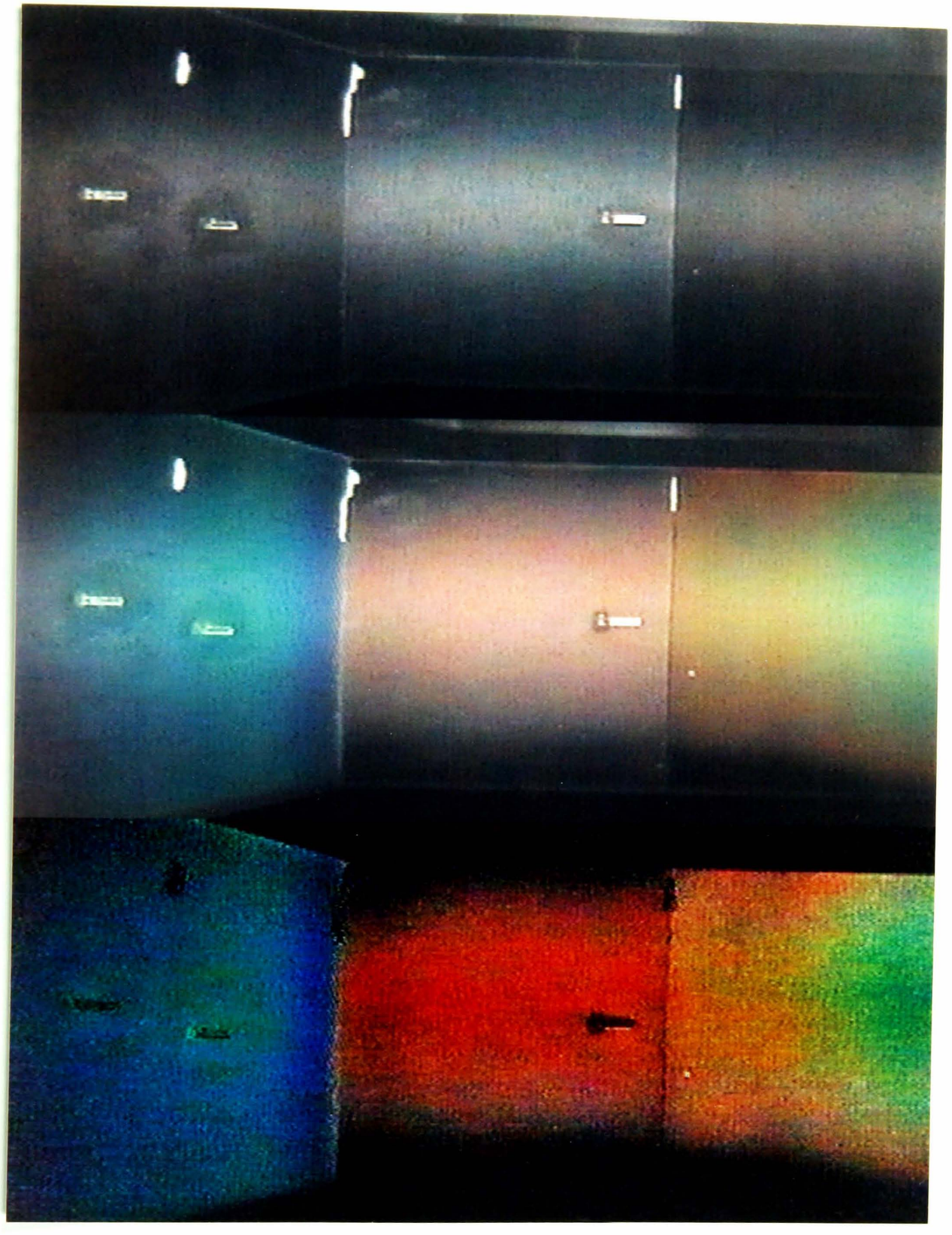

Fig. 3.6 Image of a cylindrical wind tunnel model (from top to bottom):
a) Flow off
b) Liquid crystal response during run
c) Colour image after differencing b)-a) and thresholding.

certain amount of filtering can be performed without loss of information. A very efficient image processing routine for these purposes is a median filter. In this case a the filtered pixel value is determined as the median value of all pixels within a 3x3 area around this pixel location. This process is applied to all pixels in the image. The advantage of this technique over standard smoothing is that the new pixel value will always be a value actually encountered somewhere within the 3x3 mask area and not a value that has been determined arithmetically. This routine is particularly efficient in removing salt and pepper type noise.The process is repeated in each of the three colour bands.

Once the filtered and differenced RGB values are computed, the image is converted into the HSI space using a standard image processing routine. The resulting hue values are then masked using the intensities obtained from the conversion. Now the hue values have to be matched to temperatures.

3.3.3 Colour Temperature Calibration

Due to the factors influencing the colour observed from a liquid crystal coating, a comparison of the colour recorded during a wind tunnel experiment with the colour-temperature relation measured in a calibration experiment is not straightforward. In successful attempts so far researchers made great efforts to ensure that all the factors influencing the observed colour were kept the same. In most of these cases the actual wind tunnel was a rather simple, purpose built facility (Refs.72, 74) or a blower providing the airflow over a flat plate covered with liquid crystals (Ref.73). The calibration curves published were obtained by heating a large plate to a uniform temperature, measured with several thermocouples embedded in the plate, and calculating the average hue value for the whole surface.

The typical setup in a hypersonic facility is very different from such an experiment. The models used are small and often axisymmetric, causing additional problems due to reflections and uneven illumination. Frequently the angle of the model to the observer is changed to investigate angle of attack effects. The model often has to be observed through a small window, which also serves to allow the illumination of the model. The camera and lighting conditions are always a compromise dependant on the actual model used and its position. It was felt that it is impossible to ensure comparable situations of lighting and camera position if the calibration experiment was to be performed outside the tunnel. Furthermore, the model geometry will determine the lighting and viewing positions and it does not seem valid to compare one calibration with the colour response on several very differently shaped models.

The approach taken here is therefore fundamentally different from previous work. It was decided to investigate the possibility of calibrating the liquid crystal colour response against the surface temperature by using a real wind tunnel model mounted inside the working section. This requires some alternative means of determining the surface temperature. In the HSST this can easily be achieved by using surface mounted thermocouples. To take this strategy even further, calibration and experiment were performed simultaneously. The colour change and surface temperature of a model were recorded during a wind tunnel experiment and the calibration and analysis performed afterwards. The major advantage of this approach is that it totally removes any difference between calibration and actual measurement. A disadvantage of this procedure is the introduction of a number of new problems that need to be addressed.

The obvious first problem is the number and location of the thermocouples to be used for the calibration. An ideal calibration would incorporate a large surface area at constant temperature. The hue value computed from the camera recording can then be averaged over this area to minimise all influences of camera noise or other errors. On a wind tunnel model the surface temperature is obviously not constant. The area used to sample the surface colour must be

directly surrounding the thermocouple while being small enough to assume constant temperature. The colour directly on the thermocouple can not be determined as the metal of the thermocouple will reflect light. The area used in the experiments was finally set to a small patch of 8x10 pixels. Depending on the camera location this was equivalent to an area of about 2x3 mm. The area included part of the actual thermocouple. After differencing the image from the flow-off image the reflections from the thermocouple were usually removed, leaving dark spots on the image. If calibrations from several thermocouples are to be compared, they should all be in areas of similar viewing angle, together with the main area of interest. On axisymmetric models, measurements can be concentrated on a narrow streamwise strip where the model surface is facing the observer.

The quality of a calibration obtained during a wind tunnel run is reduced from that in an ideal experiment. As the area sampled for colour is very small, camera noise is a more significant factor. The next difficulty is that the actual temperature is now determined with only one thermocouple. With a proper calibration experiment, the surface temperature can be measured with several sensors and an average value will be obtained. This is not possible here. An improvement of the calibration can be made by using more thermocouples distributed over the surface. Nevertheless each of these sensors will be at a different temperature and colour. Areas of large temperature gradient have to be avoided as readings can be erroneous due to conduction in the thermocouple and colour changes in the sampling area around it.

The number of thermocouples and their location has to be chosen carefully to ensure readings of colour and temperature throughout the whole range of the liquid crystals. In the HSST this was usually not a great problem as the running time is sufficiently large to achieve surface temperatures above the range of the liquid crystals in most cases.

After a wind tunnel experiment a large number of frames can be digitised from the video recording. For each of these frames the colour values in the patches around the thermocouple can be sampled and compared with the equivalent temperature measurements. The more thermocouples used and number of frames digitised, the larger the number of points on the calibration curve will be.

An example of the calibration curve obtained in such an experiment, using three thermocouples and 50 frames is given in Fig. 3.7. As described above, all responses with insufficient intensity have been removed by thresholding. If the sampling area around a thermocouple contained only few pixels with a colour response, then the colour determined in this case was disregarded. The cutoff point was usually selected to be around 20% of the total number of pixels in the sampling area. It can be seen that the points form a calibration curve with a scatter of about $\pm 0.25°$ for the lower temperatures and up to $\pm 1°$ at the high end. Within this scatter a calibration curve is obtained by curve-fitting a fifth order

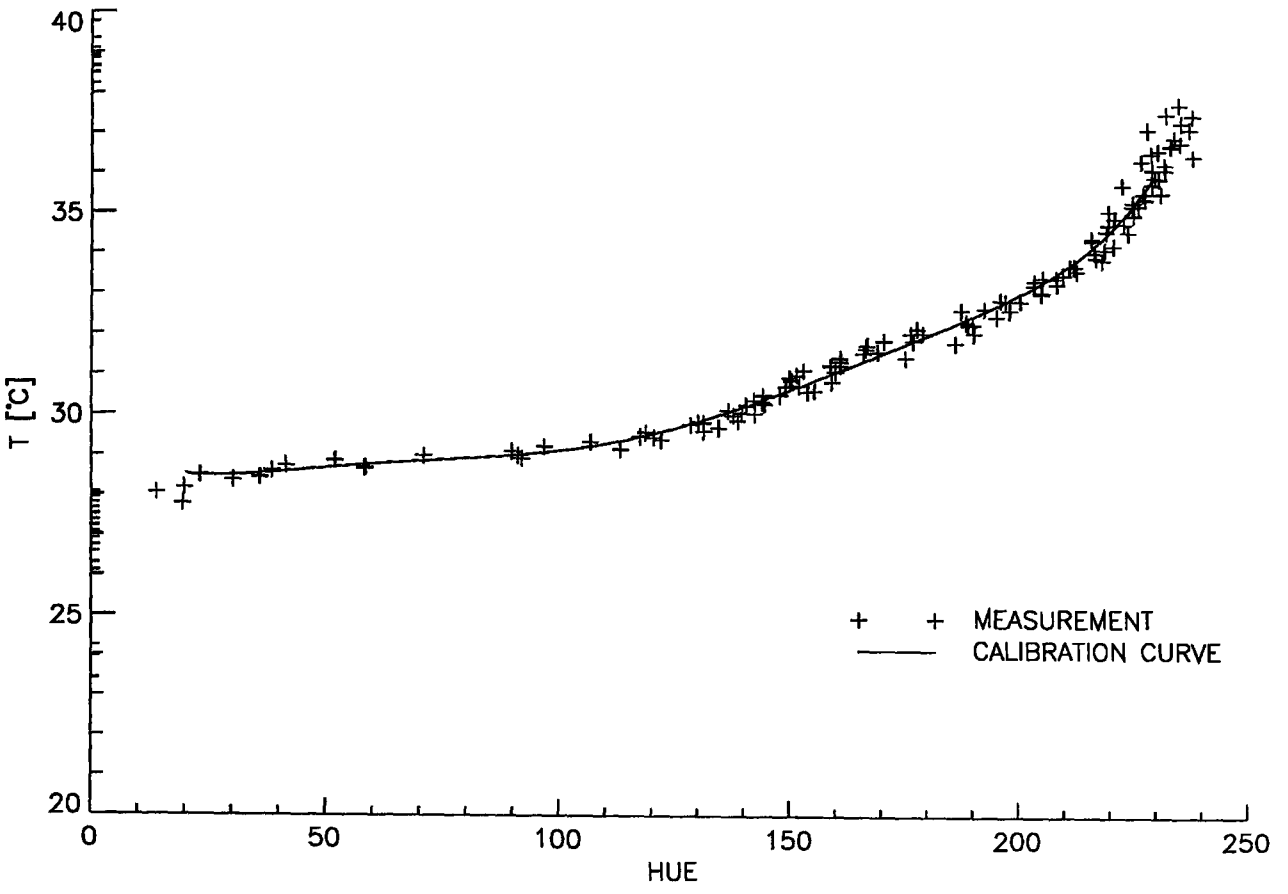

Fig. 3.7 Calibration curve obtained on a cylinder-flare model in the HSST using three thermocouples and 50 frames from the video recording

polynomial through the data points.

It is to be expected that a calibration performed in the described fashion exhibits a larger amount of scatter than an ideal calibration experiment. Nevertheless the result is encouraging and it is believed that the calibration obtained in this way is more accurate as it removes all uncertainties of comparing the colour response of different experiments. In the course of this thesis a shift of calibration curves was noticed for the same liquid crystal mixture between different experiments. This was probably due to changes in lighting, camera position and camera setup (white balance), even though attempts were made to preserve similar conditions in all cases.

A further advantage of this approach is the ease of undertaking an experiment. If for example a new wind tunnel is to be used or the liquid crystal mixture is changed, no significant changes in the procedure are necessary.If the liquid crystal mixture is to be changed only a re-spraying of the model is necessary. The image processing algorithm developed for this measurement technique is a combination of the steps necessary for calibration and analysis of the results. It will perform equally well for different liquid crystal coatings or wind tunnels.

In the case of the gun tunnel the technique has to be adjusted to the short running times. Surface thermocouples can no longer be used to record the

surface temperatures as their response time is insufficient. The temperatures required for a calibration have to be measured with platinum thin film gauges. The largest difference, however, is the fact that the colour displayed by the liquid crystals is severely affected due to the high heat transfer rates and short running times. As a result it was not possible to use a similar approach to the HSST, a calibration curve has to be determined before a gun-tunnel experiment. The procedure has been discussed in Ref.75, the main findings shall be repeated here.

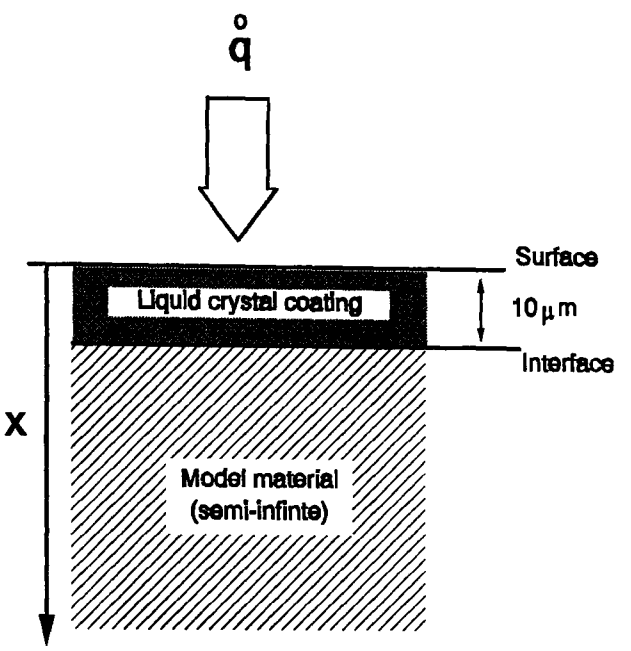

Fig. 3.8 Composition of materials used for the simulation of temperature distribution in a gun-tunnel model

Encapsulated liquid crystals and the binder material are thermally insulating materials. In the short timescale of an experiment in the gun tunnel, the temperature distribution inside the coating needs to be investigated. For these purposes a simple one-dimensional finite difference computer program has been used to calculate the temperature behaviour inside a layered material subject to a surface heat transfer. The material has been modelled as shown in Fig. 3.8. The liquid crystal coating thickness of 10μm is the minimum thickness that can currently be achieved with encapsulated liquid crystals as the size of a capsule is of this order. If a constant heat transfer onto the surface is assumed then the temperature distribution inside the liquid crystal coating and the underlying model material can be computed, depending on the time from the onset of heat transfer. The thermal properties of the liquid crystal surface coating have been assumed to be homogenous.

The temperatures at the surface and the interface between liquid crystals and model material in such a case are shown in Fig. 3.9. The material properties have been set to simulate a liquid crystal coating on a plastic model, the surface heat transfer is 100kW/m^2, a typical value for the gun tunnel. It can be seen that the surface temperature increases very quickly, whereas the temperature at the interface between the model material and the liquid crystal coating is lagging behind considerably. After about 2ms the temperature distribution between the surface and the interface is approximately linear. The temperature difference within the liquid crystal coating will now stay approximately constant. From this point on, all the temperatures inside the coating will rise by the same amount, preserving this linear variation. This effect is also illustrated by Fig. 3.10 showing the surface and interface temperatures for three different levels of heat transfer. As the running time is very short (25ms) the average rise in temperatures within the liquid crystal coating is of the same order as the temperature difference

within. If the running time was very much longer, the temperatures achieved inside the coating would reach values large enough to neglect the variation inside by comparison.

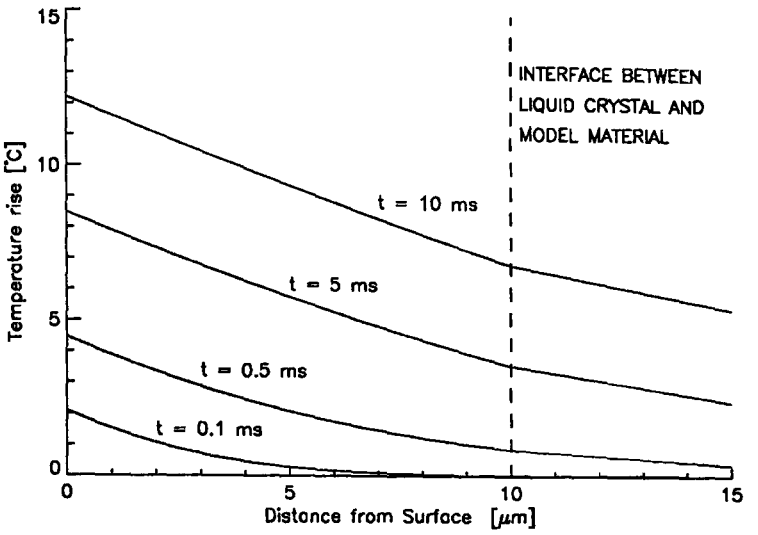

Fig. 3.9 Temperatures computed inside a liquid crystal surface coating of 10μm thickness subject to a heat transfer of 10kW/m^2 on a plastic model

The temperature variation is roughly proportional to the heat transfer onto the surface. It is this temperature difference that is causing most of the difficulties associated with liquid crystal experiments in hypersonic gun tunnels. The colour displayed by a surface coating under these conditions will be the sum of all different colours corresponding to the different temperatures encountered within. This explains why it is nearly impossible to use a narrow bandwidth liquid crystal mixture under these conditions. If, for example, the bandwidth is chosen to be one degree, less than 20% of the surface coating will actually lie in this region and display a colour. The situation will be worse for areas of higher heat transfer where this effect is even more severe. If on the other hand the bandwidth of the mixture is increased to give a better response, it will be impossible to distinguish between regions of lower heat transfer as a wide range of values of $\dot{q}$ will display a colour.

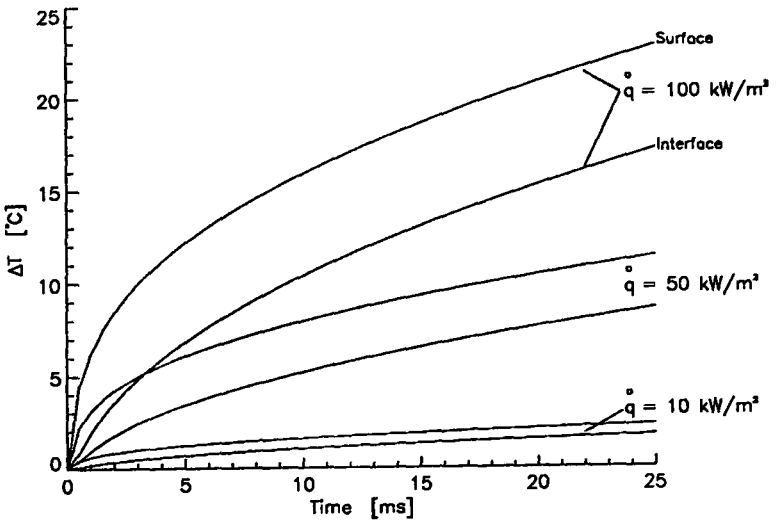

Fig. 3.10 Surface and interface temperatures at 10μm liquid crystal coating on plastic for three heat transfer levels, typical of the gun tunnel

If a large bandwidth liquid crystal is used, the non-linearity of the liquid crystal response will cause some problems. In all cases more than one colour will be displayed by the crystals at each point. As most mixtures currently available have a much larger blue region compared to the other colours, results will be dominated by blue. Nevertheless using image processing it is still possible to distinguish between different colours. In order to determine the type of liquid crystal to be used in the gun tunnel the temperatures have been computed for

three heat transfer levels covering a typical measurement range. The temperatures determining the liquid crystal response are the surface and interface temperature, the result is given in Fig. 3.10. This highlights a further difficulty when using narrow bandwidth liquid crystals. In order to be able to measure the lowest heating rate, the liquid crystals have to respond at about 3°C above ambient. This will put the response in areas of high heating into the first millisecond of the experiment, with very little opportunity to distinguish between different levels of heating. The frame rate of the recording equipment has to be fast enough to obtain sufficient images at this time. The equipment used here has a maximum frame rate of 400 f/s, this is not fast enough to capture any events in the first 2ms. For these reasons only wide-band liquid crystals have been used in the gun tunnel. The variations of temperature within the surface coating have to be taken into account when comparing the colours with a calibration. For this purpose the interface and surface temperatures of the liquid crystal coating 25ms after the onset of heat transfer are given in Fig. 3.11. With the assumption of constant heat transfer during the run, this graph gives the temperatures within the liquid crystal layer for a given heat transfer.

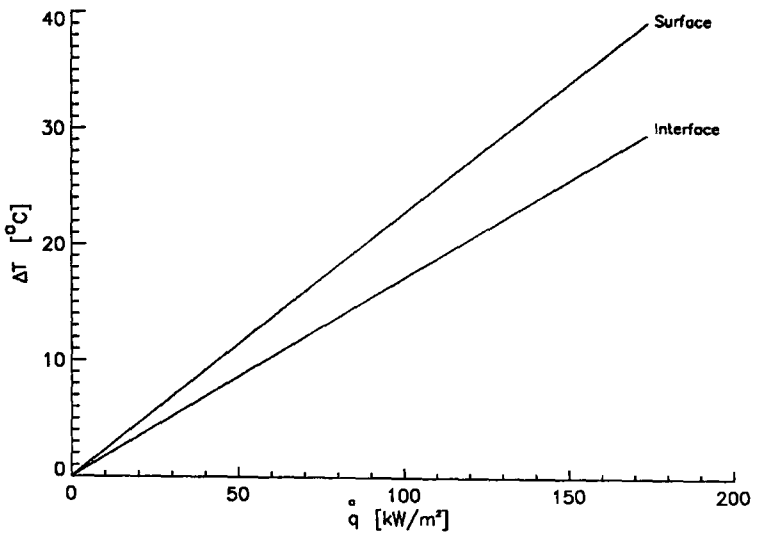

Fig. 3.11 Surface and interface temperatures on a liquid crystal surface coating 25ms after the flow start

The colour displayed will be a mixture of the colours for all temperatures within this layer. This mixing process can be approximated by calculating the average hue value for the different temperatures within the layer if a static hue-temperature calibration such as given in Fig. 3.7 is known. This will result in a final calibration curve giving the average hue value through the liquid crystal coating as a function of surface heat transfer. An example is shown in Fig. 3.12. Due to the non-linear hue-temperature dependence it is not correct to use the mean temperature inside the coating to determine the displayed colour. It is also wrong to expect any of the colours as obtained in static calibrations where the temperature throughout the liquid crystal layer is uniform.

Also shown in Fig. 3.12 is the relative intensity of the liquid crystal response. For a certain range of heat transfer values only part of the liquid crystal layer will lie in the colour band of the liquid crystals, hence the intensity of the displayed colour is reduced. In the example shown here, the colour begins to fade at a heat transfer of 82 kW/m^2 and above 110 kW/m^2 no further colour is visible. The lower values of hue, equivalent to red and yellow colours all lie in areas of reduced

response as the lowest parts of the coating are still too cold to display any colour. This explains the reduced intensities of red and yellow colours observed in gun-tunnel experiments. If a relative intensity of, say 50%, was necessary to give a colour response sufficient for the recording equipment, then the surface coating shown here will reflect colours in a range from 30 to 92 kW/m^2 with hue values ranging from 70 to 240.

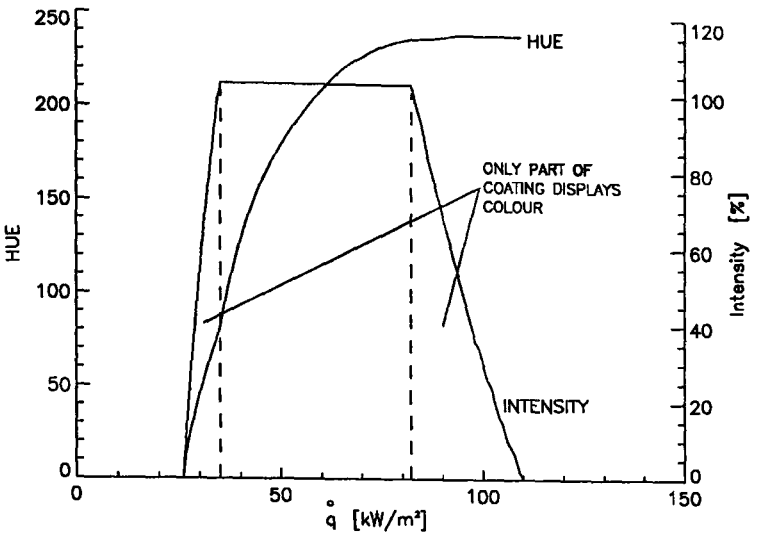

Fig. 3.12 Average hue value and relative intensity of liquid crystal response displayed by a 10μm liquid crystal coating on plastic, depending on the surface heat transfer.

The hue value of a recorded response in the gun tunnel has to be correlated to a calibration curve such as shown Fig. 3.12 to obtain the surface heat transfer. This curve will depend on a static liquid crystal calibration (giving the hue-temperature dependence), the thermal coefficients of the liquid crystals and the model material, the thickness of the coating and the time since the onset of heat transfer (running time) as well as the ambient temperature at the time of the run. The accuracy of the method can be increased if more than one frame of the run is used, but as the time will be different a new calibration curve needs to be used. It also needs pointing out that the quality of the calibration curve depends on the accuracy of the heat conduction program and the degree of validity of the constant heat transfer assumption. Modified heat transfer assumptions however can be incorporated into the computer program.

A simpler alternative to this procedure was reported by Smith and Baxter[76] who compared the colour response on a wind tunnel model with the response on a flat plate where the expected heat transfer values can be calculated using a theoretical solution. This increases the experimental error as the colour response needs to be analysed twice and the flow over the flat plate is subject to uncertainties on operating conditions and flow quality.

For facilities with a sufficiently long running time to allow neglect of the temperature variation within the liquid crystal layer, the hue-temperature calibration can be used to determine the surface temperature distribution for any recorded liquid crystal colour response. In these facilities the assumption of a step change in heat transfer is usually less well justified and a different way to obtain the surface heat transfer should be used.

3.3.4 Determination of Surface Heat Transfer

The experiments performed in the HSST have the distinct advantage over the gun tunnel in that the surface temperatures are measured at one or more locations with a surface thermocouple. This allows the computation of the surface heat transfer history at these locations. A further advantage is that a large number of frames are available for the analysis. This further spreads the range of the technique as it is possible to measure very high heat transfer rates early in the run, when all other areas do not yet display a colour, and very low heat transfer at the end of the run when the 'hot' areas are already beyond the range of the crystals. The algorithm developed for this purpose normally uses 50 frames of the recording of an experiment, avoiding images obtained during the start-up time of the tunnel (0.7s). As the calibration curve is also obtained during the same experiment, both tasks will actually be performed by the same image processing program, hence making the use of this technique very straightforward.

In order to explain the key processes involved it will be assumed at this point, that the calibration curve, such as given in Fig. 3.7, has already been obtained. For each of the 50 frames the surface temperatures can therefore be determined wherever sufficient colour response is detected. Naturally this is only possible in regions with surface temperatures within the liquid crystal range and not all surface temperatures on the model can be determined in a single frame. In a typical experiment the complete surface will have given a colour response at one point or another during the run and more than 20 temperature measurements can usually be obtained for each point on the surface.

What is now needed is a relationship to determine heat transfer; the given quantities are time since the flow start-up and surface temperature. The most commonly used relationship is the analytic solution for a semi-infinite material under a constant heat transfer. In the case of the experiments described here it is not necessary to make the simplification of constant $\mathring{q}$. The surface heat transfer will vary during the running time due to the tunnel startup, the variations in total temperature, as discussed in the Chapter 2, and the change in local surface temperature. It has been found that the error of a constant heat transfer assumption is of the order of 10% in the HSST (Ref.77). This is mainly due to the lower heat transfer during start-up of the flow. This could be reduced by injecting the model into an already established flowfield, but this requires the design of a suitable mechanism and was not an option for this study.

The only assumption used here is a similarity in the time distribution of the local heat transfer between all points on the model surface. The solution for the dependence of surface temperature rise and heat transfer for a semi-infinite slab

is given in Schultz and Jones (Ref.56) as:

$$T_s(t) = \frac{1}{\sqrt{\pi}\sqrt{\rho c k}} \int_0^t \frac{\dot{q}(\tau)}{\sqrt{t-\tau}}\, d\tau \qquad (3.5)$$

If the variation of $\dot{q}$ with time is similar on all points of the surface, then the heat transfer at every location can be expressed as :

$$\dot{q}_s(x,y,t) = factor(x,y) \times \dot{q}_0(t) \qquad (3.6)$$

where $\dot{q}_0$ is the heat transfer at an arbitrary point on the surface, for example at a thermocouple location. From (3.5) and (3.6) it follows that:

$$T_s(x,y,t) = factor(x,y) \times \frac{1}{\sqrt{\pi}\sqrt{\rho c k}} \int_0^t \frac{\dot{q}_0(\tau)}{\sqrt{t-\tau}}\, d\tau \qquad (3.7)$$

$$T_s(x,y,t) = factor \times T_o(t)$$

If the heat transfer and surface temperature rise at are known at one location on the model at a given time, then the heat transfer everywhere else on the model follows as:

$$\dot{q}(x,y,t) = \frac{T_s(x,y,t)}{T_0(t)} \times \dot{q}_0(t) \qquad (3.8)$$

Hence the local value of $\dot{q}$ is proportional to the local increase in temperature since the flow-start and this proportionality is the same for the whole model at a given time. To obtain this proportionality the measured heat transfer values from the thermocouples can be compared to their temperature rise. If more than one thermocouple is used the average proportionality value is computed to improve the accuracy. Thus $\dot{q}$ can be calculated for every pixel of the digitised frame if a measurement of wall temperature is available. After performing this for each of the 50 frames the average value of $\dot{q}$ can be computed at each pixel location. Points on the surface that have never given sufficient liquid crystal response to determine a heat transfer are assigned the value 0.

One difficulty in the application of this technique is the fact that the heat transfer value obtained with the thermocouples is extremely noisy. Fig. 3.13 shows data obtained from a thermocouple and Fig. 3.14 gives the heat transfer obtained by integrating these results. If the proportionality factor was determined from these values a large error would be introduced into the liquid crystal measurements. For this reason a 5th order least squares polynomial has been fitted to the measured temperature rise after the flow start. The result of this curve fitting is given as a solid line in Fig. 3.13. The sudden increase in temperature due to the flow

shutdown has been removed from the data. It can be seen that the curve-fit matches the temperature rise very closely without any of the noise of the original data. The analytical curve can now be integrated much faster and the resulting heat transfer curve is given in Fig. 3.14. In all cases the agreement of the data obtained from the curve-fit with the heat transfer obtained from integrating the actual measurements has been very good. Obviously it is impossible to measure any rapid changes in heat transfer as this process is similar to wide-band filtering. This is not a problem here as the liquid crystal readings will be taken after the start-up of the tunnel during the steady flow period. The justification for this approach is in the reduction of computing time for the analysis of liquid crystal response and the good agreement of the fitted heat transfer with the actual measurement in the period of interest.

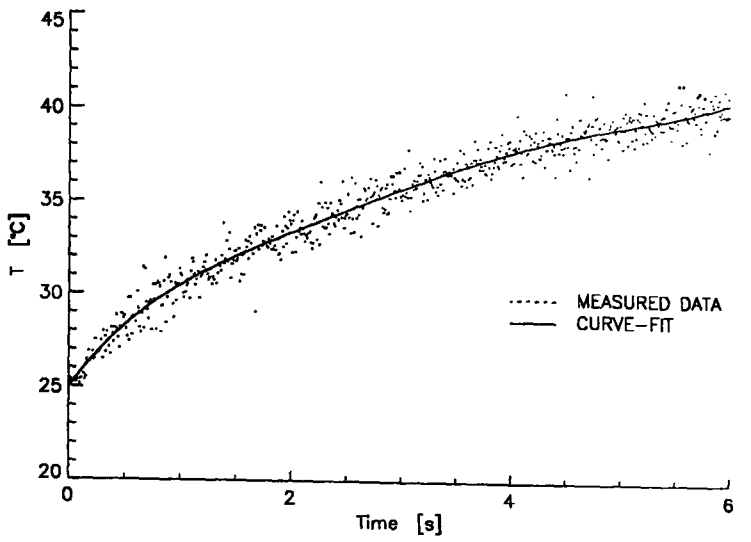

Fig. 3.13 Temperature measurements obtained from surface thermocouple compared with 5th order curve fit

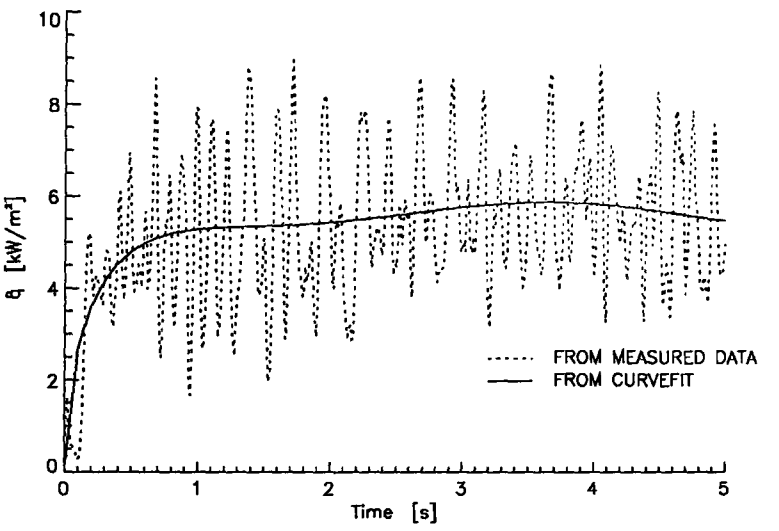

Fig. 3.14 Heat transfer as determined from thermocouple measurement compared with integration from curve fit

In all cases the heat transfer values measured with the thermocouples have also been integrated using the traditional technique. The results are then available to allow a comparison with the results obtained from the liquid crystal technique.

A further difficulty was presented by the fact that the models used in the experiments were connected to the centrebody of the wind-tunnel. During the course of a typical day of experimental work it was noticed that the centrebody started to warm up significantly due to conduction and radiation from the nozzle. This caused the model to be at a non-uniform temperature at the beginning of an experiment. To determine the surface temperature rise T_s at every point on the model the initial temperature needs to be determined. This has been achieved by using the measurements from the thermocouples and interpolating between

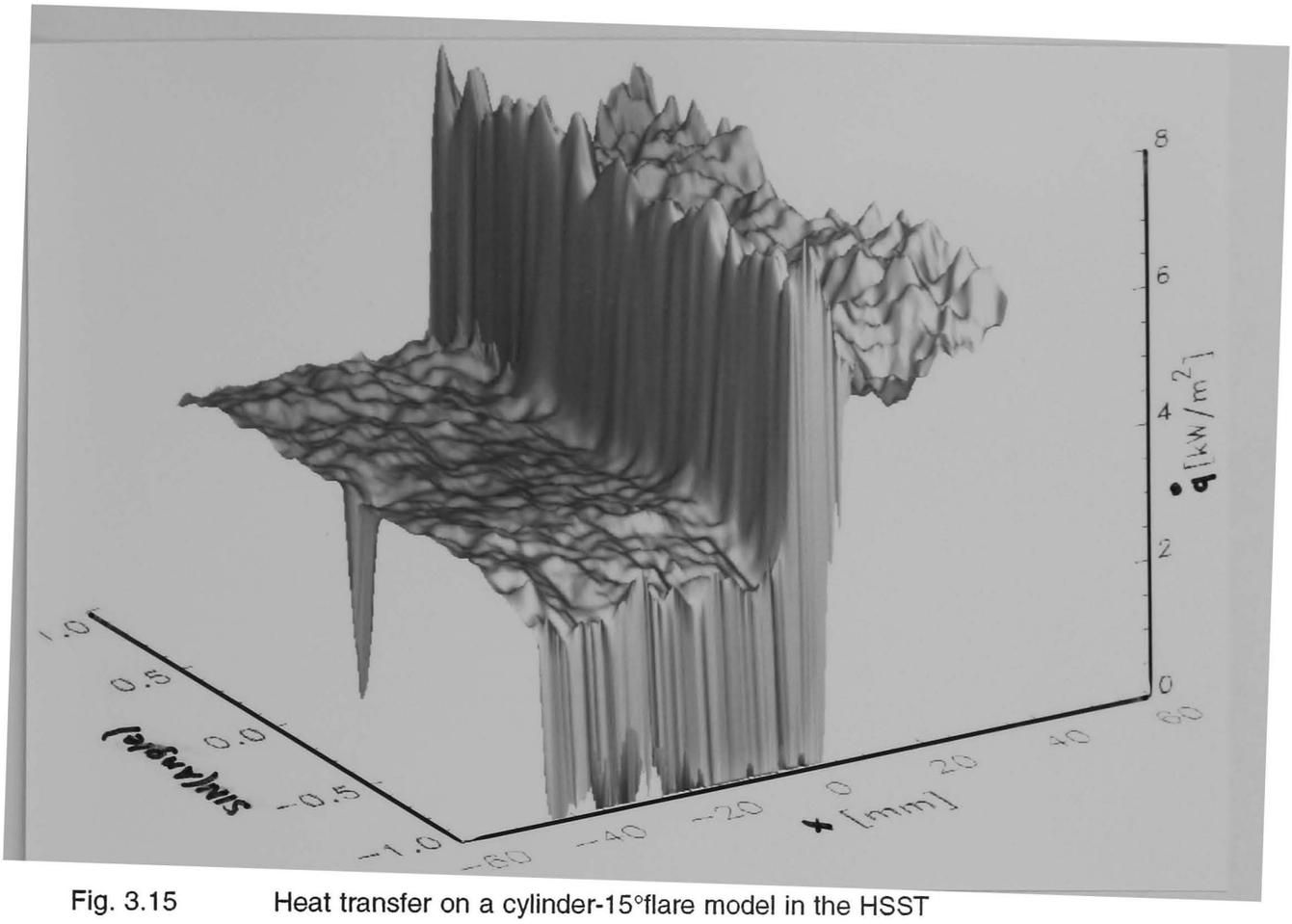

Fig. 3.15 Heat transfer on a cylinder-15°flare model in the HSST

these values. This will obviously introduce an error into the determination of heat transfer from the liquid crystal response, this error increasing with the degree of non-uniformity of the model temperature before the experiment. The magnitude of this error will be discussed in sub-section 3.3.5.

An example of a final result is shown in Fig. 3.15. It gives the surface heat transfer determined on a cylinder-flare model, emphasising the superior spatial resolution of liquid crystal measurements. It can be seen that results for the surface heat transfer have been obtained for almost all locations visible to the camera, the y=0 axis corresponds to the lower edge of the cylinder. The values obtained on the cylinder show very little variation in a spanwise direction. Hence it was possible to take sensible measurements for surface inclinations of up to 70° towards the observer. This is very encouraging for future work on more complex model geometries. It can also be seen that the lighting problems usually associated with axisymmetric models have not caused any difficulties for the application of liquid crystal thermography. In order to compare the liquid crystal measurements with the thermocouple results, a slice of approximately 10 mm width has been taken along a streamwise direction from the centre of Fig. 3.15. The average values in this slice are compared with the thermocouple readings in Fig. 3.16. It can be seen that the agreement is very good.

All liquid crystal experiments require some type of illumination. In some cases this can be the source of additional surface heat transfer onto the model surface due to infrared radiation. The effect of this additional heat transfer has been measured

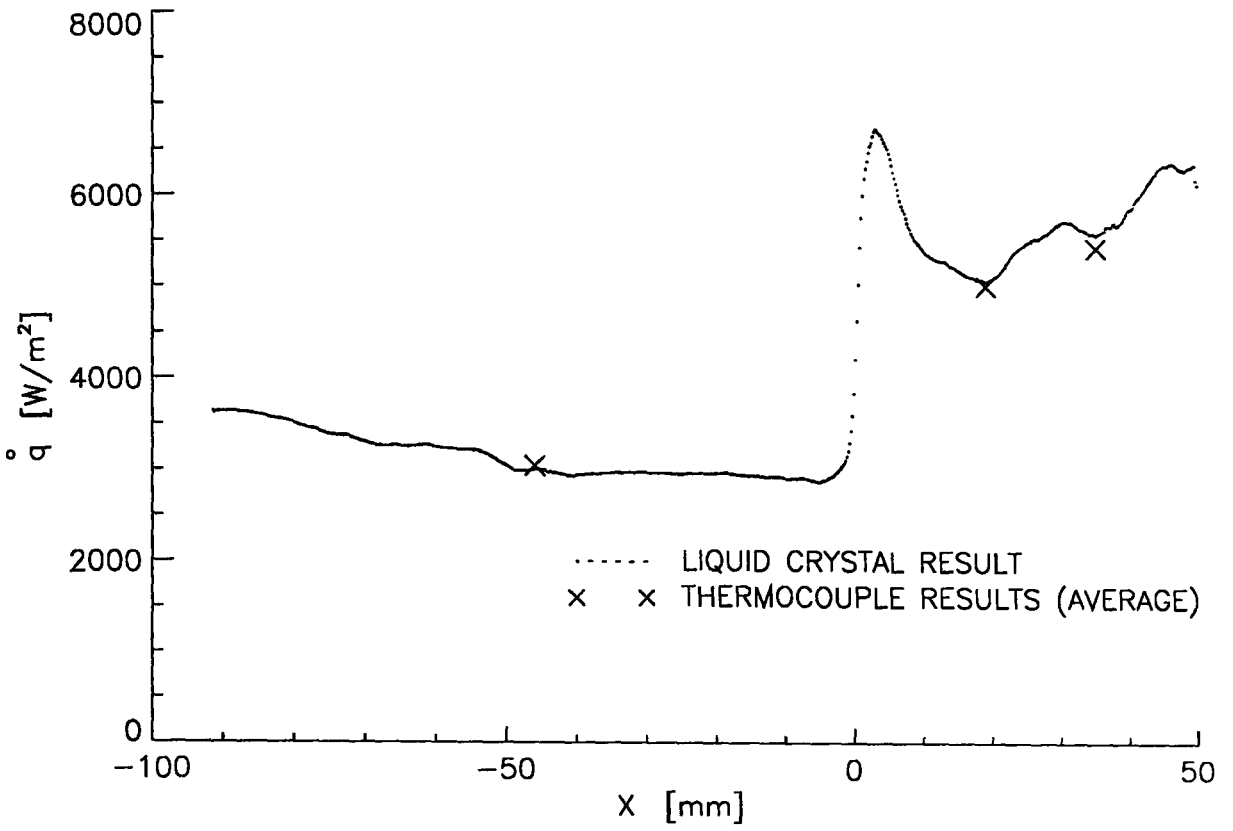

Fig. 3.16 Comparison of heat transfer values on a cylinder and 15° flare obtained with liquid crystal thermography and surface thermocouples.

with the surface thermocouples (flow-off) and is subtracted routinely from the liquid crystal and thermocouple measurements. In most cases, this correction was of the order of less than 5% of the aerodynamic heating. Quantitative values are only compared at locations where the cylinder is facing the observer, so the heating caused by the illumination has been assumed as constant in this area. It is possible to use the flow-off image to determine the relative intensity of the illumination and scale the correction accordingly, this has not been done in the current work.

The final heat transfer distribution is still subject to some variations. It has been found in the wind tunnel calibration that the total temperature is not constant during the run. Obviously the wall temperatures on the model surface are also changing with time. Due to the nature of the liquid crystal technique regions with high levels of heat transfer will respond early in the run, hence the measured values will be obtained at this time. Areas of low heat transfer, however, are measured fairly late in the run. The wall temperatures in both cases are similar as they lie in the regions of liquid crystal response, but the total temperatures do vary as described in the tunnel calibration. This variation can also be taken into account if the total temperature is monitored simultaneously. As for each measurement the wall temperature has been determined to obtain $\mathring{q}$ this can be used in conjunction with the total temperature to compute a heat transfer

coefficient. One possibility is to use the Stanton number which is defined as (from Ref. 56):

$$St = \frac{\dot{q}}{\rho_e u_e C_p (T_{aw} - T_w)}$$

where T_{aw} is the adiabatic wall temperature. This requires knowledge of the recovery factor everywhere on the model surface. In the turbulent boundary layer this can be set to:

$$r = Pr^{\frac{1}{3}}$$

In areas where the boundary layer is disturbed or subject to an interaction the recovery factor is not always known. It can therefore be advantageous to use a modified heat transfer coefficient such as described in Ref.58, using the total temperature:

$$C_H = \frac{\dot{q}}{\rho_e u_e C_p (T_0 - T_w)}$$

The value of C_H can be determined for every location on the surface, thus avoiding some of the variations in $\dot{q}$ due to the change in running conditions. It also allows an easier comparison between experiments performed at different operating conditions.

The method described to determine heat transfer values using liquid crystals in the HSST has a number of distinct advantages over other approaches. It can overcome the difficulties of a variation of surface heat transfer during the start of the tunnel and non-uniformities of model temperature before the flow-start. It supplies a large amount of data from a single experiment at very high spatial resolution, limited only by the size of the liquid crystal capsules (10μm) and the effects of cross-conduction. As a calibration of the liquid crystals is performed simultaneously with the experiment, the uncertainties and difficulties usually associated with comparing calibration and experiment are removed. Furthermore the liquid crystal mixture can be changed easily, without any need to change the procedure. This is a great advantage as it is often useful to use different liquid crystal mixtures depending on the required range and the room temperature.

The effort involved in setting up an experiment is relatively small, the liquid crystals can usually be applied on-site, and the fitting of a few surface thermocouples at convenient locations on the model surface should not present a problem. The image processing has been developed to a state where little input is required by the operator. A typical computation time for the calibration and analysis of a liquid crystal experiment using 50 frames of a video recording is about 45 minutes. Thus a quantitative result of the heat transfer on a model can usually be obtained within one or two days from manufacturing the model.

3.3.5 Accuracy of Measurements

The key process in determining the local heat transfer from the liquid crystal response is the determination of colour and the subsequent comparison with the calibration curve. It can be seen in Fig. 3.7 that the temperature can usually be determined to within one degree C. In the higher temperature range the scatter is increased, this has been taken into account by ignoring all colour values with a hue greater than 220. It was also found that the scatter in the calibration curve was mainly caused by the poor performance of the thermocouples and the amplifier used. The main problem was found to be a zero drift which did not effect the heat transfer values determined from the thermocouples. In the case of the calibrations, however, which were usually obtained from several thermocouples this resulted in a large amount of scatter. The quality of the thermocouple readings deteriorated significantly as the room temperature increased during a typical day of experimental work. The reasons for this are yet unknown but for future work a better thermocouple amplifier is required to eliminate this problem. The other contribution to the scatter in the calibration curve is camera noise.

Typical temperature rises detected with the liquid crystals are of the order of 10 to 20 degrees C. The amount of experimental error caused by a single comparison of a liquid crystal colour with the calibration curve is therefore of the order of 10%. This error is a random error and the overall importance is strongly reduced by the fact that a typical measurement on any point on the model surface is usually an average of more than 20 different readings. The error therefore reduces to below 1%.

The values determined for heat transfer for the thermocouples and the liquid crystal measurements depend on the material properties used in the computations. In the case of the work in the HSST the temperature difference within the liquid crystal layer is negligible, so only the thermal properties of the underlying material are used in the calculations. In the gun tunnel both material properties have to be determined. The properties of the model material and liquid crystals have been measured at DRA Fort Halstead and the confidence in the results is better than 5%, including the variations within the temperature range experienced. This will lead to an uncertainty of 2% in $\mathring{q}$.

In areas of large local differences in surface heat transfer, smearing of the surface temperature distribution due to conduction along the surface of the model needs to be considered. This effect is referred to as cross-conduction. The magnitude of error has been investigated by Schultz and Jones[56] for traditional techniques. A more convenient formula for estimating this effect can be found in Maise et al[78] who have been investigating a numerical technique to compensate for this problem. As an estimate for the magnitude of this error they give a formula to determine the extent of any influence due to a step in surface heat

transfer. If a 10% change in the local temperature values is set as a limit the extent can be calculated by:

$$d = 1.45 \times \sqrt{\frac{k}{\rho c} t}$$

where t is the time since the onset of heat transfer. Using the properties of ERTALYTE this length-scale becomes .05 mm for the running time of the gun-tunnel (25 ms) and 0.7 mm for the HSST (measuring time: 5 s). If the influence is to be less than 1% the length scales become 0.1 mm and 1.3 mm respectively. Hence the influence of cross-conduction can be important if very small scale surface features are to be investigated in the HSST. The theoretical assumption of a step-change in local heat transfer somewhat overpredicts the amount of error but the figures can give a guideline to its magnitude. Carlomagno[79] developed an algorithm which can reduce the measured surface temperature distribution to a theoretical result without the influence of cross-conduction. This approach is recommended if a resolution of better than 0.5 mm is desired. No correction has been applied in the current investigation.

In the gun tunnel an external calibration of the liquid crystal response needs to be used and a theoretical model of colour mixing is incorporated to determine the hue-$\dot{q}$ calibration. The uncertainties associated with this process are rather large, they are currently estimated to lie in the region of 15%. An additional source of uncertainty here is the thickness of the liquid crystal layer. The determination of a calibration curve depends on the assumption of uniform coating thickness. Several models have been tested for this thickness and it was found that the average liquid crystal thickness was between 7μm and 13μm. This introduces an uncertainty of 3% in the determination of $\dot{q}$.

If liquid crystals are to be used in very short duration wind tunnels, the response time of the liquid crystals themselves becomes an important parameter. This factor has been investigated by Ireland and Jones[80] who concluded that typical response times are of the order of 5 ms. Their work did not distinguish between an actual response time inside the liquid crystals and the time lag due to the unsteady temperature rise within the coating. The latter has been incorporated in the method described here. Therefore it can be estimated that the liquid crystal response time is shorter than described in Ref.80, of the order of 2ms. For work in the gun tunnel this will introduce a further 2% error. In future work it may be possible to include this time delay into the calibration and eliminate this error.

The largest uncertainty of the measurements performed in the HSST is the determination of model temperature before the experiment. Due to the disappointing performance of the thermocouples this can be as large as ±1°C for experiments performed very late in the day. The results obtained in the first run of the day, when the model was at uniform room temperature are not subject to this uncertainty. Therefore an additional experimental error is introduced to the

results ranging from 1% to 10%, depending on the time of the experiment. Fortunately this is not a major problem for the actual experimental method and can be removed for future work. The results presented here, however, will be subject to this uncertainty.

The illumination of the model surface was found to cause an additional surface heating of up to 5% of the aerodynamic heating. The measurements have been corrected by subtracting a constant amount from the results. This does not accurately represent the real influence of the light source and a further error of 2% can be caused by this uncertainty. Increasing the distance between the light source and the model reduces the additional heating caused by the illumination significantly, thus limiting the uncertainties involved.

During a typical experiment and between different wind tunnel runs the test conditions, such as total temperature vary, causing variations in the measurement of heat transfer. These variations are not actually measurement errors as they represent the true variations in the flow features, but they do represent a difficulty when comparing results. Therefore the results may be presented as heat transfer coefficients. This increases the level of uncertainty as the errors in determining the normalising parameters are included. This will cause a further uncertainty of 6% in the results.

To summarise the individual sources of experimental error are listed below for experiments performed in the gun tunnel and the HSST. The uncertainties due to varying operating conditions have to be added to these figures.

Source of error:	HSST	Gun Tunnel
Variation of material properties (5%):	2%	2%
Calibration error:	1% (50 frames)	15%
Variation of l.c. layer thickness:	---	3%
Response time:	---	2%
Uncertainty of initial model temperature:	1% - 10%	---
Additional heating due to illumination:	2%	---
Cross conduction:	Reduced resolution (1.3mm)	---
Total:	6% - 15%	22%

4. Experimental Investigation of Large Scale Roughness

After describing the wind tunnel and measurement techniques used in this investigation, the actual experiments can be described. As already discussed in Chapter 2 it was decided to use the DRA Fort Halstead HSST wind tunnel together with the axisymmetric contoured Mach 5 nozzle with centrebody. The effect of large scale roughness is to be investigated on the turbulent boundary layer on the centrebody. The measurements to be performed include surface pressure, boundary layer profiles and surface heat transfer.

The geometry of the models used are described in section 4.1, the results of the investigation are discussed in 4.2 - 4.4. All results are presented in figures at the end of this Chapter as it is not practical to include all illustrations in the text.

4.1 Models and Configurations

The models used in this study had to be designed to fit onto the centrebody of the Mach 5 nozzle. The aim was to provide an area of disturbance for the centrebody boundary layer followed by a smooth surface to investigate the length scale of any possible relaxation. Another aim of this work was to investigate the effect of an upstream roughness section onto a downstream adverse pressure

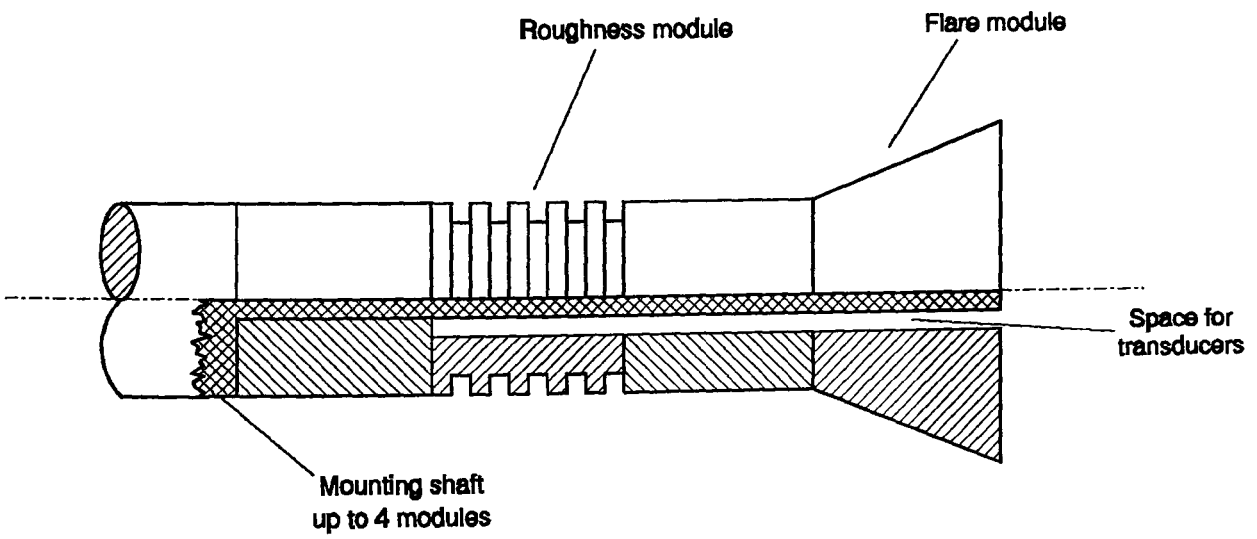

Fig. 4.1 Roughness and compression corner model in the HSST. The roughness type and compression corner angles could be varied by using different modules to make up the model.

gradient region. The roughness was to be limited to an area upstream of the adverse pressure gradient and not to extend into it.

Due to the size of the working section possible variations were limited. All areas of interest had to be visible through the working section windows, as the surface heat transfer was to be investigated using liquid crystal thermography.

The adverse pressure gradient was modelled by a compression corner. The resulting design consisted of a number of ring-shaped modules that could be fitted onto a central shaft, extending the centrebody. The compression corner was created by mounting a flare onto the end of the model. The principle arrangement is shown in Fig. 4.1. By exchanging the modules a number of combinations of

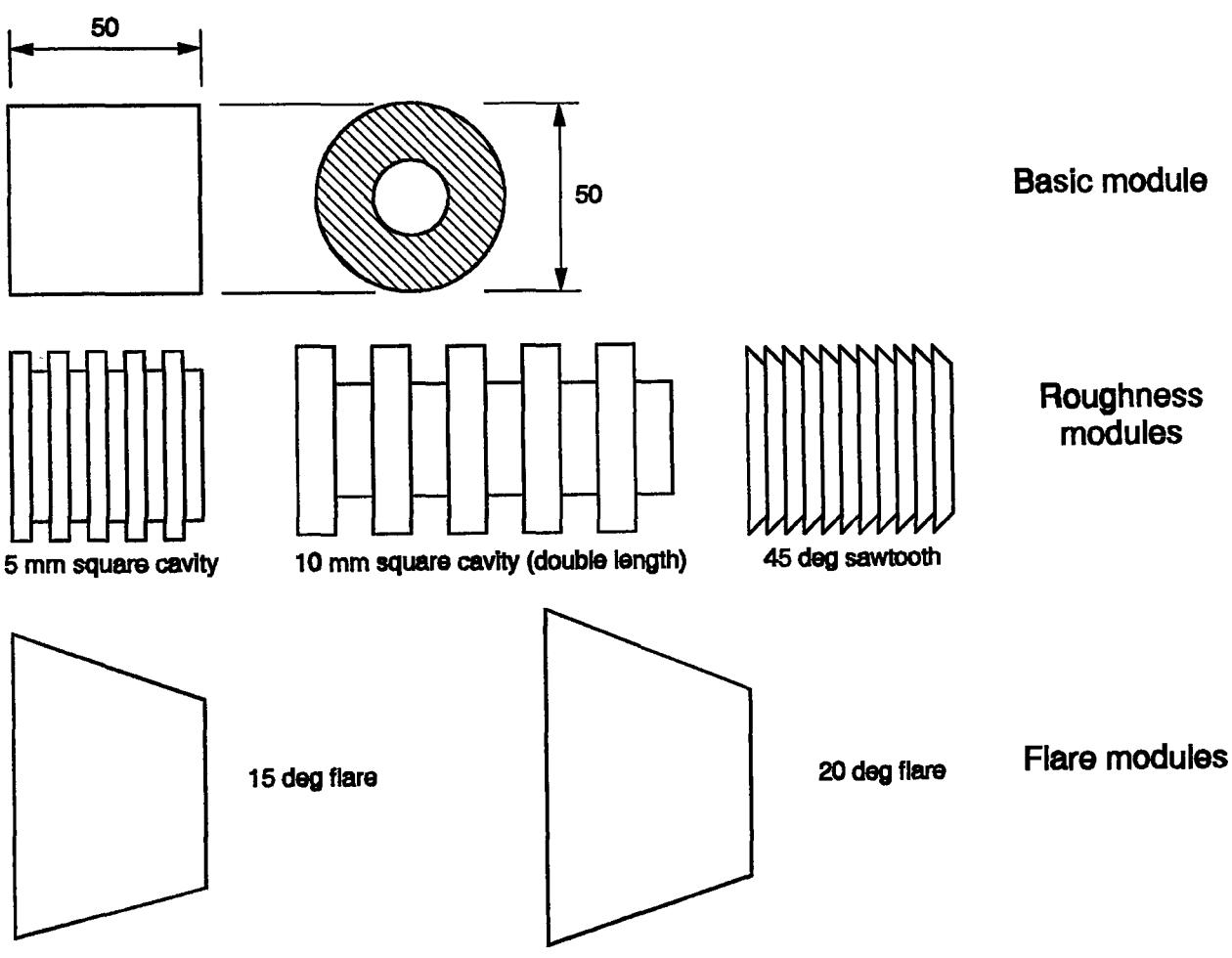

Fig. 4.2 Available modules for centrebody wind tunnel model

roughness and flare angles could be investigated. The available modules are shown in Fig. 4.2. Available roughnesses consisted of a series of sawtooth and cavities with a height of half a boundary layer thickness and a series of cavities with a height of approximately one boundary layer thickness. As seen in Fig. 2.29 the location of the roughness coincides with the estimated location of a compression wave system reflecting from the centrebody boundary layer as

discussed in section 2.5. The results obtained will therefore have an element of influence from this interaction. This could not be avoided and it was felt that the present configuration constituted the best possible compromise.

The flare angles were chosen to be 15° and 20°. Both are not expected to separate the boundary layer, the larger flare angle being very close to the expected angle of incipient separation. An angle of 30° was found to cause blockage of the flow and is therefore not used in this investigation.

All models have been manufactured of black ERTALYTE which is the trade name for a thermoplastic polyester based on polyethylene terephtalate (PETP). It was chosen for its good machinability and strength as well as thermal coefficients making it suitable for liquid crystal thermography in this facility. The physical properties have been obtained from the manufacturer and checked by DRA Fort Halstead and were used as:

Density:	1390 Kg/m^3
Thermal conductivity:	0.29 W/Km
Specific heat:	2300 J/KgK

The uncertainties and variations of these properties due to changes in temperature have been taken into account in the discussion of liquid crystal thermography in Chapter 3.

4.2 Schlieren Pictures

Fig. 4.4 and Fig. 4.5 show the schlieren pictures obtained for the flow over the cylinder and 20° flare with a smooth surface and the large cavities. The turbulent boundary layer on the flare is relatively thick and not clearly visible. The shock originating from the compression corner is easily observed in both cases. At the downstream edge of the picture the shock is just clearing the edge of the boundary layer. It is possible that it has not yet reached its maximum strength at this point. The interaction is therefore spreading over a large distance downstream from the hingeline. The boundary layer appears to be attached in both cases.

In the rough case some small waves can be seen originating from the boundary layer above the cavities. Due to the poor visibility of the boundary layer no further conclusions can be drawn at this point.

Both pictures show the oblique nozzle shock at the downstream end of the image. In the calibration experiments no shock has been detected originating from the nozzle exit. It is believed that additional blockage due to the flare increases the pressure in the working section outside of the core flow and thus causes the formation of the nozzle shock. From the location of the shock as indicated by the schlieren pictures it is possible for the shock to just clip the edge of the boundary layer before the tail of the flare. Due to the unsteadiness of the nozzle shock it appears 'wavy' in the picture, thus making the exact determination of its location impossible. Moreover the exact shock angle will also vary between different experiments due to changes in operating conditions. In the case of an impingement of the nozzle shock on the flare, some influence on the measured quantities has to be anticipated. It is believed that events are too far downstream to have a significant effect on the interaction itself.

4.3 Surface Pressure Measurements

Surface pressures have been recorded in close spacing directly behind the roughnesses and in the vicinity of the intersection of the cylinder and the flare, forming the hingeline of the axisymmetric compression corner. The positions of

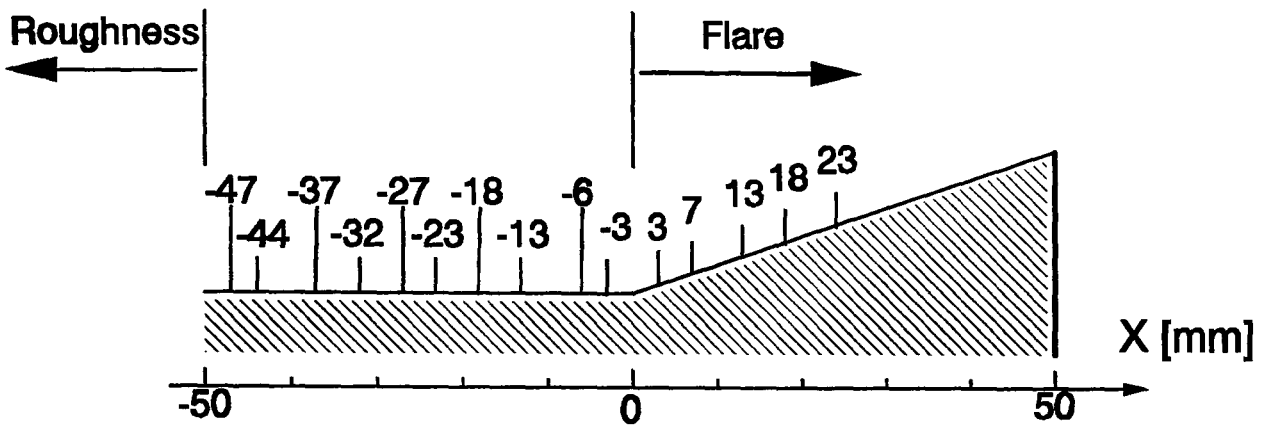

Fig. 4.3 Positions of pressure tappings

the pressure transducers with respect to the hingeline are given in Fig. 4.3. The modular structure of the wind tunnel models is a great advantage as an element fitted with closely spaced transducers can be placed in several positions, thus measuring the pressure distribution over most of the model in a few runs without exchanging the transducers. All results given are averages of several measurements to improve the accuracy. They are presented in dimensionless form by dividing with the pressure recorded simultaneously in the settling chamber. For absolute values the results have to be multiplied with the reservoir pressure as given in section 2.5.

Before investigating the pressure distributions behind the roughnesses and on the flares, Fig. 4.6 shows the surface pressures measured along the smooth centrebody. It can be seen that some variations of pressure exist along the surface. These variations are due to the uncertainties of the measurement and non-uniformities in the free stream. The average ratio of p_w to p_{res} is 1.956×10^{-3}.

Fig. 4.7 shows the pressures recorded immediately downstream of the last roughness element. Within the accuracy of the measurements there is no difference in the results between the various types of roughness. The measured pressures agree with the undisturbed wall pressure in all cases.

The next item under investigation is the influence of the roughnesses on the flow in the compression corner. Fig. 4.8 and Fig. 4.9 show the results obtained for

both flare angles. The inviscid pressures for a 15° and a 20° cone are also given for comparison. To give a feeling for the length scales the thickness of the undisturbed boundary layer δ_0 is also indicated. Both cases show a pressure rise on the flare without reaching a plateau. The maximum pressures observed are below the inviscid levels. This suggests that the interaction extends further downstream than the last measured position. The furthest downstream pressure tapping was 23 mm away from the hingeline or approximately 2.5 thicknesses of the undisturbed boundary layer δ_0. The downstream extent of the interaction is somewhat surprising but confirmed by the schlieren pictures.

Both flare angles show a decrease in pressures on the flare due to the roughnesses. The sawtooth roughness proves to have the greatest effect, whereas the small cavities cause only a small difference from the smooth wall case. In both cases the maximum reduction of pressures, caused by the sawtooth roughness, is of the order of 7%.

The pressures recorded in the vicinity of the hingeline show a different behaviour for the two flare angles. Fig. 4.10 and Fig. 4.11 give the pressures measured immediately before the cylinder-flare junction at an enlarged scale. In the case of the 15° flare no differences due to the roughnesses is noticeable within the accuracy of the measurements. In the case of the 20° flare an increase in upstream pressures can be observed for some types of roughness. This indicates an upstream movement of the shock / boundary layer interaction. The largest effect is observed for the sawtooth roughness, whereas the small cavities cause only a very small deviation from the undisturbed case. Within the resolution of the pressure measurements it is not possible to determine whether the flow has separated in the corner for any configuration.

The experiments had been performed initially with an artificially thickened and disturbed boundary layer on the centrebody due to a mechanical problem in the settling chamber. Although the results obtained in those early tests are not useful for the investigation as they deal with a turbulent boundary layer of unknown qualities, some data shall be presented here for comparative purposes. Fig. 4.12 and Fig. 4.13 show the surface pressures recorded with the disturbed boundary layer for the two flare configurations with a smooth centrebody and with the large cavities. The highest pressures recorded are further from the inviscid cone pressures than with the normal boundary layer. This indicates a delayed pressure rise due to the thicker boundary layer. Similar to the results with the normal boundary-layer there is no influence of the roughnesses on the pressure distribution at the hinge-line for the 15° flare. The results for the 20° case, however, show a very different picture. Whereas the smooth wall case shows a surface pressure distribution typical for an attached compression corner flow and similar to the other results, the large cavity case reveals a distinct increase in upstream influence, indicating a separated region before the hinge line. The boundary-layer in these cases was obviously more susceptible to the influence of the roughnesses than the normal boundary-layer.

Other investigations into the influence of roughness on the turbulent compression corner[13-16] have found a more significant change in flow structure due to roughness, even for flows that are unseparated in the smooth case. The different results obtained here seem to indicate a substantial relaxation of the boundary layer over the short distance between the roughness and the corner. Differences in the interaction can still be observed but significant changes in the flow structure appear only when the flow is close to a separation.

The pressures measured in the vicinity of the compression corner have been investigated to determine if the results are influenced by unsteadiness. The frequency response of the transducers and the mounting is sufficient to detect frequencies up to several 10 kHz. Fig. 4.14 shows the result of a frequency analysis on the surface pressure measured just upstream of the hingeline of the 20° flare with a sampling rate of 200 kHz. Sawtooth roughness was mounted upstream. The spectrum shows a distinct peak in the region of 25 kHz. Experiments performed with the pressure ports covered with tape revealed the same peak in the frequency spectrum. The frequency of this peak was found to vary between different transducers. It was therefore concluded that this pattern is due to a mounting vibration of the transducers. No other distinct feature was found in the spectrum at this position. This indicates that either no significant unsteadiness exists in the flow, or that the unsteadiness is covered by the mounting vibration and is therefore undetectable. Due to the closeness of the vibration frequency to the expected aerodynamic frequencies, filtering was not successful. No further results of the high sampling rate experiments are discussed here, future work will have to include a change of the transducer mounting to investigate the problem of unsteadiness.

4.4 Boundary-Layer Profiles

Mean pitot pressure profiles have been recorded for all combinations of roughnesses and flare angles. Traverses were located at eight streamwise positions between the end of the roughnesses and up to 23mm downstream of the hingeline on the flare. As described earlier, the measured pitot pressures have been divided by the pressures measured simultaneously in the settling chamber to remove variations caused by changes in supply pressures. In order to discuss the results from a physical point of view all measurements are presented here in the form of velocity profiles. As discussed in section 2.3.5 these are subject to uncertainties due to experimental errors and assumptions in the analysis. Therefore it is advised to use the actually measured pitot pressure profiles when comparing with the result of a CFD computation. The pitot profiles for all traverse locations are given in the appendix to this thesis.

Table 1 gives the location and model configuration for each boundary-layer traverse and summarises the boundary layer edge parameters as well as the results obtained from the curve-fitting procedure. The undisturbed boundary layer at X=-50 mm was determined to have a c_f of 0.9×10^{-3} and a $Re\delta_2$ of 1300. In a comparison of several measurements by different experimentators Fernholz[81] gives some approximate correlations for skin friction and $Re\delta_2$ depending on Mach and Reynolds number. For the conditions applicable here c_f is given as 1.1×10^{-3} and $Re\delta_2$ as 1500. The relatively good agreement between the given values and the results presented here is encouraging. It can also be concluded that the smooth centrebody boundary layer compares well with results by other authors.

The first item under investigation is the influence of the different types of roughnesses on the undisturbed boundary-layer profile. Fig. 4.15 - Fig. 4.17 show the measured velocity profiles at three different locations downstream of the roughness elements. It can be seen that the roughnesses cause the boundary layers to be less full with the sawtooth roughness having the greatest and the small cavities having the least effect. The velocities near the wall have been reduced considerably, up to 20% in the case of the sawtooth roughness. Additionally the boundary layer thickness, as given in Table 1, is increased by up to 3%. Comparing the profiles obtained at several streamwise locations it can be seen that the smooth wall boundary layer remains unchanged whereas the profiles obtained behind the roughnesses become fuller with increasing distance from the roughness end. The differences reduce and the profiles lie closer together. The velocities at the outer edge of the boundary layer show virtually no variations.

The same profiles are plotted in log-law coordinates compared with the law of the wall (Eq.(2.5)) in Fig. 4.18 - Fig. 4.20. The values of skin friction necessary to determine the shear velocities have been obtained from the curve fitting of the experimental profiles. This assumes that the theoretical profile family is valid for

boundary layers distorted by the roughness. If the real profile is shifted by a velocity shift ΔU then the estimated skin friction will be wrong as the profile is expected to conform to the smooth wall log-law. As the measurements are taken on a smooth surface it is believed that this approach is valid. Independent measurements of skin friction are necessary to determine the accuracy of this method. As a result the profiles agree in the log law region and exhibit differences in the wake strength. All profiles depart from the log law at a Y^+ of about 50. The profiles recorded downstream of the sawtooth roughness show the greatest deviation, thus indicating a large wake parameter. With increasing distance from the roughness end the wake strengths reduce for the rough profiles whereas the smooth wall profile remains unchanged. At the last traverse position the profiles still reveal differences in wake strength due to the roughness but lie closer together than further upstream.

The next item under investigation is the influence of the roughnesses on the flow behaviour in the shock/boundary-layer interaction of the axisymmetric compression corner. The first configuration under investigation is the 15° flare. The surface pressure measurements indicated an unseparated flowfield with no noticeable differences upstream of the hinge-line for the different roughnesses. The results of the boundary-layer profile measurements are given in Fig. 4.21-Fig. 4.23.

The first profile, 3mm downstream of the hinge-line appears to exhibit an inflexion. This is due to a static pressure gradient in y-direction at this location caused by the compression fan extending into the boundary-layer. A constant static pressure has been assumed in the calculation of the velocity, hence the profile presented in Fig. 4.21 is inaccurate. It can only be used for qualitative comparison between the different surfaces. The profiles obtained further downstream from the hinge-line also contain an element of distortion due to a pressure gradient, but here the corner shock is beginning to form, so that the region with a pressure gradient is more distinct and closer to the outer edge of the boundary-layer. The velocities given in these plots, particularly in the lower parts of the boundary layer are more reliable. It is obvious that, due to the compression, the boundary-layers on the flare are thinner than upstream. The roughness induced differences observed in the cylinder boundary-layer are still visible on the flare. The profiles seem to fit in two groups; the first being the smooth wall and the small cavity case and the second being the large cavity and sawtooth case. The sawtooth roughness causes the strongest departure from the smooth case profile but the large cavities have a similar effect. It can be seen from the last two profiles (Fig. 4.22 and Fig. 4.23) that the compression wave system has been displaced away from the wall by approximately 0.5mm due to the larger roughnesses. This is slightly more than the difference in boundary-layer thicknesses observed upstream (0.3mm). Hence the compression wave system has probably also been displaced upstream, but only by a small amount. The velocities near the wall are reduced for the rough cases, similar to the upstream profiles. Again, the effect reduces with increasing distance from the roughness

end. The last profile on the flare (Fig. 4.23) shows the compression corner shock located at the outer edge of the boundary layer, but not yet completely in the inviscid flow. This indicates that the end of the interaction is downstream of this location and the surface pressure is likely to continue to change. This agrees with the surface pressure measurements at this location (Fig. 4.8).

The velocity profiles in log-law coordinates are only plotted for the furthest downstream position as the uncertainties caused by the compression waves being partly embedded in the boundary-layer make the quality of the curve-fitting highly questionable. Fig. 4.24 shows the profiles at X=23mm. The results are similar to the measurements obtained upstream of the hingeline indicating agreement with the log law in the lower parts of the boundary-layer, up to Y^+=100. The profiles appear to be in the two groups discussed earlier, with the strength of the wake parameter being the main difference. The rough profiles seem to show a slightly shorter log-law region.

The next configuration investigated was the 20° flare compression corner. The boundary-layers measured on this flare can be found in Fig. 4.25 - Fig. 4.27. In this compression corner the shock system is stronger than in the 15° case. The velocity profiles close to the hinge-line are therefore more likely to be distorted due to compression waves embedded in the boundary-layer. A comparison of the results reveals similar effects as in the 15° case. The velocities near the wall are reduced for the rough cases. The effect here is stronger than for the smaller flare angle, but no principal difference can be found. The corner shock system is also displaced further away from the wall. The greatest displacement of 1 mm is seen in Fig. 4.26 caused by the sawtooth roughness. This value is considerably larger than the increase in oncoming boundary-layer thickness. This suggests that the upstream influence of the interaction has been increased and as such the formation of the corner shock system takes place further upstream. The last profiles on the flare show a closer agreement. In all cases the shock is still partly embedded in the boundary layer, hence this location is still within the interaction region. Fig. 4.28 gives this profile in log-law coordinates. For low values of Y^+ the data fits to the log law within the measurement accuracy. The lowest values of Y^+ are larger than for the 15° case therefore the overall extent of the law of the wall region is reduced.

All profiles presented here showed a relatively good agreement with the log-law in the near wall regions of the boundary-layer, considering the problems encountered with the pitot-pressures obtained near the surface. This suggests that the theoretical profile used to fit to the experimental data and obtain the surface skin friction has been very useful for this investigation. Therefore the obtained values of skin friction are also presented. For results obtained at the hingeline the pressure variation within the boundary layer due to the corner shock system makes the determination of flow velocity subject to large errors. The skin friction values obtained at these positions are included in the figures but only for completeness and not connected to the other data. When discussing the results

these values will be disregarded.

As the skin friction coefficient c_f used in the theoretical profiles is based on local boundary-layer edge conditions it is not a good parameter for comparisons as most profiles will have different edge conditions, particularly on the flares. Therefore these edge conditions have been used to calculate the local skin friction. Non-dimensionalised with the average smooth wall skin friction of the oncoming boundary-layer this gives a more suitable quantity for comparisons. The results are shown in Fig. 4.29 and Fig. 4.30.

It can be seen that the surface skin friction downstream of the roughness is reduced by all types of roughness. This can be attributed to the loss of momentum in the near wall parts of the boundary-layer that has been observed in the velocity profiles. Again the sawtooth type has the greatest and the small cavities have the least effect. The maximum reduction is of the order of 20%. The small cavity and smooth wall case tend to overlap further downstream, whereas the large cavities and the sawtooth case always retain a lower value of surface shear stress. The skin friction values on the 20° flare are considerably higher than in the 15° case. The increase of skin friction on the flare is steeper in the 20° case. In all cases the shape of the skin friction distribution along the surface has not been altered by the roughnesses. The differences in skin friction caused by the roughnesses reduce with increasing streamwise location but this reduction is very slow. The skin friction distribution appears to reach a minimum near the hingeline although no reliable measurements are available at this location. It is possible that the overall reduction in skin friction caused by the sawtooth roughness is sufficient to produce a short region of negative skin friction (separated flow) in this area.

The skin friction results confirm the trends observed in the other measurements, such as velocity profiles and surface pressures. This increases the confidence in the chosen approach, particularly in the selection of Mathews et al's theoretical velocity profile and the curve fitting procedure incorporated. Though this can not replace a skin friction measurement, these are very difficult and prone to large errors, particularly in pressure gradient regions. The procedure used here may be useful as a complementary analysis tool.

Summarising the results of the velocity profile investigations it can be said that the upstream roughnesses caused the velocities within the boundary layer to be reduced. This effect was largest nearest the wall so that the shape of the boundary-layer has also been effected, making the profiles less full. In law of the wall coordinates this effect resulted in an stronger deviation from the log law, hence an increase of the wake strength. Additionally the thickness of the boundary-layer has been increased by roughness, by up to 3%. The sawtooth roughness was found to be the most 'effective' in causing these changes and the small cavity type roughness only produced very small disturbances from the smooth wall case, often of the magnitude of the experimental accuracy. The

disturbed boundary layers were found to change back towards the undisturbed profile but no full relaxation has been observed within the scope of the measurements (6-8 δ). In all cases the effects of the roughnesses could be observed throughout the compression corner interaction with neither magnification nor weakening of the effects. No proof of a reversed flow in the compression corner was found, but this may well be a result of the resolution of the tests and the probe interference. Nevertheless it appears possible that for flows very close to separation the reduction of momentum near the wall, and hence the reduction of skin friction, is sufficient to cause an unseparated flowfield to develop a small separation.

It was also noted that the compression wave system for both flare angles has been displaced further away from the surface on the flare (up to 10% of δ) due to the two most severe upstream roughnesses. This displacement was greater than the increase in boundary layer thickness, hence it appears that the wave system has also been moved upstream. This effect was greatest for the larger flare angle. In this case a corresponding increase in the upstream influence has also been noted in the surface pressure measurements.

4.5 Surface Heat Transfer

The heat flux onto the surface has been measured using liquid crystal thermography for all configurations. A typical response of the surface coating during an experiment is given in Fig. 4.31 showing the colour response on the cylinder fitted with sawtooth roughness and the 20° flare. The liquid crystals used are of the type Licritherm TCS 811 manufactured by BDH[82] with a temperature range from 27.6°C to 41.5°C. The first picture shows the response very early during the run, 1 second after the flow start. The only colour response visible at this moment is in regions of very high heat transfer. These are the tips of the sawtooth and some parts of the flare. It is interesting to note that there appears to be a very narrow region of high heat transfer immediately downstream of the hingeline; a blue-green response is clearly visible in this area. Most of the cylindrical part of the model and some of the flare is still too cold to give a colour response. The second picture was taken 5.8 s after the start of the flow. Now areas with high heat transfer are above the range of the liquid crystals. It can be seen that the rear of the flare and the narrow region near the hingeline are in this category. The cylindrical part of the model is now mainly in the range of the coating and displays a range of colours. The bandwidth of the liquid crystal coating appears to be suitable to give a colour response for most of the surface during the length of a normal wind tunnel run. It has therefore been used for the experiments in this thesis.

The measured heat transfer for the smooth centrebody and 15° flare has already been shown in Fig. 3.15. The result for the same configuration but with sawtooth roughness is given in Fig. 4.32. The results for the smooth centrebody and sawtooth roughness for the 20° flare are given in Fig. 4.33 and Fig. 4.34. It can be seen that all cases display a similar distribution of heat transfer. The heat transfer is relatively uniform upstream of the hingeline and then experiences a sharp peak just downstream of the hingeline. Further downstream the heat transfer increases gradually. All cases show little variation in a spanwise direction. The increase of heat transfer towards the rear of the model is more severe for the 20° case. This is probably due to parts of the nozzle shock impinging on the model and causing additional heating.

When comparing these results it needs to be recalled that the operating conditions of the wind tunnel vary between different experiments. This causes a displacement of the actual levels of measured heat transfer. Due to the poor performance of the surface thermocouples a normalisation of $\mathring{q}$ to C_H was found not to improve the comparisons. The additional uncertainties were of the order of the variations in operating conditions, therefore the measured values of heat transfer are presented here.

As no significant spanwise variations exist it is easier to compare results by showing slices in a streamwise direction. To reduce the noise the results shown are averages of several slices lying in a narrow band of 10 mm width along the

centre of the image. The heat transfer on the roughness elements and immediately downstream is shown in Fig. 4.35 - Fig. 4.37. Measurements have been obtained on almost the complete surface of the roughnesses apart from the hidden surfaces. The results obtained behind the large cavities appear to lie below the smooth surface values. This is caused by variations in the operating conditions of the tunnel. The lowest part of the 45° sawtooth was subject to heating rates too low to be detected with the liquid crystal mixture used here. A number of observations can be made from these results. The large cavities were subject to heating rates comparable to the undisturbed smooth wall boundary layer for the surfaces inside the cavities and up to 20% higher at the upstream edge of an upper surface. The small cavities reveal significantly higher surface heating, up to twice the undisturbed values. The largest peaks were observed with the sawtooth roughness, reaching as much as three times the undisturbed heat transfer at the outer edges. The values of $\mathring{q}$ in the grooves was lower than for the undisturbed boundary layer. The extreme values of heat transfer observed at the edges of the roughnesses are subject to measurement errors due to cross-conduction. It is possible that the actual heat transfer value right on the point of a sawtooth roughness lies above the peak values measured here. Nevertheless this value can not be determined with any other technique and the results presented here are probably the best estimate that is achievable. For all types of roughness an area of increased heat transfer can be seen just downstream of the last roughness element. This increase in heat transfer is limited to a short distance of about 10 mm ($\approx 1.0 \times \delta$) after which the normal surface heat transfer is re-established. Within the accuracy of the measurements and due to the variations in operating conditions it cannot be established if any differences in heat transfer persist at this point, as noted for the surface skin friction.

Fig. 4.38 compares the heat transfer rates downstream of the roughnesses and on the 15° flare. An overshoot in $\mathring{q}$ just downstream of the hingeline can clearly be seen for all cases. The increased heat transfer levels are limited to an area between the hingeline and 5 mm downstream, this is the equivalent of half a boundary layer thickness in terms of the upstream boundary layer. This peak is largest for the smooth surface case. The sawtooth roughness has the smallest overshoot compared to the heat transfer upstream of the hingeline. The large cavity case appears to be below the other configurations, this is caused by increased surface temperatures during the course of this particular experiment.

The heat transfer measured for the 20° flare and various roughnesses is given in Fig. 4.39. The results are basically similar to the 15° case, but the differences in the level of $\mathring{q}$ are increased. Most of the experiments leading to these results have been subject to significant variations in surface temperature and tunnel operating conditions. The peak heat transfer near the hingeline is increased in comparison with the smaller flare. It can also be seen that some cases show a strong increase in heat transfer at the downstream end of the model, this is caused by parts of the nozzle shock system impinging on the flare. Due to the larger flare angle the blockage in the working section is increased and the model

surface is closer to the edge of the useful flow. The differences caused by the roughnesses are limited to a reduced peak and a slight increase in the upstream influence before the hingeline.

The heat transfer rates have also been used to compute heat transfer coefficients, using the local wall temperature and the measured total temperature. The results are given in Fig. 4.40 and Fig. 4.41 together with the computed skin friction coefficients for the smooth centrebody and the 15° and 20° flare. Both coefficients are normalised with the free-stream properties. It can be seen that outside the interaction region the agreement between the heat transfer coefficient and $C_f/2$ is good. This indicates that Reynolds analogy is valid. The exact formula for Reynolds analogy in turbulent boundary layers is (see Ref.83):

$$St \approx \frac{c_f/2}{1+13(Pr^{2/3}-1)(c_f/2)^{1/2}}$$

The heat transfer coefficient computed here, C_H, is obtained by using the total temperature instead of the recovery temperature. The relation between the Stanton number and the heat transfer coefficient is:

$$C_H = \frac{T_r - T_w}{T_0 - T_w} St$$

For the operating conditions this gives the following proportionality:

$$C_H \approx 0.8\, St$$

which of the order of the Reynolds analogy factor. Therefore the simplified analogy is used here:

$$C_H \approx \frac{1}{2} c_f$$

Also given in Fig. 4.40 and Fig. 4.41 are the surface pressure distributions for the same configurations. In both cases the increase in heat transfer and wall pressure through the corner interaction is very different in shape. This is a surprising result as it is generally assumed in turbulent hypersonic compression corners that both quantities will exhibit a similar behaviour for this type of flow as found in Coleman a. Stollery[32], and Hankey and Holden[84]. In the cases presented here, however, the heat transfer distribution shows a rapid increase and an overshoot whereas the surface pressure rises only slowly without reaching a plateau within the range of the measurements. The flow in both cases is presumed to be unseparated, therefore an overshoot in heat transfer is unusual. A closer examination of available experimental data however, reveals a few cases were the heat transfer distribution shows a distinct peak while the surface pressure distribution shows a gradual increase towards a plateau without overshoot. One example can be found in Coleman and Stollery's data[85] in the

case of the 30° compression corner and other examples can be seen in experiments performed by Holden[30]. In all cases the flow was very close to separation or mildly separated. A computation of the flow in a turbulent hypersonic compression corner performed by Edwards[85] showed a spike in the heat transfer distribution upstream of the hingeline. The flow in this case was separated and it was found that this feature was caused by a secondary separation bubble underneath the primary separation. The feature observed here, however, is located downstream of the corner in unseparated flow.

An explanation can be found in the scale of the events. The peak in heat transfer is limited to a small area very close to the hingeline and only of the length of half the oncoming boundary layer thickness. Due to the effects of cross conduction the distribution shown here is likely to be more spread than the actual heat transfer. This makes such an event very difficult to detect with traditional measurement techniques. If surface heat transfer sensors were used in this study, with a spacing of a boundary layer thickness, then the results would compare well with other measurements as the heat transfer peak would be overlooked and the increase of heat transfer downstream is similar to the pressure rise. This can explain why such a feature has not been noticed more widely.

A possible cause of such an event can be the existence of a very small region of separated flow in the corner as illustrated in Fig. 4.42. As the heat transfer is determined by events very close to the surface where the temperatures reach a maximum such a small separation can cause the observed peak in heat transfer. If the size of the bubble is well below the thickness of the boundary layer the outer streamlines need not be distorted. The pressure distribution in such a case is almost the same as for nominally unseparated flow. This idea is not entirely new, in his discussion of turbulent compression corner flow Holden[83] remarks that incipient separation can be detected at very different corner angles depending on the method used. If the separation is detected in the surface pressure distribution then usually much larger angles for incipient separation are stated than those determined with surface oil flow visualisation. This leads him to suggest that a separation may exist inside the laminar sublayer well before it reaches a size large enough to cause a pressure distortion. Apart from this suggestion the idea was not further discussed and the possible effects on surface heat transfer have not been addressed. The lack of compression corner data with a similarly sized turbulent boundary layer and measurements of comparable resolution to the results presented here makes a further investigation difficult.

In order to test the hypothesis of the existence of a small separated region near the hingeline, surface flow visualisation with shear stress sensitive liquid crystals was been performed. The liquid crystals used are of the type Hallcrest BCN-192[86]. As this type of liquid crystal is not encapsulated in a binder the appearance is that of an oily film rather than a solid coating. When used in wind tunnel experiments, this gives a similar effect to surface oil flow visualisations with an

additional colour response depending on the magnitude of the skin friction. For temperatures above 55°C the coating becomes colourless. Fig. 4.43 shows the response of the surface coating on a 15° and 20° flare approximately 3 s after the flow-start. Both experiments were performed without any roughness. The results confirm the existence of a small separated region as a separation line can be seen just upstream of the flare/cylinder junction. In the reattachment region the surface temperatures are already above the liquid crystal clearing point, therefore the reattachment line is not visible. Careful examination of the models after the experiment gave an approximate location for the reattachment. The separation was located approximately 3 mm upstream of the corner for the 15° flare and about 4 mm upstream for the 20° case. The reattachment was found to be 1.5 mm downstream. The accuracy of the measurements is limited to about 1 mm. By assuming the dividing streamline to be a straight line between separation and reattachment the height of the separation bubble is calculated to be around 0.3 mm. This is equivalent to 3% of the undisturbed boundary layer thickness and only just larger than the laminar sublayer. Using the undisturbed boundary layer profile, the Mach number at this distance from the wall is between 1 and 2. The total pressure is of the order of 20% of the free stream value. It is believed that the an increase in pressure at reattachment is not measured because of the relatively low momentum of the flow at this position. It is possible, however, that a peak in pressure exists but remains undetected due to the spacing of the transducers.

The peak in heat transfer was observed about 2 mm downstream from the corner. This agrees well with the location of the reattachment line as detected from the flow visualisation. The maximum heat transfer at this location was found to be up to 15% higher than the levels measured further downstream on the flare. The existence of such a localised peak in surface heat transfer at relatively moderate flare angles can have significant implications for the design of control surfaces. In order to be able to predict such a phenomenon with CFD codes it appears to be important to model the physics in the sublayer. Future research will have to address this problem in the light of turbulence modelling.

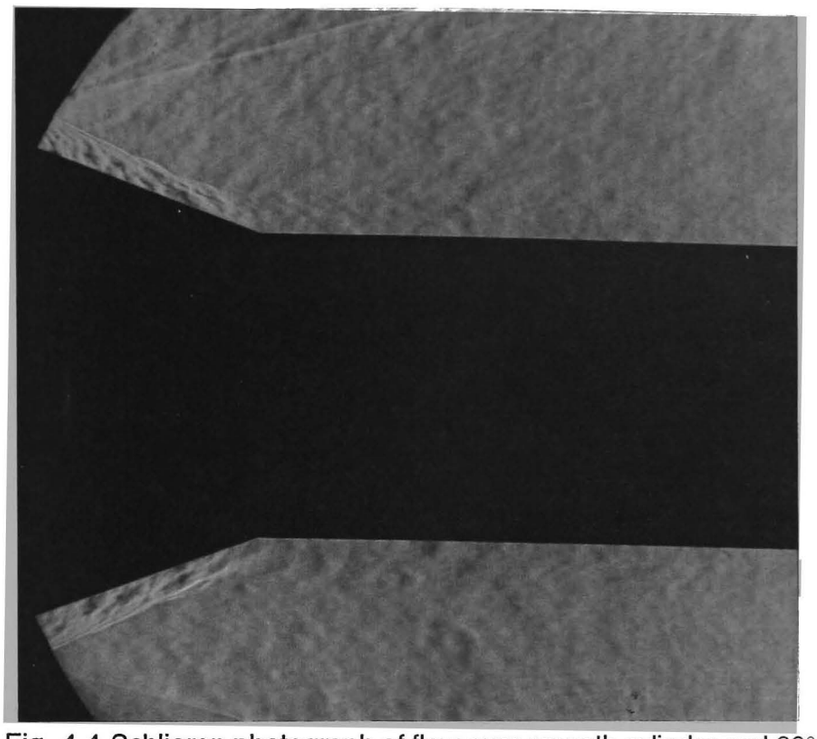

Fig. 4.4 Schlieren photograph of flow over smooth cylinder and 20° flare

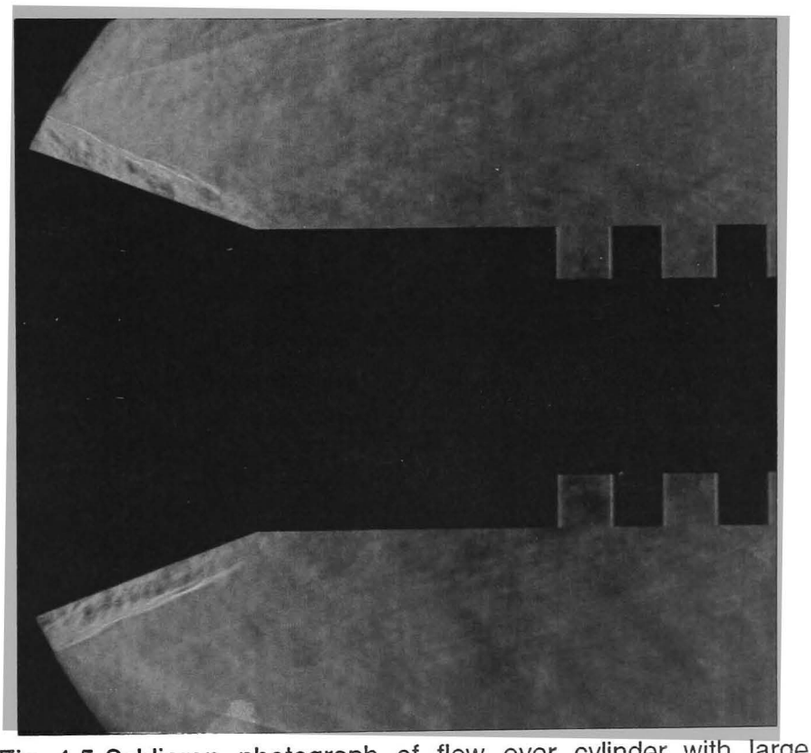

Fig. 4.5 Schlieren photograph of flow over cylinder with large cavities and 20° flare

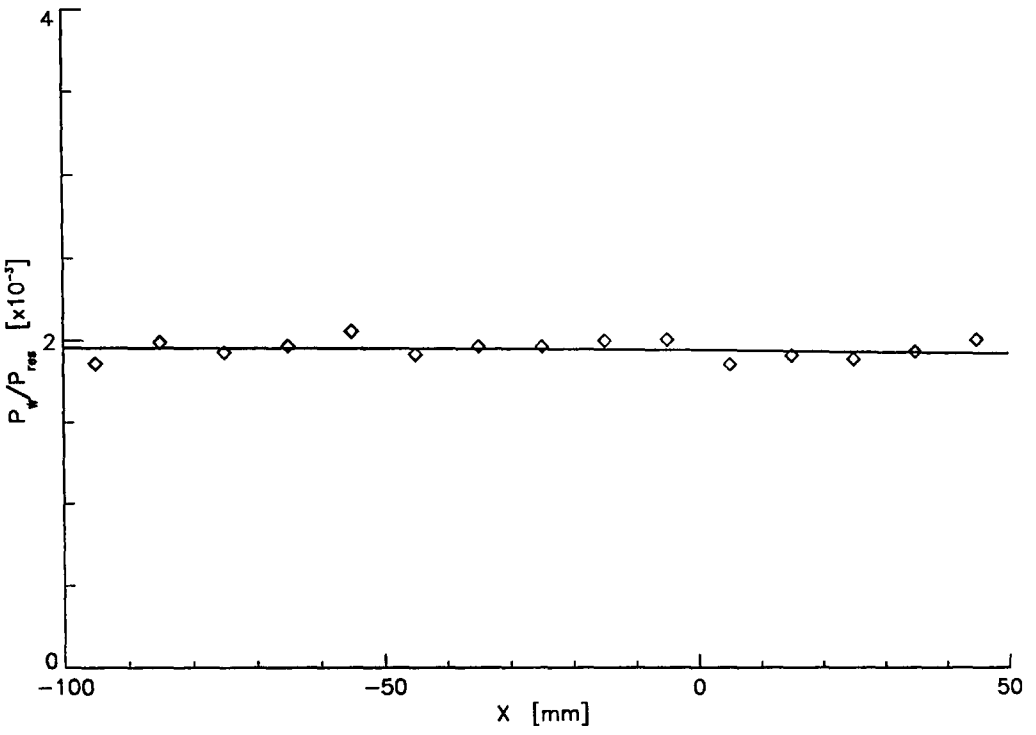

Fig. 4.6 Surface pressure on centrebody

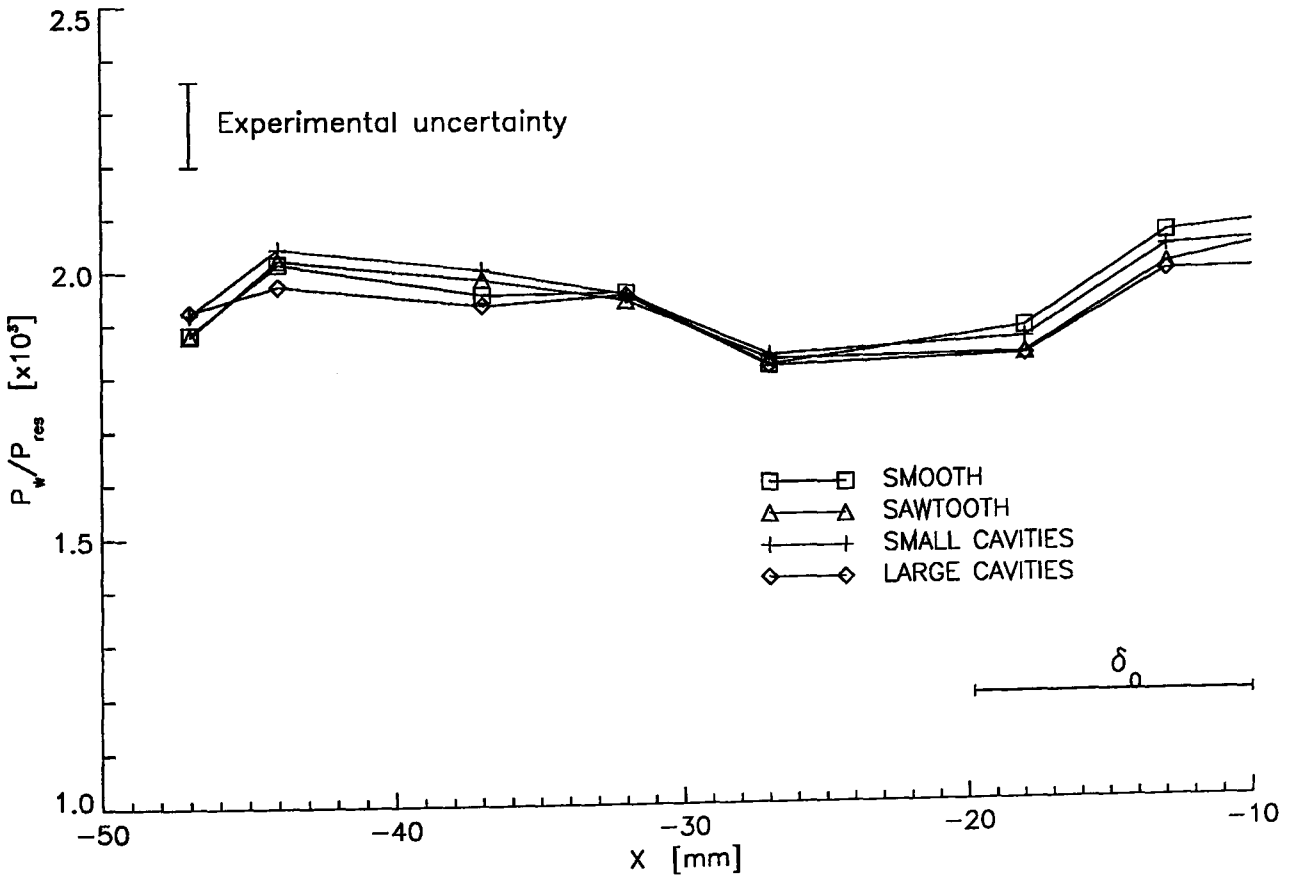

Fig. 4.7 Surface pressures measured downstream of the roughnesses
δ_0: Thickness of undisturbed boundary layer

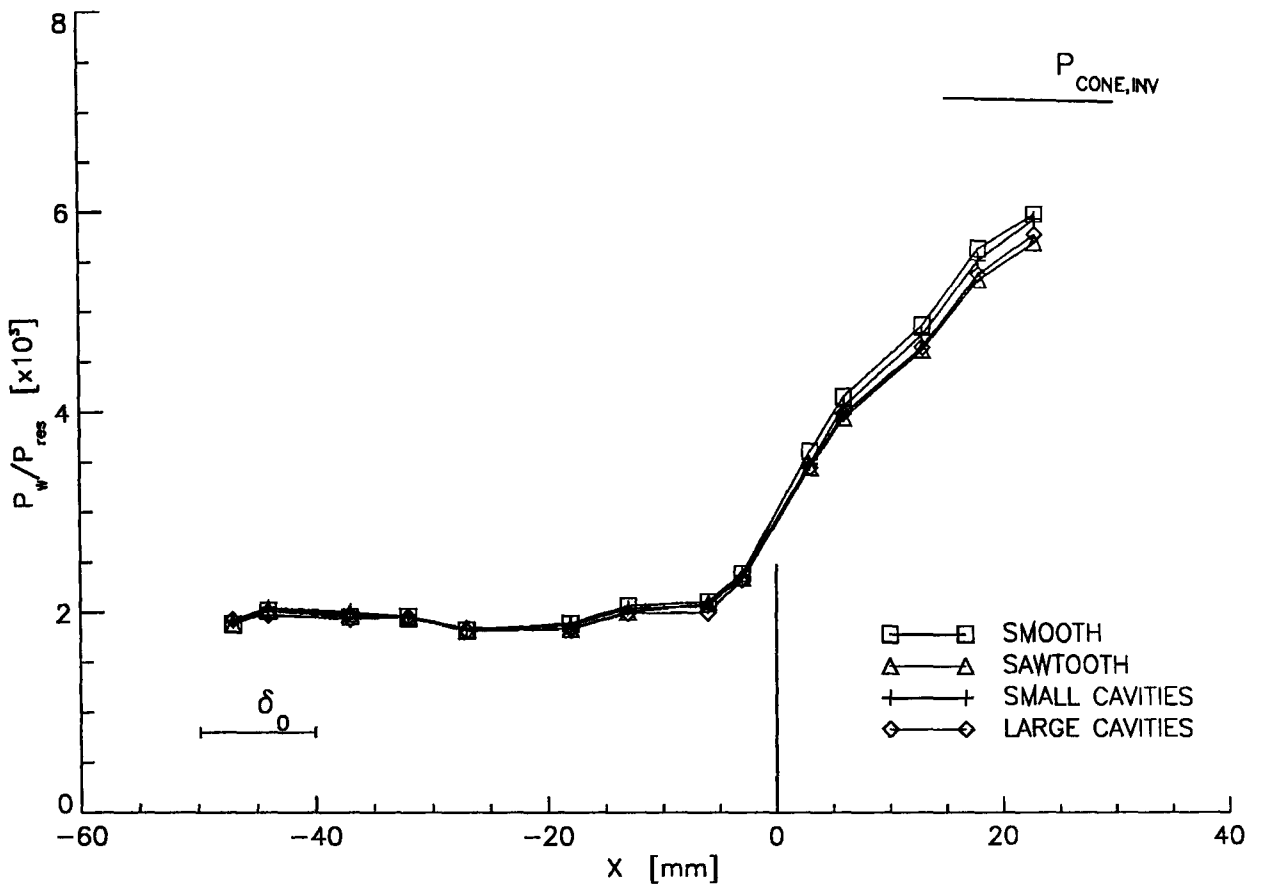

Fig. 4.8 Surface pressures on cylinder and 15° flare

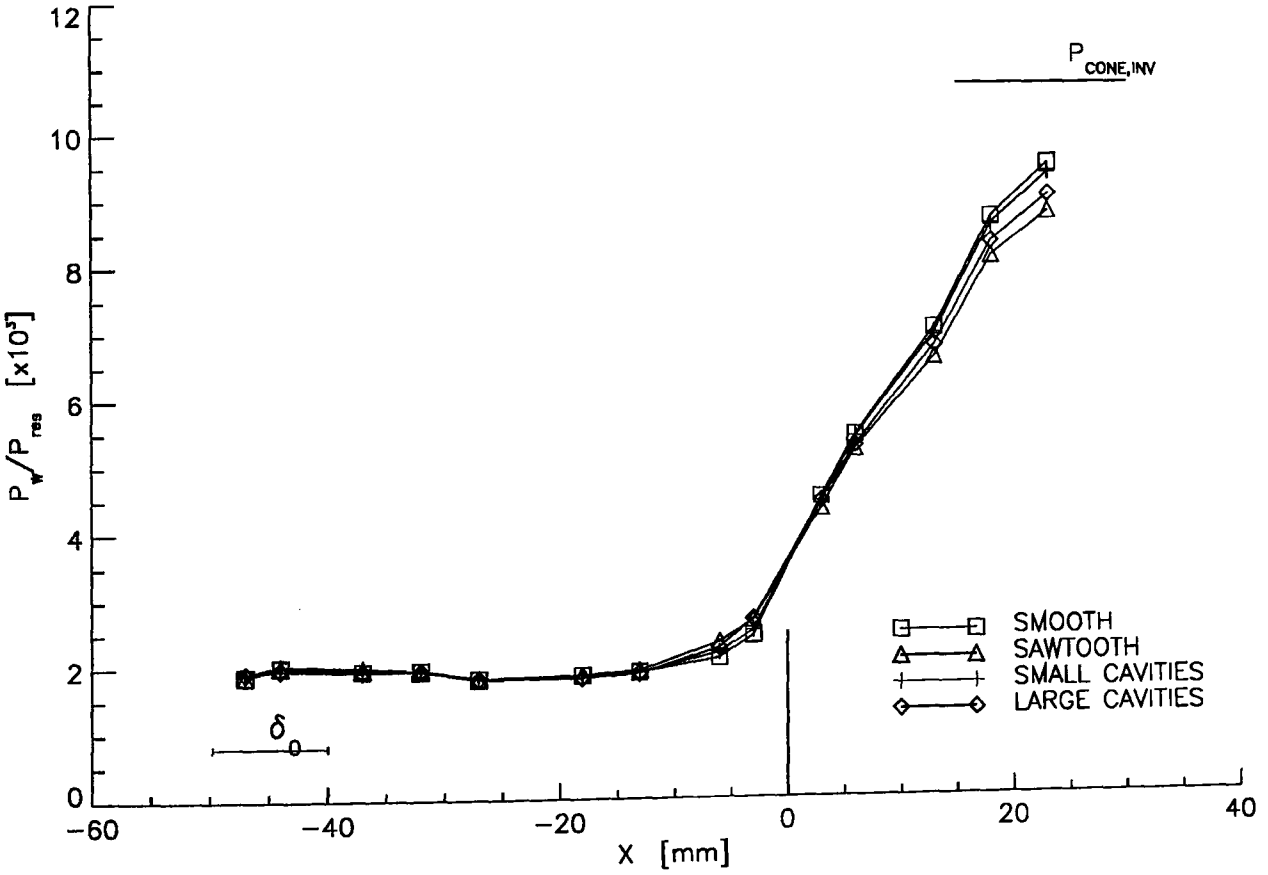

Fig. 4.9 Surface pressures on cylinder and 20° flare

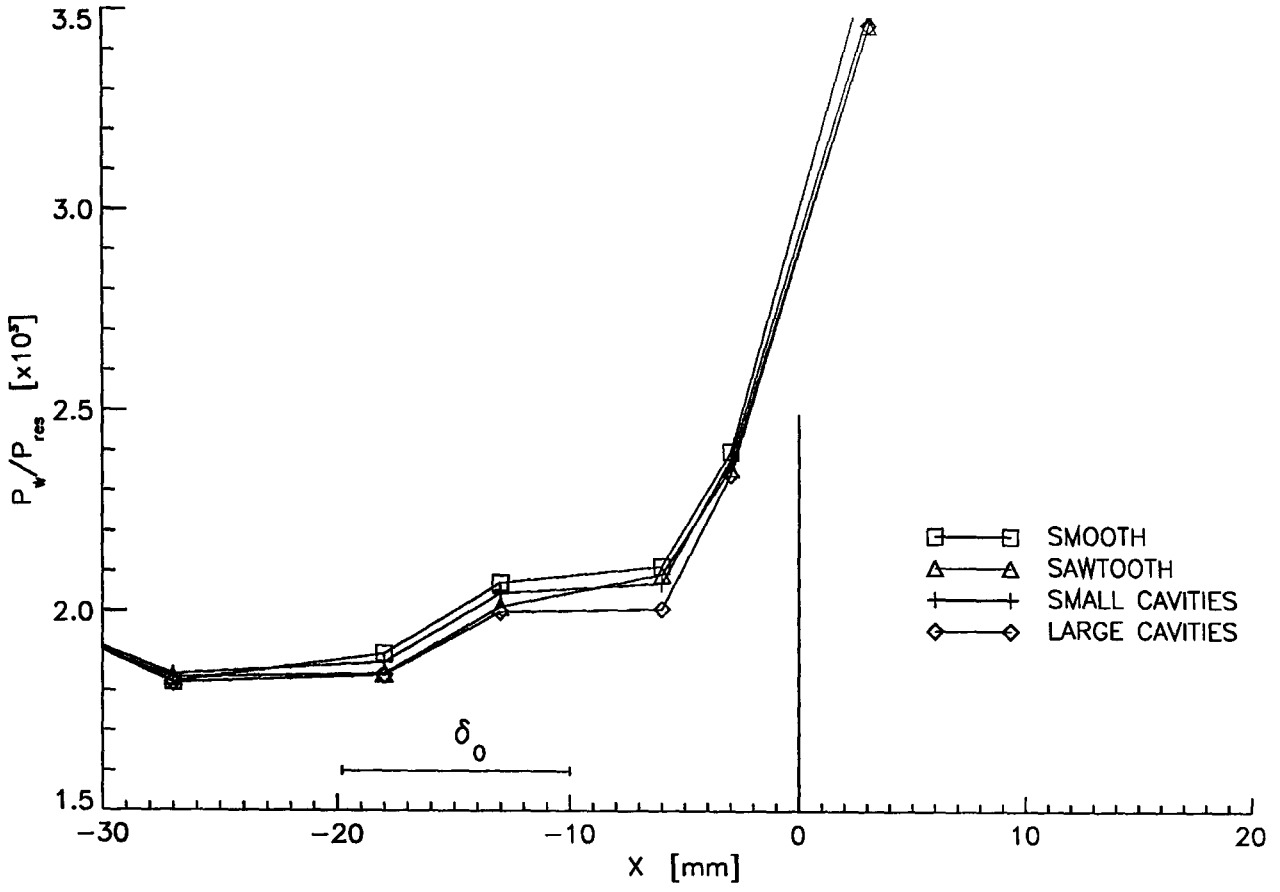

Fig. 4.10 Pressures for the 15° flare case measured in the vicinity of the hinge-line

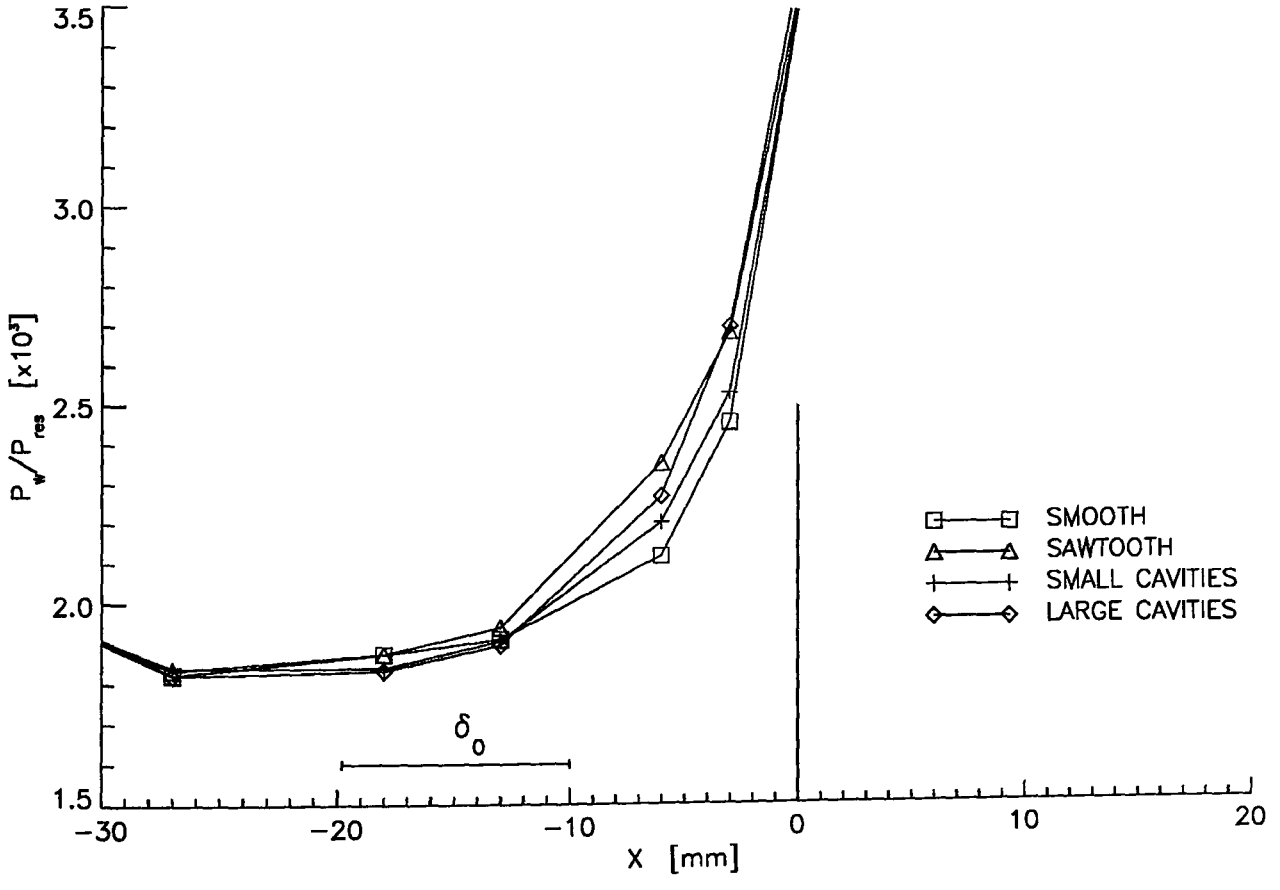

Fig. 4.11 Pressures for the 20° flare case measured in the vicinity of the hinge-line

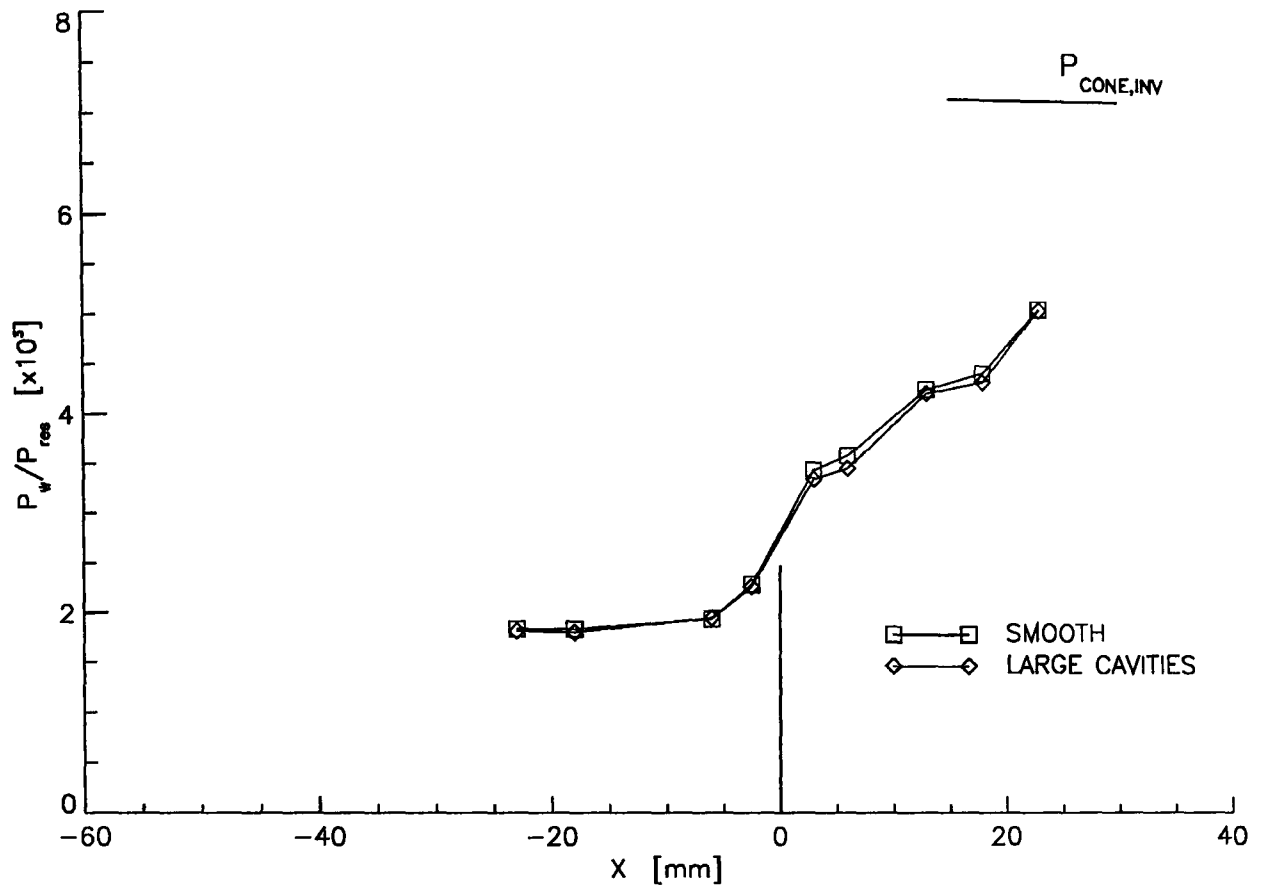

Fig. 4.12 Surface pressures for 15° flare case with disturbed inflow boundary-layer

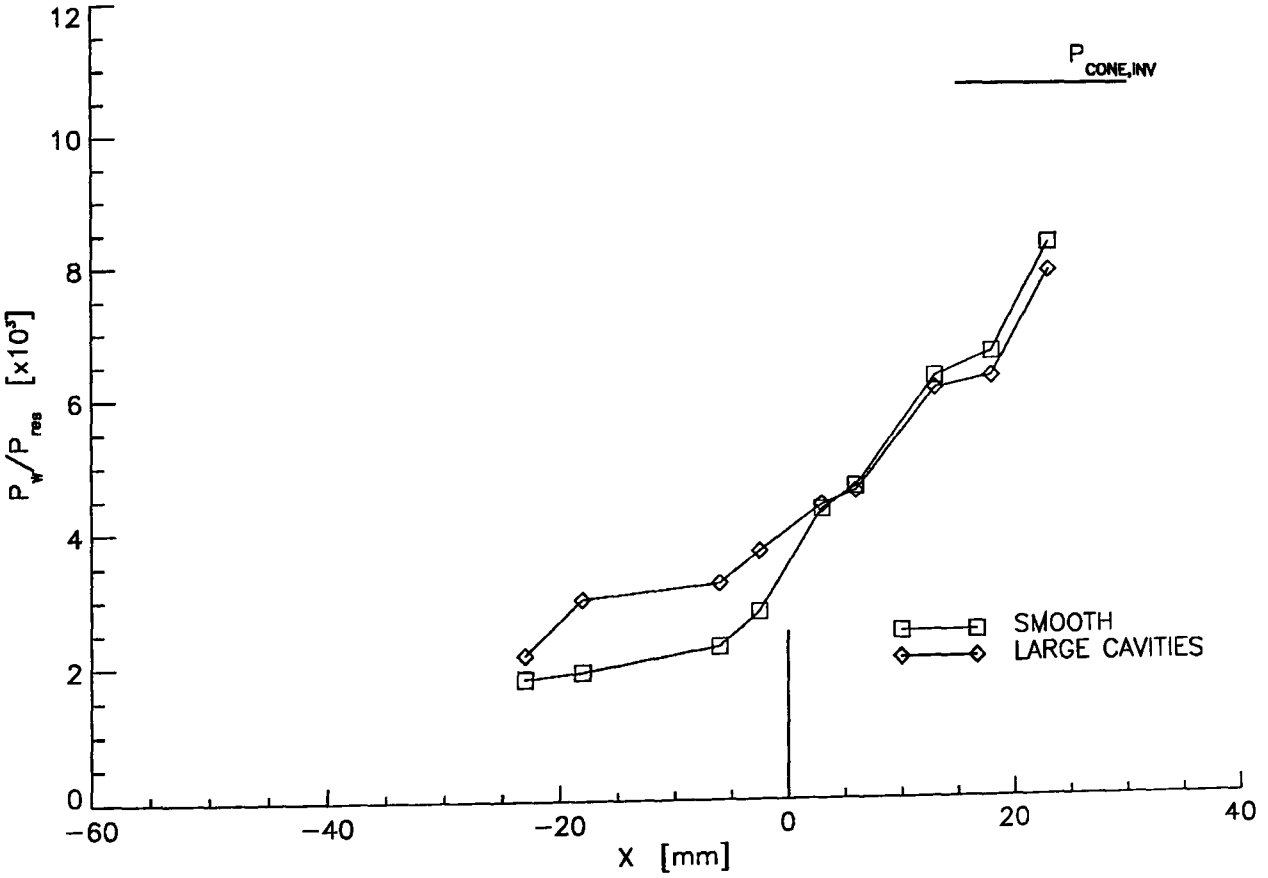

Fig. 4.13 Surface pressures for 20° flare case with disturbed inflow boundary-layer

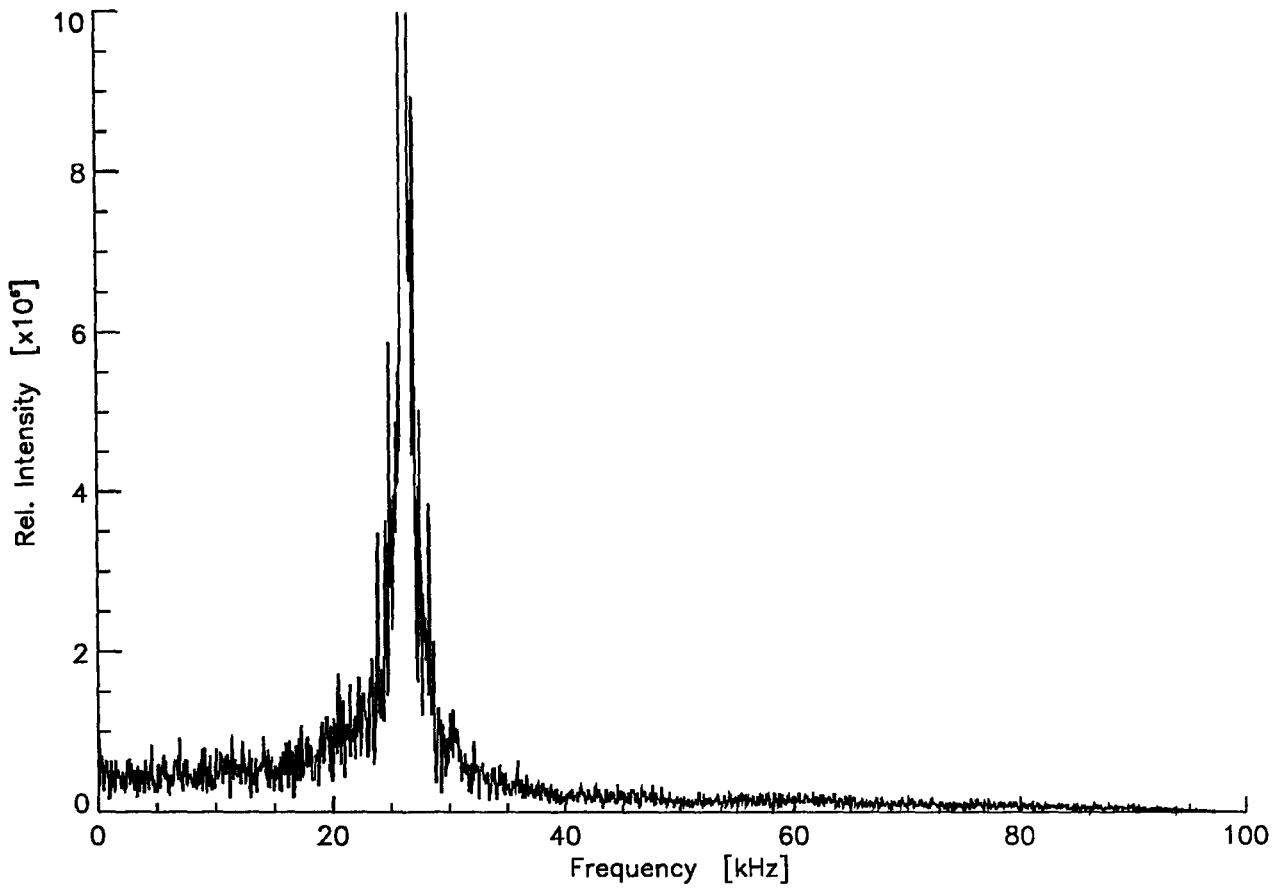

Fig. 4.14 Frequency spectrum of measured surface pressure near hingeline of 20° flare with sawtooth roughness

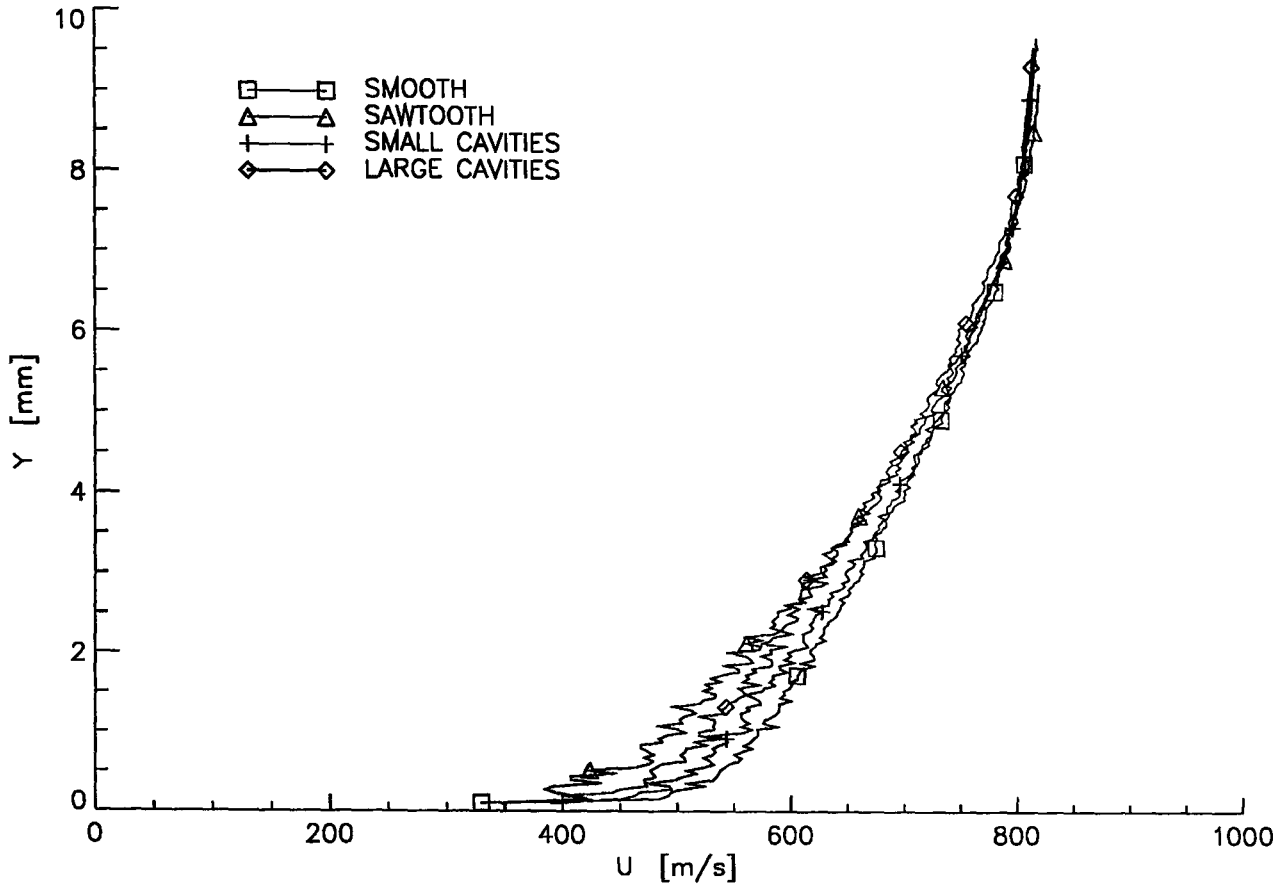

Fig. 4.15 Velocity profiles immediately behind roughness X=-50mm

Fig. 4.16 Velocity profiles 13mm behind roughness X=-37mm

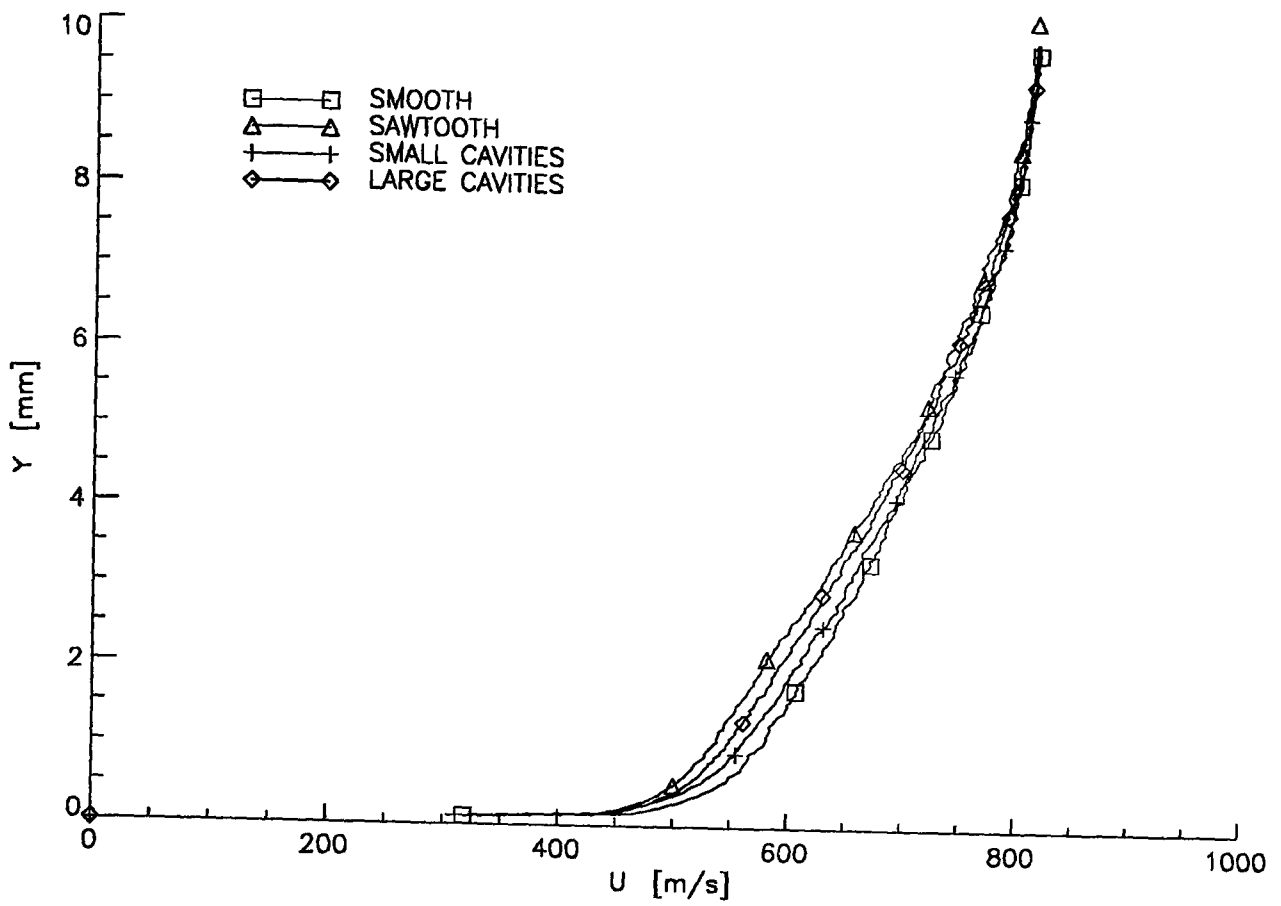

Fig. 4.17 Velocity profiles 32mm behind roughness X=-18mm

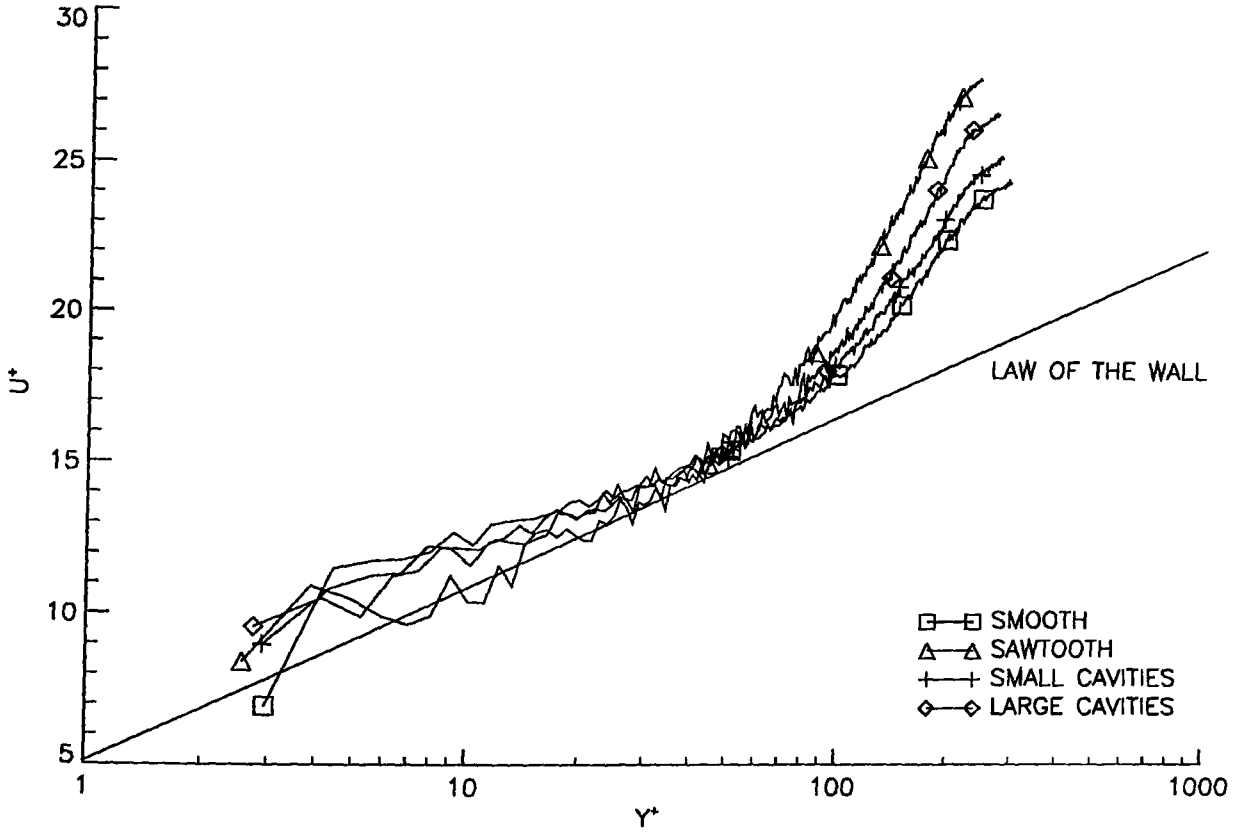

Fig. 4.18 Velocity profiles in log-law coordinates immediately behind roughness X=-50mm. Skin friction as estimated from curve-fit procedure.

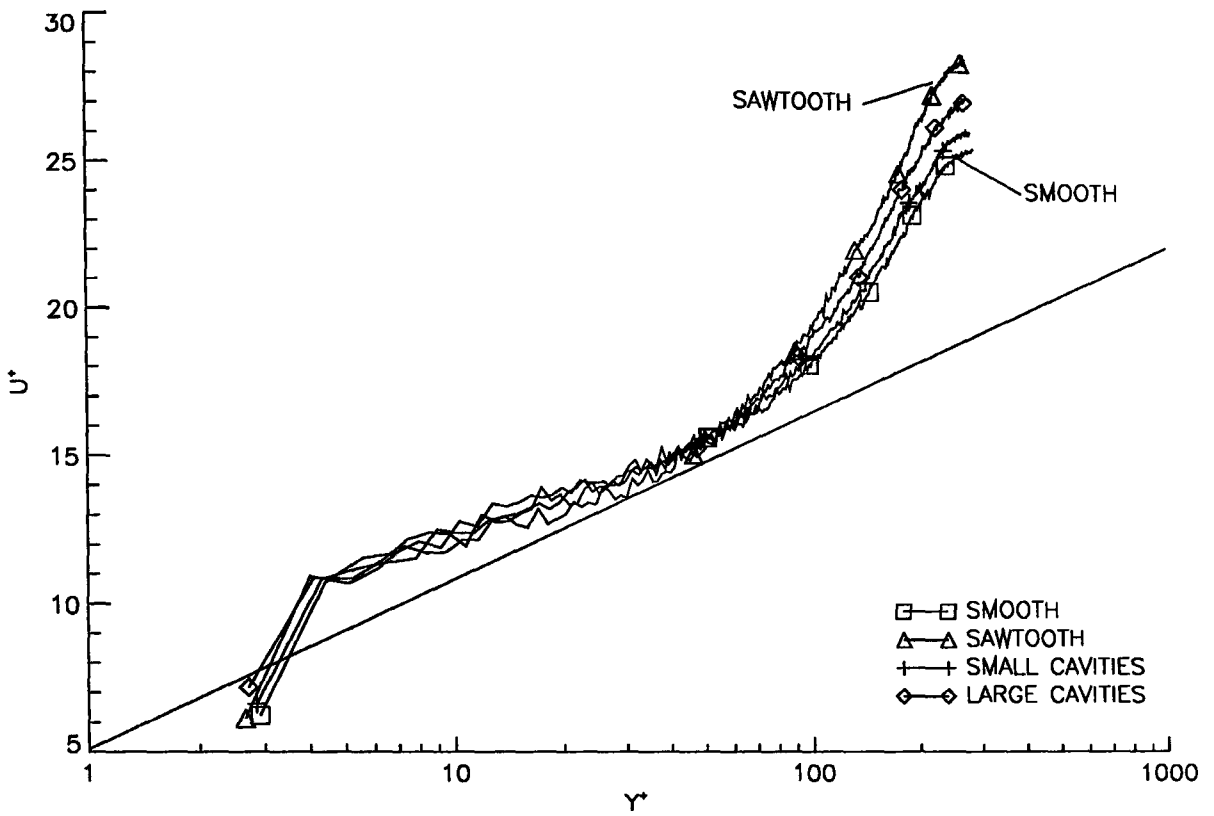

Fig. 4.19 Velocity profiles in log-law coordinates 13mm behind roughness X=-37mm. Skin friction as determined from curve-fit procedure

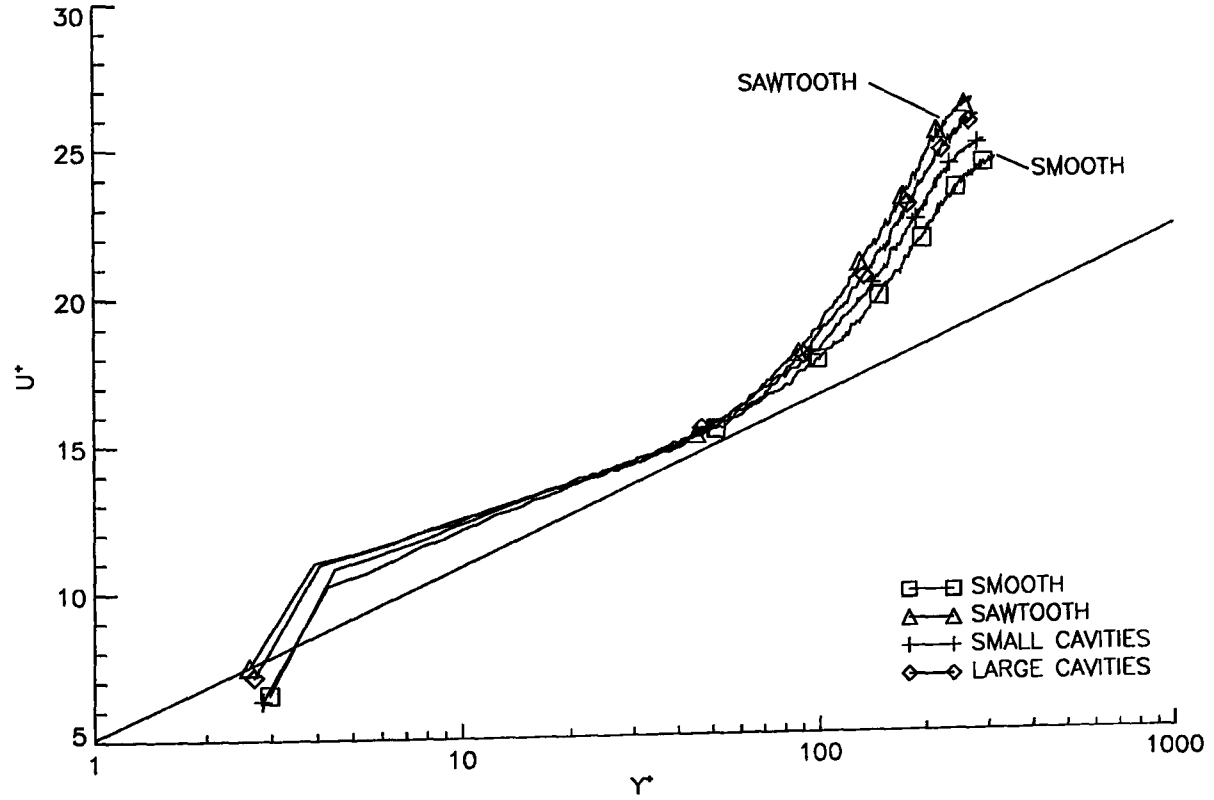

Fig. 4.20 Velocity profiles in log-law coordinates 32mm behind roughness X=-18mm. Skin friction as determined from curve-fit procedure

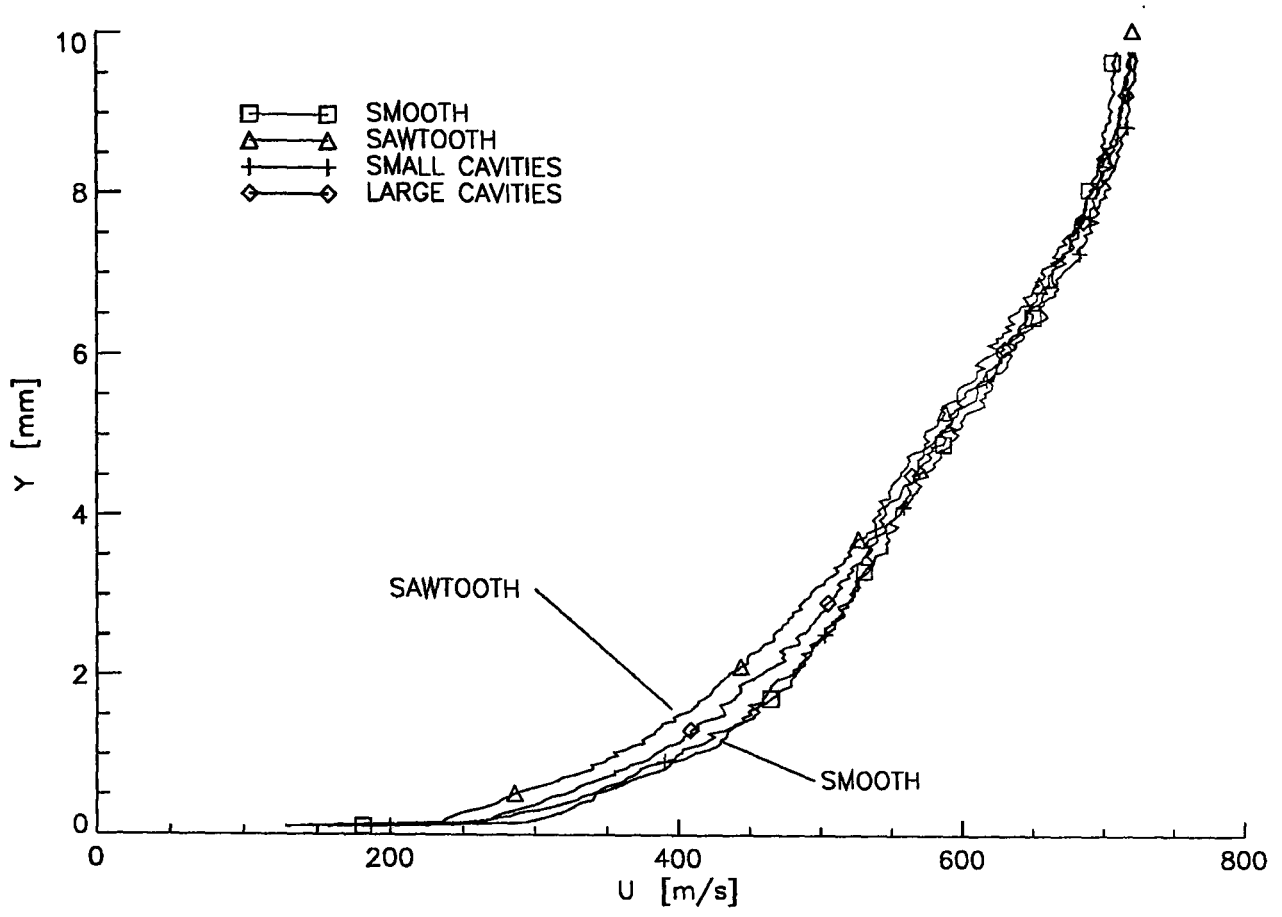

Fig. 4.21 Velocity profiles on 15° flare X=3mm

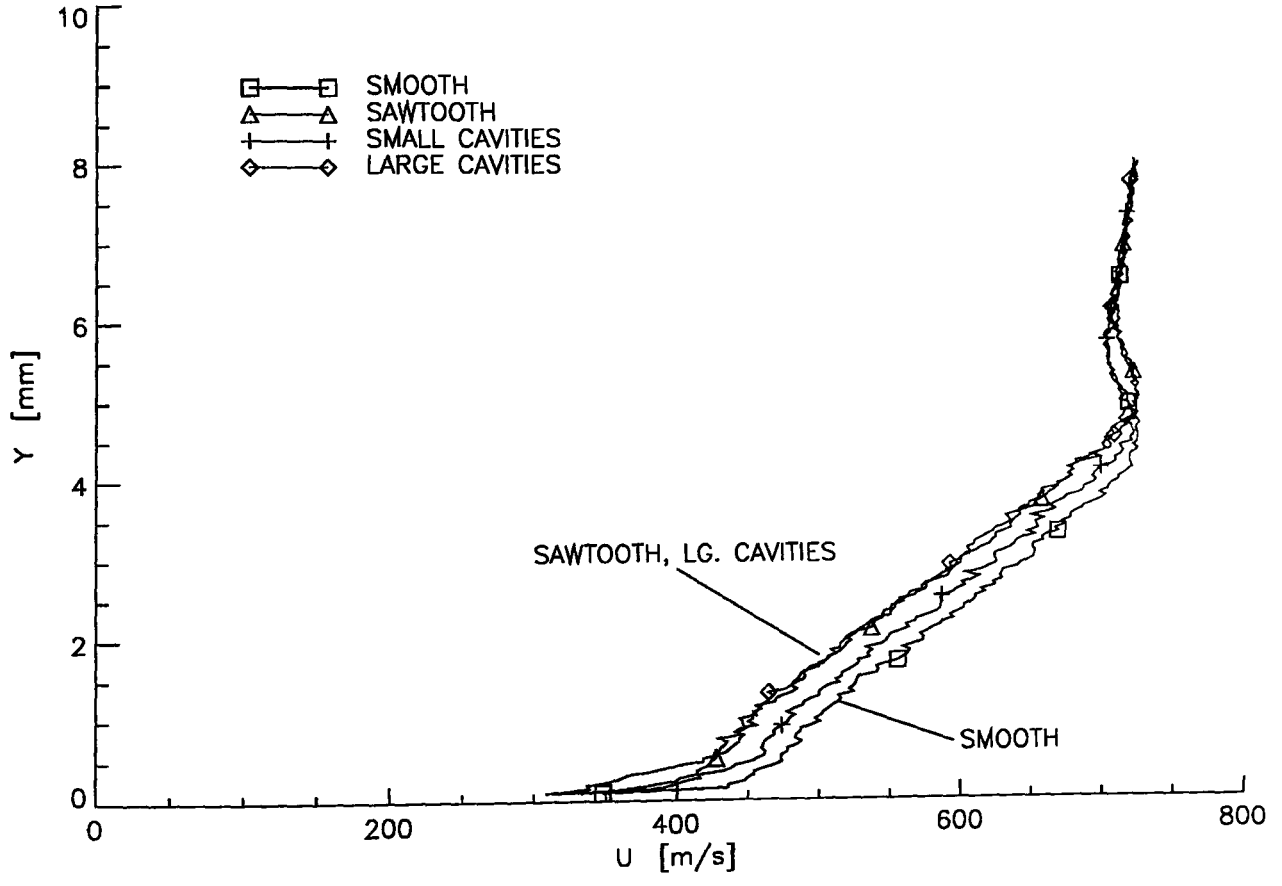

Fig. 4.22 Velocity profiles on 15° flare X=13mm

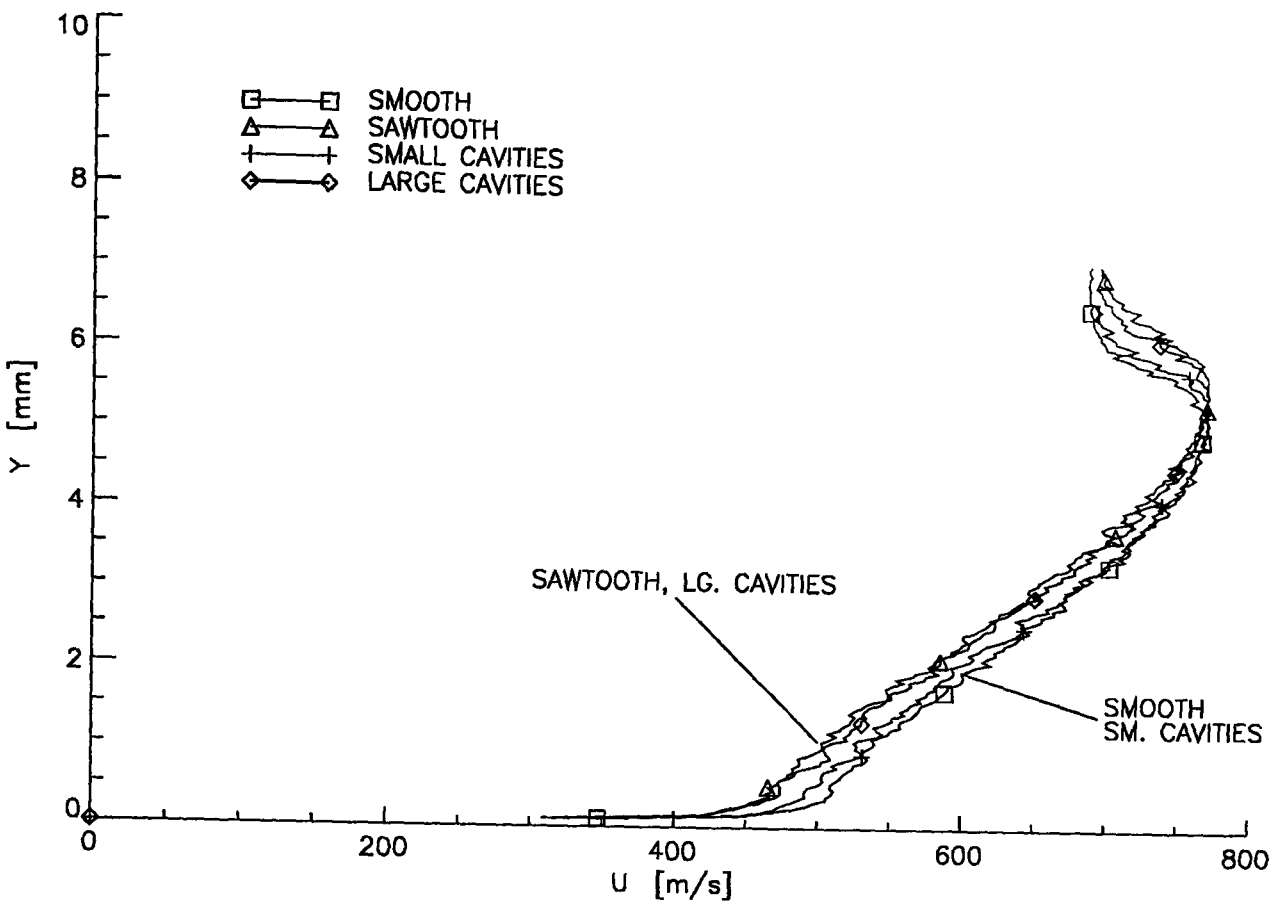

Fig. 4.23 Velocity profiles on 15° flare X=23mm

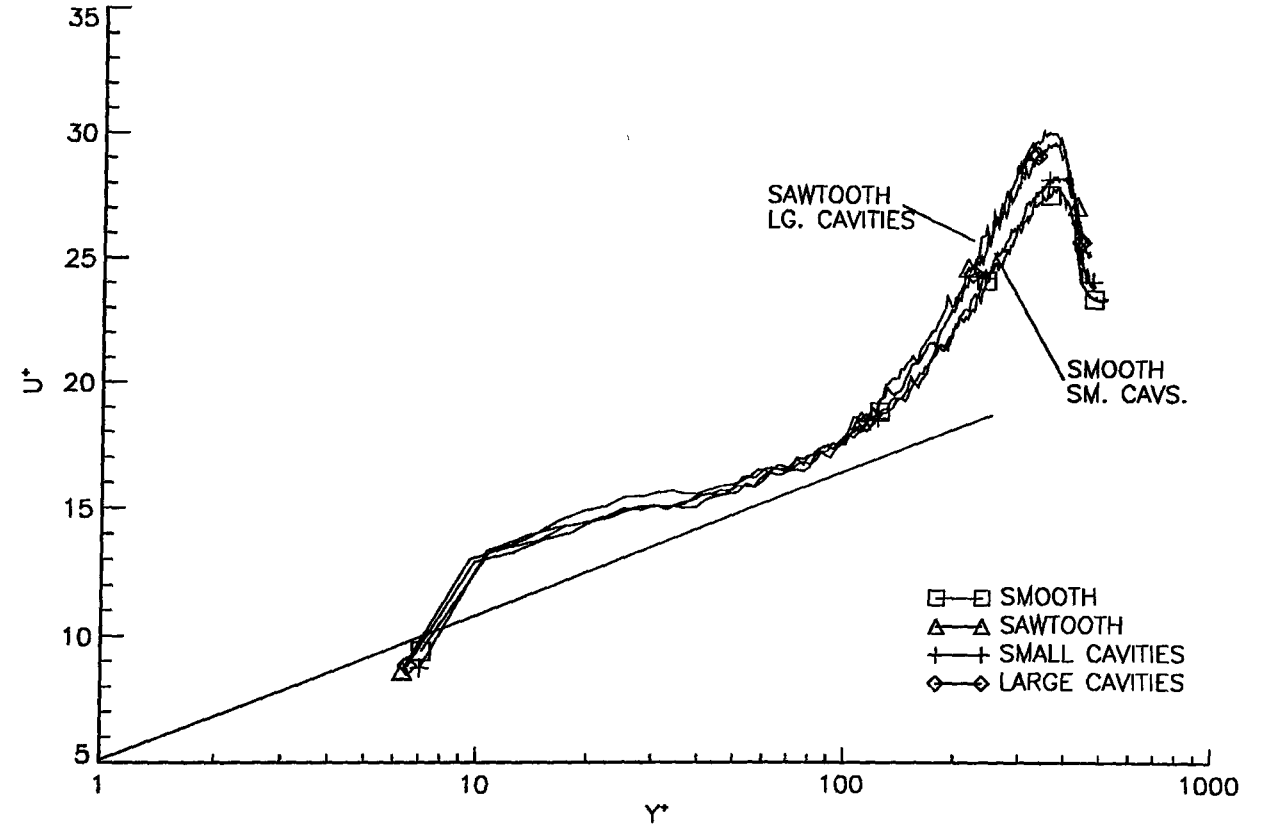

Fig. 4.24 Velocity profiles in log-law coordinates on the 15° flare X=23mm. Skin friction as determined from curve-fit procedure

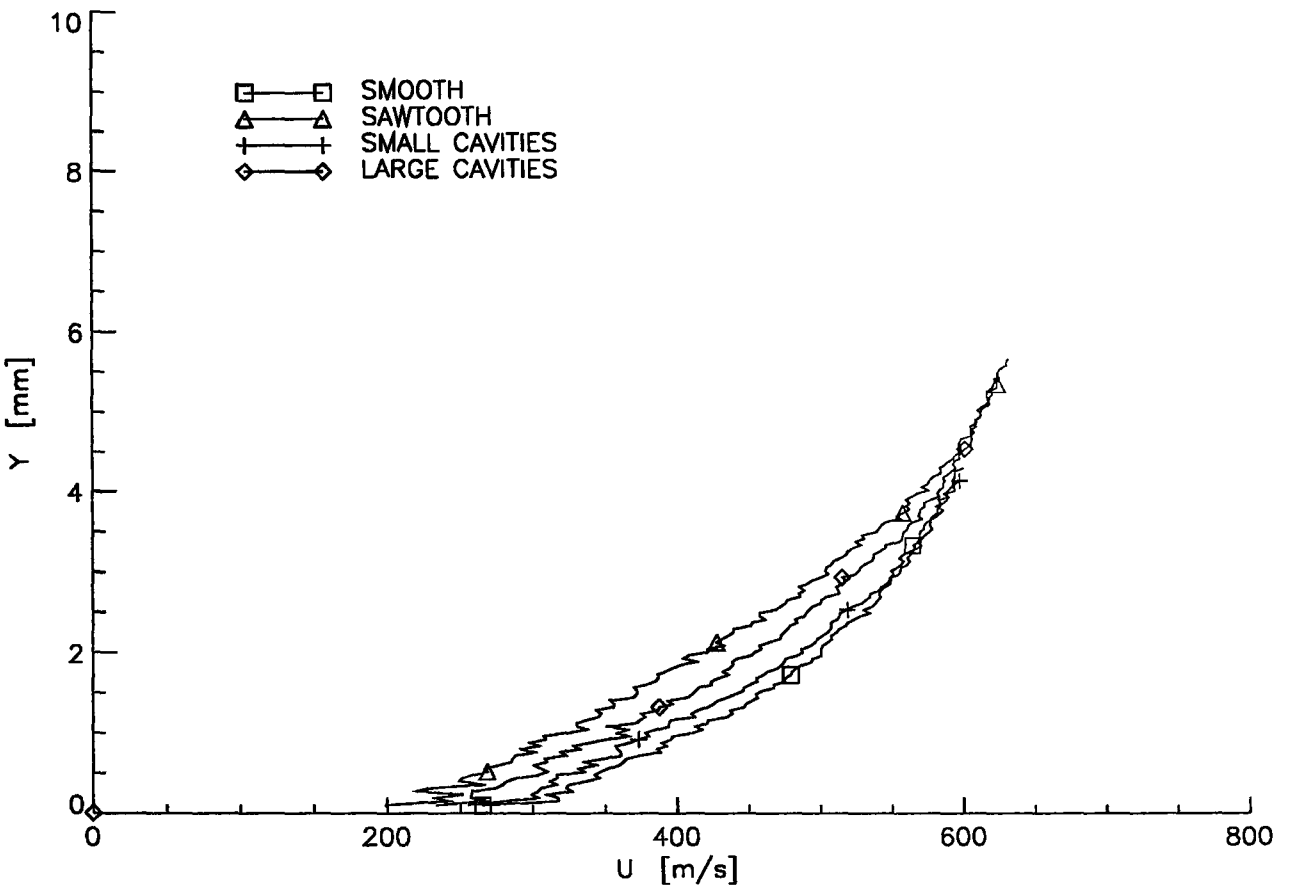

Fig. 4.25 Velocity profiles on 20° flare X=3mm

Fig. 4.26 Velocity profiles on 20° flare X=13mm

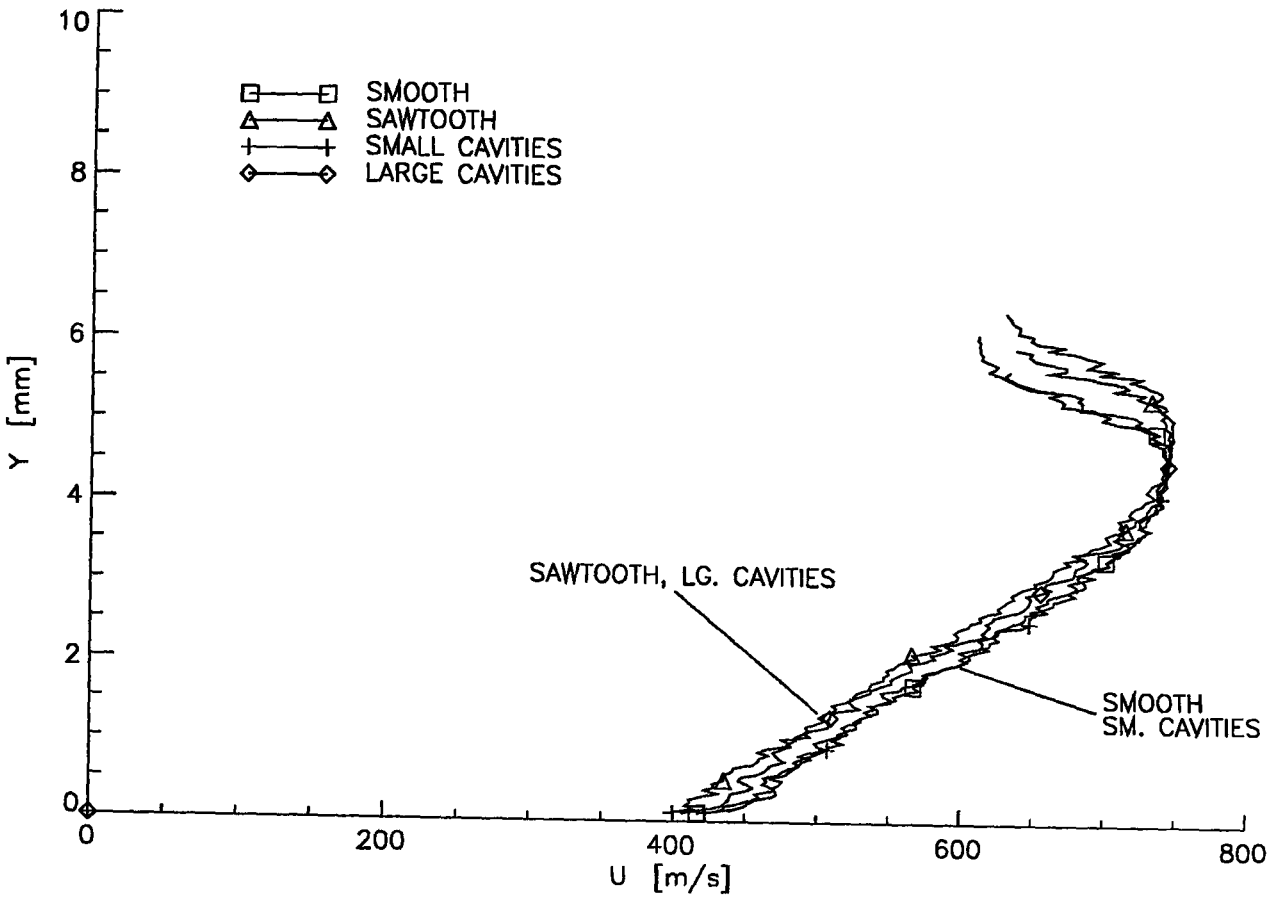

Fig. 4.27 Velocity profiles on 20° flare X=23mm

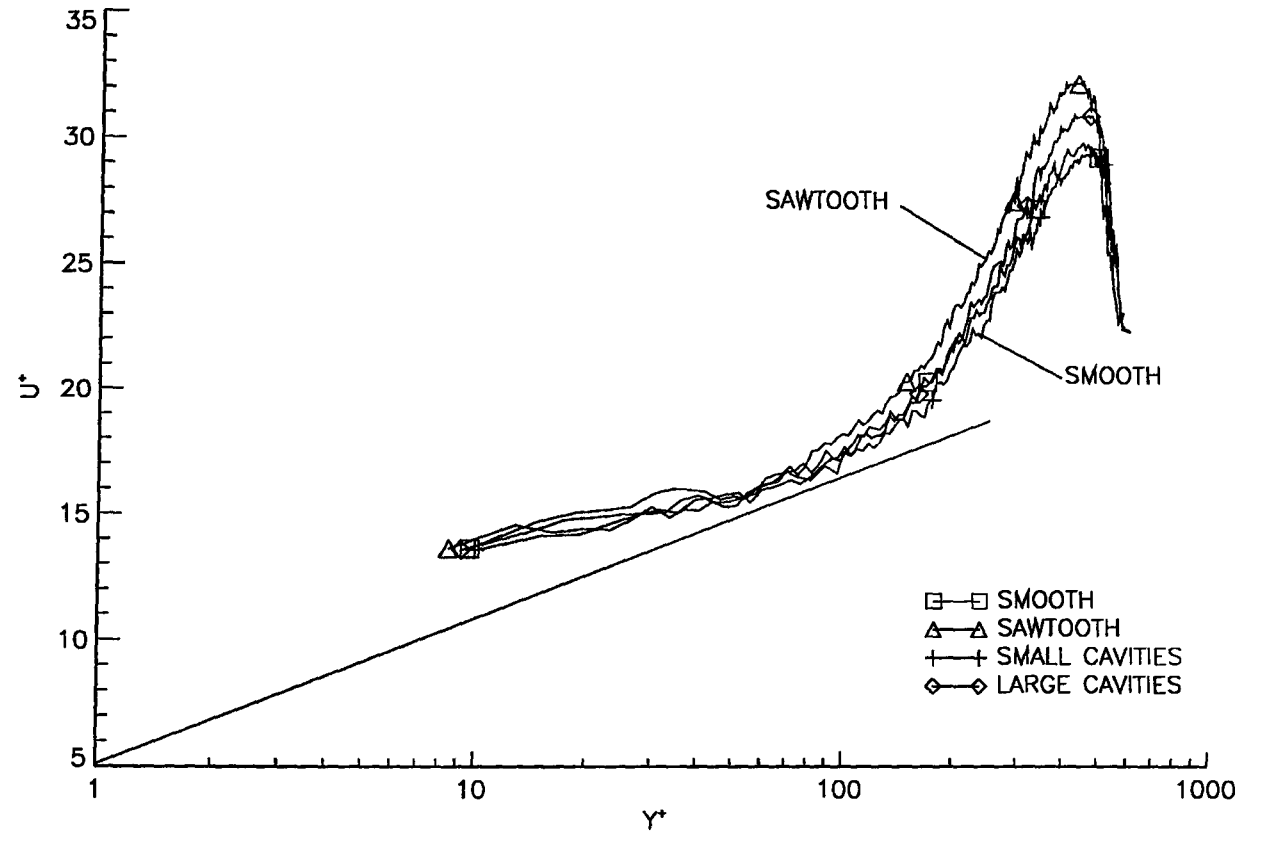

Fig. 4.28 Velocity profiles in log-law coordinates on 20° flare X=23mm. Skin friction as determined from curve-fit procedure

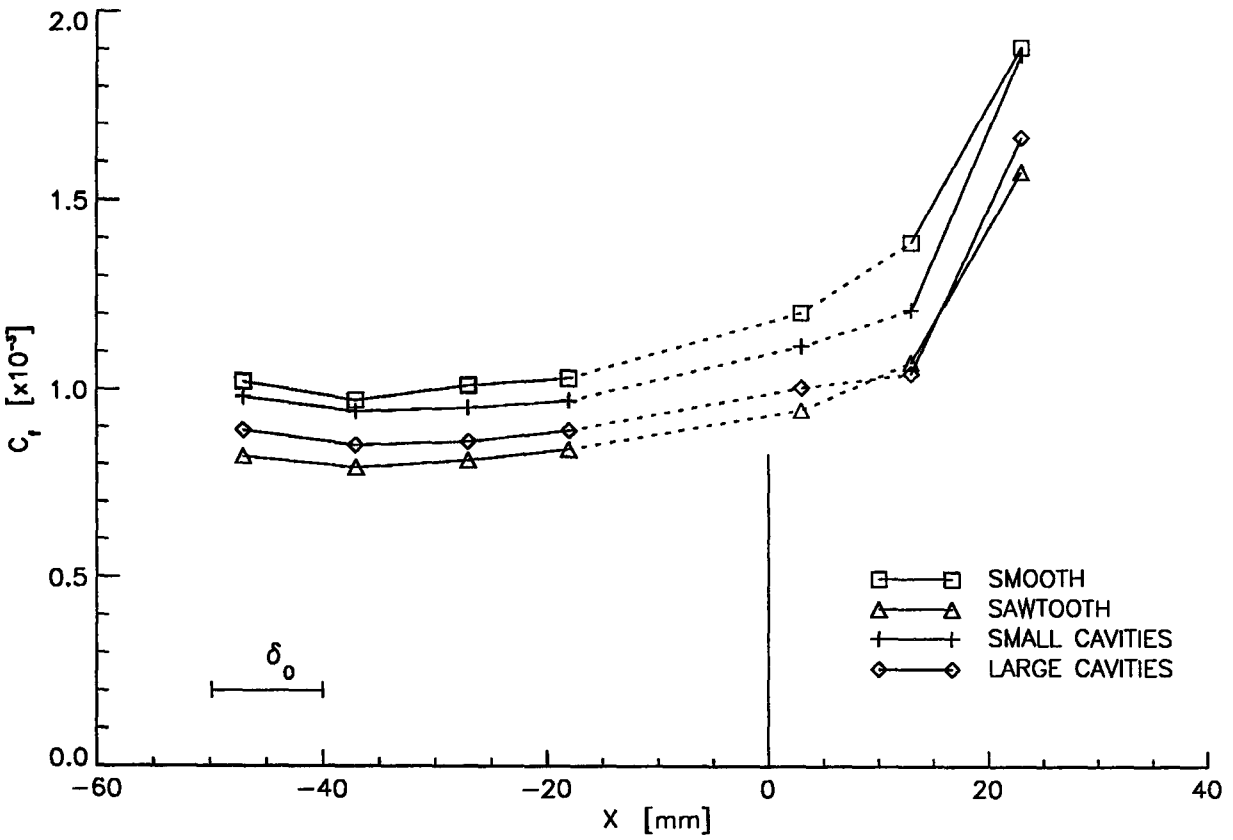

Fig. 4.29 Skin friction as obtained from curve-fit procedure, normalised by freestream conditions, on cylinder and 15° flare.

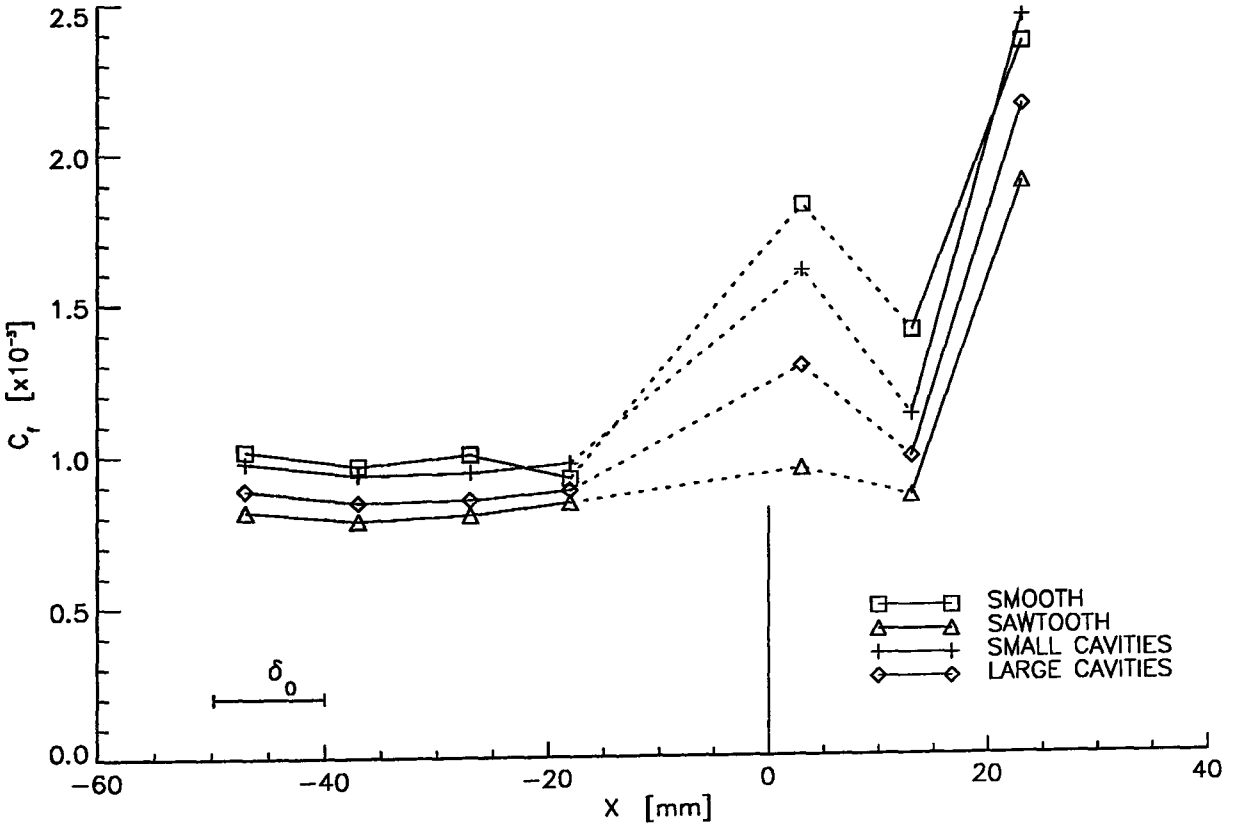

Fig. 4.30 Skin friction as obtained from curve-fit procedure, normalised by smooth wall value, on cylinder and 20° flare.

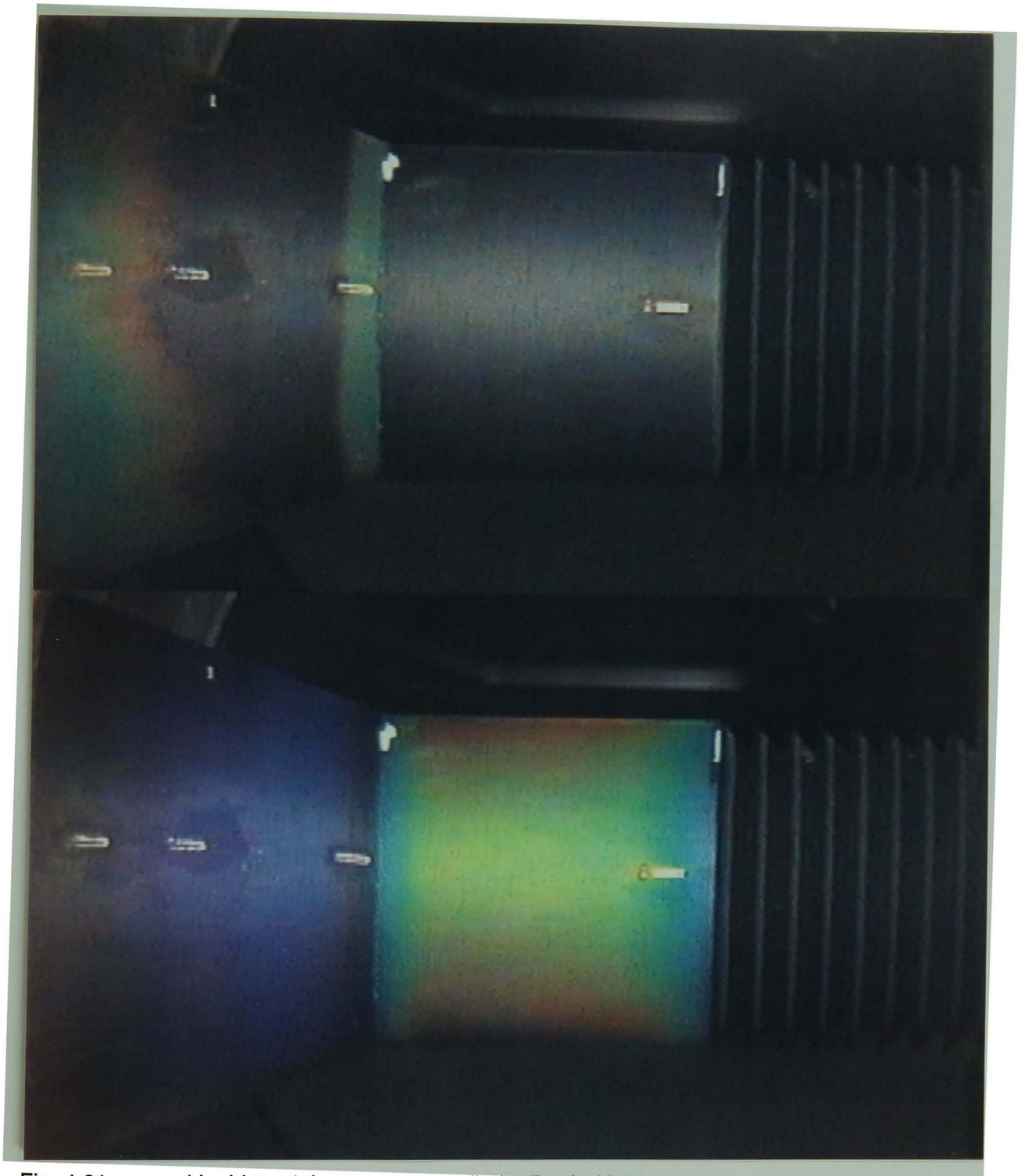

Fig. 4.31 Liquid crystal response on cylinder fitted with sawtooth roughness and 20° flare 1 s (top) and 5.8 s (bottom) after the flow-start

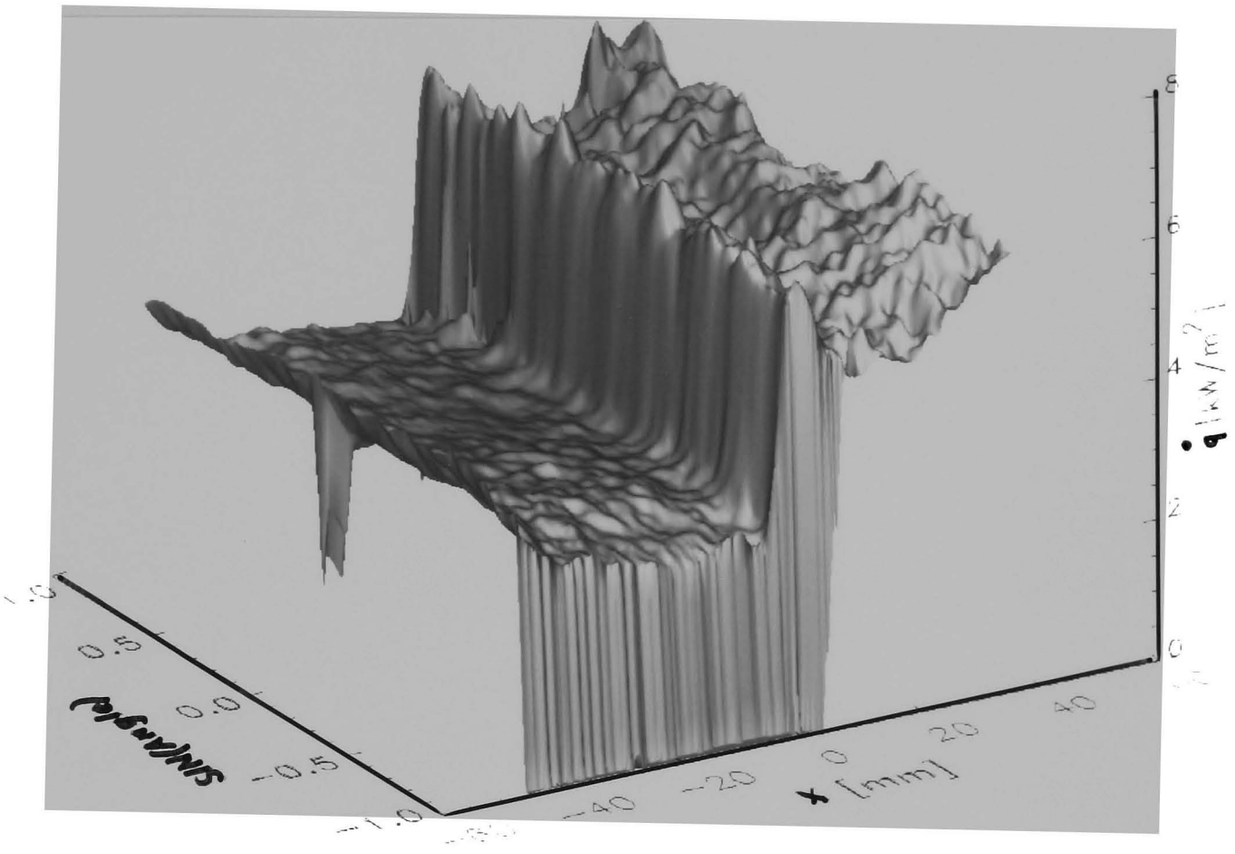

Fig. 4.32 Surface heat transfer on cylinder and 15° flare with sawtooth type roughness. The area shown extends from the end of the roughness elements to the end of the flare.

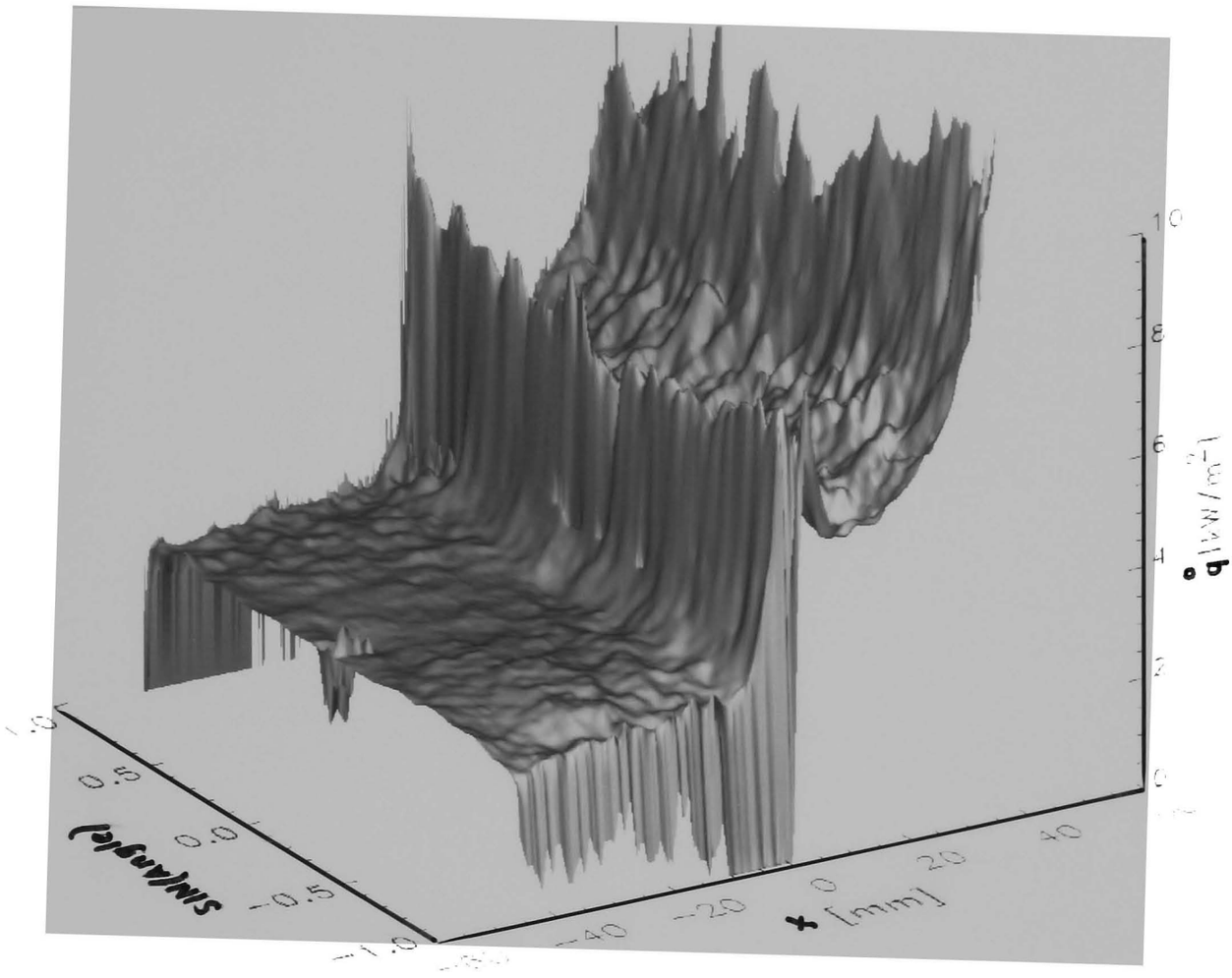

Fig. 4.33 Surface heat transfer on cylinder and 20° flare. Smooth centrebody

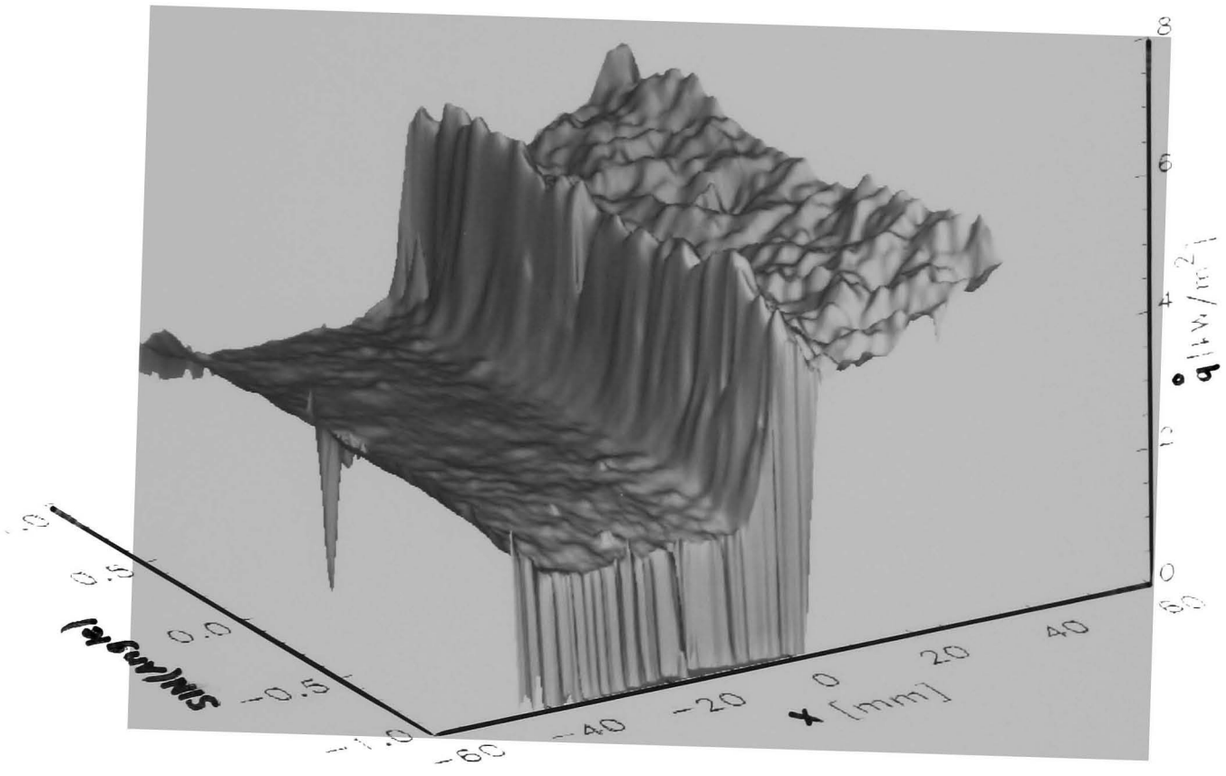

Fig. 4.34 Surface heat transfer on cylinder and 20° flare. Sawtooth roughness

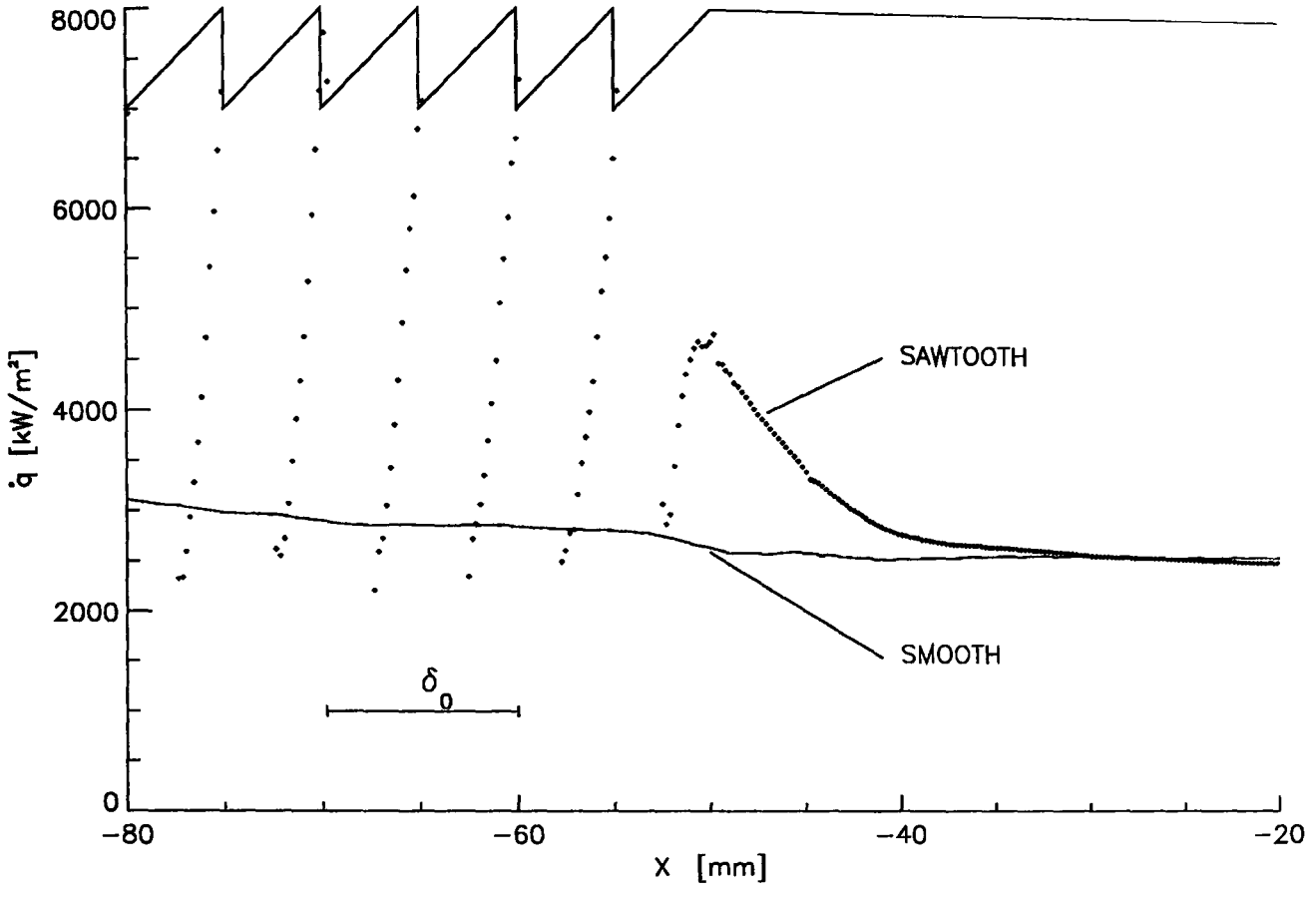

Fig. 4.35 Surface heat transfer for smooth centrebody and sawtooth roughness

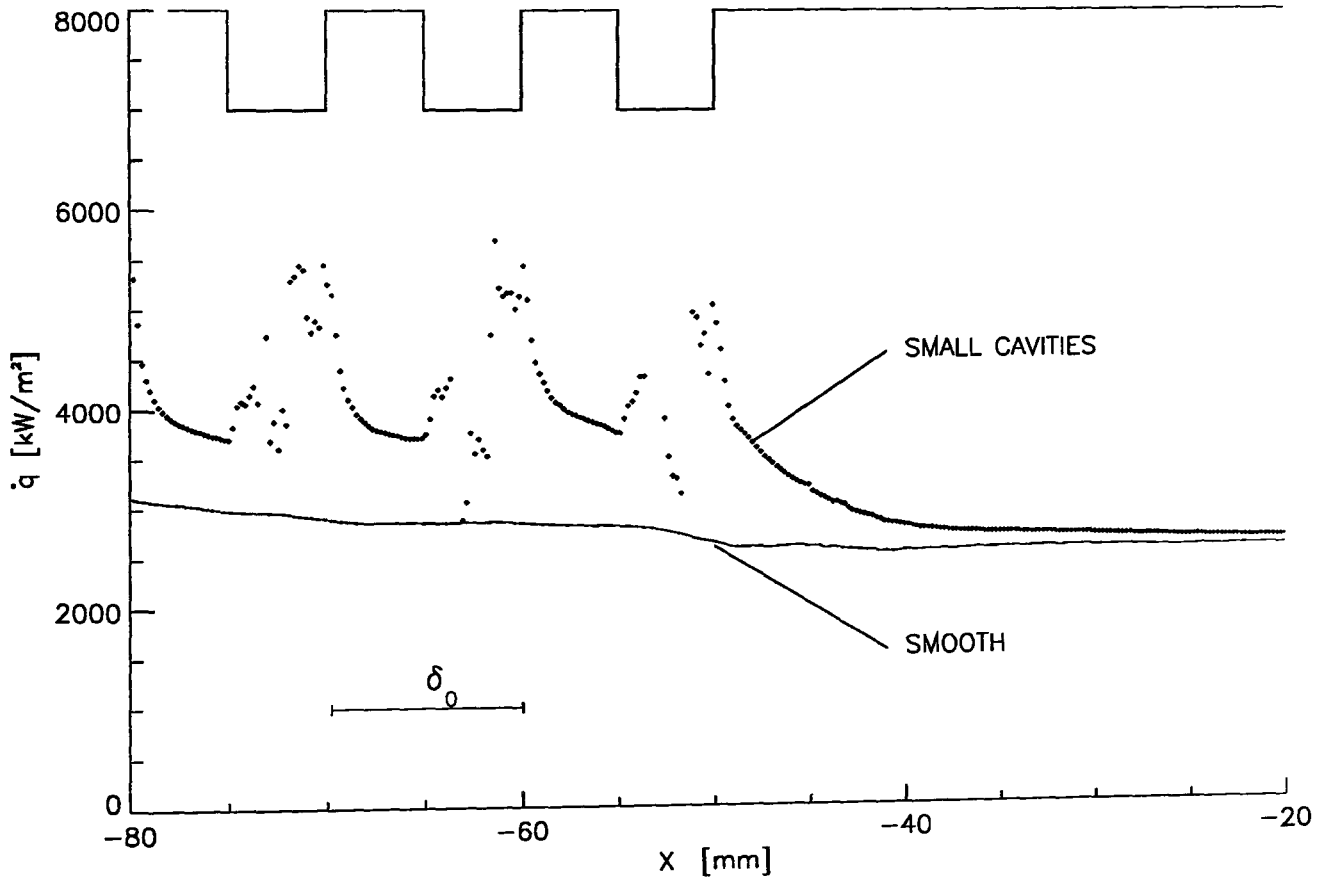

Fig. 4.36 Heat transfer for smooth centrebody and small cavities

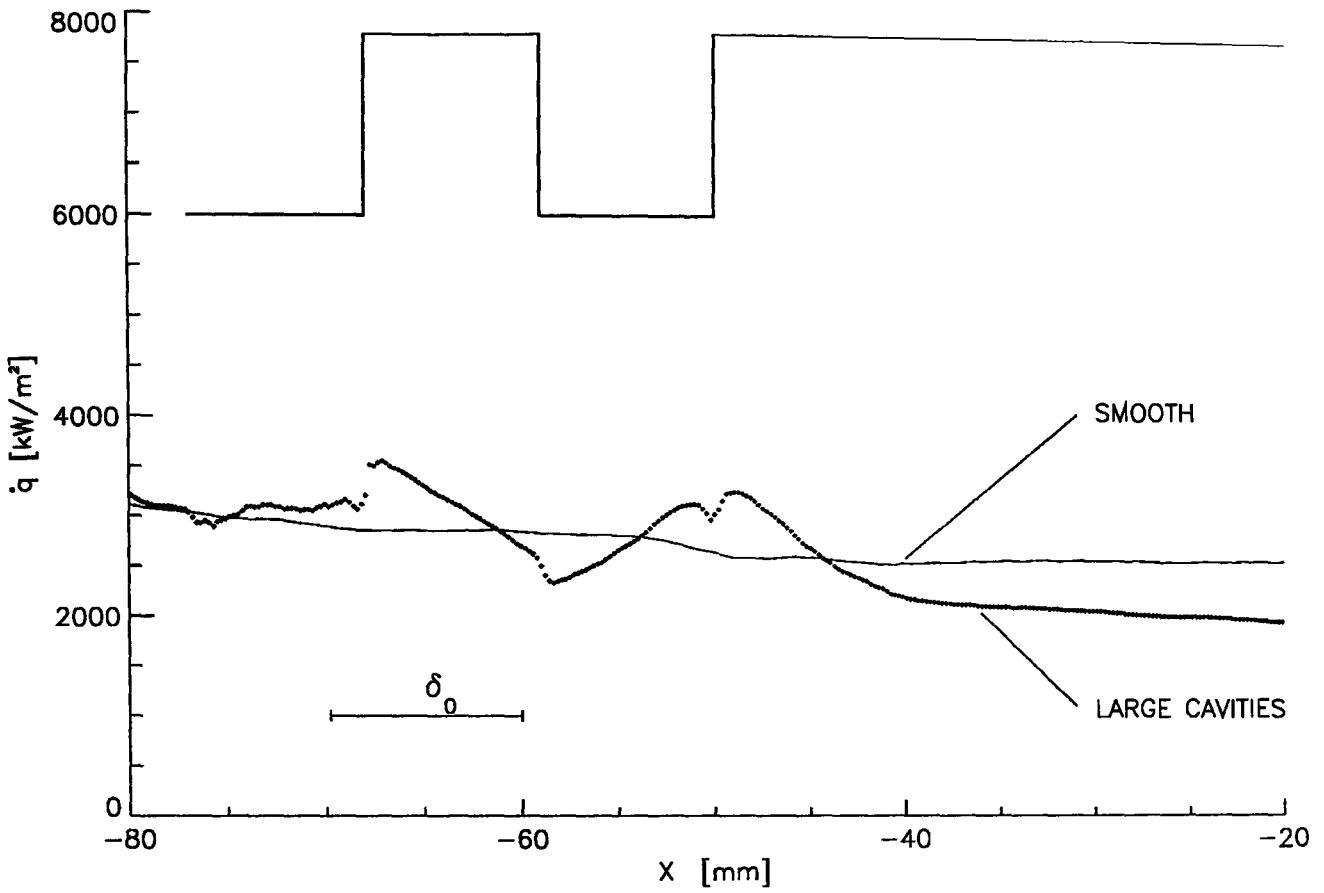

Fig. 4.37 Heat transfer for smooth centrebody and large cavities

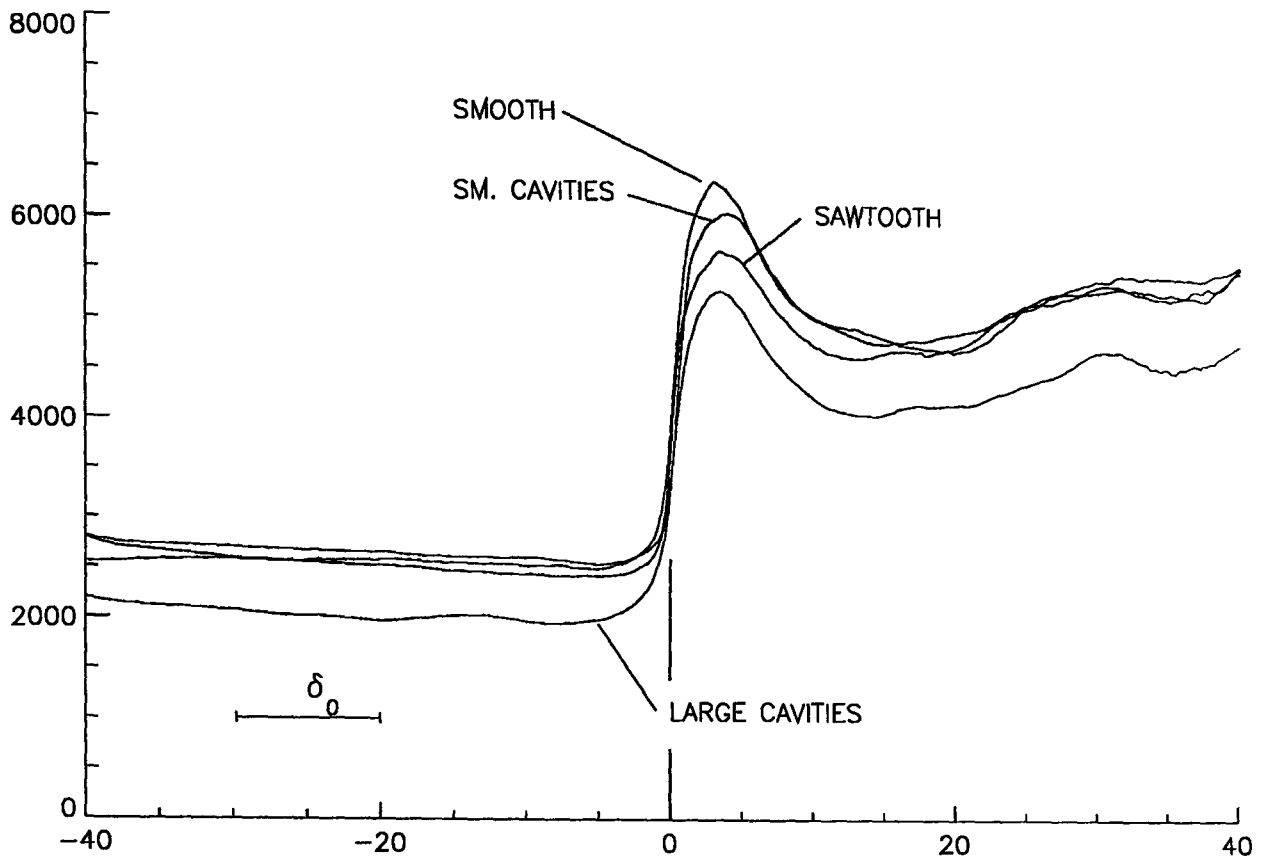

Fig. 4.38 Influence of roughness on heat transfer on cylinder and 15° flare

Fig. 4.39 Influence of roughness on heat transfer on cylinder and 20° flare

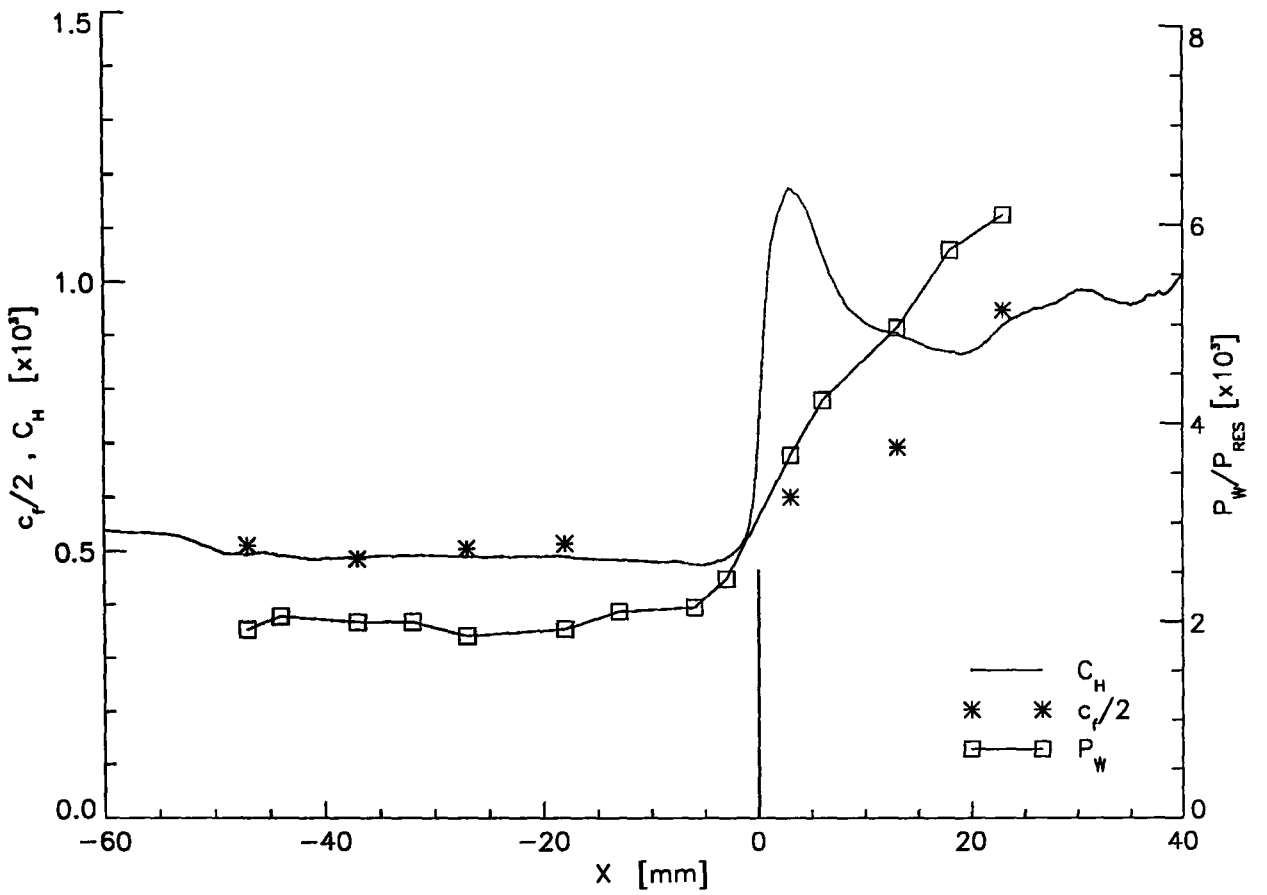

Fig. 4.40 Comparison of heat transfer coefficient, skin friction coefficient and surface pressure distribution for smooth centrebody and 15° flare

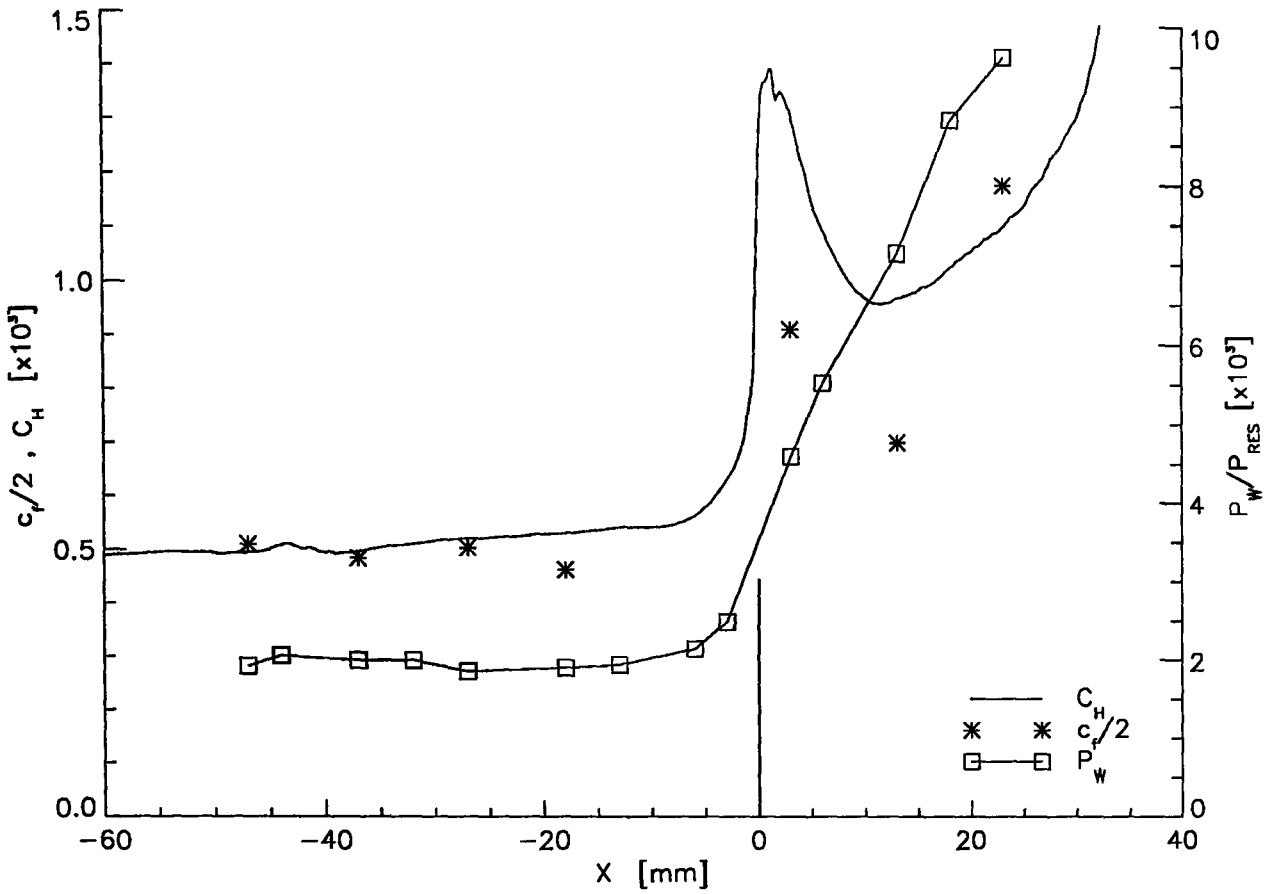

Fig. 4.41 Comparison of heat transfer coefficient, skin friction coefficient and surface pressure distribution for smooth cylinder and 20° flare

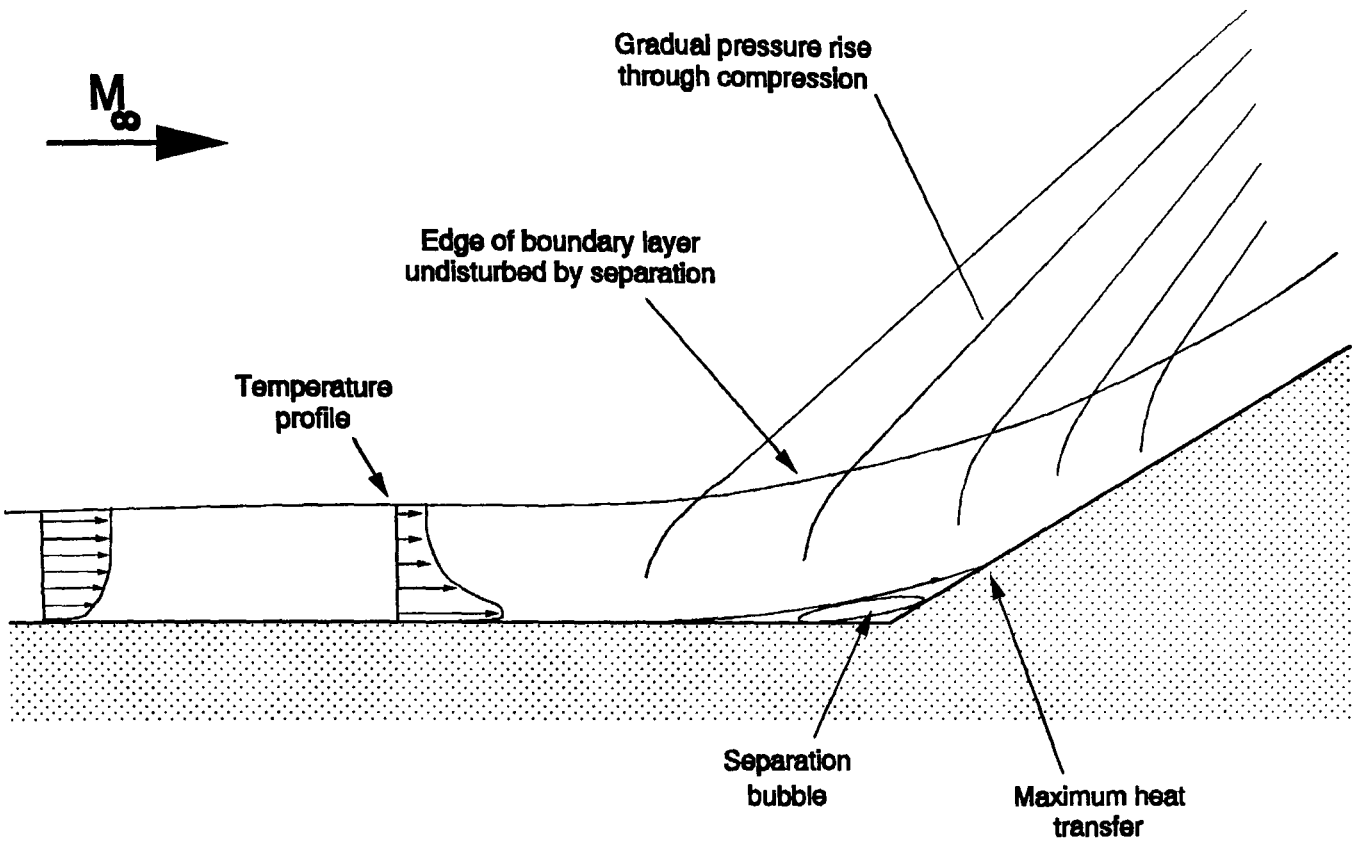

Fig. 4.42 Proposed flow model for turbulent compression corner flow in nominally unseparated interaction

Fig. 4.43 Shear stress sensitive liquid crystal flow visualisation. Flow right to left
Top: 15° flare
Bottom: 20° flare

5. Conclusions

An experimental investigation into the effect of large scale regular two-dimensional roughness onto a turbulent boundary layer has been performed at Mach 5 on axisymmetric models. The roughness was limited to a short length with a subsequent smooth surface. The behaviour of the boundary layer profile modified by the roughness in a compression corner has also been investigated.

The flow conditions in the wind tunnel have been determined to allow a comparison of experimental results obtained in this facility with computer code simulations. It is suggested that a re-design of the Mach 5 centrebody nozzle be considered as some undesirable flow features were found for this configuration.

Liquid crystal thermography has been developed for routine usage in hypersonic short duration facilities. It was found to provide very high resolution surface maps with an accuracy comparable to other methods. The technique allows testing of configurations in relatively little time providing a large amount of useful data and is in this respect superior.

Roughnesses investigated were a sawtooth shaped roughness of an element height of half a boundary layer thickness δ and two square cavity shaped roughnesses with dimensions of 0.5 δ and 1.0 δ. The compression corner was located approximately 5 δ downstream of the roughness end formed by flare angles of 15° and 20°. Measured quantities included heat transfer, surface pressure, and pitot pressure profiles. Velocity profiles and skin friction were derived from the measured quantities

The turbulent boundary layer on the undisturbed, smooth surface was found to be comparable to other results in thickness and skin friction. The heat transfer in the rough area was found to be significantly above the smooth wall values. The highest peaks in heat transfer were measured on the tip of the sawtooth shaped roughness with up to 3 times the smooth wall results. The least increase in heat transfer was caused by the large cavities reaching approximately 1.5 times the undisturbed value.

The roughnesses were found to increase the boundary layer thickness by up to 3% and decrease the amount of fullness of the boundary layer profiles. All boundary layer profiles showed a region of agreement with the log-law. The undisturbed boundary layer had a significant wake component. Roughness was found to reduce the area of validity of the log-law. The largest effect was noted with the sawtooth shaped roughness, whereas the small cavities had only little effect.

Downstream of the roughness all quantities changed towards the smooth wall values. The surface pressures were found to be uninfluenced by the roughnesses. Surface skin friction was found to be up to 20% lower than the comparable smooth wall value. This was found to be due to the reduction of velocities close to the surface and the largest effect was caused by the sawtooth roughness. With increasing distance from the roughness the profiles became fuller and the differences in skin friction decreased. This change was found to take place very slowly and after 8 boundary layer thicknesses discrepancies were still clearly visible. The surface heat transfer downstream of the roughness was found to be significantly increased. Within 1.5 boundary layer thicknesses the levels of heat transfer were back to the undisturbed levels. The downstream areas of influence of the roughnesses were found to be different for surface pressure, heat transfer and skin friction with surface pressure being not influenced at all and skin friction showing the longest reaching influence.

Both flare angles investigated appeared to have attached flow in the compression corner. The surface heat transfer distribution exhibited a sharp peak at approximately 0.2 δ downstream of the hingeline. The surface pressure distribution showed a gradual increase in pressure behind the hingeline without reaching a plateau or the inviscid pressure level. The upstream influence of the interaction was limited to less than 0.5 δ from the hingeline. The boundary layer profiles on the flare showed reduced thickness and a steeper slope near the surface.

The introduction of roughness had only little effect on the flow features at the compression corner. The pressures on the flare were reduced by the roughnesses. In the case of the 15° flare no influence was visible upstream of the corner. The upstream influence was increased for the 20° flare. The peak in the heat transfer distribution was widened and slightly reduced by the roughnesses.

One result is shown comparing the flow over the 20° corner for two roughnesses with a modified inflow. This result was obtained with a faulty settling chamber in the wind tunnel, resulting in an artificially thickened and distorted boundary layer. In this case the roughness caused a previously unseparated flow to show a distinct separated region in the corner.

The boundary layer profiles on the flare confirmed the changes observed further upstream. Roughness caused a thickening of the boundary layers and a reduction in skin friction. These changes were observable all the way through the interaction with only little change in a streamwise direction. There is a possibility that the reduction of skin friction in the sawtooth case was large enough to move part of the overall distribution to negative values, thus causing a small separation.

It is believed that the reduction in peak pressures is caused by the decrease in velocities in the outer edge of the profile and the thickening of the boundary layer due to the roughnesses. The effects of the roughnesses on the profiles were

found to remain visible for a long time. An influence of roughness onto the upstream influence of the interaction was only visible for the higher flare angle. This influence is believed to be caused by the reduction of velocities very close to the surface and can cause a large separation which has been shown in one case. It is believed that the sensitivity of the interaction to changes in the oncoming boundary layer profile is dependent on the closeness of the flow to separation. Even though the loss of velocities close to the surface is visible in the profiles for some time, the relaxation on the smooth surface upstream of the hingeline is sufficient to limit the effect of this on the interaction. This is a different result from other studies which investigated rough compression corner flows and found a significant effect of roughness on interaction length even for flows which were sufficiently far from separation in the smooth wall case.

All changes due to roughness were found to be largest for the sawtooth roughness. The large cavities, being twice the size of the sawtooth, caused a comparable disturbance of the boundary layer whereas the small cavities had only little effect. An exception are the results of the heat transfer measurements in the rough areas where the smaller cavities exhibited significantly greater peak values of $\mathring{q}$ than the cavities of double the size.

Apart from the immediate corner region and the vicinity of the roughnesses Reynolds analogy between skin friction and heat transfer was found to be valid within engineering accuracy.

The significant difference in the shape of heat transfer and surface pressure distribution has been compared to other results. It is proposed that a very small scale separation exists in such a nominally unseparated flow which causes a peak in heat transfer at reattachment without disturbing the surface pressures at the sensor locations. The existence of a separated region has been confirmed by surface flow visualisation. The maximum height of the separation bubble was estimated to be of the order of 3% of a boundary layer thickness.

Future work is suggested to investigate the unsteadiness of the flow in the immediate vicinity of the compression corner and the influence of roughness on typical frequencies. This requires changes in the transducer mountings to reduce the vibrations encountered in this thesis. It is also suggested that some attention be directed to the flow over sawtooth-shaped roughnesses. The flow features in this configuration and the square cavities are still not completely understood. A study could include variations of size and sawtooth angle to investigate the mechanisms behind the flow disturbances caused by these surfaces.

The phenomenon of a small scale separation in a nominally unseparated flowfield requires further research. It may be interesting to investigate flows with different flare angles and find the angle causing the onset of separation. The spatial resolution of surface pressure measurements needs further improvement to allow investigation of this flow feature.

6. References

1. J.D.Anderson, "Hypersonic and High Temperature Gas Dynamics", McGraw-Hill, Inc. ,1989

2. C.C.Lin, "Turbulent Flows and Heat Transfer", Princeton University Press, 1959

3. J.Nikuradse, "Strömungsgesetze in rauhen Rohren", Forsch. Ing.-Wes. H. 361, 1933

4. R.A.Antonia, R.E.Luxton, "Turbulent Boundary Layer over a Change in Roughness", J.F.M. Vol.48, P.4, pp.721-761, 1971

5. R.A.Antonia, D.H.Wood, "Calculation of a Turbulent Boundary Layer Downstream of a Small Change in Surface Roughness", Aeronautical Quarterly, Aug.1975

6. A.J.Grass, R.J.Stuart, M.Mansour-Tehrani, "Three-Dimensional Structure of Dominant Instabilities in Turbulent Flow over Smooth and Rough Boundaries", AIAA 91-0333, 1991

7. A.Sigal, J.E.Danberg, "New Correlation of Roughness Density Effect on the Turbulent Boundary Layer", AIAA Journal, Vol.28, N0.3, 1991

8. K.G.Winter, K.G.Smith, L.Gaudet, "Measurements of Turbulent Skin Friction at High Reynolds Numbers at Mach Numbers of 0.2 and 2.2", RAE TM Aero 884, 1965

9. K.G.Winter, L.Gaudet, "Turbulent Boundary Layer Studies at High Reynolds Numbers at Mach Numbers Between 0.2 and 2.8", RAE R&M No.3712, 1970

10. L.Gaudet, "Integral Boundary Layer Parameter Relationships and a Skin Friction Law Derived From a Velocity Profile Family For Two Dimensional Incompressible Flow", RAE TM Aero 2080, 1986

11. H.H.Fernholz, P.J.Finley, "A Critical Commentary on Mean Flow Data for Two-Dimensional Compressible Turbulent Boundary Layers", AGARDograph No.253, 1980

12. A.Laganelli, N.E.Scaggs, "Equivalent Sandgrain Methodology for Compressible Flows", AIAA 90-1718

13. P.J.Disimile, N.E.Scaggs, " An Investigation into Wedge-Induced Turbulent Boundary Layer Separation on a Uniformly Roughened Surface at Mach

6.0", AIAA 89-2163, 1989

14. P.J.Disimile, N.E.Scaggs, "The Effect of Separation on Turbulent Boundary Layer Characteristics over a Smooth Surface at Mach 6.0", AIAA 90-3028, 1990

15. P.J.Disimile, N.E.Scaggs, "Mach 6 Turbulent Boundary Layer Characteristics on Smooth and Rough Surfaces", AIAA 91-1762, 1991

16. P.J.Disimile, N.E.Scaggs, "Turbulent Boundary Layer Characteristics over a Flat Plate/ Wedge Configuration at Mach 6", AIAA Journal, Vol.30 No.1, 1992

17. M.S.Maurice, G.L.Seibert, "The LV Measured Turbulent Structure of Mach 6 Flow over a Roughened Flat Plate with a Compression Ramp", AIAA 89-2164, 1989

18. K.R.Czarnecki, W.J.Monta, "Boundary Layer Velocity Profiles and Skin Friction due to Surface Roughness on an Ogive Cylinder at Mach Numbers of 1.61 and 2.01", NASA TN D-2048, 1963

19. W.J.Monta, K.R.Czarnecki, "Drag due to Two-Dimensional Surface Roughness in a Turbulent Boundary Layer at Mach 3 with and without Heat Transfer", NASA TN D-4746, 1968

20. G.H.Christoph, A.W.Fiore, "Numerical Simulation of Flow over Rough Surfaces Including Effects of Shock Waves", ARL TR 75-0028, Feb. 1975

21. M.S.Holden, "Studies of Surface Roughness Effects in Hypersonic Flow", Final Report No. 7018-A-2, AFOSR, 1983

22. M.S.Holden, "Studies of Boundary Layer Transition and Surface Roughness Effects in Hypersonic Flow", ARVIN-CALSPAN Rep. 6430-A-5, 1983

23. M.S.Holden, "Studies of the Structure of Attached and Separated Regions of Viscous/Inviscid Interaction and the Effects of Combined Surface Roughness and Blowing in High Reynolds Number Hypersonic Flows", CUBRC Rep. No. 88682, 1988

24. X.Zhang, J.A.Edwards, "Experimental Investigation of Supersonic Flow over Two Cavities in Tandem", AIAA Journal, Vol.30, May 1992, pp.1182-1190

25. D.E.Berg, "Surface Roughness Effects on the Hypersonic Turbulent Boundary Layer", PhD Thesis, CALTECH, 1977

26. J.A.Edwards, X.Zhang, "Some Aspects of Supersonic Flow over a Cavity Cascade", AIAA 86-2025, 1986

27. R.I.P. Viosinet, "Combined Influence of Roughness and Mass Transfer on Turbulent Skin Friction at Mach 2.9", AIAA 79-0003, 1979

28. S.Holmes, L.C.Squire, "A Numerical Study of Supersonic Flow Over a Compression Corner with Different Incoming Boundary-Layer Profiles", AIAA 90-1453, 1990

29. M.S.Selig, A.J.Smits, "Effect of Periodic Blowing on Attached and Separated Supersonic Turbulent Boundary Layers", AIAA Journal Vol.29, No.10, pp.1651-1658, 1991

30. M.S.Holden, "Studies of the Mean and Unsteady Structure of Turbulent Boundary Layer Separation in Hypersonic Flow", AIAA 91-1778, 1991

31. J.L.Stollery, "Some Aspects of Shock-Wave Boundary Layer Interaction Relevant to Intake Flow", AGARD CP 479

32. G.T.Coleman, J.L.Stollery, "A Correlation Between Pressure and Heat Transfer Distribution at Supersonic and Hypersonic Speeds", Aeronautical Quarterly Vol.26, 1975

33. D.H.Rudy, J.L.Thomas, A.Kumar, P.A.Gnoffo, S.R.Chakravarthy, "Computation of Laminar Hypersonic Compression Corner Flows", AIAA Journal, Vol.29, No.7, pp.1108-1113

34. J.H.Preston, "The Determination of Turbulent Skin Friction by Means of Pitot Tubes", J. Roy. Aer. Soc. 58, pp.109-121, 1954

35. A.Sigalla, "Calibration of Preston Tubes in Supersonic Flow", AIAA Journal TN, Aug. 1965, p. 1531

36. D.S.Dolling, "Problems in the Validation of CFD Codes through Comparison with Experiment", AGARD CP 514-36, 1992

37. J.L.Stollery, D.J.Maull, B.J.Belcher, "The Imperial College Hypersonic Gun Tunnel", J. R. Aer. Soc. vol 64, 1964

38. C.V.Hurdle, "Calibration of the R.A.R.D.E. High Supersonic Intermittent Wind Tunnel", R.A.R.D.E. Memorandum 29/68, 1968

39. A.Pope, K.L.Goin, "High Speed Wind Tunnel Testing", J.Wiley & Sons, 1965

40. E.M.Winkler, "Design and Calibration of Stagnation Temperature Probes for Use at High Supersonic Speeds and Elevated Temperatures", J. Applied Physics, Vol.25, No.2, 1954

41. --, © Paul Beckman Company, Elkins Park PA, USA

42. W.J.Duncan, A.S.Thom, A.D.Young, "Mechanics of Fluids", 2nd ed., Arnold, 1970

43. H.U.Meier, J.C.Rotta, "Temperature Distributions in Supersonic Turbulent Boundary Layers", AIAA Journal Vol.9, No.11, pp. 2149-2156, 1971

44. H.U.Meier, R.L.Voisinet, D.F.Gates, "Temperature Distributions Using the Law of the Wall for Compressible Flow with Variable Turbulent Prandtl Numbers", AIAA 74-596, 1974

45. E.R.van Driest, "Turbulent Boundary Layer in Compressible Fluids", Journal of Aeronautical Sciences 18, 145-160, 1951

46. D.C.Mathews, M.E.Childs, G.C.Paynter, "Use of Coles' Universal Wake Function for Compressible Turbulent Boundary Layers", J.Aircraft Vol.7 No.2, 137-140, 1970

47. F.O.Thomas, C.M.Putnam, H.C.Chu, "Measurement of the Nonlinear Spectral Dynamics Characterizing a Shock Wave/Turbulent Boundary Layer Interaction", AIAA 91-0653, 1991

48. B.T.Gibson, D.S.Dolling, "Exploratory Study of Wall Pressure Fluctuations in a Mach 5, Sharp Fin-Induced Turbulent Interaction", AIAA Journal Vol.30, No.9, 2188-2195, 1992

49. D.Coles, "The Law of the Wake in the Turbulent Boundary Layer", JFM, Vol.1, Pt.2, 191-226, 1956

50. H.U.Meier, "Measuring Techniques for Compressible Turbulent Boundary Layers", DLR-FB 77-49, 1977

51. W.Gracey, "Wind-Tunnel Investigation of a Number of Total-Pressure Tubes at High Angles of Attack, Subsonic, Transonic and Supersonic Speeds", NACA-Report 1303, 1957

52. D.G.Mabey, H.U.Meier, W.G.Sawyer, "Some Boundary Layer Measurements on a Flat Plate at Mach Numbers from 2.5 to 4.5", AGARD-CP-93, pp 2-1 to 2-11, 1972

53. J.J.Korte, "A CFD-Based Aerodynamic Design Procedure for Hypersonic Wind-Tunnel Nozzles", AGARD CP 514-36, 1992

54. P.A.Jacobs, R.J.Stalker, "Mach 4 and Mach 8 Axisymmetric Nozzles for a High-Enthalpy Shock Tunnel", Aeronautical Journal, Nov.1991, pp.324-334

55. I.E.Beckwith, W.D.Harvey, F.L.Clark, "Comparison of Turbulent Boundary Layer Measurements at a Mach number of 19.5 with Theory and Assessment of Probe Errors", NASA TN D 6192

56. D.L.Schultz, T.V.Jones, "Heat-Transfer Measurements in Short-Duration Hypersonic Facilities", AGARDograph No. 165, 1973

57. W.J.Cook, E.J.Felderman, "Reduction of Data from Thin Film Heat Transfer Gauges: A Concise Numerical Technique", AIAA Journal, Vol.4, No.3, pp561-562, March 1966

58. G.Simenoides, "The VKI Hypersonic Wind Tunnels and Associated Measurement Techniques", VKI-TM 46, 1990

59. "Measure Surface Temperature with a Response Time as little as 1 Microsecond", Medtherm Corp., Huntsville, Alabama, USA, Bulletin 500, 5-82, 1982

60. Ray Stalker, University of Queensland, Private Communication

61. Rapid Response Thermocouple (Type K), stock no. 256-130, RS Components Ltd, PO Box 99, Corby Northants NN17 9RS, 1993

62. P.A.Denman, J.K.Harvey, R.Hillier, "Experimental Study of Attached Boundary Layer and Turbulent Base Flow", 2nd INRIA Workshop on Hyp. Flows for Re-Entry Problems, Antibes, 1991

63. G.M.Carlomagno, L.deLuca, T.Alziary de Roquefort, "Heat Transfer Measurements with an Infrared Camera in Hypersonic Flow", Computers and Experiments in Fluid Flow, Comp. Mech., Springer Verlag, pp. 467-476, 1989

64. M.F.Westby, "Heat Transfer Rates on a Blunted Cone in Rarefied Hypersonic Flow Using Infra-Red Thermography", RAE TM Aero 2186, 1990

65. H.L.Boerrigter, "An Introduction to the Use of Infrared Thermography in the H3 Wind Tunnel", VKI IN 90, June 1991

66. E.J.Klein, "Liquid Crystals in Aerodynamic Testing", Aeronautics a. Astronautics, July 1968, pp. 70-73

67. "Literature review: The Use of Thermochromic Liquid Crystals in Heat Transfer and Flow Visualisation Research", Hallcrest product and application information, Hallcrest Liquid Crystal Technology Ltd, Poole, England

68. T.V.Jones, S.A.Hippensteele, "High Resolution Heat Transfer Coefficient Maps Applicable to Compound Surfaces using Liquid Crystals in a Transient Wind Tunnel", ASME Heat transfer division, Vol.71, 1987

69. Z.U.Haq, G.T.Roberts, R.A.East, "Interference Heating near Fin-Body Junctions on Hypersonic Vehicles", 1st Europ. Symposium on Hypersonic Flow, ESTEC, 1991

70. N.Akino, T.Kunugi, K.Ichimiya, K. Mitsushiro, M.Ueda, "Improved Liquid-Crystal Thermometry Excluding Human Color Sensation", J. o.Heat Transfer, Transactions o. t. ASME, Vol.111, May 1989

71. K.Ichimiya, N.Akino, T.Kunugi, "A Fundamental Study of the Heat Transfer and Flow Situation Around Spacers (a single row of several cylindrical rods in cross flow)", Int. J. Heat Mass Transfer, Vol.33, No.11, pp. 2451-2462, 1990

72. C.Camci, K.Kim, S.A.Hippensteele, "A New Hue Capturing Technique for the Quantitative Interpretation of Liquid Crystal Images used in Convective Heat Transfer Studies",ASME Int. Gas Turbine and Aeroengine Congress, Orlando, 1991

73. N.Toy, E.Savory, "Quantitative Assessment of Surface Temperatures using Liquid Crystals and Digital Imaging", IMECHE Conf. on Optical Methods and Data Processing in Heat and Fluid Flow, City University London, April 1992

74. K.H.Platzer, C.Hirsch, D.F.Metzger, S.Wittig, "Computer based areal surface temperature and local heat transfer measurements with thermochromic liquid crystals (TLC)", Exp. in Fluids 13, 26-32, 1992

75. H.Babinsky, J.A.Edwards, "Quantitative Heat Transfer Measurement using Liquid Crystal Thermography in an Hypersonic Gun Tunnel", IUTAM Symposium on Aerothermochemistry of Spacecraft and Associated Hypersonic Flow, Marseille, September 1992

76. A.J.D. Smith, D.R.J. Baxter, "Liquid Crystal Thermography for Aerodynamic Heating Measurements in Short Duration Hypersonic Facilities", ICIASF '89 Record, 1989

77. H.Babinsky, J.A.Edwards, "The Application and Analysis of Liquid Crystal Thermographs in Short Duration Hypersonic Flow", AIAA 93-0182, 1993

78. G.Maise, M.J.Rossi, "Lateral Conduction Effects on Heat-Transfer Data obtained with the Phase-Change Paint Technique", NASA CR-2435, 1974

79. G.M.Carlomagno, "Characterisation of Hypersonic Flows in a Wind Tunnel", IUTAM Symp. on Aerothermochemistry of Spacecraft and Associated Hypersonic Flows, Marseille, Sept. 1992

80. P.T.Ireland, T.V.Jones, "The Response Time of a Surface Thermometer Employing Encapsulated Thermochromic Liquid Crystals", J. Phys. E. Sci. Instrum. 20, pp. 1195-1199, 1987

81. H.Fernholz, "Eine Berechnungsmethode für kompressible turbulente Grenzschichten mit Druckgradient Null an adiabaten oder isothermen Wänden", DLR FB 69-06, 1969

82. --, Merck BDH Limited, Poole

83. F.M.White, "Viscous Fluid Flow", McGraw-Hill, 2nd Ed., 1991

84. W.L.Hankey, M.S.Holden, "Two-dimensional Shock Wave Boundary Layer Interactions in High Speed Flows", AGARDograph 203

85. G.T.Coleman, J.L.Stollery, "Heat Transfer in Hypersonic Turbulent Separated Flow", Imperial College Aero Rep. 72-05, 1972
also in J.F.M. Vol.53, P.4, 1972

86. J.A.Edwards, Private communication

87. Hallcrest LCT Ltd., Stepnell Reach, 541 Blandford Rd., Poole, BH16 5BW

7. Tables

Table 1: Results of boundary-layer traverses

X : Position as measured from hinge-line. Negative numbers are upstream
Surf. : Roughness type.
SM = smooth
ST = sawtooth
SC = small cavities
LC = large cavities
Flare : Flare angle
M_e : Edge mach number as used for curve-fitting to theoretical profile
p_0 : Total pressure, measured in settling chamber
p_w : Wall pressure at profile location
u_e : Edge velocity as obtained from curve-fitting
δ : Boundary layer thickness, as obtained from curve-fitting
δ_1 : Displacement thickness
c_f : Local skin friction coefficients, as obtained from curve-fitting

X [mm]	Surf.	Flare	M_e	p_0 [x10^3] [N/m^2]	p_w/p_0 [x10^3]	u_e [m/s^2]	δ [mm]	δ_1 [mm]	c_f [x10^3]
-50	SM	0	4.98	707.6	1.89	815.9	9.83	4.37	0.88
-50	ST	0	4.90	704.0	1.88	819.1	9.27	4.51	0.70
-50	SC	0	5.00	708.0	1.92	813.9	9.46	4.53	0.81
-50	LC	0	4.95	706.3	1.93	813.8	9.72	4.73	0.73
-47	ST	0	4.89	701.0	1.88	820.5	9.88	4.59	0.73
-47	SC	0	4.98	703.5	1.92	814.2	9.67	4.46	0.83
-47	LC	0	4.98	696.5	1.93	814.6	10.03	4.77	0.75
-37	SM	0	4.96	705.3	1.96	814.9	9.86	4.59	0.81
-37	ST	0	4.97	705.6	1.99	816.6	10.17	5.09	0.65
-37	SC	0	4.98	692.2	2.01	812.9	9.82	4.75	0.76
-37	LC	0	4.97	706.7	1.94	816.2	10.07	4.92	0.71
-27	SM	0	4.97	704.1	1.82	821.8	10.17	4.34	0.92
-27	ST	0	4.93	700.4	1.83	821.5	10.40	4.79	0.79
-27	SC	0	5.02	704.3	1.84	820.5	10.22	4.54	0.83
-27	LC	0	5.02	706.7	1.83	819.3	10.30	4.84	0.75

X [mm]	Surf.	Flare	M_e	p_0 [$x10^3$] [N/m^2]	p_w/p_0 [$x10^3$]	u_e [m/s^2]	δ [mm]	δ_1 [mm]	c_f [$x10^3$]
-27	SM	15	4.98	708.0	1.82	822.2	10.61	4.35	0.87
-27	ST	15	4.91	707.3	1.83	822.6	10.42	4.84	0.74
-27	SC	15	4.96	709.0	1.84	821.6	10.35	4.45	0.85
-27	LC	15	5.02	708.3	1.82	819.9	10.34	4.81	0.76
-27	SM	20	4.97	707.7	1.82	821.5	10.40	4.36	0.89
-27	ST	20	4.90	705.1	1.84	823.2	10.44	4.83	0.74
-27	SC	20	4.96	705.0	1.83	822.2	10.42	4.47	0.84
-27	LC	20	5.03	707.8	1.82	821.2	10.50	4.84	0.78
-18	SM	15	4.96	705.4	1.89	819.6	10.60	4.57	0.89
-18	ST	15	4.90	693.4	1.84	816.1	10.40	4.92	0.77
-18	SC	15	4.98	705.2	1.87	817.8	10.20	4.67	0.84
-18	LC	15	4.94	704.1	1.84	818.9	10.50	4.83	0.80
-18	SM	20	4.96	693.7	1.87	815.3	9.60	4.57	0.81
-18	ST	20	4.90	689.9	1.88	817.1	10.70	4.97	0.76
-18	SC	20	4.96	702.7	1.84	821.4	10.50	4.57	0.87
-18	LC	20	4.96	706.5	1.83	818.8	10.50	4.85	0.79
3	SM	15	5.34	708.1	3.64	713.9	11.40	7.95	0.47
3	ST	15	5.31	707.1	3.50	722.0	11.40	8.10	0.39
3	SC	15	5.22	708.9	3.52	722.7	11.30	7.77	0.47
3	LC	15	5.30	706.8	3.40	727.4	11.30	7.91	0.43
3	SM	20	4.90	691.8	4.55	600.8	4.37	3.18	0.68
3	ST	20	4.91	692.3	4.38	633.0	5.74	4.29	0.37
3	SC	20	4.93	699.7	4.49	597.4	4.18	3.08	0.60
3	LC	20	4.92	695.1	4.48	624.7	5.48	4.04	0.48
13	SM	15	4.00	707.1	4.93	718.0	7.94	3.53	0.72
13	ST	15	4.00	707.4	4.68	723.0	8.10	3.86	0.58

X [mm]	Surf.	Flare	M_e	p_0 [x10^3] [N/m^2]	p_w/p_0 [x10^3]	u_e [m/s^2]	δ [mm]	δ_1 [mm]	c_f [x10^3]
13	SC	15	4.00	706.1	4.83	721.0	8.12	3.76	0.64
13	LC	15	4.00	705.3	4.70	722.2	8.12	3.91	0.56
13	SM	20	4.00	695.5	7.10	658.7	6.96	3.50	0.50
13	ST	20	4.00	700.4	6.65	670.3	7.90	4.06	0.33
13	SC	20	4.00	694.1	7.01	663.1	7.91	3.94	0.41
13	LC	20	4.00	695.8	6.83	666.7	7.78	3.94	0.37
23	SM	15	4.00	703.4	6.07	686.9	7.20	2.55	0.80
23	ST	15	4.00	708.2	5.78	694.0	7.18	2.70	0.69
23	SC	15	4.00	710.5	6.02	690.0	6.73	2.40	0.79
23	LC	15	4.00	709.7	5.87	693.0	7.00	2.61	0.72
23	SM	20	3.68	697.3	9,57	608.9	6.20	1.96	0.74
23	ST	20	3.73	711.0	3.73	626.8	6.47	2.20	0.62
23	SC	20	3.70	710.5	3.70	622.4	5.74	1.83	0.78
23	LC	20	3.73	710.7	3.73	629.9	6.02	2.02	0.69

Appendix

Fig A.1 - A.14: Pitot pressure profiles for all traverse locations.

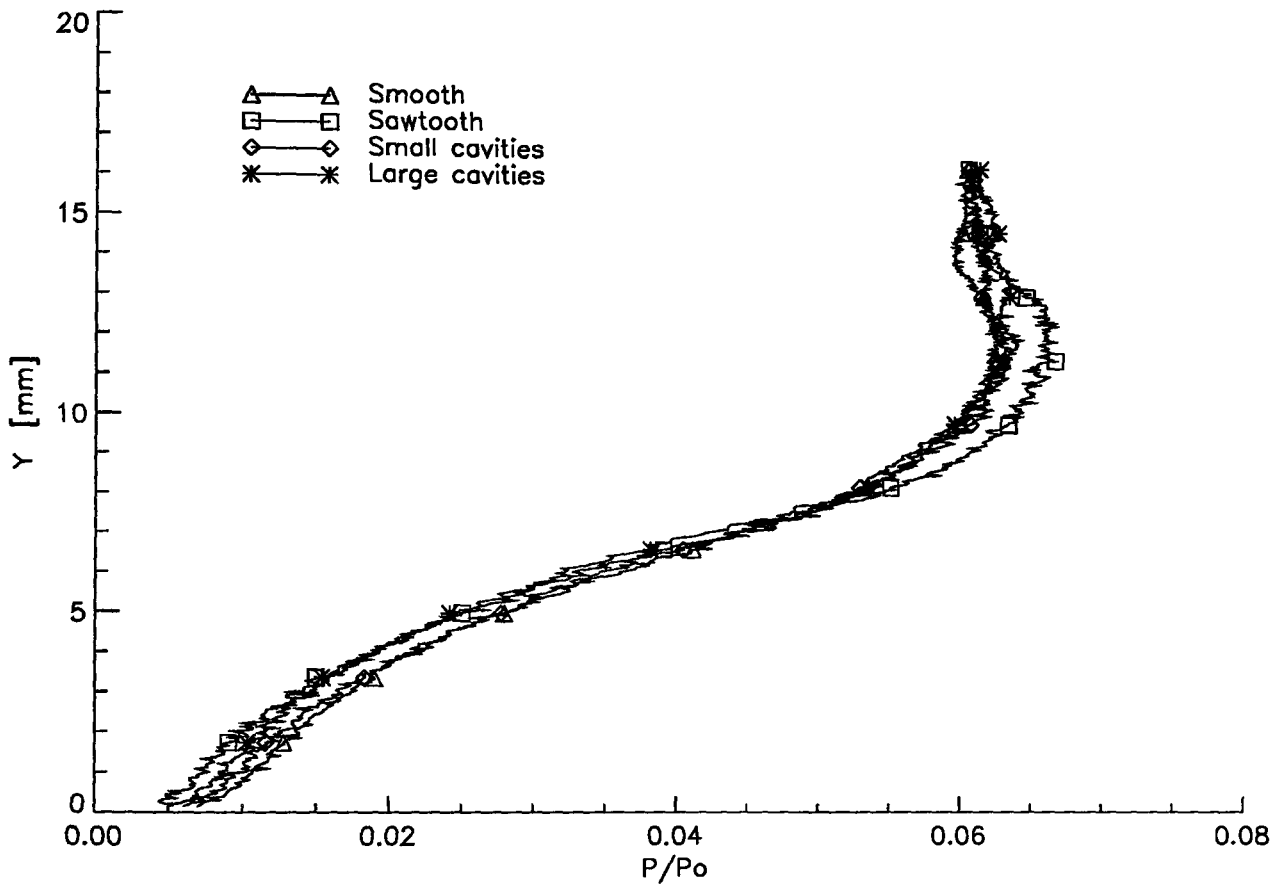

Fig. A.1 Pitot pressure traverses at X=-50

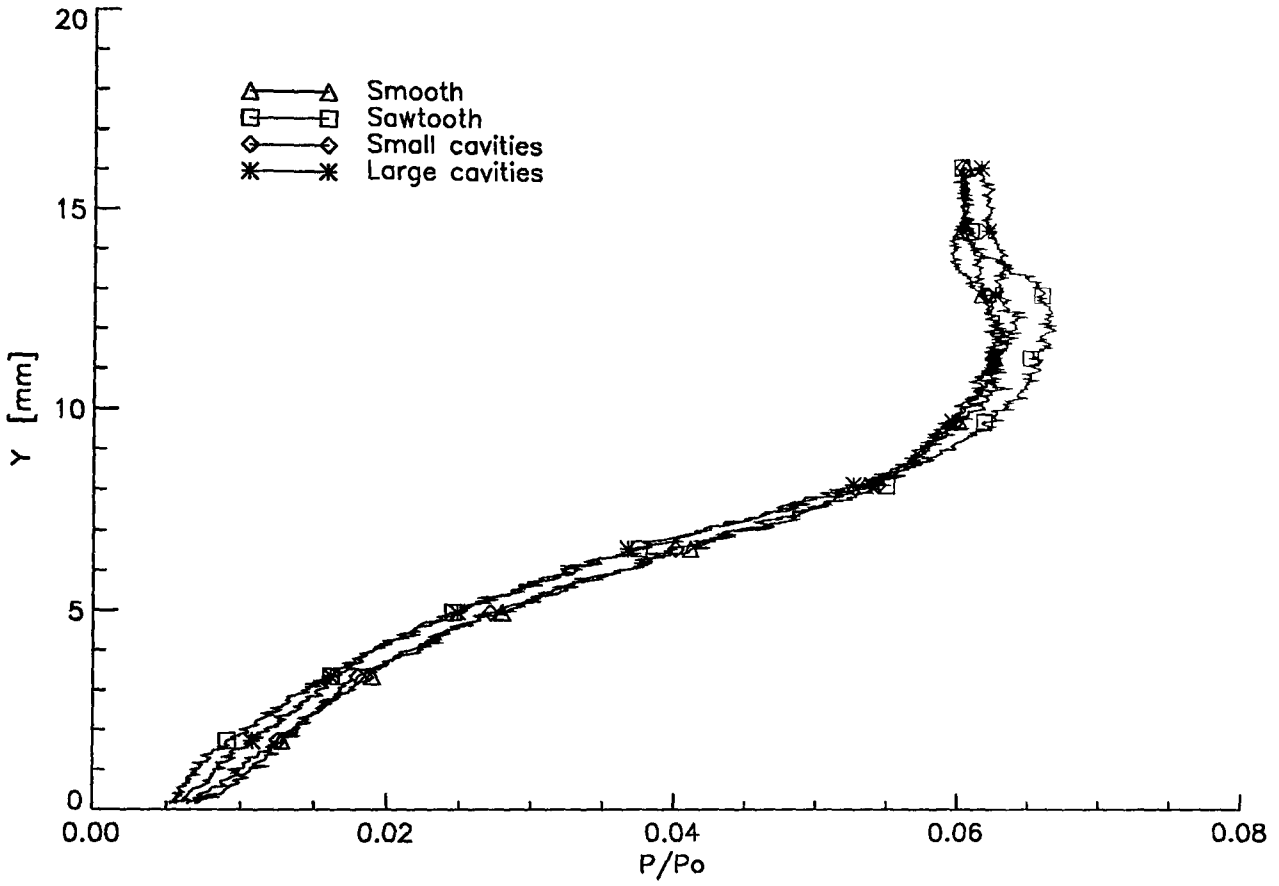

Fig. A.2 Pitot pressure traverses at X=-47

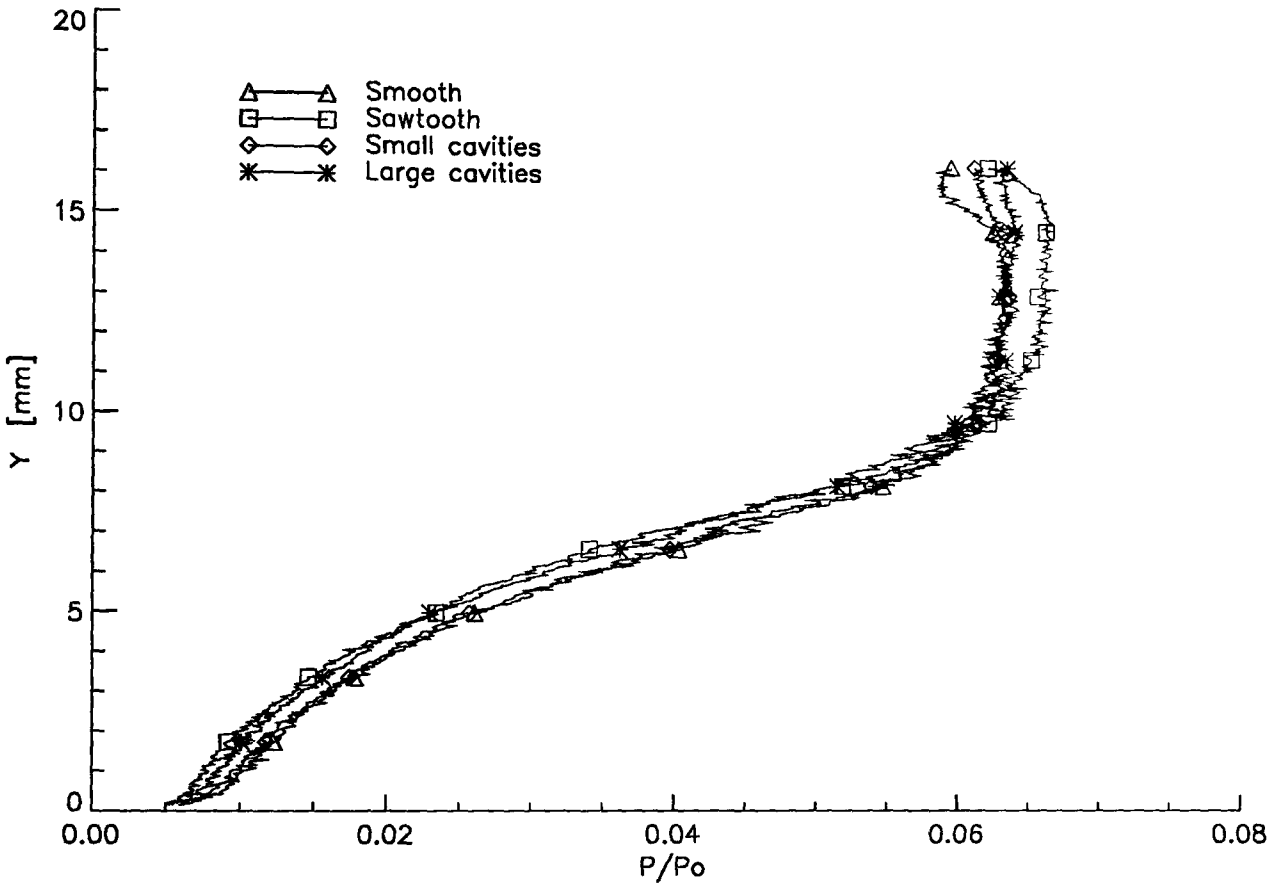

Fig. A.3 Pitot pressure traverses at X=-37

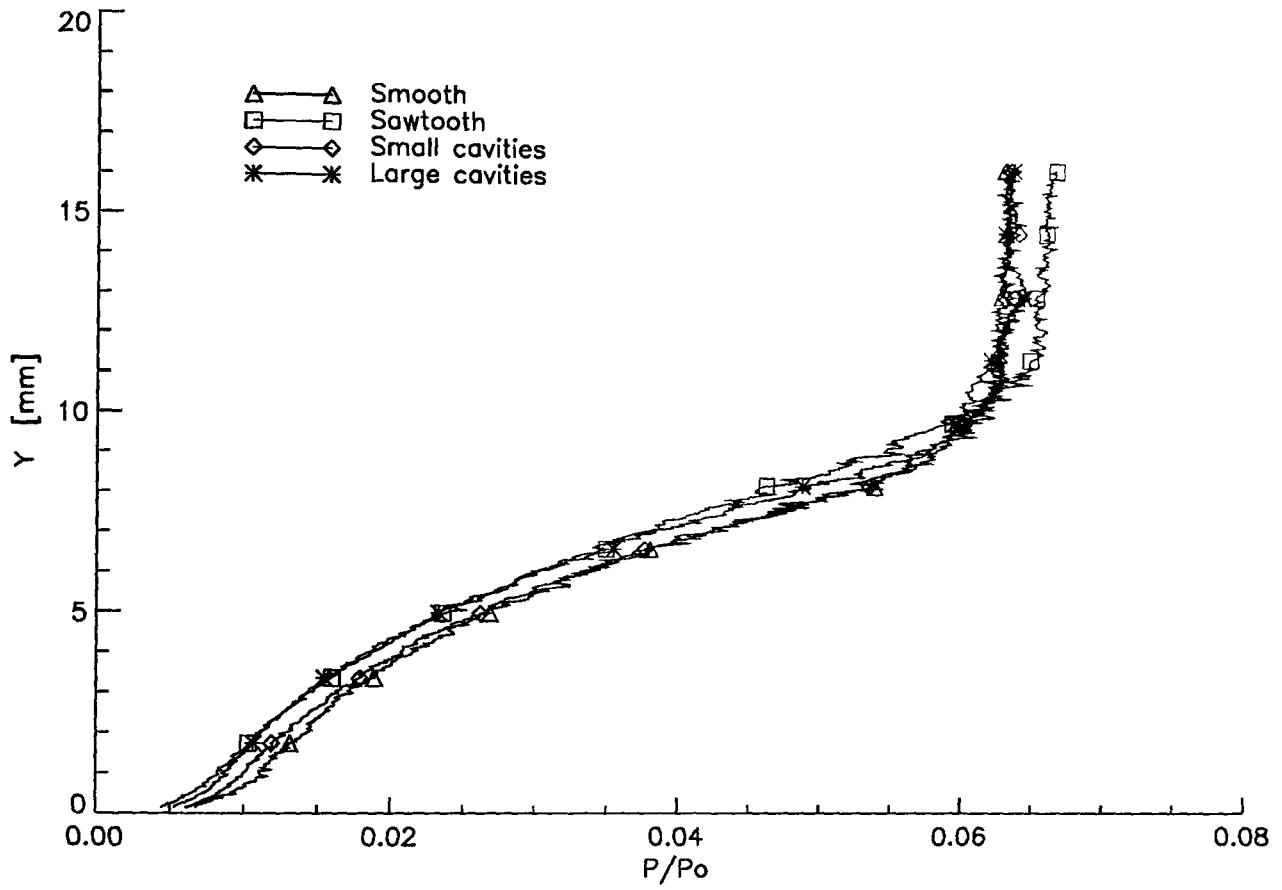

Fig. A.4 Pitot pressure traverses at X=-27

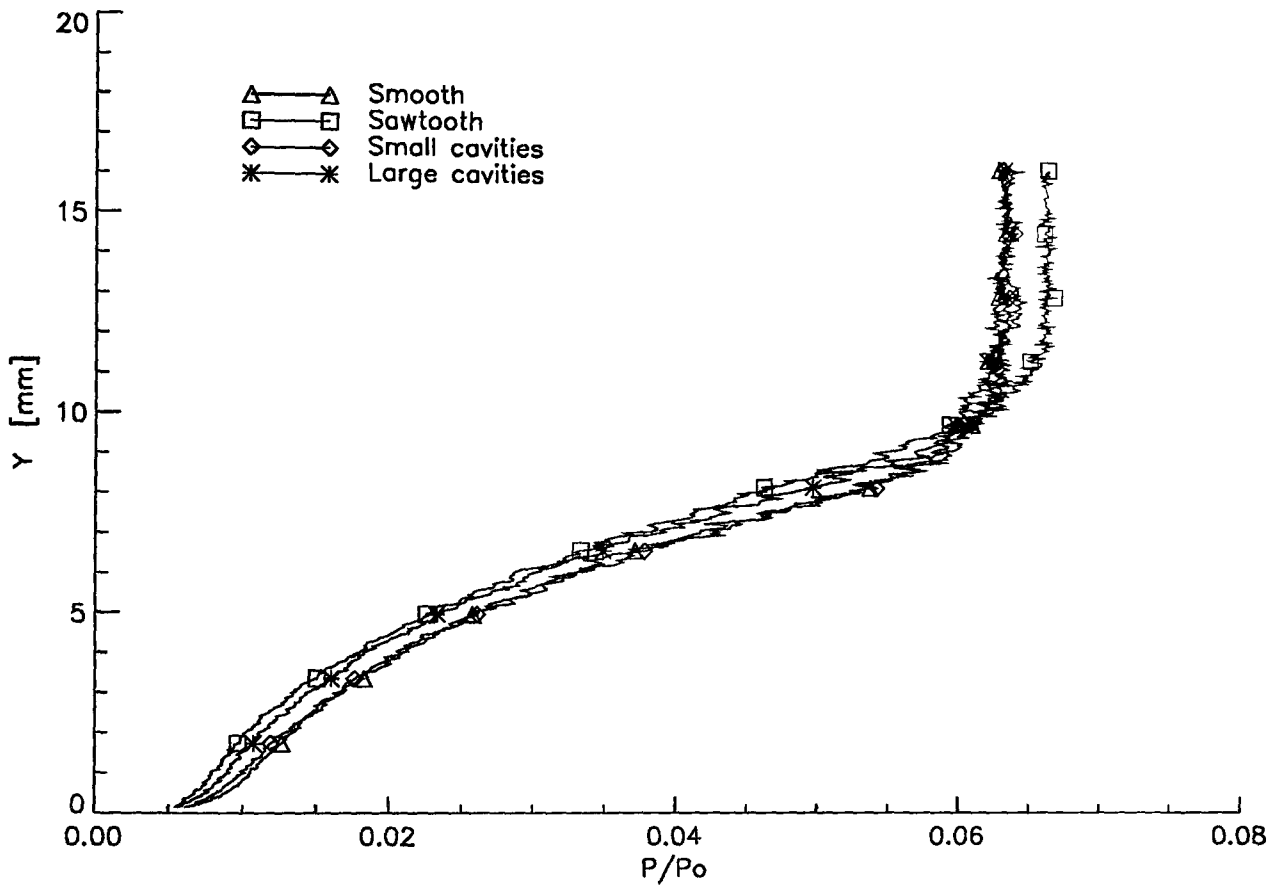

Fig. A.5 Pitot pressure traverses at X=-27. Flare angle: 15°

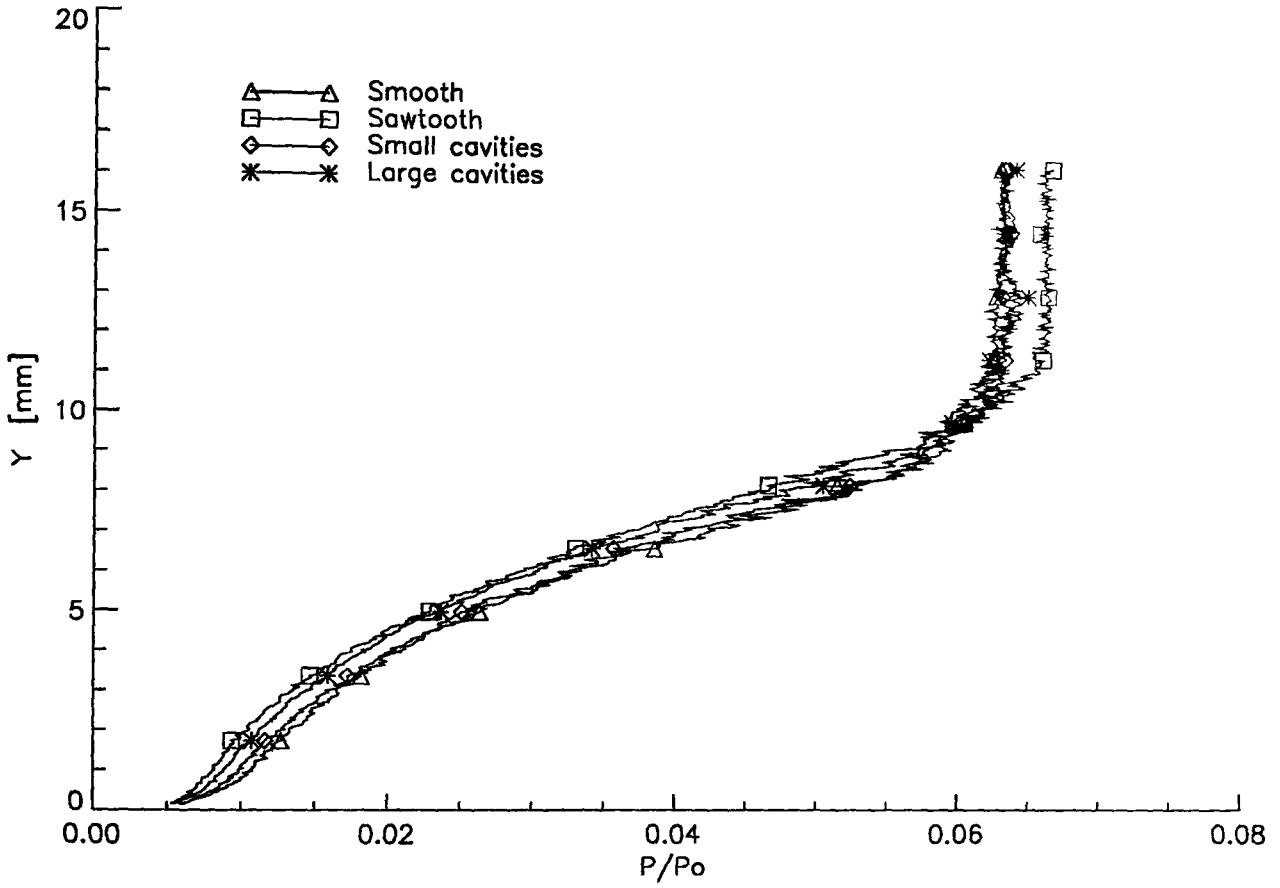

Fig. A.6 Pitot pressure traverses at X=-27. Flare angle: 20°

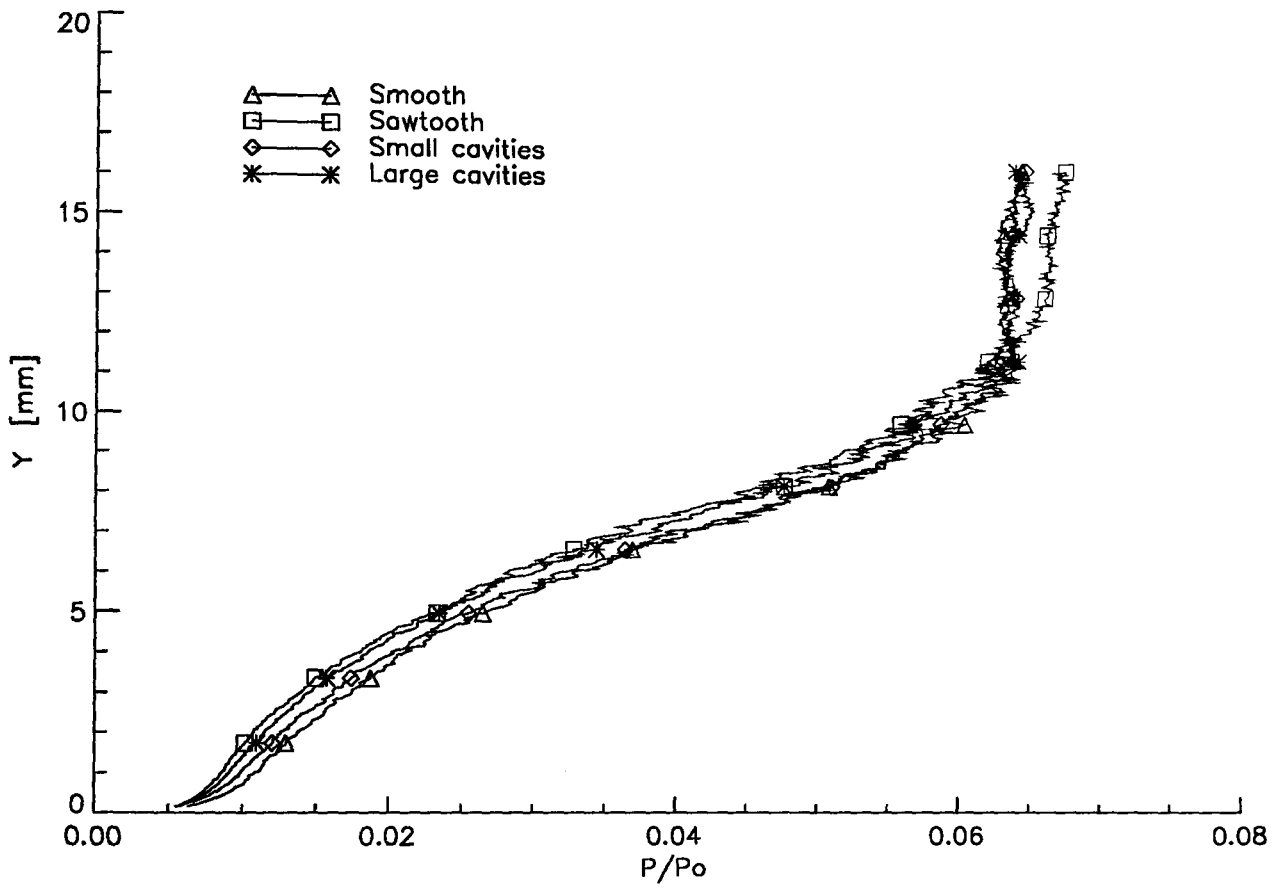

Fig. A.7 Pitot pressure traverses at X=-18. Flare angle: 15°

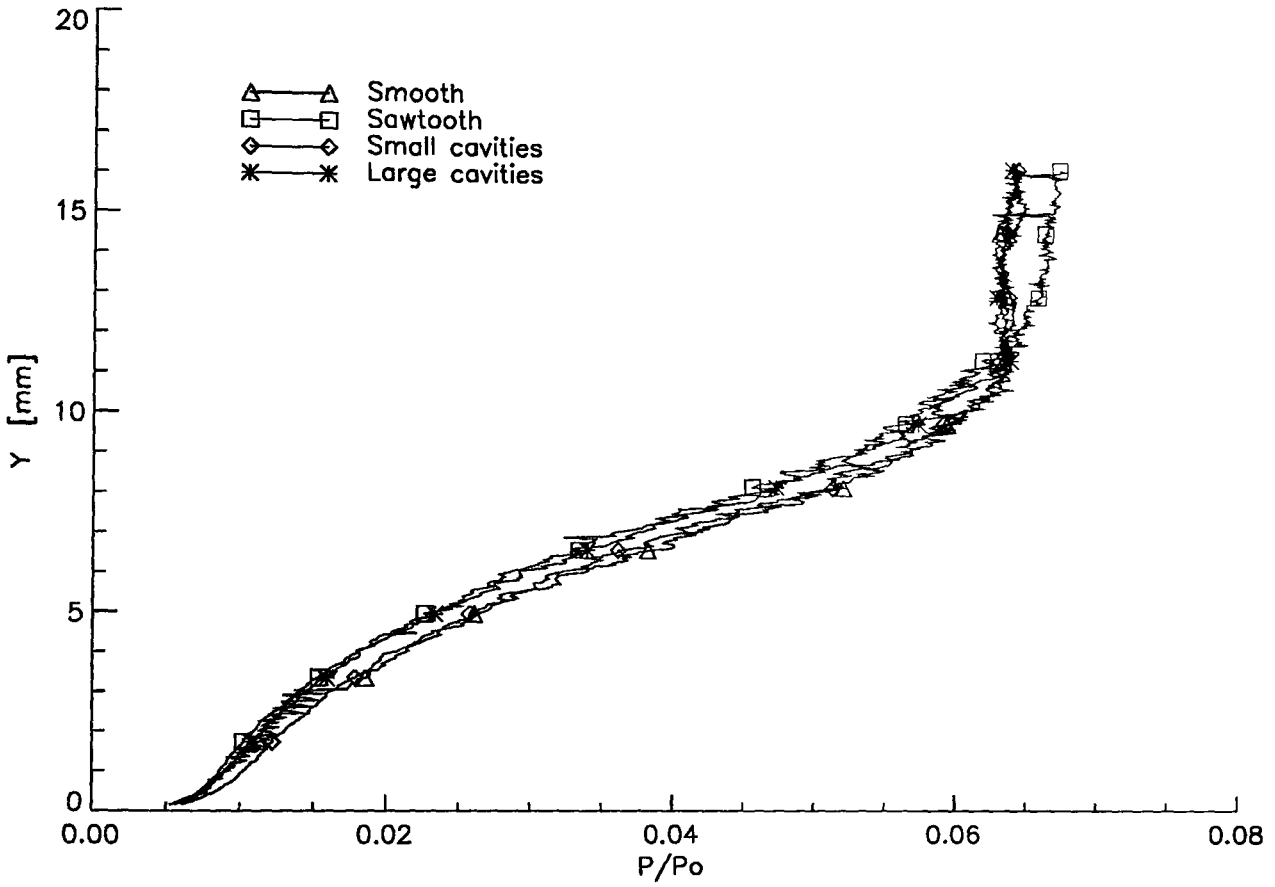

Fig. A.8 Pitot pressure traverses at X=-18. Flare angle: 20°

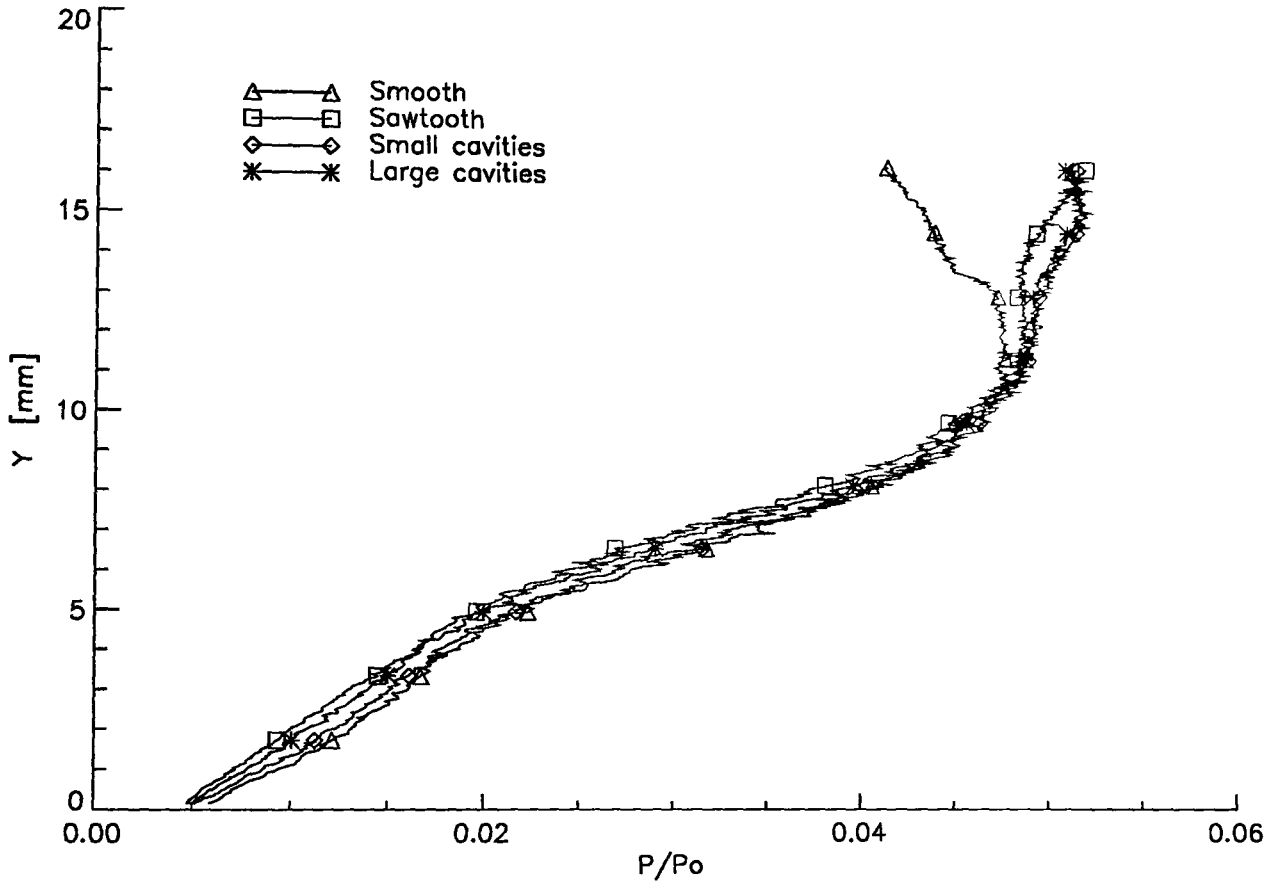

Fig. A.9 Pitot pressure traverses at X=3. Flare angle: 15°

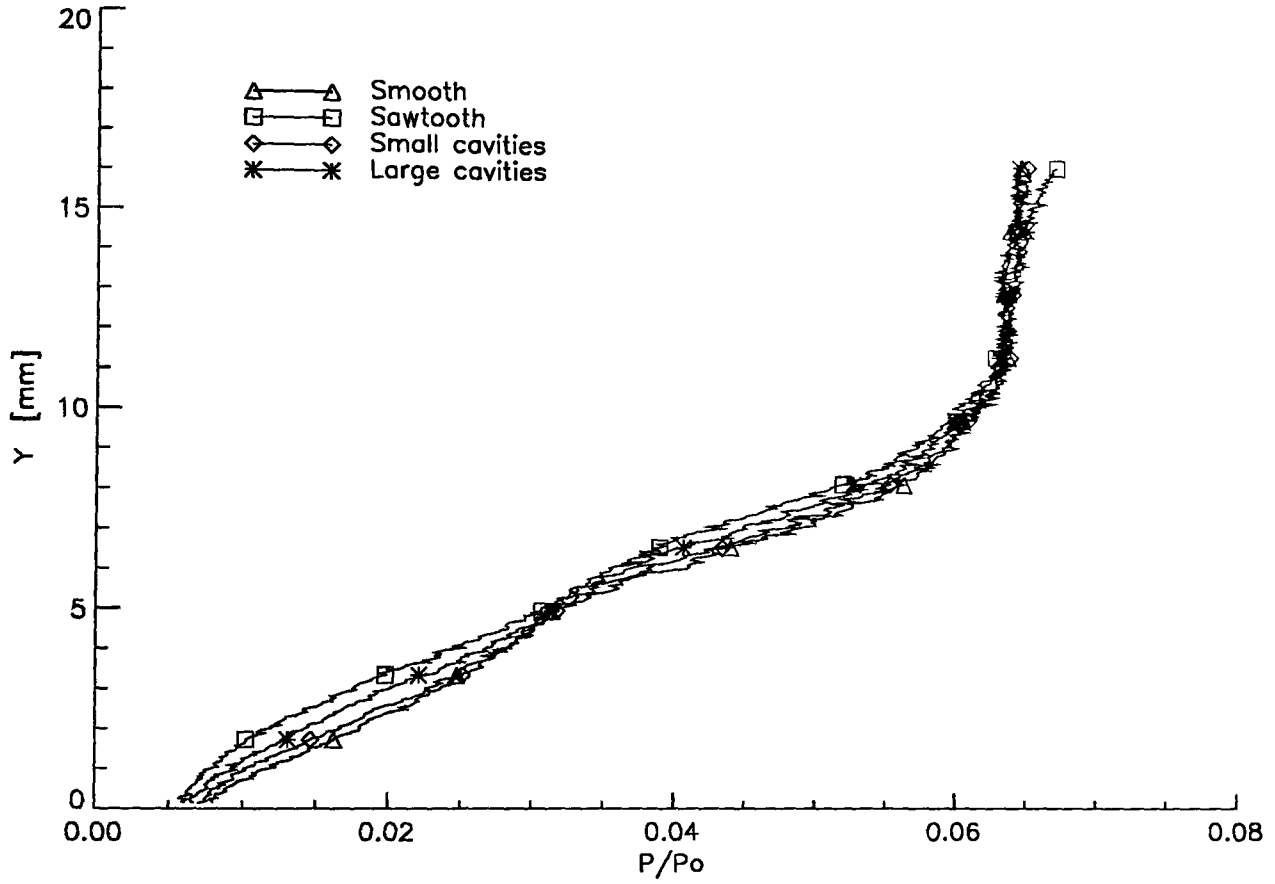

Fig. A.10 Pitot pressure traverses at X=3. Flare angle: 20°

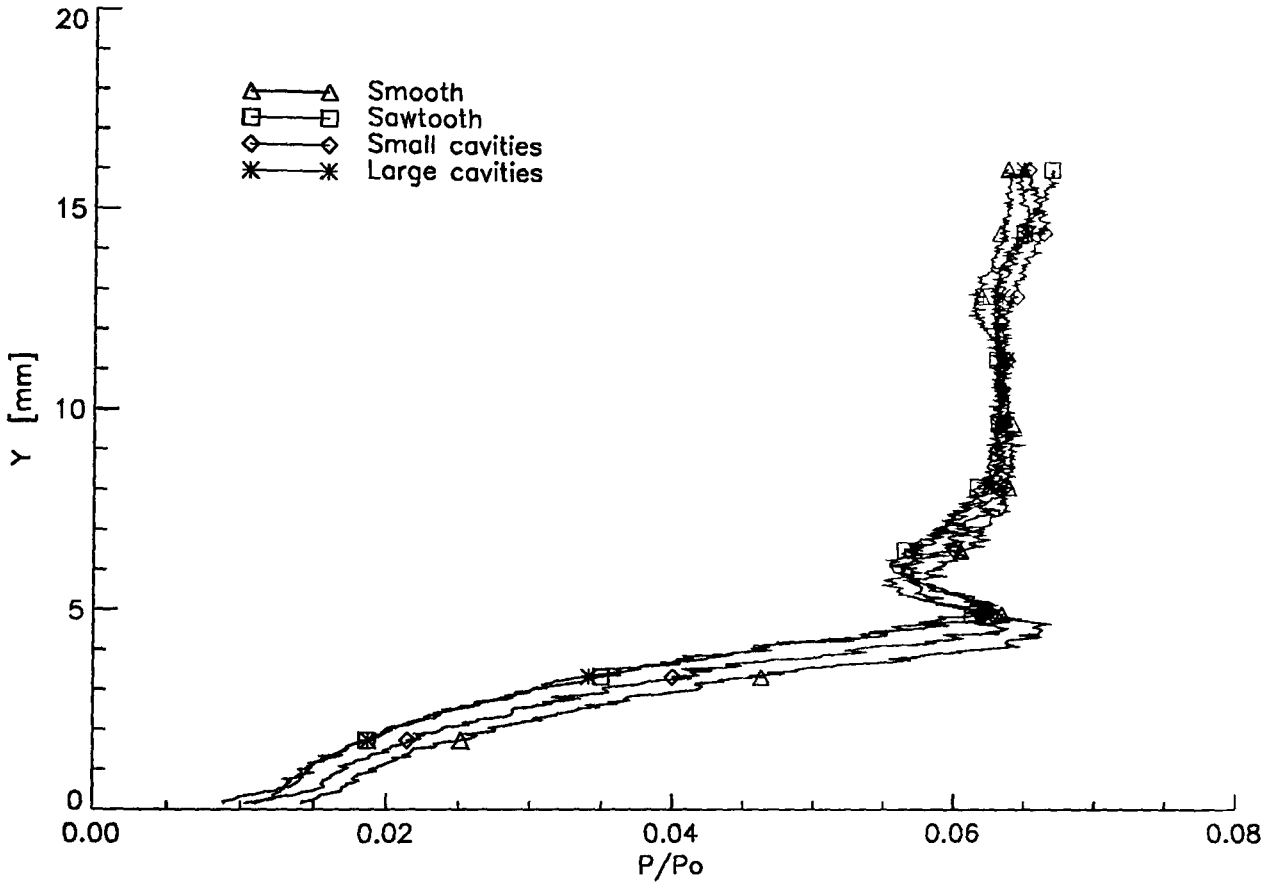

Fig. A.11 Pitot pressure traverses at X=13. Flare angle: 15°

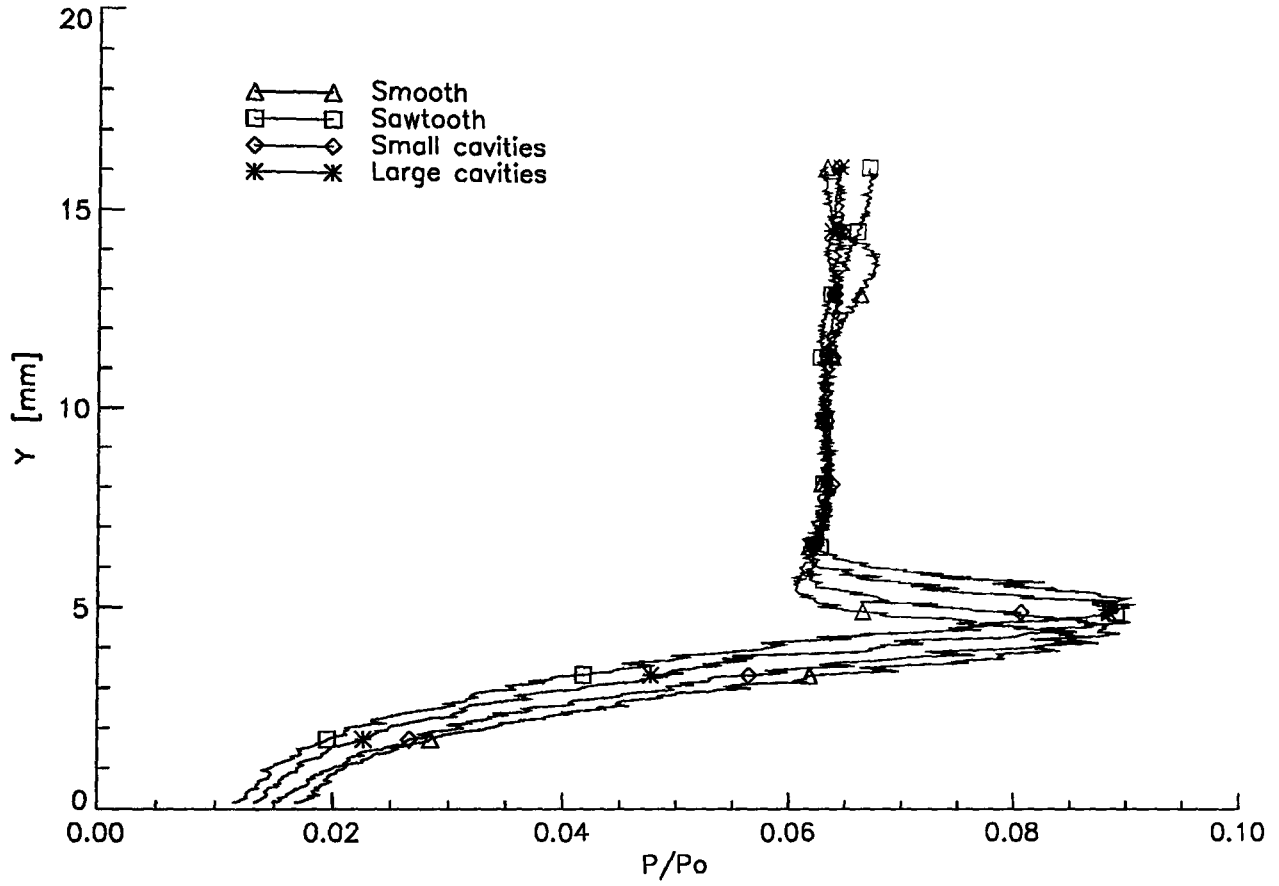

Fig. A.12 Pitot pressure traverses at X=13. Flare angle: 20°

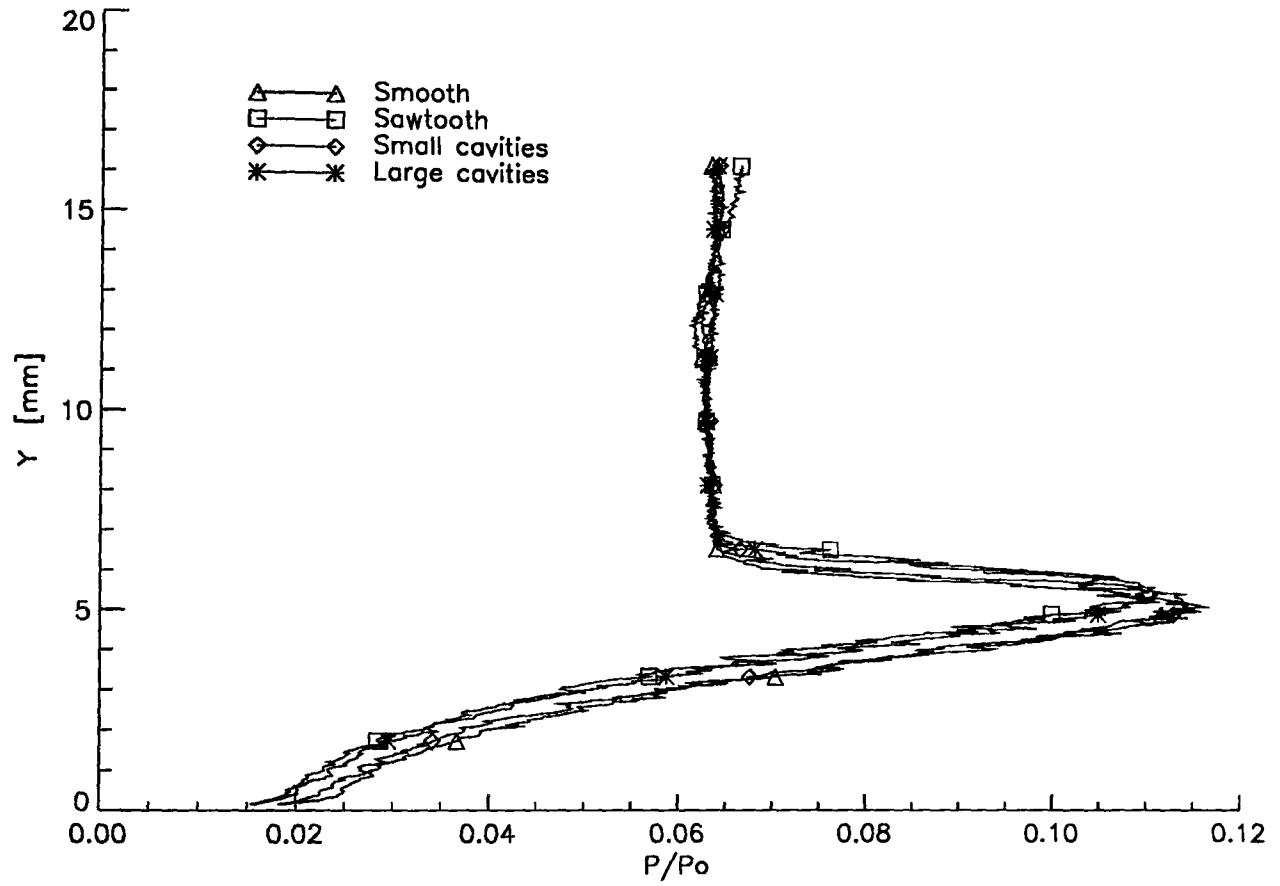

Fig. A.13 Pitot pressure traverses at X=23. Flare angle: 15°

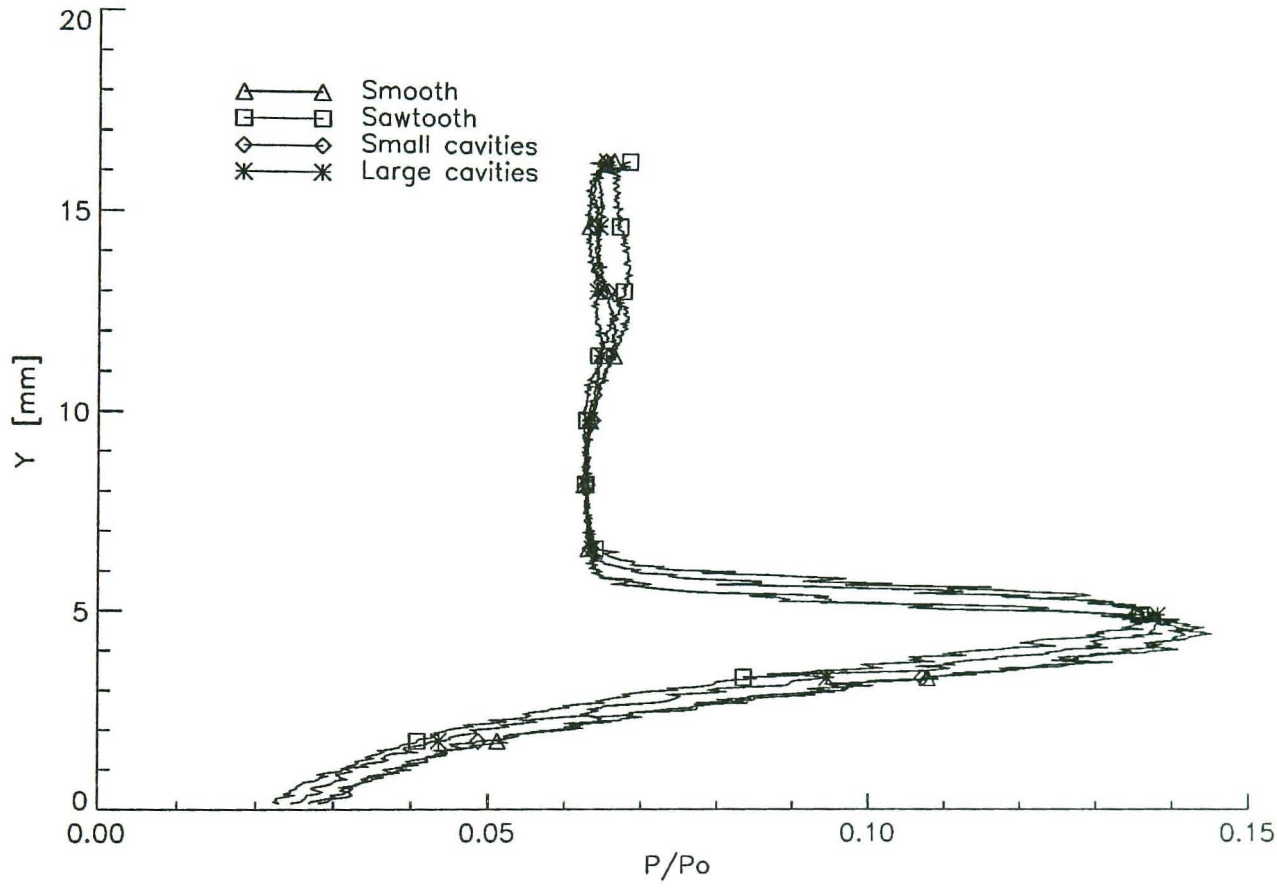

Fig. A.14 Pitot pressure traverses at X=23mm. Flare angle: 20°